Mutual Proximity Effects in Hybrid Superconducting-Ferromagnetic Nanostructures

James Wells

Royal Holloway College
University of London

A dissertation submitted to the University of London
for the degree of Doctor of Philosophy

October 2013

Declaration of Authorship

I James Wells hereby declare that this thesis and the work presented in it is entirely my own. Where I have consulted the work of others, this is always clearly stated.

Signed: _____

Date: _____

Abstract

The project aimed to create hybrid nanostructures consisting of superconducting and ferromagnetic regions and to measure mutual proximity effects within them, these being the penetration of superconductivity into the ferromagnet and the changes on the S-side resulting from an intrusion of the ferromagnet's order. The size and geometry of the ferromagnetic parts of the system were controlled during nanofabrication to create inhomogeneous magnetisation. Recent theory predicted such magnetic structures could produce extraordinary triplet superconductivity penetrating into the ferromagnet over distances impossible for conventional spin singlet superconductivity.

By developing a new technique for shadow evaporations, Andreev interferometers were fabricated to probe the transport properties of the SFS systems. Superconducting phase coherent transport was successfully observed which survived over a distance two orders of magnitude greater than can be explained by singlet spin pairs. Studies were conducted into the contributions of various system parameters in an attempt to improve the yield of samples displaying the superconducting proximity effect, and to better understand the variations observed between different measured samples.

Magnetic force microscopy imaging and subsequent tailoring of the nanoscale ferromagnets for more reproducible magnetic structure were undertaken. The coherence length of the ferromagnet was increased by both raising the purity of the materials in the structure as well as conducting measurements at ultralow temperatures in the mK range. While studying the impact of the ferromagnetic proximity effect, phase diagrams were established with regions corresponding to normal, superconducting and gapless states. Great success was achieved in controlling the suppression of a proximity superconductor via the addition of a carefully controlled thin oxide layer at the interface. Based on the ferromagnetic proximity effect a novel Andreev interferometer was developed.

Acknowledgements

First I would like to offer my sincere thanks to my supervisor Professor Victor Petrashov, whose continuous guidance and support have been an indispensable help throughout the project. From the department at Royal Holloway I would like to thank Dr Rais Shaikhaidarov, Dr Chris Checkley, Dr Richard Marsh and Connor Shelly for their input and advice on matters both technical and theoretical. Technical assistance from Massimo Venti, Francis Greenough and Ian Murray was also greatly appreciated. I would like to thank Olga Kazakova at the National Physical Laboratory for allowing me access to their Magnetic Force Microscopy apparatus.

Enlightening discussions were enjoyed with Dr Ray Davis, Dr Andrea Iagallo and Dr Vladimir Antonov. I would also like to extend my thanks to those members of the Royal Holloway department who have contributed to my enjoyment of the last four years. These include Dr Chris Harrison, Paco Cordobes, Dr Lev Levitin, David Voneshen, Toby Willis, Terence Giles, Kristian Kent, George Nichols, Dr Aya Shibahara, Dr Uthay Sivaperumal, James Poulton and Robert Cantrill.

Most importantly I would like to thank my mother and my sister for their unwavering support over the years, and my girlfriend Claire for all she has done for me and her patience during my research. My father did not live to see me complete this project, but without his engaging me in physics from a young age and his continuous encouragement over the years it is unlikely that I would have pursued my education to this level. For this I am thankful.

Contents

List of Figures

List of Tables

Chapter 1

Introduction

The aim of this project was to investigate the mutual effects of ferromagnetic and superconducting components upon each other when included within composite nanostructures. Experiments were designed to investigate both the penetration of the superconducting order parameter into adjacent ferromagnetic material, as well as the establishing of ferromagnetic order within the superconductor close to the interface. The leaking of supercurrent from a superconductor into a touching normal metal was first observed by Holm and Meissner in 1932 [1]. This process, known as the proximity effect, has been extensively researched in the decades since and a wide range of literature published on the subject. More recently a new class of hybrid ferromagnetic-superconducting nanodevices have emerged where mesoscopic ferromagnetism and superconductivity come together, with great prospects for fundamental physics and practical applications [2].

This new area of research has come about due to recent advances in the understanding of how superconductivity penetrates into a strongly polarised ferromagnetic conductor with an exchange energy much larger than the superconductor's energy gap. This penetration depth was previously regarded as being negligible due to the coherence length within the ferromagnet (ξ_F) being extremely short ($\xi_F = \sqrt{\hbar D/2\pi K_B T_{\text{Curie}}} < 5\text{nm}$ where D is the diffusion constant of the ferromagnet and T_{Curie} is the Curie temperature). Conventional singlet Cooper pairs, consisting of electrons with opposite spins and momenta, cannot survive over distances greater than ξ_F in a ferromagnet as they are destroyed by the exchange field differently influencing the two spin bands. This short-range singlet proximity effect has been well investigated and documented.

It was quickly realised that triplet Cooper pairs with parallel spins are impervious to the exchange field, and various mechanisms of triplet pairing were proposed [3]. However, these early suggestions for triplet pairing were still limited to very short penetration ranges. Their symmetry requirements were incompatible with the frequent elastic scattering occurring within such diffusive conductors, as a result they would only survive over a few nanometers.

This picture was brought into question by several experimental results in the late 1990s and early 2000s [4–7] that indicated the possibility of a much longer range proximity effect in strong disordered ferromagnets. Spurred on by this new evidence, new theoretical activity has produced novel mechanisms for the generation of long-range parallel spin triplet pairs which are tolerant to both elastic scattering processes and the exchange field of a ferromagnet [8]. This new breed of triplet is not created within homogeneous ferromagnetic material, but instead requires a short-range inhomogeneity in the magnetic structure close to the F/S interface. The penetration of this new breed of triplet Cooper pairs is limited to the coherence length within a non-magnetic metal ($\xi_N = \sqrt{\hbar D/2\pi K_B T}$ where T = temperature of system) which is orders of magnitude larger than ξ_F, allowing superconducting proximity effects to penetrate hundreds of nanometers into strongly ferromagnetic material. These new ideas were initially investigated and further experimental evidence obtained via the incorporation of intrinsically inhomogeneous magnetic structures such as the rare earth metal holmium and magnetic multilayers into proximity effect experiments [9–11].

The newly emerging mesoscopic class of magnets, where the magnetic structure may be engineered via its geometry, offers an environment where inhomogeneities can be specifically crafted into magnetic structures. Lying at the border between objects so small that they behave as single dipoles and larger ones which divide into multi domain structures, such magnets have already received a large amount of attention for their potential applications in high density information storage and spintronics [12–14]. Several stable magnetic states such as the magnetic vortex have been successfully imaged after having been predicted within certain geometries by modelling [11, 15].

In this project, nanoengineered ferromagnets and superconducting wires were fabricated in composite stuctures using novel techniques to produce Andreev interferometers. The transport properties of these nanostructures were then measured at

low temperature with the aim of observing a long-range superconducting proximity effect within the ferromagnetic material and investigating the wider behaviour of the system. Using this technique, evidence was observed of a superconducting proximity effect penetrating the ferromagnet over a distance two orders of magnitude larger than allowed for singlet Cooper pairs.

Further studies were conducted in an attempt to improve the yield of coherent samples, investigate the variations in the data obtained and ascertain their contributions to the observed effects. Magnetic force microscopy imaging of fabricated structures was carried out, as well as changes to the compositions of the hybrid nanostructures and the experimental temperature.

A study of the decoupling effect of an oxide barrier at the F/S interface was conducted to investigate how this effected the ferromagnetic proximity effect. This investigation also rendered a new method of producing short SNS junctions suitable for use in a novel type of Andreev interferometry with the potential for magnetometry and read out of superconducting states. In addition to this, new phase diagrams were obtained showing the behaviour of such induced SNS junctions.

Chapter 2

Background

This initial chapter introduces the areas of physics underpinning the project. The first sections discuss superconductivity, its phenomena and its applications in nanostructures. The existing evidence, both theoretical and experimental, for a long-range proximity effect in ferromagnetic material is then examined. The field of geometrically engineered mesoscopic ferromagnets is introduced next, while the final part covers the effect of a ferromagnet on a proximity superconductor, known as the ferromagnetic proximity effect.

2.1 Superconductivity and Superconducting Proximity Effects

The realisation that electrical resistance drops suddenly to zero within some materials when cooled below a certain temperature triggered one of the great subjects of scientific research in the last century. Intensive study of the phenomenon has revealed many unusual effects related to it, and unlocked much of the underlying physics. This section introduces some of the key aspects of superconductivity relevant to the project. These include flux quantisation, the Josephson effect, the physics of S/N interfaces, Andreev reflection and SNS junctions.

2.1.1 Superconductors

While all materials tend to exhibit a reduction in electrical resistance as their temperature is decreased, until the discovery of superconductivity all materials were assumed to inhibit the flow of current to some finite degree at all temperatures.

The sharp change in behaviour between a finite resistance and dissipationless current flow at a material specific temperature indicated that something dramatic and fundamental had changed within these systems. The complete exclusion of magnetic field from superconducting objects known as the Meissner effect was also noted during early studies. These are the two properties of superconductors which are most well known.

Bardeen, Cooper and Schrieffer provided a microscopic theory of superconductivity in 1957 [16]. In it they showed that electrons in superconducting materials were bound together in pairs of equal and opposite spin and momentum via an attraction arising from the exchange of phonons between them. These Cooper pairs as they were named are held together by an attractive force transmitted between them through the crystal lattice by phonons.

Electrons are particles with a spin of 1/2. Like other fermion types, when grouped in a system in thermodynamic equilibrium they are subject to Fermi Dirac statistics. Discovered by the two scientists independently in 1926 [17, 18], this describes one of the two ways in which a system of indistinguishable particles may be distributed over a set of discrete enegy states. Each energy state may only contain a single particle due to the restriction put in place by the Pauli exclusion principle. At zero temperature the individual electrons pack into the lowest unoccupied energy states, filling all of those available up to a state known as the Fermi level.

By joining into pairs with equal and opposite spin and momentum, however, the electrons can form an entity which has a total spin of zero and thus behaves as a boson. As such they are subject Bose Einstein statistics which is the second possible set of rules which can dictate how particles are distributed over energy states. Particles subject to this rule set are known as bosons and are not limited to single occupancy of energy states. As a consequence at low temperature they are able to undergo Bose-Einstein condensation and co-occupy the lowest energy state, below that of the unpaired electrons at the Fermi energy. As bosons are not subject to Fermi Dirac statistics or the Pauli exclusion principle they are all capable of occupying the same energy state and as a consequence can be described by a single coherent wavefunction.

$$|\Psi(r,t)|exp(i\phi(r,t)) \tag{2.1}$$

Despite a superconductor containing a vast number of individual charge carriers, it can be described by a single macroscopic wavefunction. Several important implications of this macroscopic quantum behaviour are described in the following sections.

Flux Quantisation

One of the consequences of the macroscopic quantum wavefunction of a superconductor is flux quantisation. In essence this rule forces the flux cutting a superconducting loop to assume integer multiples of value known as the flux quantum

$$\Phi_0 = \frac{h}{2e} = 2.067833758\text{x}10^{-15} \text{ Wb} \tag{2.2}$$

This quantisation of the flux is due to the phase of the superconductor being limited to an integer number of complete "oscillations" around the circumference of the loop, meaning that the phase change over one complete turn of the loop must be zero or an integer multiple of 2π.

The wavelength of the electron pairs within a superconductor is related to the momentum P of their centre of mass by the de Broglie relationship

$$\lambda = \frac{h}{P} \tag{2.3}$$

We shall consider the case of a superconductor connecting two points X and Y. If there is no current flowing between the two points then the momentum of the electron pairs will be zero and the wavelength will be infinite. As a consequence the phase of the electron-pair wave is the same at points X and Y.

If a constant supercurrent passes between X and Y then the electron pairs will have a momentum P and the electron-pair wavelength will become finite. As a result a phase difference $(\Delta\phi)_{XY}$ will exist between the points X and Y, which remains constant in time [19] . The phase difference between two points which a plane wave is travelling past is given by

$$(\Delta\phi)_{XY} = \phi_X - \phi_Y = 2\pi \int_X^Y \frac{\hat{\text{x}}}{\lambda}.d\text{l} \tag{2.4}$$

where $\hat{\text{x}}$ is a unit vector in the direction of the wave propogation and and dl is an element of a line joining X and Y. As already stated for the electron-pair wave

$\lambda = h/P$ and the momentum of a pair $P = 2mv$ where m is the electrons mass and v the velocity of the pairs in the current which is related to the supercurrent density J_s by $\mathrm{J}_s = \frac{1}{2}n_s.2e.v$ where n_s is the density of superelectrons. Using these relations the wavelength can be shown to be equivalant to

$$\lambda = \frac{hn_s e}{2m\mathrm{J}_s} \tag{2.5}$$

Given that the direction of the supercurrent flow is parallel to $\hat{\mathrm{x}}$ the phase difference between the points X and Y due to the current is

$$(\Delta\phi)_{XY} = \frac{4\pi m}{hn_s e}\int_X^Y \mathrm{J}_s.d\mathrm{l} \tag{2.6}$$

Applied magnetic fields also have powerful effects on the phase of the electron pair wave. The momentum of electron pairs in a magnetic field takes the form $P = 2mv + 2eA$ where A is the magnetic vector potential. As a result when in the presence of a magnetic field, the phase difference between the points X and Y is given by the following expression in which the first term can be regarded as the phase difference due to the current and the second term as being the phase difference due to the magnetic field

$$(\Delta\phi)_{XY} = \frac{4\pi m}{hn_s e}\int_X^Y \mathrm{J}_s.d\mathrm{l} + \frac{4\pi e}{h}\int_X^Y \mathrm{A}.d\mathrm{l} \tag{2.7}$$

If the line of superconductor between X and Y is then extended to join points X, Y, Z and X in a closed loop then the change in phase around this loop is equal to

$$(\Delta\phi) = \frac{4\pi m}{hn_s e}\oint \mathrm{J}_s.d\mathrm{l} + \frac{4\pi e}{h}\oint \mathrm{A}.d\mathrm{l} \tag{2.8}$$

By the application of Stokes' theorem, and given that the curl of the magnetic vector potential gives the magnetic field (B), this can be treated in the following way where S is the area contained inside the loop.

$$(\Delta\phi) = \frac{4\pi m}{hn_s e}\oint \mathrm{J}_s.d\mathrm{l} + \frac{4\pi e}{h}\int\int_S \mathrm{B}.d\mathrm{S} \tag{2.9}$$

As the wavefunction of the superconductor must be single valued at any point [20], the total change in flux over one complete loop must always equal $2\pi n$ where

n is an integer. From this we obtain

$$\frac{m}{n_s e^2} \oint \mathrm{J}_s.d\mathrm{l} + \int\int_S \mathrm{B}.d\mathrm{S} = n\frac{h}{2e} \tag{2.10}$$

The left part of the above was named the fluxoid enclosed by the path by F. London and is given the symbol ϕ'. It comprises the line integral of the current density around the loop as well as the magnetic flux threading the loop. As the wavefunction of the superconductor must be single valued, the fluxoid is constrained to taking the values of integer multiples of the flux quantum $\Phi_0 = h/2e$.

2.1.2 Gapless Superconductivity

Conventional superconductors exhibit a gap in available energy states above that occupied by the Cooper pairs and below those occupied by the lowest energy quasi-particles. Δ denotes the magnitude of the energy gap within a superconductor. The first measurement proving the existence of the superconducting energy gap was published by Corak in 1946 [21].

In a conventional superconductor under certain conditions it is possible for the energy gap to be zero while the superconducting state is maintained [22]. By doping the superconducting material with a magnetic impurity, profound changes can be made by both increasing the critical temperature and decreasing the size of the energy gap. A small percentage of magnetic impurity in a material can completely destroy superconductivity within it. By plotting the energy gap size against T_c over a range of impurity concentrations it becomes apparent that Δ is reduced at a faster rate than T_c. At certain impurity concentrations the energy gap disappears while the sample itself remains superconducting.

As will be examined in later sections, magnetic impurities within a superconductor are destructive to conventional singlet Cooper pairs. As the proportion of magnetic impurity is increased, the fraction of Cooper pairs being decohered into free electrons increases. As long as some Cooper pairs remain, the material can still carry a supercurrent. Eventually, the level of spin polarisation from the magnetic doping means that no Cooper pairs can exist and the capacity to carry supercurrent drops to zero. A phase exists where the level of doping is sufficient that a supercurrent can be carried by the remaining Cooper pairs, and yet the free electron component is sufficient to allow radiation to be absorbed at arbitrarily low energies.

The low energy states normally prohibited by the energy gap are able to be filled, and thus the energy gap will drop to zero.

Gapless superconductivity can similarly be induced by the application of a large external magnetic field or current applied through the material, in each case the principles are similar, with a proportion of the Cooper pairs being broken and some remaining.

2.1.3 Josephson Effects

The possibility of quantum tunnelling of single electrons was first suggested early in the 20th century. By the middle of the century the capacity for single particles to tunnel through barriers which would be classically insurmountable was widely acknowledged. Single electron tunnelling may occur between two normal metals separated by a thin barrier provided that the total energy of the system is conserved and that there is an empty state for the electron to tunnel into.

Before 1962 dissipationless supercurrents had been observed passing between superconductors separated by a thin insulating layer, these results had been attributed to tiny imperfections in the insulating layer allowing minute short circuits to exist around the insulator. In 1962 Brian Josephson [23] predicted the behaviour of such a supercurrent tunnelling across a thin barrier and the hunt for definitive proof was on. Anderson and Rowell provided the first experimental proof in 1963 [24]. The discovery of the ability of Cooper pairs to tunnel introduced an exciting new field of research in superconductivity.

As the gap between two separate independent superconductors is made very small, Cooper pairs begin to be able to tunnel across the gap, and the wavefunction of the superconductors becomes coupled. Further reduction of the separation will result in the interaction between the superconductors increasing and the phases of their waves becoming more and more intertwined. If the separation is reduced to zero then they will behave as one continuous superconductor, there will be one definite relation between the phases throughout both objects.

If the separation of two superconductors is suitably small then a continuous flow of Cooper pairs will tunnel across it, maintaining their pairing in the process. This produces a continuous supercurrent flowing across the junction with an upper limit dictated by a critical current I_c. For two superconductors with phases ϕ_1 and ϕ_2

the phase difference between them over a weak link in the absence of an applied external magnetic field is

$$\Delta\phi = \phi_1 - \phi_2 \tag{2.11}$$

In the case of a short junction placed within a non-zero magnetic field however the equation 2.11 is not gauge invariant [25]. The gauge invariant phase difference for such junctions in the presence of a magnetic vector potential (A) is given by

$$\Delta\phi = \phi_1 - \phi_2 - \frac{2\pi}{\Phi_0}\int_2^1 A.dl \tag{2.12}$$

where 1 and 2 are points directly opposite across the junction barrier and Φ_0= the magnetic flux quantum

The supercurrent traversing the weak link(I_s) is then given by

$$I_s = I_c sin\Delta\phi \tag{2.13}$$

This relationship relates the size of the tunnelling current in the junction to the phase of the superconductor on either side. As a result the supercurrent is at a maximum when $\Delta\phi = \frac{\pi}{2}$ at which point $I_s = I_c$.

If there is some variation in the Josephson current over time, a voltage will develop across the gap between the superconductors. This voltage is dependent on the rate of change of the phase difference and is given by

$$2eV = \hbar\frac{d\Delta\phi}{dt} \tag{2.14}$$

where t = time. Equations 2.13 and 2.14 represent the fundamental Josephson equations which describe the behaviour of a Josephson junction.

The weak link that forms a Josephson junction may take many forms and could be a thin layer of oxide or some other insulator (SIS) junction, a thin section of normal material (SNS junction), a constriction in the wire or a point contact.

S/N Interfaces

It was noted by Holm and Meissner in 1932 [1] that a normal metal brought into contact with a superconductor experiences variations to its conductance within the region closest to the boundary. Known as the proximity effect, this phenomenon

consists of Cooper pairs diffusing from the superconductor into the normal region and maintaining phase coherence over a distance ξ_N to allow the region within ξ_N of the S/N interface to carry a finite supercurrent. The Cooper pair density within the S region closest to the boundary is also subsequently decreased. There is no definite boundary between the S and N regions. The density of Cooper pairs gradually rises moving through the N region towards the interface and into the S region. It is important to note that any impurities within a superconductor or proximity normal material will reduce ξ, and thus inhibit the proximity effect. This means that the fabrication process must be tailored to minimise contamination.

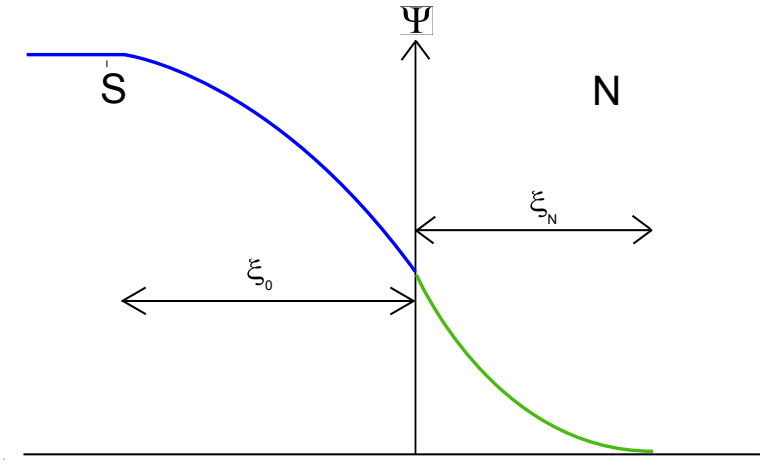

Figure 2.1: Illustration of the decay of the superconducting wavefunction at the interface between the superconducting and normal materials. ξ_0 is the coherence length within the superconductor while ξ_N is the coherence length within the normal metal.

According to Ginzburg Landau theory the square modulus of the superconducting order parameter (Ψ) describes the density of Cooper pairs within the superconductor [26]. Ψ has a value of zero for all temperatures above T_c and a non-zero value below T_c representing how deep into the superconducting phase it is. Moving through the S region towards the interface Ψ begins to decay at a distance from the interface which is equal to ξ_0. Within the normal metal Ψ continues to decay, and is given by e^{-x/ξ_o} where x is the distance from the interface .

The average path length through a material which an electron covers before being scattered is called the mean free path $l = \nu_F \tau$. In many-electron systems, electrons are scattered by interactions with each other and the lattice through which they move. The average distance over which an electron can travel while retaining its phase memory by avoiding inelastic scattering is called the phase coherence length

(Phase Breaking Length) $L_{\phi} = \sqrt{D\tau_{\phi}}$. At low temperatures electron-electron and electron-phonon scattering are both reduced. As a result the phase coherence length increases.

If the dimensions of the normal metal are significantly larger than the mean free path of an electron within it then it is described as being in the "diffusive" or "dirty" limit. The distance over which a Cooper pair may remain coupled within a normal metal is the coherence length (ξ) and within a normal metal in the dirty limit it is given by

$$\xi_N = \sqrt{\frac{\hbar D}{2\pi K_B T}} \tag{2.15}$$

where D = Diffusion constant in the normal metal, K_B = Boltzman constant, T = Temperature

$$D = \frac{v_F l}{3} \tag{2.16}$$

If the dimensions of the normal metal are smaller than l then it is described as being in the "clean" limit and

$$\xi_N = \frac{\hbar v_F}{2\pi K_B T} \tag{2.17}$$

SNS Junctions

An SNS junction as already discussed comprises a short section of normal metal interrupting a superconducting wire. At each interface the wavefunction from the superconductor penetrates the normal metal, gradually decaying over the coherence length ξ_N. If the length of the normal region is less than $2\xi_N$ then the wavefunctions from each of the superconductors will overlap as shown in Fig 2.2. In this eventuality Cooper pairs are able to traverse the entire length of the normal metal while maintaining coherence, and thus a finite supercurrent can pass through it. The critical current (I_c) of the normal metal will be significantly lower than that of the superconducting material itself as the Cooper pair density in this region will be much lower. I_c in an SNS junction was demonstrated by de Gennes [27] to be related to the junctions length (L) by

$$I_c(L) \propto e^{-L/\xi_N} \tag{2.18}$$

the critical current will have a dependence upon the temperature (T) of the form

$$I_c(T) \propto e^{-T/T_0} \tag{2.19}$$

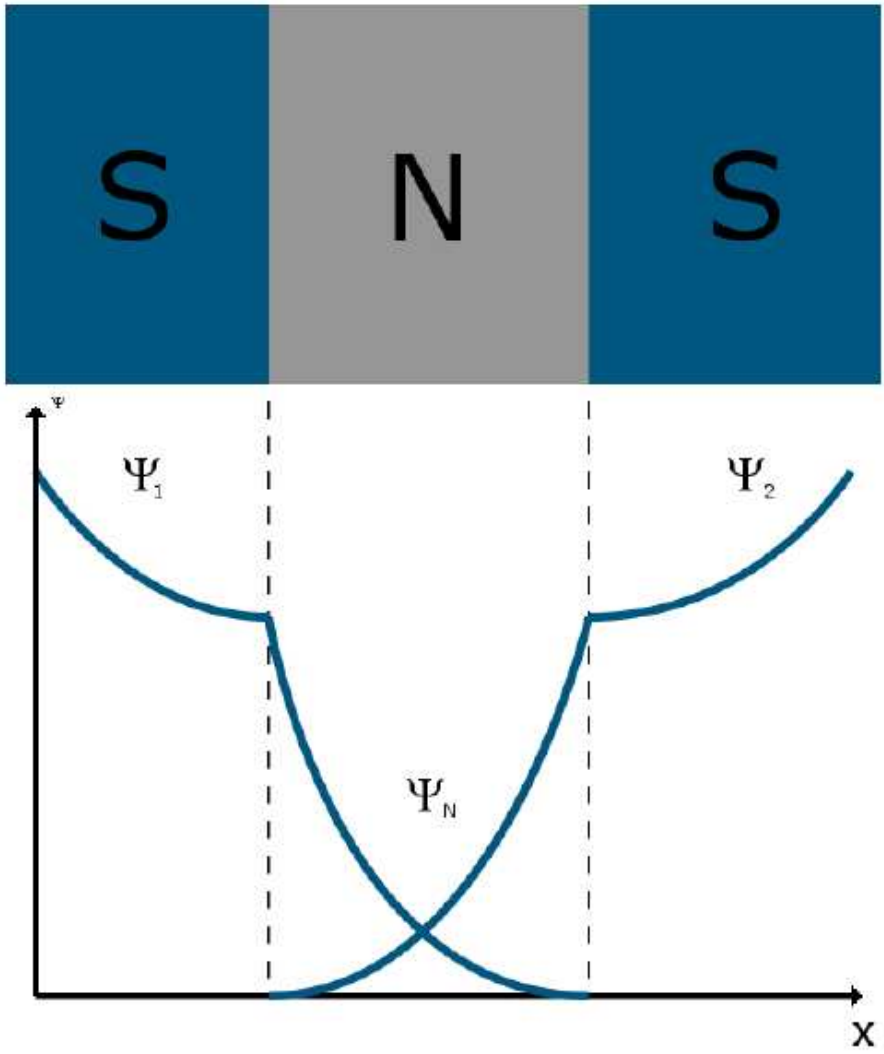

Figure 2.2: Illustration of overlapping wavefunction penetrations within a normal metal from two superconducting contacts [28].

2.1.4 Josephson Critical Current in SNS Junctions

In [29] an experimental and theoretical study of the Josephson effect in diffusive SNS junctions is made. Nb-Cu-Nb junctions were fabricated with highly transparent interfaces and the data obtained from them compared with theoretical results providing excellent quantitative agreement. These studies focused on junctions where the normal metal length was much larger than the elastic mean free path, but smaller than the phase breaking length. An energy is calculated for the junction indicating

the strength of the proximity effect. Called the Thouless energy, this is given by $E_{Th} = \hbar D/L^2$ where $D = \nu_F l_e/3$ is the diffusion constant of the normal metal and L the length of the normal section.

Two different theoretical approaches are employed depending upon whether the sample is at high or low temperature. In the high temperature regime, where $K_B T \gg E_{Th}$, the following expression is applicable within the N region away from the N/S interfaces.

$$eR_N I_c = 64\pi K_B T \sum_{n=0}^{\infty} \frac{L}{L_{\omega_n}} \frac{\Delta^2 exp(-L/L_{\omega_n})}{(\omega_n + \Omega_n + \sqrt{2(\Omega^2 + \omega_n \Omega_n)})^2}$$

where R_N is the normal metal resistance, $\omega_n = (2n+1)\pi K_B T$ known as the Matsubara frequency, $\Omega_n = \sqrt{\Delta^2 + \omega_n^2}$ and $L_{\omega_n} = \sqrt{\hbar D/2\omega_n}$. This temperature range best describes the types of experimental environments attainable using the cryogenic systems available during this project.

At higher temperatures where $\Delta \ll K_B T$ this equation is in good agreement both with the experimental data described within the publication and also the previously obtained theoretical predictions by Likharev [30].

At lower temperatures, where $K_B T \lesssim E_{Th}$ the calculation is far more complicated. This is not relevant to the experiments described within this project.

2.1.5 Andreev Reflection

While the existence of the proximity effect had been proven, the mechanism by which a current could flow from a normal metal region into a superconductor was at first a mystery to researchers. The huge size of the energy gap within the superconductor in comparison to the energy of the electrons within the system meant that there would be no available energy states within the superconductor for the single electrons to enter. A solution to this problem was published by Andreev in 1964 [31]. Electrons incident upon the S/N interface were retroreflected back down the path of the incident electron as a hole with the opposite charge, spin and momentum. The reflection of the hole represented a transfer of 2e across the N/S interface and thus avoided a single particle transmission. Each reflection transmits 2 electrons with identical spin across the interface. Cooper pairs, however, favour forming pairs with antiparallel spins. Electrons injected into the superconductor from the normal region therefore remain unpaired initially, before condensing into Cooper pairs

with electrons of the opposite spin band from other Andreev reflections over a short distance from the S/N interface. If only one spin band is being injected, or the electrons within the normal metal are highly polarised such as in a ferromagnet or a normal metal subjected to a magnetic field, then Cooper pairs will not be able to form within the S region. Holes within the normal region are also capable of undergoing Andreev reflection and under certain circumstances multiple Andreev reflections may occur where an electron/hole reflected from one interface is retroreflected from the other interface of an SNS junction and resultant hole/electron again crosses the normal region to begin the reflection process again.

Probably the most important aspect of Andreev reflection for this project is that the particles reflected from the interface back into the normal region carry with them phase information from the superconductor. If the superconductor has a phase ϕ_s then an electron reflected from it will gain a phase change of $+\phi_s$ while a hole will inherit a phase change of -ϕ_s upon reflection. The incident and reflected particles are time reversed versions of each other and will remain correlated for a distance L

$$L = \sqrt{\hbar D E} \tag{2.20}$$

where D = the diffusion constant of the material and E is the energy of the reflected particles. L_ϕ is the maximum possible value of L in a system and is known as the phase breaking length. It represents the longest average path an electron can cover without being subjected to an inelastic scattering event.

The Thouless energy E_{Th} in SNS systems was introduced in section 2.1.4 and is directly linked to the junction length (L). This is the critical energy below which electron-hole pairs will be able to remain correlated across the entire system.

$$E_{Th} = \frac{\hbar D}{L^2} \tag{2.21}$$

The constant stream of incident and retroflected particles at each interface leads to constructive and destructive interference effects within the normal metal, which results in modulation of the normal metal resistance. Each of the superconducting electrodes that border the normal section of an SNS junction can be described by a macroscopic wavefunction according to the Ginzburg-Landau theory. When the difference between the complex phases of the two superconducting electrodes ($\Delta\phi$) is an integer multiple of 2π, a maximum correlation occurs between particles due to

constructive interference which induces an energy gap in the normal metal similar to that seen in superconductors. This gap then reduces as the phase difference is increased, until it disappears when $\Delta\phi = n\pi$. This type of induced energy gap was first measured experimentally by Gueron et al in 1996 using tunnelling spectroscopy to probe the density of states of a normal metal in contact with a superconductor. Later work by Ostrovsky [32] demonstrated that this energy gap was not in fact complete, but that there was a small number of energy states within it. This type of incomplete energy gap is known as a soft gap.

By introducing an energy gap to the normal region a phase will also then be associated with it. When $\phi = 2\pi n$ the resistance is reduced by constructive interference. When $\phi = \pi n$ the resistance is unmodulated.

2.1.6 The Andreev Interferometer

Andreev reflection is the foundation stone of a device known as the Andreev interferometer. Here an SNS junction is implemented where the junction length L is greater than the coherence length but shorter than the phase breaking length. In this format no supercurrent will flow though the junction, however phase information is still transmitted between the N/S interfaces. This is because Cooper pairs are unable to maintain coherence across the length of the junction and thus a dissipationless current cannot flow. Individual electrons are able to travel across the junction with their phase remaining unchanged, as a result they can carry information about the phase of the two superconductors across the breadth of the junction. Modulation of the resistance of the normal region will therefore occur as a function of the phase difference between the two superconducting electrodes, this is due to interference between the reflected particles within the junction.

$$R = R_0 - \boldsymbol{\gamma}(1 + cos\phi) \tag{2.22}$$

where R_0 = the unmodulated resistance of the normal metal, and $\boldsymbol{\gamma}$ is a factor dependent on system conditions such as the diffusion constant of the normal metal and the quality of the N/S interfaces.

The phase difference between the S/N interfaces can be controlled by passing a bias current through it. Alternatively, and most usefully for this project, if the superconductors at each interface are extended to form a loop with a small normal

section then the phase difference may be controlled by varying the flux threading it. Changes in the flux will change the current circulating in the loop resulting in changes to the phase at each interface.

Petrashov et al published the first experimental evidence of such interference effects in SNS junctions in 1993 [33]. Here the magnetoresistance of a set of ring shaped metal nanostructures was measured. Three different geometries were measured as shown in Fig 2.3. In the structures with superconducting islands placed on the current carrying wires the Aharanov-Bohm oscillations measured were 100 times larger than those observed in the completely normal structure. When the superconducting islands were placed on the small side ears which do not directly carry the current through the structure, resistance oscillations with a period of a flux quantum $\Phi_0 h/2e$ were observed. While this early experiment clearly indicated that the superconductor was having a significant effect upon the sample's magnetoresistance, the geometry of the design made control of the phase difference between the superconductors impossible.

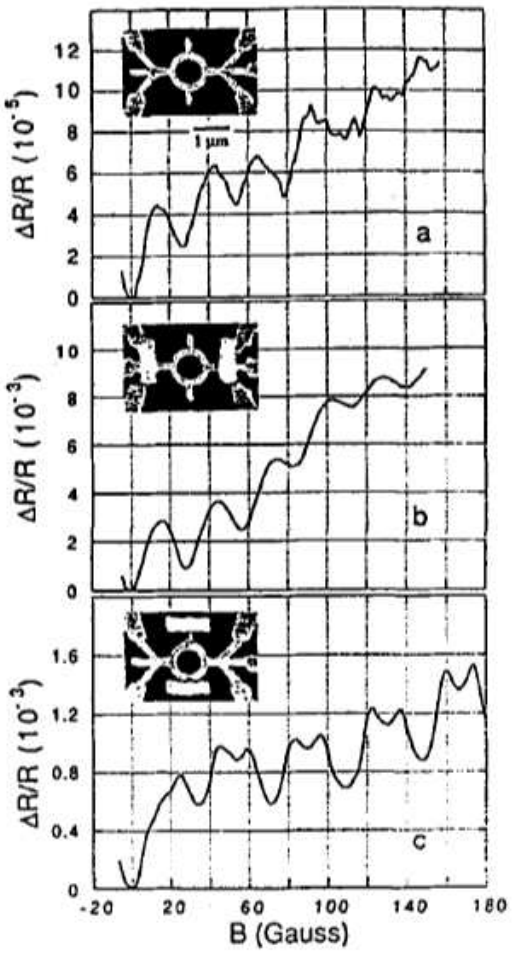

Figure 2.3: Results from Petrashov's 1993 paper [33]. a) Rings with no superconductor in contact show Aharanov-Bohm oscillations with a period of $h/2e$. b) Rings with superconducting islands placed on the current carrying leads show oscillations with the same period but with the amplitude enhanced 100 times. c) When the superconducting islands are placed on the side arms the oscillations have a phase of h/4e.

In the following year Petrashov's group published an improved version of the experiment [34]. By attaching a superconducting loop to a ring of normal material similar to that used in the the previous experiment they were able to demonstrate the resistance of the normal metal oscillating as a function of the phase across it. The phase of the superconducting electrodes was shown to be controllable via either the flux through the superconducting loop or an applied bias current.

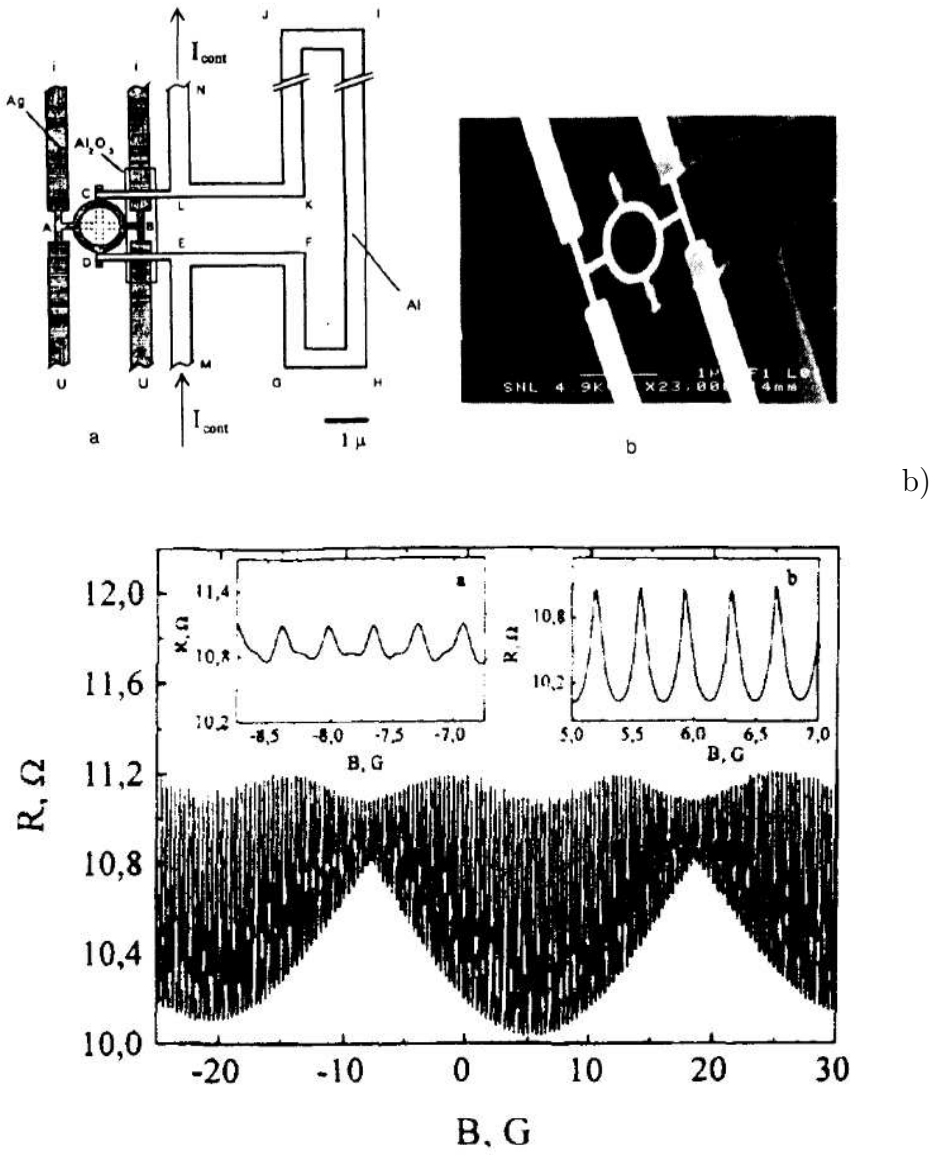

Figure 2.4: The top image is a diagram of the sample measured by Petrashov et al in [34]. When cooled to 20mK oscillations were observed in the conductance of the small silver ring as a function of the flux through the larger aluminium loop. In the illustration on the top left the components marked in black are made of the normal metal silver. The small loop in the cross is unnecessary for the device to function as an interferometer. The white components are constructed from aluminium, which is a superconductor below 1.2K. A change in flux though the area enclosed by the Al loop of one flux quantum produces one complete oscillation in the resistance of the silver section of the loop. The bottom image outlines the results obtained from this experiment with clearly defined conductance oscillations.

These results were again improved upon in 1995 [35] when a loop of superconductor attached to a mesoscopic cross of normal metal was measured. The horizontal section of the cross provided contacts for the S/N interfaces while the vertical arms provided contacts to perform resistance measurements on the cross. The phase

across the SNS junction was again shown to be controllable by either modifying the flux throught the loop or passing a current through the loop using the leads included for this purpose. Excellent results were produced with clear phase periodic conductance oscillations with a period of 2π.

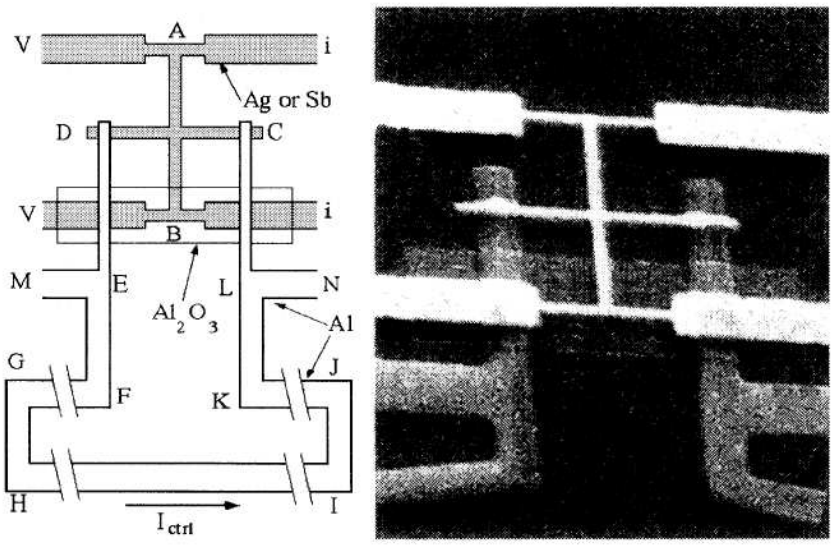

Figure 2.5: The structure measured by Petrashov's group in [35] This model has formed the basis of many of the interferometers measured since. A four point resistance measurement of the normal metal cross is possible using the leads labelled V V I I. The phase difference between D and C can be modulated either by controlling the flux cutting the Al loop or by passing a current through the loop between contacts M and N.

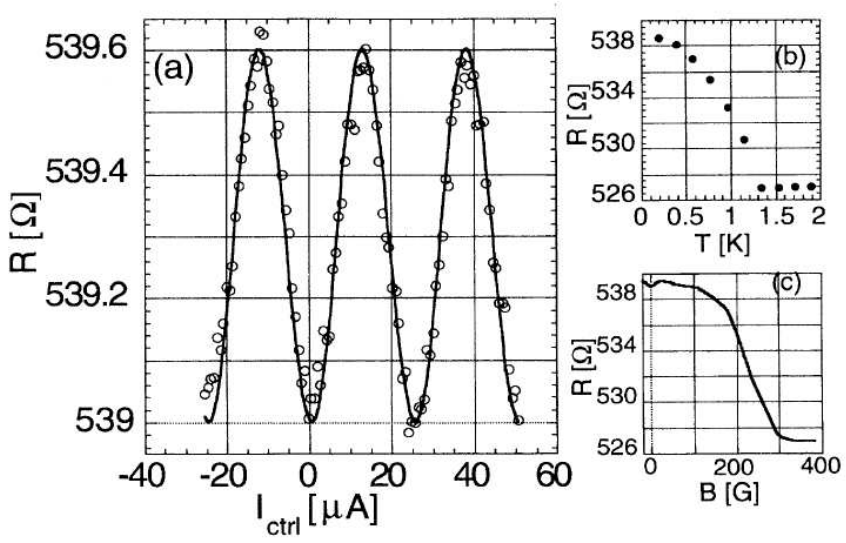

Figure 2.6: Experimental results from one of the samples measured in [35]. Clear phase dependent oscillations are observed in the resistance of the normal metal cross.

2.2 Mesoscopic Ferromagnetism and Associated Proximity Effects

Magnetism even within small systems such as nanostructures is a complex subject involving large numbers of particles and the balancing of a number of conflicting contributions to the overall magnetisation. In most materials the effect of thermal disordering is too great for long-range order to manifest. In some cases however, magnetic moments align to a common direction without the application of any external field. This spontaneous ordering below a certain critical temperature is known as ferromagnetism.

Research has recently focused upon the new class of mesoscopic ferromagnets. In this size range of between 50-1000nm the magnetic structure of the objects is governed by their shape. In objects smaller than this range (microscopic) the spins tend to align in a uniform direction to produce a single large dipole. In objects larger than a micron it becomes energetically favourable for the magnet to split into multiple domains in order to minimise the magnetostatic energy. Modern nanofabrication and imaging techniques are sufficiently advanced to allow different mesoscopic magnet shapes to be engineered and their magnetic structures probed. Predictions of the magnetic structures resulting from different geometries can be made using various simulation packages. In this project the Object Orientated MicroMagnetic Framework was used to carry out simulations.

2.2.1 Magnetic Interactions

In order for long-range order such as ferromagnetism to be established between the magnetic moments of a solid it is necessary for a balance to be struck between the different interactions that influence each magnetic moment's local neighbours.

Magnetic Dipolar Interaction

This describes the energy between two neighbouring magnetic dipoles based upon the magnitudes of the interacting dipoles, the distance separating them and their orientation relative to each other. For the case of two moments with $\mu = \mu_B$ where $\mu_B = \frac{e\hbar}{2m_e}$ at a distance of $r \approx 1\mathring{A}$ the magnitude of the effect $\approx 10^{-23}J$ or approximately 1K. As many ferromagnetic materials, including all of those used

within this project, order at many hundreds of Kelvin (Cobalt at 1394K), it is evident that other interactions must be responsible for the onset of long-range ordering in the majority of magnetic materials. Some materials have Curie points within the milliKelvin range however, and in these cases the magnetic dipolar interaction does become important.

Exchange Interaction

Exchange interactions are a quantum mechanical effect between identical particles that can affect both bosons and fermions. Among other well known effects they are responsible for ferromagnetic behaviour in materials. Indistinguishable particles are subject to exchange symmetry, this means that if two identical particles are exchanged then their wave functions must be either unchanged due to a symmetric wavefunction, in which case they are referred to as bosons, or inverted in sign due to an antisymmetric wavefunction in which case they are known as fermions. The exchange interaction was derived by both Heisenbeg and Dirac in 1926 while a proposal for the mechanism underpinning it was proposed by Heisenbeg in 1928.

Dirac later showed that the critical aspects of the exchange interaction between two electrons could be described by a very strong coupling between the spins of the electrons of the type

$$W = -2J_{ex}s_a.s_b \tag{2.23}$$

where J_{ex} is the exchange energy, which is dependent upon the angle between the spin vectors s_a and s_b between the two electrons. We can extend this principle to describe the effect between whole atoms using

$$W = -2J_{ex}S_a.S_b \tag{2.24}$$

where S_a and S_b are the total spin vectors of each atom. If J_{ex} is positive then the system favours parallel spin alignments and tends to produce ferromagnetism. If J_{ex} is negative then antiparallel spin neighbours are favoured, leading to an anti-ferromagnetic alignment. We can also see from these equations that the exchange interaction is equal to zero in any complete shell of electrons as in this case S=0. Permanent magnetic dipoles in atoms and ions must be the result of partially filled electron shells.

The cause of so few materials exhibiting ferromagnetism at room temperature is that few electron configurations allow for a large enough magnetic moment to exist. The coupling energy must be great enough to overcome the thermal agitation energy of the system K_BT. As the temperature of different materials is reduced, an increasing number reach the tipping point known as the Curie temperature where the exchange coupling is strong enough to align the spins in spite of the thermal vibration.

2.2.2 Domain Wall Formation and Magnetic Structure

In general most macroscopic ferromagnetic objects not exhibit any net magnetisation. The reason for this is that a macroscopic ferromagnet divides itself up into a complex domain structure. Within each domain all of the moments will have an identical orientation, however every domain will have its own direction. These regions of uniform spin polarisation vary in size depending upon the material, but are typically between 10^{-4} and 10^{-6}m in size. Averaged over the whole material the contributions from all of the different domains cancel out to provide a negligible net magnetisation. In order to produce an overall magnetisation of a piece of ferromagnetic material, it must be placed within a strong magnetic field. By doing this the domains are forced towards being orientated in the direction of the field. By dividing into domains a ferromagnetic body reduces the extent of the stray magnetic field escaping from it as shown in Fig 2.7. The stray field has an energy density of $B^2/8\pi$ per unit volume. The smaller the volume filled by the stray field, the smaller its energy will be.

An important factor to consider in relation to domain formation in ferromagnetic objects is the magnetostatic energy. This is the magnetic potential energy associated with any magnetic object when placed within a magnetic field. In the case of strong single domain ferromagnets, magnetostatic energy is present even in the absence of an external magnetic field. This is due to the internal demagnetising field, which is orientated in the opposite direction to the sample's magnetisation, as this is the shortest path for magnetic flux to take between the two "poles" of the object. This internal field of a uniformly magnetised ferromagnet opposes the magnetisation that produced dipole to begin with. The magnetostatic energy can be regarded as the amount of work required in order for the magnetic dipole of the

single domain body to exist in spite of the internal or demagnetising field of the object. Strong ferromagnets divide into magnetic domains as a way of minimising this magnetostatic energy.

Landau and Lifschitz demonstrated in 1935 that domains form as a method of energy minimisation [36], to reduce the magnetostatic energy associated with the object as a result of its external magnetic field. To do this the magnetisation attempts to form closed flux loops within the object. The creation of domain walls is limited due to the energy required for their formation. Domain walls can form so long as the decrease in the magnetostatic energy that results is greater than the energy required in order to form the domain wall.

Domain walls require energy in order to form due to the finite number of magnetic moments within the domain wall being forced to point out of the crystallographic easy axis [37]. At the intersection between two domains there is a region in which the orientation of the magnetic moments realigns between the direction of the domains and as a result the moments are not orientated in either domain. The domain wall energy is defined as being the difference in energy of the composite moments in their out of domain orientation as compared with if they were orientated as a part of one of the bulk domains. It is dictated by the exchange interaction energy, which increases the domain wall thickness due to being minimised when neighbouring spins align parallel, and the anisotropy of the material, which has a thinning influence upon the domain walls due to being minimised when the spins are aligned along the crystal's easy axis.

The exact placement, size and orientation of domains within an object is dictated by the need to balance the lowest possible magnetostatic energy with the energy required to form the domain structure. The main factors that decide the domain structure of a ferromagnet are the exchange energy, level of impurities, demagnetising field, geometry and the magnetocrystalline anisotropy.

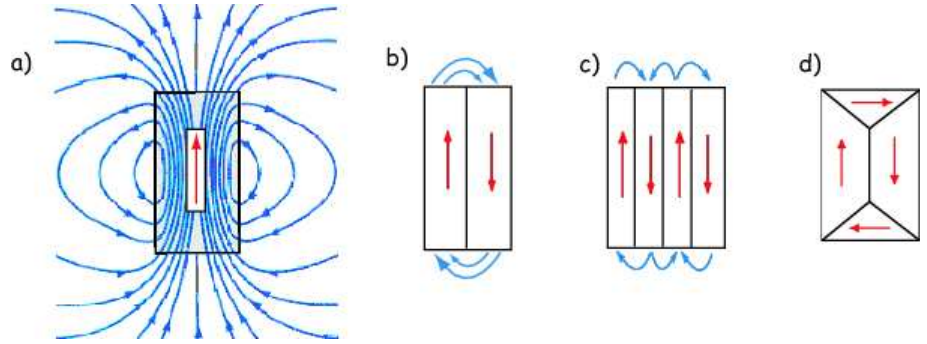

Figure 2.7: Diagram showing how domain wall formation reduces the stray field of a ferromagnet. In a) the magnet is a single domain bar magnet with a large external field. This external field is reduced in b) by the division of the magnet into two domains facing in opposite directions. In c) the stray field has been further reduced by splitting into 4 domains. In d) the stray field has been completely removed by the creation of a closed domain system. Diagram adapted from [38].

Magnetocrystalline Anisotropy

Many crystal lattices have an axis along which it is favourable for moments to align. The additional energy required to align the moments out of plane with the easy axis is known as the anisotropy energy. The aniosotropy energy is far larger in asymmetrical crystal structures than those that are highly symmetrical. In those lattices where the anisotropy energy is large, it becomes an important factor in deciding the magnetic structure of the material. Domains form in such a manner as to balance the energy of the stray field from the ferromagnet with the energy used in the domain wall formation. If the anisotropy energy of the crystal is high then the unfavourably aligned spins within the domain wall will cost large amounts of energy meaning that fewer are able to form.

Impurities

Impurities within a ferromagnetic crystal will act as point defects in the wider lattice. Domain walls tend to snag upon such defects. The ferromagnetic films used in this project will always comprise irregular polycrystalline structures with an unavoidable, although minimalised level of impurities. Both the impurities and multi crystal nature of the ferromagnet introduce random elements into the ferromagnetic structure of any designs produced in the clean room at Royal Holloway. These have the potential to impact the domain formation within the structure.

2.2.3 Mesoscopic Ferromagnetism

Recent advances in electron lithography and clean room fabrication methods as well as the availability of high resolution techniques for the imaging of magnetic structures have enabled the study of ever smaller and more finely detailed ferromagnetic material. There are three distinct regimes associated with ferromagnetic objects depending on their size.

As already discussed, a macroscopic sample of ferromagnetic material will be divided into many domains. The exact structure will be defined by its attempt to minimise its magnetostatic energy under the influence of numerous conflicting factors. At the other end of the scale, in microscopically sized magnets less than 50nm in size domain walls will never form as the magnetostatic energy is insufficient to justify the energy required to form them. Such small magnetic particles will behave as a single indivisible domain. Between this single dipole and the larger multiple domain regimes there exists a size range (50-1000nm) of mesoscopic in which the magnetic structure of objects is largely dictated by their geometry. In thin films the magnetic moments will favour alignment in the plane of the film. This tendency along with the the shaping forces previously discussed in this chapter give rise to stable reproducible magnetic structures within thin mesoscopic ferromagnets of specific geometries. Using these facts, recent work has been done within this department [39] using the OOMMF modelling script to predict a variety of magnetic structures within different shapes of mesoscopic ferromagnets, these have been subsequently demonstrated using magnetic force microscopy.

2.2.4 Modelling of Mesoscopic Ferromagnets and Magnetic Nanoengineering of Structures

Several projects have developed increasingly detailed methods to produce simulations of how magnetism behaves when constrained within mesoscopic structures. These include Nmag, magpar and OOMMF [40–42]. Using these methods, predictions can be made of specific geometries in which stable magnetic stuctures will exist. Using modern clean room techniques these nanomagnets can be reliably fabricated and their magnetism probed using a wide range of techniques with ever improving resolution.

Modelling of Magnetic Domain Structure

Modelling of mesoscopic ferromagnetic systems has been done in this project using the Object Orientated Micro Magnetic Framework (OOMMF) [42]. This is a joint project between the Information Technology Laboratory and the National Institute of Standards and Technology and has been developed to calculate the local magnetisation across an object whose shape, size, composite material and many other factors can be dictated by the user. First the user must design the object's shape, load it into the program and specify its size. Next they must enter a range of parameters relating to its composition such as the demagnetisation, exchange field, external field and anisotropy. The user must also specify a cell size, this is the size of the cubes into which the script breaks the object when performing the calculation. The smaller the box size, the more accurate and detailed the result, but also the more complex the calculation. The RAM available on the system being used for the calculation will place a limit on how small the user may select the cell size. The script's process is based upon repeated iterations of an integration of the Landau-Lifshitz equation solved quickly using approximations based on the finite difference method [43].

$$\frac{dM}{dt} = -|\nu| M_x H_{\text{eff}} - \frac{|\boldsymbol{\nu}|\alpha}{M_s} M_x (M_x H_{\text{eff}}) \tag{2.25}$$

where ν= 221 kHz/(A/m) which is the electron gyroscopic ratio, M=Magnetisation, α= The Landau Lifschitz damping coefficient which is a dimensionless constant, M_s= saturation magnetisation of material, and H_{eff}= the effective field which results from the sum of the magnetostatic, exchange, anisotropy and external field contributions.

The damping coefficient α represents an attempt to account for energy dissipation within the micromagnetic system occuring over lengthscales shorter than the cell size used. As a result the value used is largely dependent upon the chosen cell size. When the cell size is large it will include more degrees of freedom to lose energy to and so the damping coefficient must be larger to account for this [44].

OOMMF was used in this project to model vortex and other closure domain structures in mesoscopic ferromagnets using a variety of different shapes and materials. The material parameters and object geometry were initially set along with the calculation cell size. A random intitial magnetisation was selected to reflect the

disordered nature of the material when deposited via thermal evaporation. When the script was run the evolution of the magnetic structure could be observed over the iterations until a stable magnetisation was reached and the calculation terminated.

The Magnetic Vortex

One well documented and studied example of a nanoengineered stable mesoscopic ferromagnet is the magnetic vortex structure. Observed within thin mesoscopic discs, this consists of a constantly rotating magnetisation circulating around the plane of the disc with a thin but intensely powerful magnetisation extending from its centre, perpendicular to the plane of the disc. This alignment can be understood in terms of the principles already discussed. The exchange interaction causes the spins to attempt to align parallel to each other and the the thin nature of the film makes it energetically favourable to align in the plane of the disc. The diameter of the disc is not large enough to permit the formation of multiple domains, however the magnetostatic enegy of the object in a single domain state is too great to be stable. The circular rotating magnetisation minimises the stray field and avoids the large numbers of out of plane spins contained within domain walls. The vortex core arises from the conflicting direction of moments on either side of the centre of the disc. It is essentially a domain wall between the opposite spin directions on either side of the disc's cente. If the disc is too thin then the vortex core may be unable to form, in this case the disc will form a single domain structure.

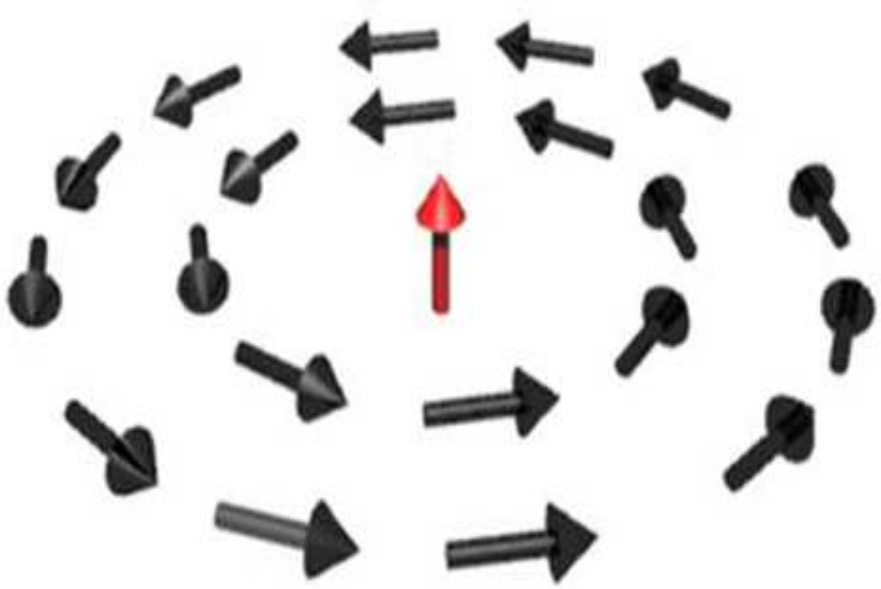

Figure 2.8: Illustration of the spin arrangement within a magnetic vortex [45].

The vortex has been established theoretically for a long time, but it was not experimentally possible to verify its existence until 2000 when Shinjo et al fabricated thin permalloy (Ni_{80} Fe_{20}) discs of 1 micrometer diameter and 50nm thickness and used a high resolution magnetic force microscope to map their magnetic structure including the perpendicular core [15]. While it is one of the most accessible methods available, magnetic force microscopy is not the best method for imaging the structure of mesoscopic ferromagnets. MFM resolution is limited to approx 20nm which is significantly larger than some features such as the vortex core (10nm). In addition, the stray field from the MFM tip can interfere with the magnetisation of the the structure being imaged. Various other imaging methods have been suggested and attempted. Spin polarised scanning tunnelling microscopy (SP-STM) has been used by Wachowiak [46] to map magnetic vortices in iron discs right down to the subcore structure. SP-STM is excellent for this task as it can resolve structures at the atomic scale, if an antiferromagnetic probe tip is used then it will not interact with the structure being imaged. By using different thicknesses of antiferromagnetic coating on the tip, the equipment can be used to probe both the in plane and out of plane magnetisation of a vortex. This allows the curling magnetisation of the disc and the out of plane core to be probed in great detail.

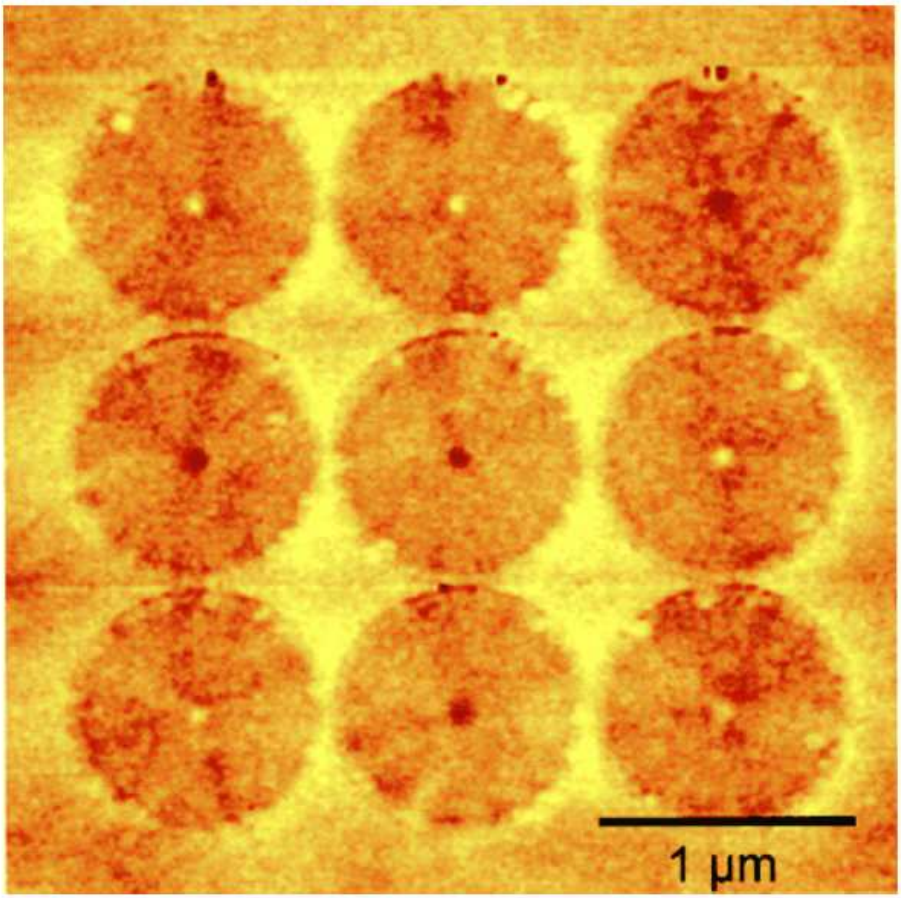

Figure 2.9: MFM image from Shinjo's group clearly showing the vortex structure with perpendicular core at each disc's centre [15].

Novosad and his co workers have published work on the nucleation and annihilation of of magnetic vortex structures in mesoscopic permalloy discs [47]. Magnetic vortex states were observed in Py discs 60nm thick with diameters of 200 400 600 and 800nm. High resolution MFM techniques were used to image the out of plane magnetisation of the vortex cores. The effect of applied external fields upon vortices of different diameters was studied via the magneto-optical Kerr effect.

In 2008 the same group published work on the dynamics of magnetic vortex structures [48]. When a sufficient external field is applied, the vortex core precesses in a circular motion around its rest position. Theoretical predictions are compared with experimental data collected on this effect.

Much interest has been focused on the magnetic vortex in recent years for its potential applications in various fields [12]. An array of discs produced without the influence of any external field will produce a random scatter of upward and downward pointing cores as well as vortex chiralities (direction of rotation of the in-plane magnetisation). The stability of the vortex structures and the capacity

for the core direction and chirality to be switched by the outside influence of, for example, an MFM tip has generated great interest in their potential as an option for producing future high density non-volatile data storage devices.

The stability of the magnetic vortex structure within thin disc structures is investigated theoretically in [49]. A phase diagram is presented showing the calculated vortex stability with varying disc thickness and diameter. The phase diagram contains a region at the smallest radii and thicknesses where discs will form uniform single domains; if the radius of the disc is similar to or smaller than its thickness then a uniform magnetisation will result. If the radius of the disc is large compared to its thickness then stable vortices may form. Between the stable vortex and single domain regions, a shaded area indicates the disc parameters which may produce metastable vortices.

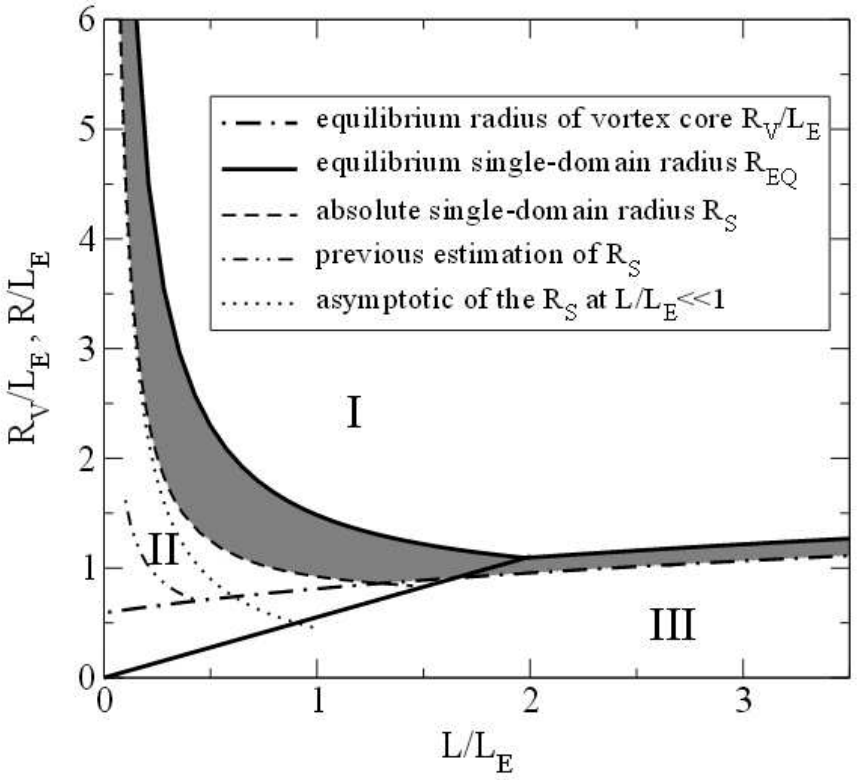

Figure 2.10: Vortex stability diagram from [49]. I= Vortex state, II = magnetised uniformly in plane, III =magnetised uniformly parallel to the cylinder axis. The shaded region denotes where vortices are metastable. This theoretical model does not take into account the possibility of the fractured radial domain states observed in the results chapter 5.6.1. As will later be discussed, in real systems at larger diameters the discs will tend to split into multi domain closed structures. This eventuality is not included within this model.

Further Closed Domain Mesoscopic Systems

Other mesoscopic ferromagnetic shapes have been proven to display specific stable magnetic structures. One example is the antivortex which was first observed by the group at Royal Holloway in cobalt crosses with 1μm branches 100nm wide and 40nm thick with 150nm bulbs at two neighbouring tips [39]. This structure which is the topological counterpart of the vortex was observed as a stable state within the cross after magnetic reversal. The cross was exposed to an 800Oe magnetic field in a direction diagonal to the cross (See Fig 2.12 for cross shape and magnetisation direction) which was then removed. After applying a weaker 250Oe field in the opposite direction, the cross was found to have fallen into the antivortex state as shown in part d of Fig 2.12. The antivortex is characterised by two opposite arms of the cross with magnetisation pointing towards the centre of the cross while in the other two arms it points out (Fig 2.11). The meeting of the inward facing magnetisations at the centre and their deflection into the outwardly magnetised arms produces the antivortex state.

Other types of closure domain vortex type structures have been observed in mesoscopic ferromagnets of various geometries. In [50] triangular shapes are examined while in [51] squares of permalloy are shown to be capable of exhibiting a vortex type structure.

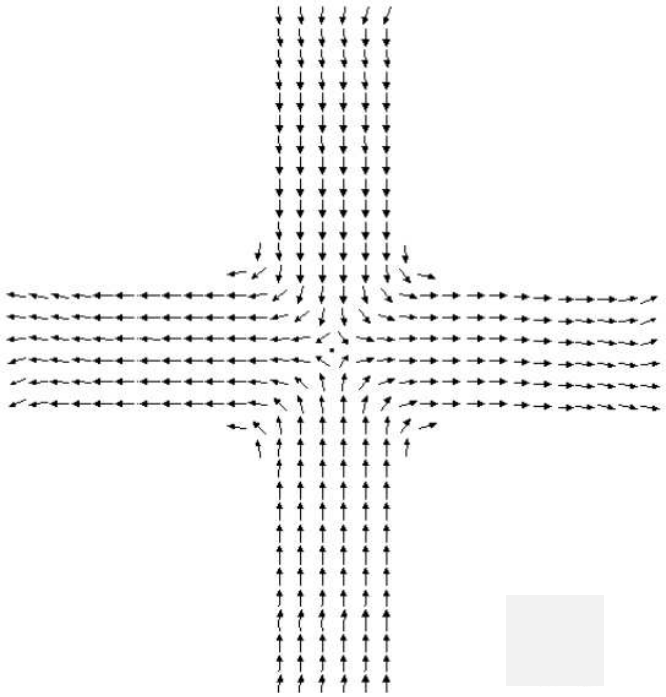

Figure 2.11: Diagram of the magnetisation of the antivortex state [39].

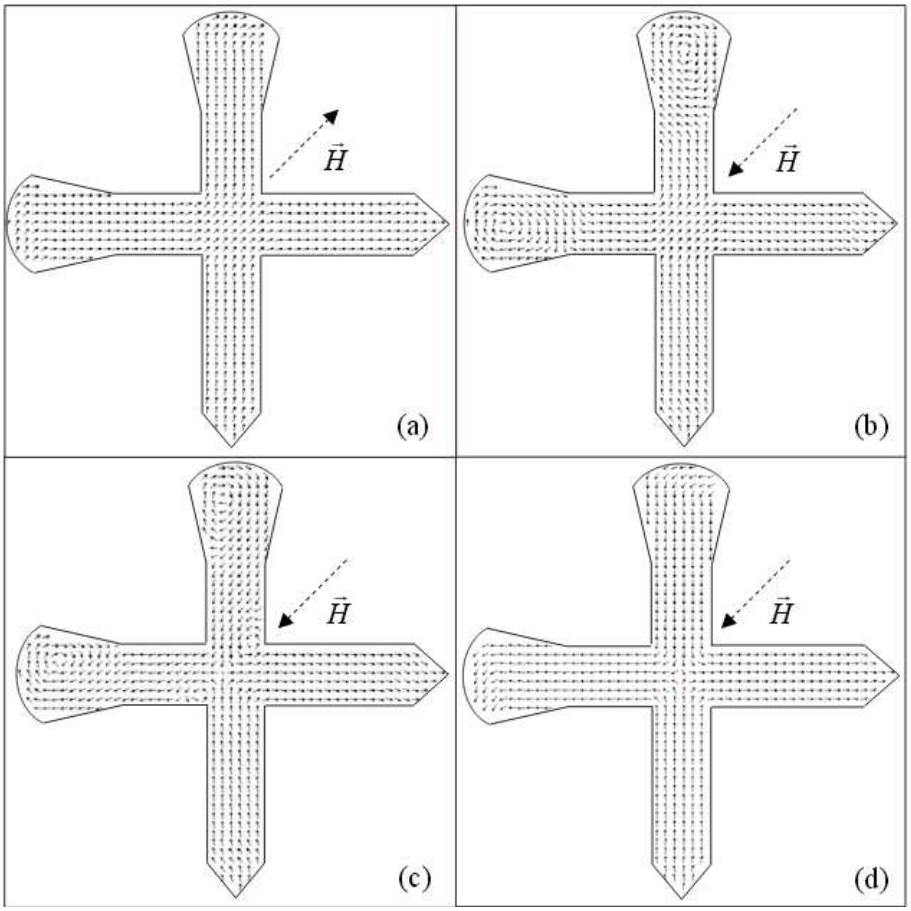

Figure 2.12: Shape of ferromagnet used in antivortex study as well as the magnetisation directions used to drive it into the antivortex state [39].

2.2.5 Superconducting Proximity Effects in S/F/S systems

As already discussed a conventional ferromagnetic object will comprise a large number of spin polarised domains, these can vary in size between a few microns to a few hundred microns. As with S/N systems a spin singlet superconductor containing electron pairs with antiparallel spins will tend to leak these Cooper pairs into touching ferromagnetic material via Andreev reflection. Upon entering a ferromagnet the exchange interaction places a strong influence upon the electrons to align their spins parallel. As a result conventional antiparallel Cooper pairs injected into a ferromagnet lose phase coherence extremely quickly [52]. Due to this effect the coherence length within a ferromagnet is reduced to

$$\xi_F = \sqrt{\frac{\hbar D}{2\pi K_B T_{\text{curie}}}} \tag{2.26}$$

As the temperature in superconducting systems is generally much lower than

the Curie temperature of the ferromagnet, the ferromagnetic coherence length ξ_F is much shorter than the normal metal coherence length ξ_N. As a result antiparallel Cooper pairs barely penetrate the ferromagnet, and so the proximity effect involving the penetration of singlet Cooper pairs is negligible, normally decaying over distances of ≈1nm.

The cause of this short-range destruction of conventional Cooper pairs is that on entering the ferromagnet the spin up and spin down bands will undergo different splitting under the influence of the exchange field. Singlet Cooper pairs consist of two electrons with opposite momenta $+K_F$ and $-K_F$ and opposite spins (↑) and (↓). The total momentum of the Cooper pair will be $K_F+(-K_F)=0$

The exchange interaction can be considered as a Zeeman Field. Upon entering the field, both of the electrons will experience a change in energy proportional to the exchange energy. The exchange splitting will shift the Fermi momenta for the spin (↑) electron from K_F to $K_F + \frac{\mu_B H}{\nu_F}$ and for the spin(↓) electron from $-K_F$ to $-K_F + \frac{\mu_B H}{\nu_F}$ where μ_B= the Bohr magneton and ν_F is the Fermi velocity. The result is a Cooper pair with a non-zero momentum of $\frac{2\mu_B H}{\nu_F} \neq 0$. As a consequence of this non-zero momentum the singlet condensate begins to oscillate in space and quickly decays.

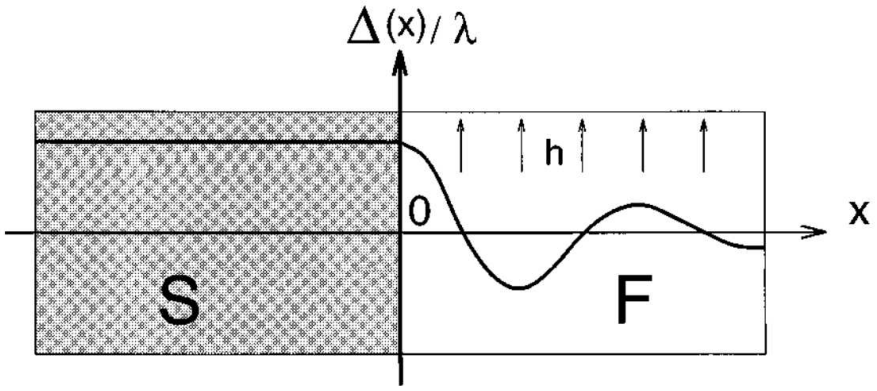

Figure 2.13: Illustration of the exchange field dependent spatial variation of the singlet condensate within a ferromagnet [53].

2.2.6 Early Experimental Evidence of a Long-Range Superconducting Proximity Effect

It is well known that ferromagnetic material has the capacity to inhibit superconducting proximity effects within it. The singlet component has been shown to os-

cillate and decay over a lengthscale of <5nm from the interface in strong ferromagnets [53–55]. By using weakly polarised ferromagnets such as Nb-Cu this length can be increased, and the spatially oscillating decay of the singlet condensate measured [56]. One of the first works to question the simplicity of this picture was by Petrashov's group in 1994 [4]. They discovered that the conductance of nickel nanostructures could be greatly modified by switching small islands deposited on top between superconducting and normal states. When the islands entered the superconducting state, a large change in the nickel's conductance was found to extend more than 30 times the value of ξ_F for singlet pairs. While theoreticians were yet to suggest a process to explain such observations, experiments on S/F systems gathered pace.

In 1998 Pannatier's group published measurements indicating a proximity effect which decayed over much longer lengthscales than theoretically predicted. An aluminium island was placed on top of a cobalt wire and its influence found to extend much further than predicted from the exchange field of the ferromagnet [5].

In 1999 Petrashov's group published measurements showing a proximity effect induced modulation of the conductance of Ni two orders of magnitude larger than that predicted from theory. Here mutual effects were seen when a nickel bar was placed with a clean interface to Al components [6].

Chandrasekhar's group conducted their own study which was published in 2001. Here they measured both the interface and main body of submicron Ni structures connected to superconducting Al for a range of interface qualities [7]. In this particular study it was demonstrated that the bulk nickel displayed no measurable proximity effect, however the interfaces were shown to display strong temperature, field and current bias dependences. While this work raises questions about the cause of the behaviour seen in those studies with complex interfaces between the superconductor and ferromagnet, in the case of [6] the interface was measured and shown to be transparent indicating that, in this experiment at least, the whole of the measured effect can be attributed to a proximity effect.

2.2.7 Long-Range Superconducting Proximity Effect Theory

Theoreticians tried to explain the mechanism that produced the long-range proximity effects observed in experiments. This involved attempting to describe a mechanism where parallel spin pairs can form with zero centre of mass momentum in order to propagate over long distances. Parallel spin triplet states ($\uparrow\uparrow$) or ($\downarrow\downarrow$) formed from spin mixing and spin flip scattering processes provided a solution as to how such pairs could be formed.

Spin Mixing

One concept that is a critical consideration in order to account for novel superconducting effects in S/F systems is spin mixing [57]. This process provides a mechanism for Cooper pairs which most favourably form the singlet state ($\uparrow\downarrow - \downarrow\uparrow$) to be converted into a triplet formed from opposite spins (($\uparrow\downarrow + \downarrow\uparrow$) . It is the first of two steps necessary in order to produce equal spin triplet pairings. Spin mixing is an omnipresent aspect of systems including interfaces involving ferromagnets with a high level of spin polarisation. The splitting of the spin up and spin down energy bands by the exchange field causes a shift in the pair amplitude R which means that their contributions will be proportional to $e^{\pm(K_{F\uparrow}-K_{F\downarrow})R}$.

The shift in the pair amplitude produces a mixture of singlet and triplet states as a consequence of differing phase shifts aquired by the up and down spin band electrons as they cross the S/F interface. This mixture of spin states produced is known as the Fulde-Ferrell-Larkin-Ovchinnikov phase (FFLO phase) [58, 59].

$$((\uparrow\downarrow + \downarrow\uparrow) \rightarrow (\uparrow\downarrow e^{iQR} - \downarrow\uparrow e^{-iQR}) = (\uparrow\downarrow - \downarrow\uparrow)cos(QR) + i(\uparrow\downarrow + \downarrow\uparrow)sin(QR)) \tag{2.27}$$

Figure 2.14 shows how the spin singlet and opposite spin tripet components formed by spin mixing penetrate into different materials from the interface. The results vary greatly depending upon the strength of the exchange field (level of spin polarisation) within the ferromagnet. Without a mechanism for the opposite spin triplet states to be converted into parallel spin triplets however, the penetration depth of the triplet component in the ferromagnet is again short. It is comparable

with that of the singlet state due to the inherent centre of mass momentum resulting from the pairing of phase shifted spin up and spin down band electrons. In addition, once inside the ferromagnet the spin bands continue to undergo increasing spin splitting resulting in a very fast suppression. The bottom picture in the Figure 2.14 shows how Cooper pairs in a very strongly spin polarised ferromagnet are destroyed by the exchange field in the interface barrier before they can even enter the ferromagnet. A form of spin mixing does still occur in such systems however, as the Cooper pairs undergo phase changes when penetrating the interface region quantum mechanically. The electrons of each Cooper pair aquire a spin dependent phase shift of $\pm\theta$ when entering the barrier due to the highly spin polarised nature of the environment. This phase shift in sufficiently strong ferromagnets results in spin mixing to produce a region approximately 15-150nm thick next to the interface in which singlet and opposite spin triplet components coexist.

$$(\uparrow\downarrow - \downarrow\uparrow) \rightarrow (\uparrow\downarrow e^{i\theta} - \downarrow\uparrow e^{-i\theta}) = (\uparrow\downarrow - \downarrow\uparrow)cos(\theta) + i(\uparrow\downarrow + \downarrow\uparrow)sin(\theta) \qquad (2.28)$$

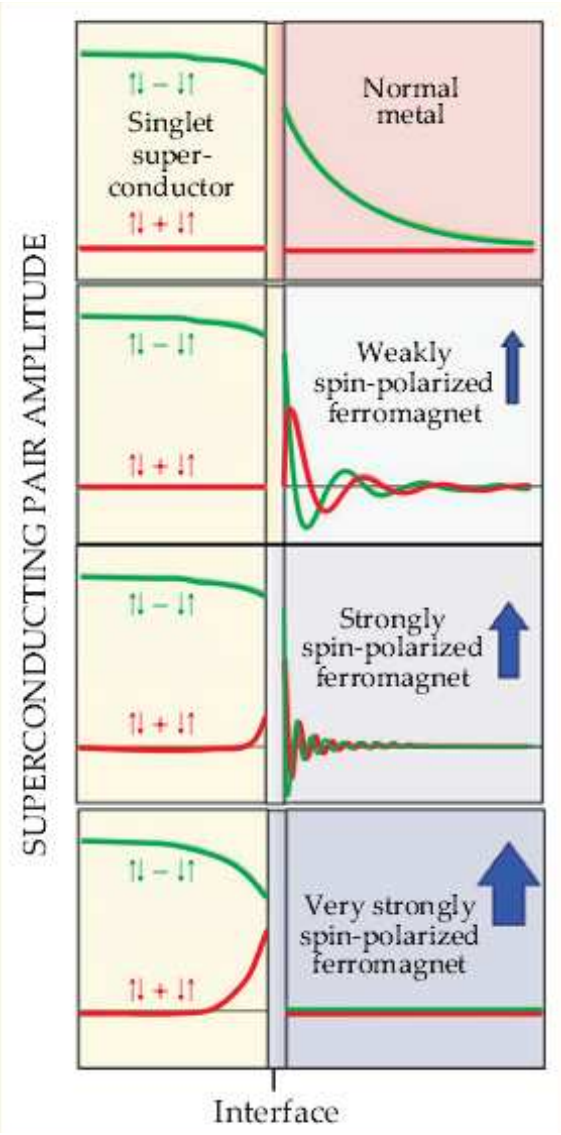

Figure 2.14: Diagram taken from [2] illustrating the differing penetrations of the singlet and opposite spin triplet states present during spin mixing in a range of materials with different levels of spin polarisation in the F region.

The FFLO state provides a mechanism through which electron pairs may form with a non-zero net momentum. Pairing can still occur when the electon energies and momenta are different for the two spin bands.

Spin Flip Process

The spin flip scattering process provides a mechanism for the conversion of opposite spin triplet pairs produced via the spin mixing process to be converted into even spin triplet pairs unaffected by the exchange field and capable of surviving over long distances within a ferromagnet. Therefore it requires that an appreciable concentration of opposite spin triplet pairs are already present through a spin mixing process in the system. Singlet spin states are rotationally invariant. This means that they are the same irrespective of quantisation direction. The three triplet states however $(\uparrow\downarrow + \downarrow\uparrow)$ $(\uparrow\uparrow)$ $(\downarrow\downarrow)$ all transform between each other when the direction of quantisation changes. Most importantly, the opposite spin triplet $(\uparrow\downarrow + \downarrow\uparrow)$ in the y-basis is transformed into the equal spin form $i(\uparrow\uparrow + \downarrow\downarrow)$ in the z-basis. This implies that if the quantisation direction is flipped before the propagating opposite spin pairs decay then a stable even spin triplet component can be created with the capacity to penetrate through the ferromagnet over the lengthscale associated with a normal metal ξ_N.

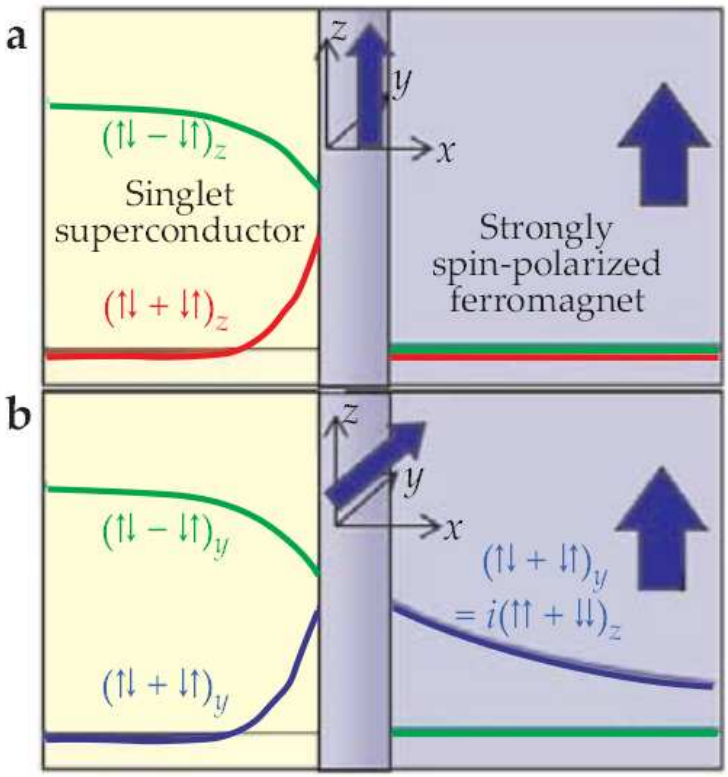

Figure 2.15: Diagram taken from [2] illustrating the spin flip scattering process converting the opposite spin triplet state into an equal spin triplet state due to a magnetic inhomogeneity in the interface region.

Theoretical Predictions of Long-Range Proximity Effect in S/F Systems

Beginning in 2001 Sebastian Bergeret, Anatoly Volkov and Konstantin Efetov published a succession of papers [8, 60–63] considering an S/F system in which the ferromagnet's magnetisation rotates in a tight spiral close to the interface. Due to the spin quantisation following the direction of the rotating magnetisation, a long-range parallel spin triplet component was predicted within the ferromagnet.

Figure 2.15 shows how in the case where the interface or region close to it is magnetised in the same direction as the bulk ferromagnet then there is no generation of same spin triplet component and the singlet and opposite spin components oscillate and decay over negligible distances. If the interface or region close to it has a magnetisation that differs from the bulk then a long distance same spin triplet may be generated.

The long-range component generated in such a system is unusual. The presence of the exchange field allows time reversal symmetry to be broken. Conventional superconductivity can be described in terms of the Cooper pairs being odd under an exchange of spin coordinates and even under an exchange of spatial or time co-ordinates. The relation between the time co-ordinates corresponds to a sign change in frequency if the time variables are Fourier transformed. This state can be expressed as being a even-frequency, singlet, even-parity superconducting state. The triplet state generated within the inhomogeneous ferromagnet differs from this. The exchange field of the ferromagnet lifts time reversal symmetry, allowing an odd-frequency triplet even-parity state to exist [64, 65].

Naturally Inhomogeneous Ferromagnetism

As will be seen later in this chapter, the pursuit of controllable and reproducible inhomogeneous magnetic structures forms a major part of this project. Helical ordering of moments arises naturally in many of the rare earth metals. The layered state of their crystal lattices and the way in which the separate layers interact gives rise to this phenomenon. Holmium is one such material which has been used due to this particular property in studies requiring magnetic inhomogeneities over small lengthscales. Figure 2.16 shows the magnetic structure of this material. In each layer the magetisation rotates 30°from the previous while maintaining the same 80°angle with the c-axis.

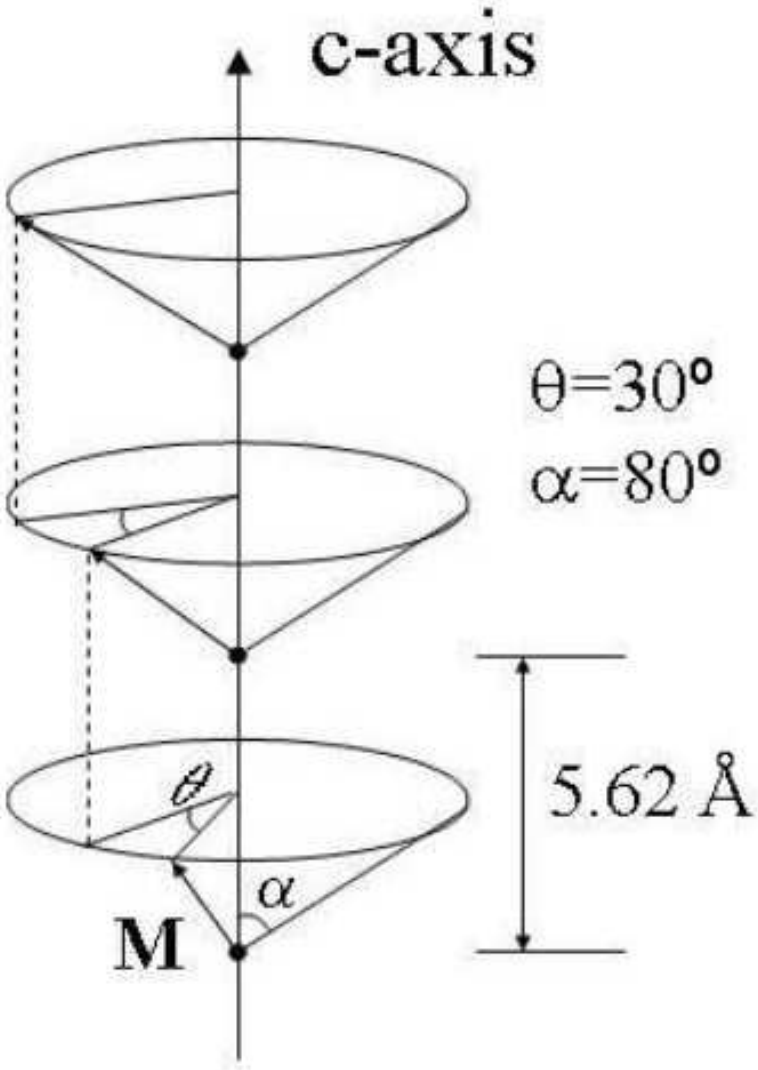

Figure 2.16: The rotating helical magnetic structure of holmium from [9]. Magnetisation M rotates by 30°each atomic layer along the c-axis at an angle of 80°to this axis.

2.2.8 Recent Experiments on Long-Range Superconducting Proximity Effects

Based on the theoretical predictions of the experimental conditions necessary for a long-range spin triplet, several different approaches have been attempted so far in the search for evidence in ferromagnets. In [9, 10] intrinsically inhomogeneous ferromagnets such as holmium are used, [66] takes the holmium based work further by demonstrating the ability for a spin triplet supercurrent generated in a thin holmium layer to penetrate deeply into a neighbouring layer of homogeneous ferromagnet. In [67] the possibility of a spin triplet within the half metallic ferromagnet

$Cr0_2$ is investigated, and in [11] multilayers of magnetic and non-magnetic material are used with varying magnetisations between neighbouring spin polarised layers.

Work on the coupling of superconductors through ferromagnetic material was published by Ryazanov in 2001 [56]. Here two strongly superconducting niobium wires were separated by a thin layer of weakly ferromagnetic copper-nickel alloy. Evidence was presented that an FFLO state was induced within such an SFS sandwich. π junction behaviour was also observed. I_c was found to generally increase with decreasing temperature. At a certain maximum I_c was found to drop abruptly to zero, after which it began to rise gradually again. This behaviour is indicative of a change between a 0 phase difference across the junction at high temperatures transitioning into a π phase difference at lower temperatures. π junctions have been implicated for potential uses in qubits and other emerging technologies. Triplet correlations within ferromagnetic Josephson junctions were predicted in [68] to be able to produce both 0 and π junction behaviours.

In 2006 the collaboration between Petrashov and Sosnin at Royal Holloway reported the successful measurement of conductance oscillations within the rare earth ferromagnet holmium as a function of the phase between two superconducting electrodes attached as part of an interferometer device [9]. Here a long-range proximity effect was seen to penetrate from the superconducting aluminium into holmium over distances that far exceeded those possible for spin singlet or opposite spin triplet pairings. In all of the measured samples the distance between the electrodes was at least $2\xi_F$, while in the largest functioning junctions, oscillations were seen in holmium wires of 150nm in length. The only predicted mechanism which could explain this behaviour is the equal spin triplet generated via spin mixing and spin flip processes in the region immediately adjoining the superconductor.

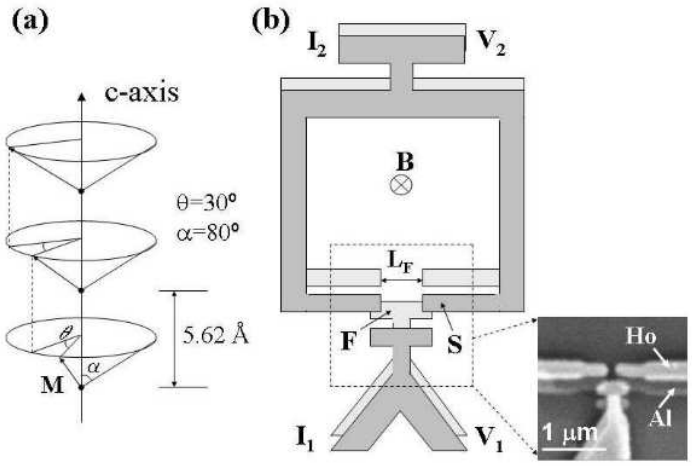

Figure 2.17: Diagram taken from [9] showing the helical magnetic structure of holmium as well as the interferometer design used in the experiment. The small inset shows an SEM image of one of the SFS junctions measured in the experiment.

The work on holmium was further developed by a group at Cambridge led by Robinson [10]. In 2010 they published their own detection of a long-range supercurrent within an SFS junction. In this work they use the intrinsic inhomogeneity of holmium in a thin layer next to the superconductor to generate a long-range triplet pairing. Once generated this stable triplet then propagates through a neighbouring layer of the homogeneous strong ferromagnet cobalt. The decay lengths of the proximity effect in a Nb-Co-Nb junction were compared with those observed in the Nb-Ho-Co-Ho-Nb junctions. It was found that the supercurrent penetrated significantly further into the Nb-Ho-Co-Ho-Nb junction than the Nb-Co-Nb one, and that the coherence length in the structure including Ho was of the same order of magnitude as that in a normal metal. This matches the predictions made for the parallel spin triplet mechanism as it indicates that the supercurrent was unaffected by spin splitting within the ferromagnet.

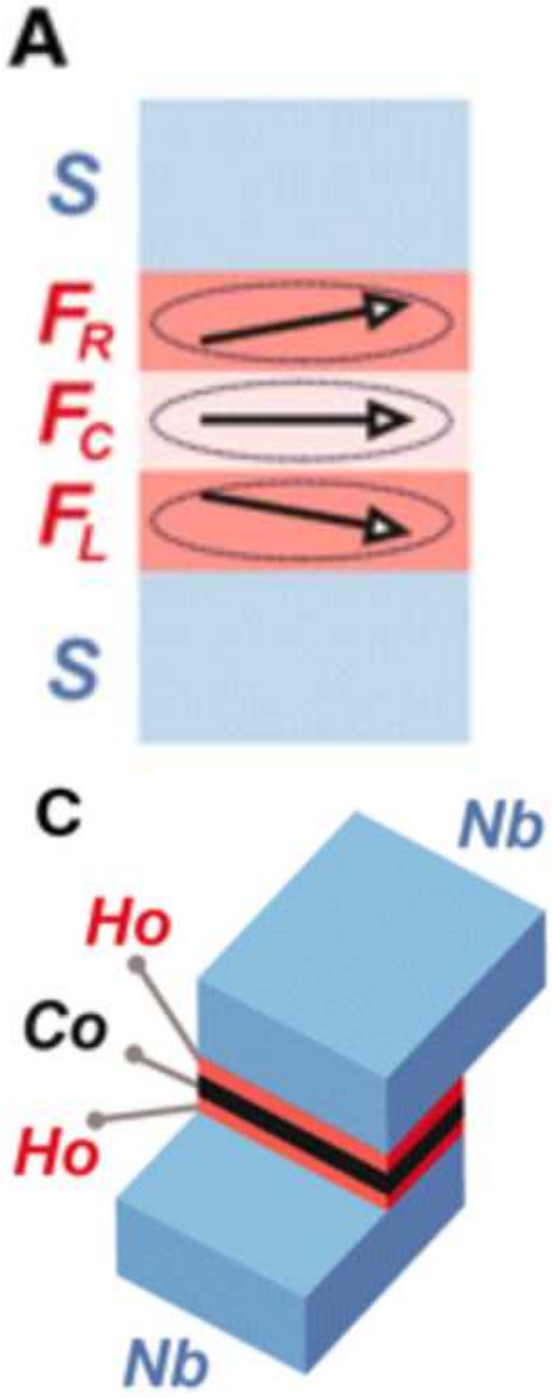

Figure 2.18: Diagram taken from [10] showing the Nb/Ho/Co/Ho/Nb sandwich used in the experiment to demonstrate the propagation of a long-range triplet component through an inhomogeneous ferromagnet.

A similar experiment has been conducted by Birge et al. [11]. Here a strongly ferromagnetic cobalt wire was capped on either end with thin layers of a weakly ferromagnetic alloy such as PdNi or CuNi. The critical current of the junctions was found to be stable up to cobalt thicknesses of 28nm, this indicates a proximity effect penetrating undiminished into the homogeneous layer one order of magnitude

further than predicted by singlet Cooper pair theory.

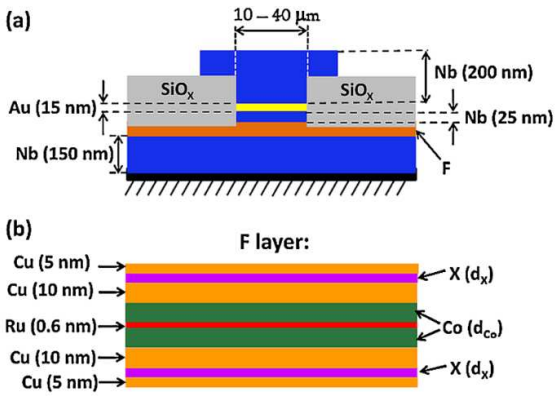

Figure 2.19: Diagram of the composite sandwich nanostructure measured by Birge et al in [11]. The Au layers between the different layers of ferromagnet play no active roll in the device, but merely act as a buffer to isolate the different magnetisations from each other.

The Long-Range Proximity Effect in Nanoengineered Magnets

The fields of mesoscopic nanomagnets and odd triplet superconductivity were brought together when it was proposed by Kalenkov, Zaikin and Petrashov [69] that a magnetic vortex could provide an excellent environment to search for a long-range proximity effect. In the paper a ferromagnetic vortex contained within a thin disc is connected to two superconducting electrodes, each of which partially overlaps the disc. Using the quasiclassical Usadel equations, they predict that a long-range triplet pairing will be produced within the ferromagnet which will be capable of carrying a measurable supercurrent. The curling magnetisation of the vortex provides the magnetic inhomogeneity near the S/F interface for the conversion of opposite spin triplets into same spin triplets. The paper shows that the expressions for the singlet and opposite spin triplet components within the ferromagnet (F_0, F_h) are each dependent upon the exchange field (h). As a result they are both expected to decay over similar lengthscales $\xi_h \approx \sqrt{\frac{D}{h}}$. The equal spin triplet component (F_t) is not dependent upon h and thus in a ferromagnetic environment is expected to survive over a much larger lengthscale dictated by the temperature (T) $\xi_T \approx \sqrt{\frac{D}{T}}$. As in general $h >> T$.

The paper also makes some promising predictions about the size of the supercurrent that the vortex may be able to carry. In a case with both superconductors having equal energy gaps $\Delta_{1,2} = |\Delta|$ and assuming that ϵ_{Th} is smaller than $|\Delta|$ then

in the limit where $T << \epsilon_{Th}$ the critical current of the junction (I_c) is given by

$$I_c = \frac{D^2 \epsilon_{Th}}{edh^2 r_1 r_2 \sigma} \tag{2.29}$$

where d is the disc thickness.

In the case where $\epsilon_{Th} << T << |\Delta|$ I_c has an exponential dependence on temperature

$$I_c \approx \frac{TD^2}{edh^2 r_1 r_2 \sigma} e^{-L\sqrt{\frac{2\pi T}{D}}} \tag{2.30}$$

where L is the separation between the S/F interfaces.

When compared with an SNS system of identical geometry, it was found that the result for the SFS system is smaller than that for the SNS system by a factor of $\approx \epsilon_{Th}^2/h^2$. This is only possible in the limit of extremely thin films, where $d \leq \xi_h$. This would be unfeasable in a real world situation as films so thin would form a single domain rather than a vortex structure. For thicker films the value of I_c for the triplet supercurrent will be lower.

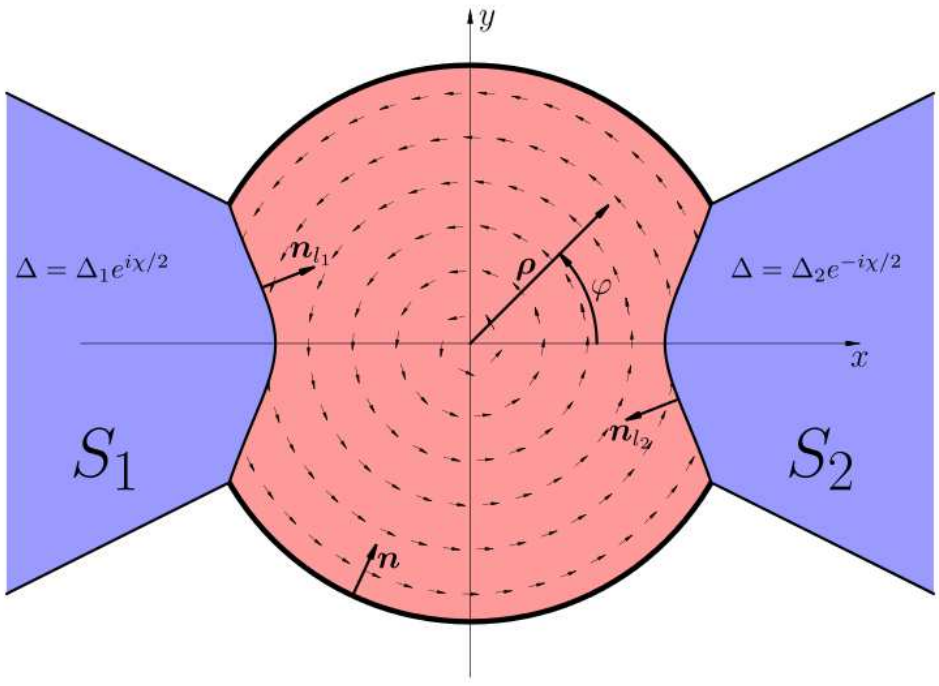

Figure 2.20: Diagram taken from [69] showing the type of system being modelled.

It is important to note that in the model discussed in this section, barriers were placed at each S/F interface to block the ferromagnetic material from influencing

the superconductor. This theoretical tunnelling barrier negates the need for consideration of the counter effect of the ferromagnet upon the superconductor region bordering the interface although this may not give a complete picture of how a real world system would behave. Penetration of spin polarised ordering into the superconductor could weaken the superconductor and affect the injection of Cooper pairs into the ferromagnet. This model again predicts the unusual odd frequency of the long-range triplet component in order to maintain the non-violation of the laws of quantum mechanics.

2.2.9 Ferromagnetic Proximity Effect in Superconductors

While much research has examined what happens within the non-superconducting material due to the proximity effect, the reciprocal proximity effect, that of the normal/ferromagnetic material upon the superconductor is just as important in any consideration of S/N or S/F systems.

While the proximity effects so far discussed have centred on a penetration of the superconducting phase order from the S region into the F, the ferromagnetic order parameter will also leak across the interface from the F region into the S.

In Tokuyaku's article from 1988 [70], the penetration of ferromagnetic order into the superconductor is described in terms of electrons reflecting from the S/F interface having their spin influenced by the highly polarised environment and resulting exchange field at the border between the two materials.

This paper examines the interaction between electrons tunnelling from a thin film of conventional superconductor into the interface barrier which has an associated exchange energy due to the magnetic moments of the adjacent ferromagnet. The pair breaking effects on the Cooper pairs by the magnetic boundary, the transition temperature and the energy gap of the superconductor are all examined.

A Zeeman type splitting of the quasiparticle density of states is noted within the superconductor which is interpreted as an internal field having been induced within the superconductor. This field is a result of the spin of reflected particles being rotated by the interaction with the internal field of the interface boundary.

In this work the quasiclassical theory of superconductors formulated by Eilenberg, Larkin, Ovchinnikov and Eliashberg is used as it has the capacity to deal with superconductivity within the kind of restricted geometries being discussed. In order

to model the effect of an S/F interface, boundary conditions are added to the original quasiclassical theory. The boundary conditions will depend greatly upon several interface qualities such as its roughness, reflectivity and magnetic properties.

A case is considered in which a superconductor occupies all the space z>0 and is bounded by a ferromagnetic insulator interface at z=0. Fig 2.21 shows the suppression of the energy gap in the region of the S/F interface while Fig 2.22 shows the exchange field induced in the superconductor by the proximity ferromagnet. This exchange field influences a region up to ξ_0 (coherence length) away from the superconducting interface while its maximum is dictated by the spin mixing angle θ. θ describes the scattering matrix used to generate the spin rotation at the S/F interface in this model, the closer its value to π the greater the probability of reflected particles undergoing a spin rotation until at $\theta = \pi$ the probability is 1 and the interface is a perfect pair breaker. When θ is close to π the energy gap close to the interface drops to zero. At smaller values of $\theta < pi$ and especially $\theta << 1$ the pair breaking effect is reduced and and the magnetic boundary does not completely destroy superconductivity at the interface. The limit of $\theta = \pi$ is most applicable for the kinds of strong ferromagnet used in this project, such as nickel. Experiments on systems where $\theta << 1$ would require rare-earth-oxide materials.

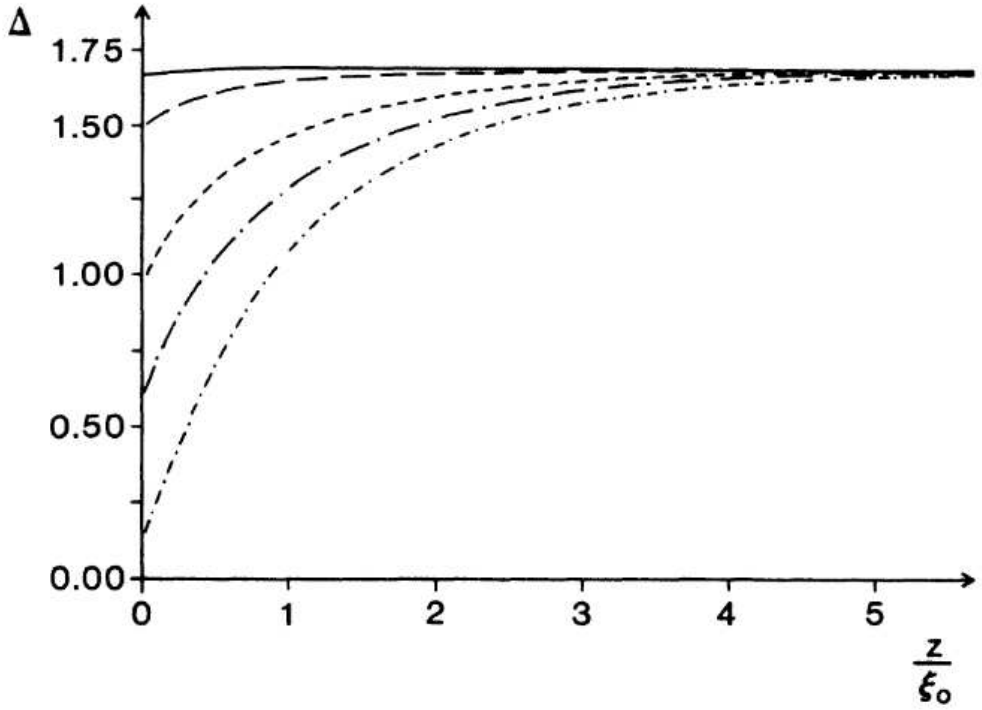

Figure 2.21: Figure from [70] showing how the order parameter of the superconductor is affected by the ferromagnetic interface for different values of the spin mixing angle θ. $s\theta$=0.2 (solid), 0.6 (long dash), 1.2 (short dash), $\pi/2$ (long dash-dot) and 3 $\pi/4$ (short dash-dot).

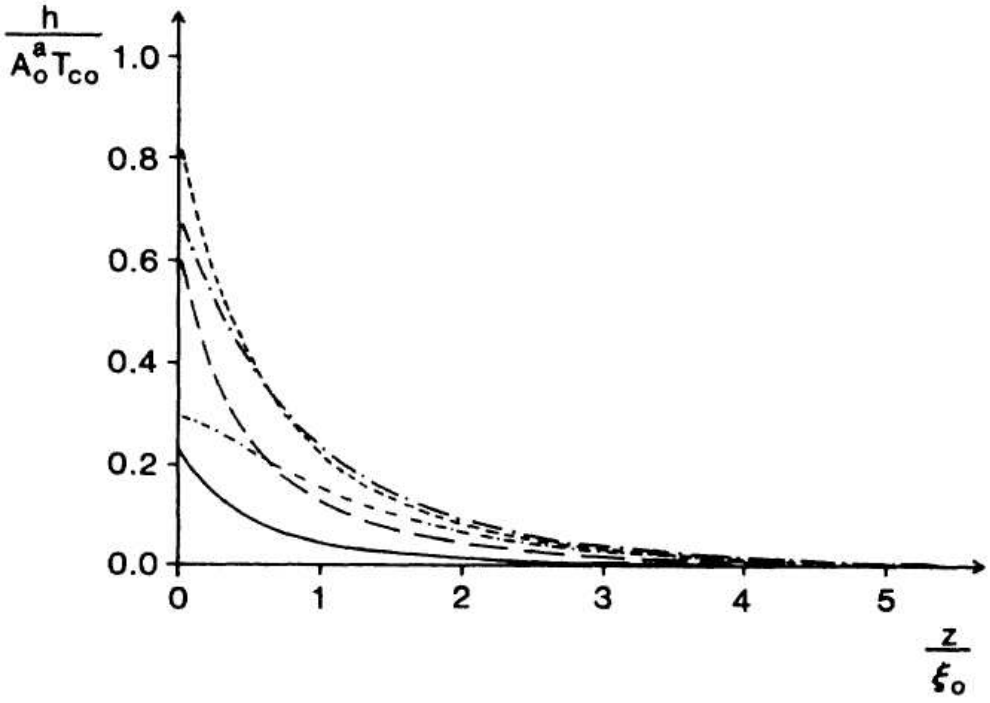

Figure 2.22: Figure from [70] showing the induced exchange field as a function of the distance from the S/F interface

In the 2000's Bergeret and other authors [71,72] published theoretical work which continued to examine the inverse proximity effect in S/F systems. They demonstrated that while at an F/N interface ferromagnetic order may only penetrate the normal metal over short distances limited by the exchange length; if that normal material is reduced below its T_c then the magnetic moment may penetrate into the superconductor over long distances equivalant to the superconducting coherence length ξ_s, with an associated reduction of the magnetic moment in the F region close to the interface. The direction of the induced magnetisation in the S region is opposite to that of the F region. The magnetisation of the S region cannot be explained by a leakage of the exchange field due to the short range of this interaction. The long-range of the effect indicates that its mechanism is linked to the correlations between electrons within the superconductor.

To better understand the process which gives rise to the inverse proximity effect it can be considered as follows. In a conventional superconductor contacting a ferromagnet, the Cooper pairs can be regarded as individual objects comprising two electrons with opposite spins such that the total magnetic moment of each pair is zero. Cooper pairs completely within the S region contribute nothing to the magnetisation of the superconductor. Provided that the exchange field of the ferromagnet is not so strong that it destroys all Cooper pairs in the vicinity, it is possible for Cooper pairs close to the interface to overlap with one electron having entered the ferromagnet and the other remaining within the superconductor. The high level of spin polarisation in the F region will mean that only one spin band is able to enter the ferromagnet, which in turn leaves a surplus of electrons from the other spin band still within the S region close to the interface. As these electrons have the opposite spin to those that have entered the F region, the induced magnetisation is in the opposite direction. As Cooper pair size is limited by the coherence length ξ_0, the induced magnetisation penetrates no deeper than this.

The first direct measurement of the inverse proximity effect within a superconductor was published by Silanpaa and Heikkila [73] in 2001, the effect of a proximity Ni structure to a superconducting Al wires is investigated using tunnel spectroscopy to probe the density of states (DOS) of the superconductor close to the interface. Fixed position normal metal tunnel probes are attached to the superconductor with the differential conductance measured being proportional to the density of states.

One Cu tunnel probe is attached to the Al wire 180nm from the Ni/Al interface

(approx $1\xi_s$ from interface) and a second 10μm from the interface. The contrast between the conductance in the superconducting region affected by the ferromagnet and the bulk superconductor far enough from the interface to be unaffected is investigated. The Al/Ni deposition was carried out in an unbroken UHV environment with minimal time between the two depositions in order to maximise the interface transparency. The Al wires were briefly oxidised before the deposition of the Cu probes in order to provide the low tunnelling barrier necessary for tunnelling spectroscopy. When the differential conductance properties of the structure were measured at 100mK using standard lock-in amplifier techniques, the suppression of superconductivity close to the interface was obviously apparent. The experimental structure is illustrated in Fig 2.23 and the disparity between the data from the proximity and distanced probes is shown in Fig 2.24.

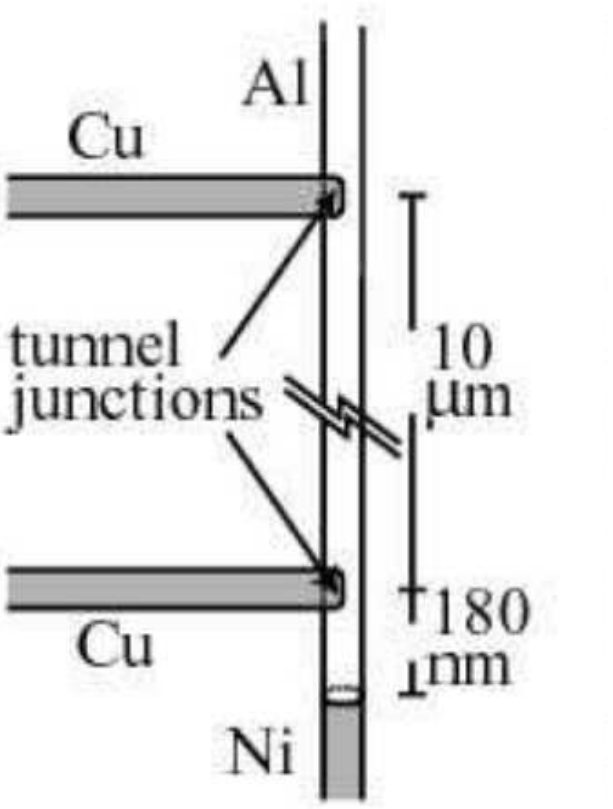

Figure 2.23: Diagram of the experimental structure used by Heikkila's group in [73]. The different arms allow the sample to be probed 180nm from the S/F interface and 10 microns from it.

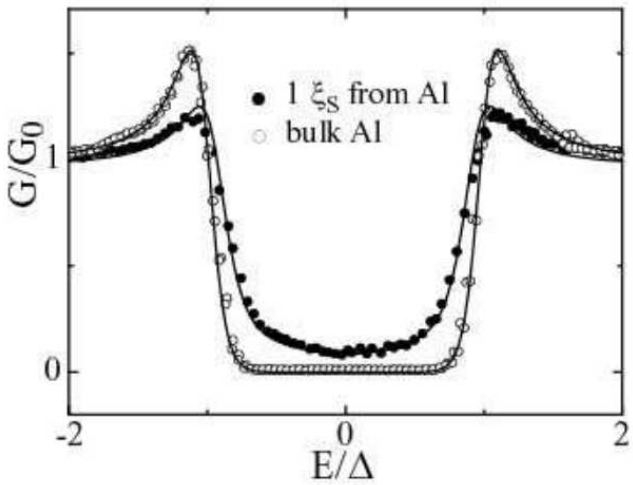

Figure 2.24: Data from [73] showing the contrast between the normalised differential conductance measured via the probe in the region affected by the ferrromagnet (180 nanometers from interface) and that in the unaffected region (10 microns from interface). Both sets of data were measured at 100mK. The effect of the ferromagnet is clearly discernable.

Xia and Palevski [74] published measurements of the magnetisation of a proximity superconductor using the polar Kerr effect. This is a form of microscopy that relies on the changes that light undergoes when reflected from a magnetised surface, these can include changes to both the polarisation and reflected intensity. The physics underlying the effect are similar to those of the Faraday effect, however the Faraday effect describes the changes that light undergoes during transmission through a magnetic material. In Polar Kerr microscopy the light being used to probe the sample is first passed through a polarising filter, then reflected from the sample before being passed through a second analyser polarising filter and on into a photodetector. If the sample is magnetised then the difference in polarisation between the incident and reflected light will be converted into a change in the light intensity by the analyser filter.

This experiment provided clear, unambiguous proof of the penetration of magnetisation into the superconductor by probing the S part of an S/F sandwich using light with an optical penetration depth much smaller than the thickness of the superconducting layer. By measuring the difference in polarisation between the incident and reflected light, it is possible to discern whether there is a degree of magnetisation in the sample. In both Al/(Co-Pd) and Pb/Ni samples a signal was first detected at T_c, which increased with decreasing temperature. The Pb/Ni system produced very

weak but discernable results with the polarisation undergoing a rotation of the order of 150nanorad. The Al(Co-Pd) system showed a much more pronounced effect as the temperature was lowered which was in agreement with predictions by Bergeret et al [72].

Chapter 3

Sample Design and Fabrication

A large section of this project has centred on mastering complex nanofabrication techniques and their refinement and optimisation to meet the stringent experimental requirements. The progression of the project from relatively simple 4 point measurements of single discs connected by two aluminium wires, to the inclusion of mesoscopic ferromagnets into precisely controlled Andreev interferometer structures was fuelled by the need for continuous improvement and innovation of fabrication techniques. For good interface quality, the Dolan bridge technique was first mastered then embellished to create fabrication techniques of the highest quality and reproducibility possible with the equipment and resources available. All of the processes described within this chapter were carried out, and where appropriate developed, by me in the clean room at Royal Holloway.

3.1 Preparation of Sample Chips for Nanofabrication

All samples used in this project were fabricated on 7mm chips divided out of larger 3 inch silicon oxide wafers. Photolithography was employed to imprint the gold contact wires and orientation crosses for 68 chips onto each wafer. Photolithography was ideal for this process as it is a relatively quick method of exposing the large areas required, provided that the finest parts of the structure are larger than the diffraction limit. The arrangement of the contact layer on a chip is shown in Fig 3.1. Each chip consisted of a set of 16 gold contact pads arranged around the edge. From each pad a gold wire extended towards the middle of the chip. These wires provided the

bridge between the macroscopic connections to the measurement apparatus and the microscopic connections to the fabricated nanostructures. At the centre of each chip the 16 wires converged at the edges of a square of clean substrate 80x80 microns in size. This region at the centre of the chip is known as the sample space, and is the area in which the nanostructures were fabricated. Electrical connections to the outer measurement system were made via either bonded wires or pogo pin connections at the contact pads.

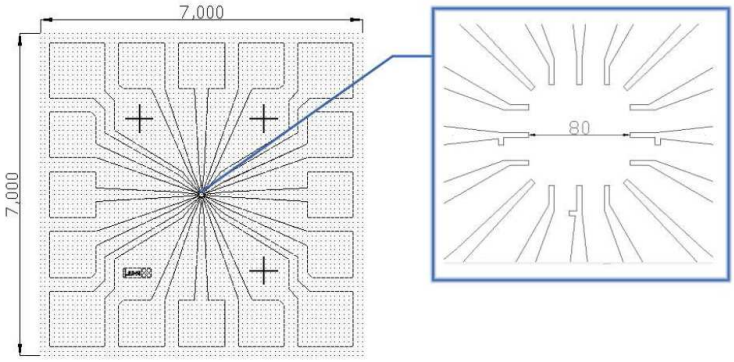

Figure 3.1: Diagram of the photolithography mask used to produce the gold contact layer. The design is formed from areas of chromium on the surface of a glass plate. This mask can then be placed over a resist coated wafer before exposure to ultra violet light.

To prepare a waferload of chips, the substrate was initially cleaned in acetone followed by isopropanol to remove any dust and then etched with an oxygen plasma for 5 minutes to remove any residual organic matter adhering to the surface. After this a layer of LOR-5B resist was spun on the substrate surface at 3000rpm and baked at 150°. A layer of S1813 photoresist was then deposited and spun at 4500rpm before being baked on a hotplate at 90°for 5 minutes. This double layer of resist is a common technique where the material used for the bottom layer dissolves in the developer solution at a faster rate than the top layer. The top layer is formed of a high resolution and comparatively development resiliant material. The top layer forms a perfect stencil of the lithographed design upon development while the bottom layer dissolves faster to produce a slight undercut around the edges of the design. This undercut provides breaks in the film at the edges of the structure, allowing for clean lift-off.

A mask consisting of glass plate with the lithography pattern printed on its surface in chromium was then placed flush with the surface of the wafer, and the

unshielded areas of resist exposed in a UV lightbox. The wafer was then placed in microposit developer MF 319 for around 80 seconds to remove the exposed areas of resist and expose the substrate. Subject to satisfactory pattern and undercut definition when examined under an optical microscope, the wafer was then placed back into the plasma etch system and briefly exposed to an oxygen plasma to remove any residual resist on the exposed subtrate. The wafer was then ready to be loaded into the thin film deposition system.

In order for the gold to adhere to the substrate, a thin layer (5nm) of nichrome (nickel/chrome alloy) was first deposited across the wafer at 5×10^{-5}Torr. Without breaking vacuum, a second source within the chamber was then used to deposit 80nm of high purity 99.999% gold across the wafer at the same pressure.

After film deposition the wafer was immersed in microposit remover 1165 at 50°, until all of the unwanted gold and resist had gone. A thin layer of resist was then spun and baked onto the wafer to keep the surface clean from dust before a diamond cutter was used to divide the wafer into individual chips.

3.2 Fabrication of Hybrid Nanostructures

3.2.1 Electron Lithography

The photolithography process detailed in the previous section at best can produce a resolution of a few microns. To pattern the designs for nanoscale structures a highly-focused beam of electrons from a scanning electron microscope (SEM) is used to expose areas of resist. This process is called electron lithography. The SEM system available for the project was capable of producing 100nm wide wires. Lithography designs were initially laid out using the AutoCAD software. Once the framework of the design was completed, the file was imported into the NanoMaker software where the appropriate electron doses for each area were set. The NanoMaker software provided the communication link to control the SEM as a lithographic tool.

Like the photolithography technique, the first step in electron lithography was to coat the clean substrate in a suitable e-beam resist. Again the 2 layer undercut method is commonly used to provide clean breaks in the film at the edges of structures. A common combination for this is copolymer for the bottom layer with PMMA placed on top, although many other combinations are possible. All of the

structures detailed in this thesis were produced using positive resist processes, in which the process of exposing regions of resist breaks down the polymer chains making them more susceptable to removal in an appropriate solvent. The unexposed resist is left behind to mask the substrate where required. Negative resist techniques are also possible where the exposure process hardens the resist by causing the polymer chains to crosslink to provide tough, insoluble regions of resist. In this process the unexposed resist is then dissolved to leave the areas of exposed resist covering the selected areas of substrate. The negative resist process was unsuitable for the work carried out in this project.

The resist coated chip was loaded into the vacuum chamber of the SEM and after beam focusing and alignment had taken place the design was exposed by bombarding the necessary areas of resist with the electron beam. Like the UV light used in the photolithography process, the electron stream breaks down the resist to leave the exposed regions far more soluble in the developer solution than those that are untouched. The dose of electrons each area receives must be carefully controlled and the effect of scattering from other nearby areas of exposure must be taken into account. If the dose is too low the design will not develop at all. If some areas of resist receive larger doses than others, their development rates will differ. If this is the case, one part of the design may be overdeveloped and have lost its fine detail before another part is completed. If the dose is too high then the polymer bonds within the resist may begin to crosslink to produce areas of resist which are impervious to the developer solution.

The scattering of the electron beam as it passes through the resist creates broadening of the design and reduces the fine detail. Known as the proximity effect this challenge was dealt with by careful selection of the dose for each area, depending on what other features lay nearby, and the use of a high energy electron beam to minimise scattering.

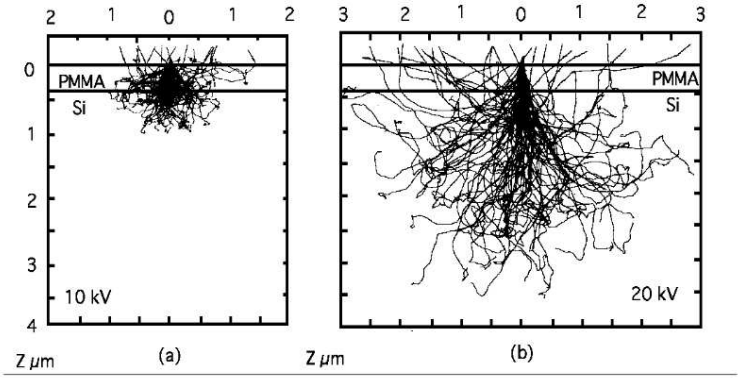

Figure 3.2: A simulation of electron scattering during electron lithography at accelerating voltages of 10kV and 20kV. At the higher accelerating voltage of 20kV, the degree of scattering within the PMMA layer is reduced [75].

3.2.2 Thin Film Deposition

A range of materials have been used during this project. All of the films used within this thesis were produced via thermal evaporation of material at pressures ranging between 5×10^{-5}Torr and 9×10^{-7}Torr depending on the film quality required. A diagram of the evaporation system used is shown in Fig 3.3. The bell jar contains a platform upon which the sample can be mounted on a rotating holder. Below the platform are two sets of electrodes between each of which a source may be mounted. Above the sample holder is a plasma etch system allowing the chip to be cleaned in the same vacuum environment in which the evaporation takes place. The bell jar was evacuated via rotary and diffusion pumps. As well as allowing the sample to be turned between the plasma etch and the evaporation sources, the rotating sample holder also allowed angular evaporations to be carried out. These were crucial to the project. The film thickness deposited was measured via a vibrating quartz crystal. As material landed on the crystal the changes to its vibration were measured. By consideration of the material type being deposited, it was possible to calculate the mass deposited over the crystal's area and thus the film thickness.

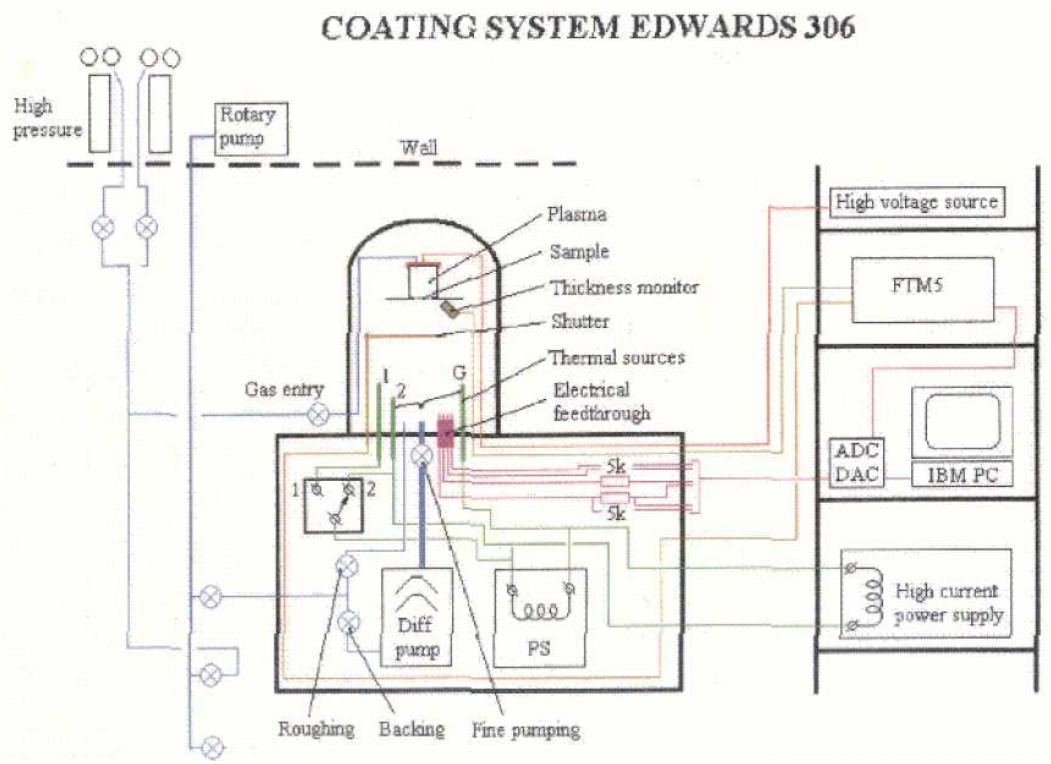

Figure 3.3: The inside of the modified Edwards thin film evaporation system used for the contact layer deposition and shadow evaporation techniques [76].

3.2.3 Shadow Evaporation Technique

The most simple method of fabricating hybrid nanostructures is to do repetitions of resist depostition/e-beam lithography/thin film deposition/lift off for each material. While each step of this process is comparatively easy, achieving high quality or reproducible interfaces between different material layers is extremely hard, as between evaporations the film is open to the atmosphere and thus is likely to develop an oxide layer depending on the material. Achieving the requisite level of alignment for each round of lithography is also extremely difficult. The overlap of the aluminium wires with the ferromagnet is tiny, and even a slight error in positioning will result in misaligned wires which do not connect.

In order to reduce the probability of bad interfaces or misalignment between the layers, it was preferable to reduce the number of exposures to a single one which encompassed both layers offset by a precalculated value. The two materials were then evaporated at different angles from separate sources through a predesigned stencil suspended at a relatively large height above the substrate. This is in essence the Dolan bridge or shadow evaporation technique, which is well documented [77].

This was the initial idea behind the fabrication techniques developed for the project. Here the use of a bilayer of resist to produce an undercut was extended to leave a bridge of the upper resist layer left suspended above the substrate. This cavernous undercut allows material evaporated from 2 precise angles to land in contact, to produce continuous hybrid structures.

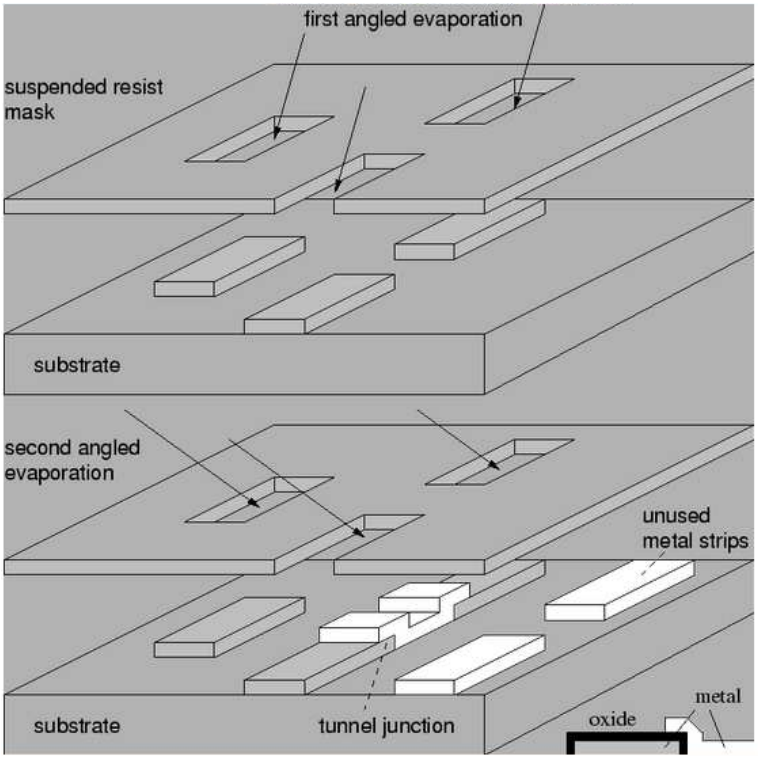

Figure 3.4: Diagram illustrating how the conventional Dolan Bridge technique or shadow evaporation technique may be used to create junctions. It is a powerful, although complicated technique. Even in comparatively simple nanostructures the position of the unused strips has to be given great consideration to prevent them interfering with the structure to be measured [78].

3.2.4 Modification to the Shadow Evaporation Technique

From early work it was apparent that the shadow evaporation technique provided both a better probability of correctly aligning the ferromagnetic and superconducting layers, and that those correctly aligned samples would benefit from greater control of the interface properties. Early samples revealed further issues which were addressed through improvements to the fabrication process. The conventional shadow evaporation technique produces two identical structures which slightly overlap at a critical point to produce the composite part of the structure. This method, however, commonly results in a large quantity of unnecessary material lying on the substrate,

and in some cases under or on top of functioning parts of the structure. Often this results in few problems with the functioning or conduction of the structure as long as there are no short circuits created by extraneous material. In the case of the S/F heterostructure, special consideration must be given to the additional material due to the mutual proximity effects between the superconductor and ferromagnet. Unwanted ferromagnetic material in close proximity to functioning areas of superconductor will at best suppress superconductivity within these regions and at worst could create unwanted normal regions within the structure. Either of these possibilities has the potential to highly complicate the sample's physics and behaviour.

Any unwanted material that lands on the wall of the resist undercut can generally be removed without trace, provided that it is removed promptly and not allowed to collapse onto the substrate. From this observation a solution to the defunct material from the two angle evaporation was devised. By careful construction of the the NanoMaker design to avoid straight wires in the plane of sample rotation, as well as the use of extreme angles during the shadow evaporation, it was possible to ensure that all of the unwanted ferromagnetic material landed on the resist wall and was removed during the specially tailored lift-off procedure. This fabrication method introduced various design constraints such as the use of diagonal wires to traverse distances in one plane, as well as limits on the width of cumulative design features in close proximity in case their undercuts joined up to allow undesired ferromagnet to hit the substrate. Figure 3.5 illustates the stages of the modified shadow evaporation technique.

While the use of extreme angles in the shadow evaporation removed the unwanted ferromagnetic material from the substrate, it also dramatically increased the distance between the 2 parts of the design (that for the Al and Ni). The size of the undercut needed to link the two components of the design was also subsequently increased, and as a result the undercut produced by the conventional Dolan bridge technique was no longer suitable. The resist bridge became too large to be stable and collapsed onto the substrate. As the lower layer of resist was eaten away evenly in all directions, a large area of precarious but unnecessary overhang was created which increased the fragility of the fabrication process. To combat these issues the Dolan bridge was modified with the inclusion of a thin but durable layer of germanium between the two resist layers. The first exposure of the design of the 2 layer evaporation was then conducted as normal. When the design was developed, the solution removed the

exposed areas of the top layer of resist but was unable to penetrate the germanium, leaving the under layer untouched. A plasma of sulphur hexafluoride and oxygen was then used to etch holes into the sturdy germanium layer in order to use it as the stencil. The undercut for this design was created using its own separate e-beam exposure. Rather than the huge non-directional undercut achieved by simple overdevelopment of the underlayer of resist, the undercut exposure created a specific region to be removed between the two components to be joined up. The design benefited from a stronger bridge layer and a more specific undercut which gave the necessary region better support than the standard Dolan bridge technique. The selective undercut germanium bridge design allowed for the perfection of a 2 angle evaporation technique which facilitated the control of S/F interface properties and the elimination of unwanted ferromagnetic material on the substrate. Both of these achievements were critical to the progress of the project.

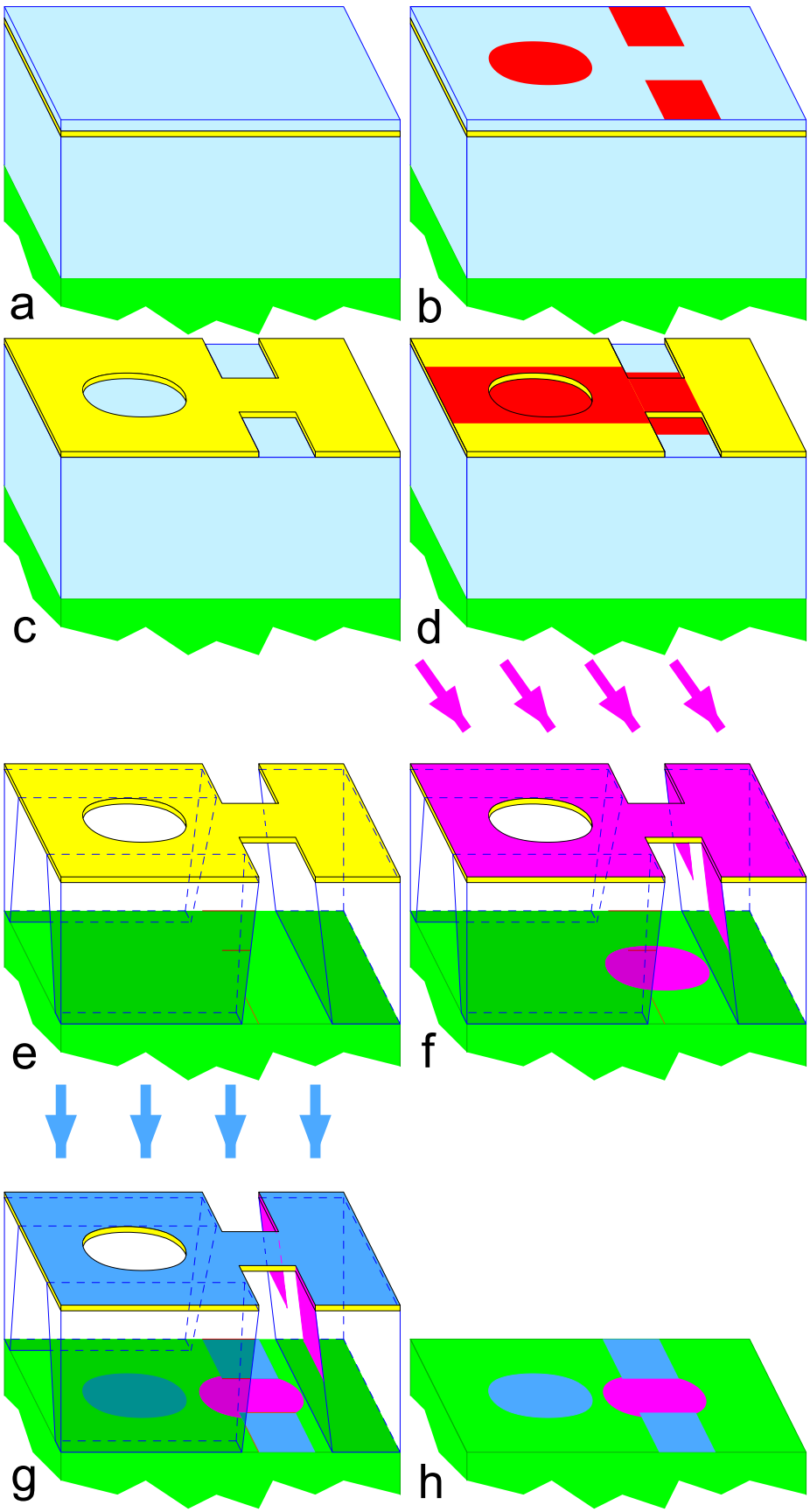

Figure 3.5: Diagrams showing the modified shadow evaporation technique. a) Shows the trilayer of copolymer, germanium and PMMA resting on the silicon oxide substrate. b) Shows the pattern of the first e-beam exposure. c) Shows the stencil etched into the Ge layer. d) Is the undercut exposure area. e) Shows the undercut after the second development. f) The high angle ferromagnet deposition. g) The superconductor deposition. h) The finished structure after lift-off.

Chapter 4

Experimental Apparatus

4.1 Cryostats

4.1.1 Heliox He3 Top Loading Cryostat

The majority of the data exhibited in this thesis was collected from samples loaded in this cryostat. While its base temperature of 240mK was not as low as that attainable using other systems, the ease and speed with which sample sets could be exchanged and the capacity to load up to four chips at once made this system an attractive option for high turnover sample testing. The principle of the fridge is relatively simple. A large reservoir of liquid He4 is the primary coolant from which a thin intake delivers a steady trickle to the 1K pot. A rotary pump reduces the vapour pressure within this chamber and He4 evaporation cools it to approximately 1.3K. The chamber outside the 1K pot is part of a separate gas system around the samples themselves which contains He3. He3 gas condenses on the cold wall of the 1K pot and drips down to form a pool around the samples. A charcoal sorption pump within this chamber accelerates the rate of evaporation to reduce the temperature of the samples to approximately 240mK. When the He3 pool has completely evaporated the samples will begin to warm up. At this point the captured He3 is released from the charcoal by heating it to to 45K. The released gas recondenses on the 1K pot and recools the samples. Due to the single-shot nature of the fridge, measurements were interupted ever 36 to 48 hours to recondense the fridge. Temperature dependence of samples above the base temperature could be investigated by slightly heating the sorb to strike a balance between the cooling power of the He3 and applied power to the heater.

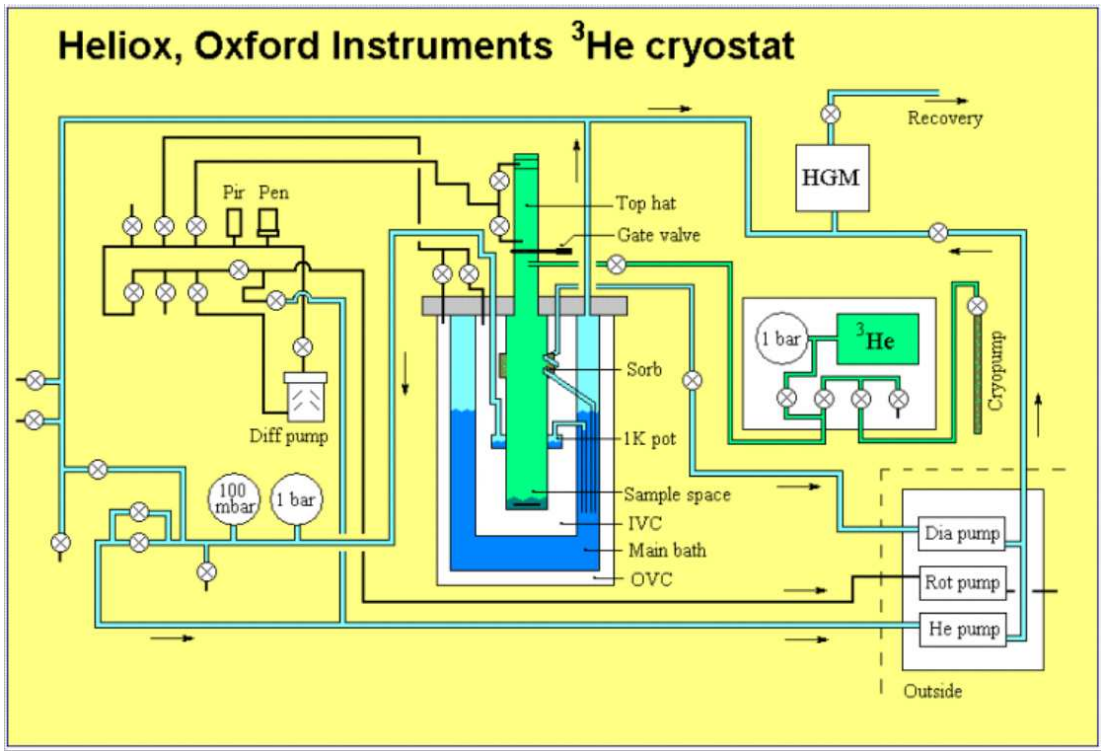

Figure 4.1: Diagram of the Heliox He^3 cryostat and helium systems [79].

4.1.2 Dilution Refrigerator

In the later stages of this project, a small number of measurements were conducted in the sub 50mK range using a dilution refrigerator. First built at Leiden University in 1964 [80], this breed of cryostat provides the only continuous cooling method to reach temperatures below 300mK, and the capacity in optimised systems to reach as low as 2mK. A cold mixture of He3 and He4 (<870mK) within the mixing chamber separates to form a He3 rich phase and a He4 rich phase. The He3 rich phase will consist of almost entirely He3 while the He4 rich phase, even at the lowest temperatures will still contain at least 6% He3. When the He4 phase is pumped upon by the rotary pump a far greater proportion of He3 will be removed than He4. To address this imbalance He3 passes across the phase boundary to replenish the He4 phase. It is this evaporation of He3 across the phase boundary which provides the fridge with its cooling power. He3 heavy gas pumped out of the He4 phase is recirculated to provide continuous cooling power within the mixing chamber. The thermometers installed on the dilution fridge used within this project had only been calibrated as low as 50mK. While it was found that the fridge's operating base temperature was lower than this, an exact value is not known. Time constraints

meant that only one set of measurements was conducted on this equipment.

4.2 Transport Measurements

Conventional 4 probe transport measurements were carried out on structures throughout the project, using lock-in amplifiers and stable Yokogowa type voltage/current sources. The lock-in amplifier technique was used to minimise the noise level due to the small sized signals measured.

A low fequency AC signal from the lock-in amplifier was combined with DC voltage from a high stability source. These signals were combined before a large bias resistor (typically 100kΩ or 1MΩ) was used to produce a low noise probing current in the range of 0-150nA, while the bias current through the structure was varied over an approximate range of 0-60μA depending on the critical current of the structure. Voltage probes on either side of the nanostructure were connected to a low noise voltage pre-amplifer at room temperature. The output from the pre-amplifier was then transferred to the lock-in amplifier where by comparing the excitation signal returning from the structure with the reference signal originally generated, the majority of the noise could be eliminated. A diagram of the 4 probe measurement system is shown in Fig 4.2. To vary the magnetic field the heliox cryostat contained a superconducting coil, the current through this coil was controlled via a high stability DC source. Due to the tiny size of the sample loops in comparison to the solenoid coil, the change of field across the sample is negligible.

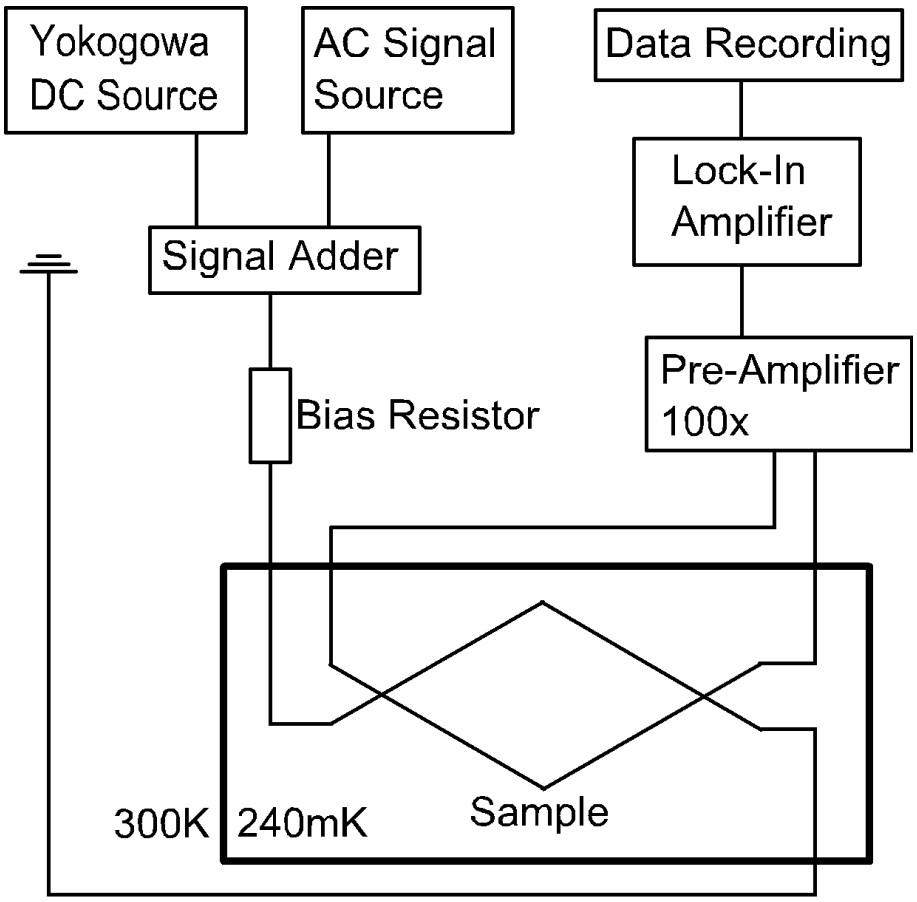

Figure 4.2: Diagram of the 4 probe measurement system.

4.3 Atomic/Magnetic Force Microscopy

Atomic and Magnetic force microscopy (AFM) (MFM) imaging of mesoscopic ferromagnets as well as hybrid nanostructures was carried out by the author during visits to the National Physical Laboratory. The measurements were carried out at room temperature using a MultiMode microscope. The instrument operated in the lift scan mode at a lift height of 40nm. Standard Co.Cr tips (Bruker MESP, $H_c \approx$ 400Oe. Moment $\approx 10^{-13}$ emu). The tip was magnetised in the direction normal to the sample.

AFM was originally invented by Binnig, Quate and Herber in 1986 [81], it works on the principle of bringing an extremely fine probe tip mounted on a cantilever into very close proximity to the sample surface and then measuring the force exerted on the tip by the sample via the deflection of the cantilever. The cantilever deflection is normally measured with a photodiode array via the slight changes in position of the reflected beam which result. The system can be set up to measure various different

forces although the most common are the Van der Waals forces as described by the Lennard-Jones potential which gives the potential between two atoms located at a distance r from each other. In this case the foremost atom on the probe tip and the nearest atom of the sample surface.

AFM measurements can be carried out with the tip in constant contact with the sample or with the tip maintained at a constant distance from the surface by a piezoelectric actuator. The best image resolution with the least probability of sample or tip damage is achieved using a dynamic or tapping mode. Here the tip is kept suspended at a set distance above the sample surface, while being driven to oscillate at an amplitude of around 1nm close to the resonant frequency of the cantilever. The changes to the phase of the oscillations caused by the interaction between the tip and the sample are recorded and processed to produce an image of the surface. By measuring at a set distance using such a technique it is possible to attain high resolution while minimising the probability of damaging either the sample or the AFM probe.

MFM works in a similar way to AFM, but the tip which is used is coated in a layer of ferromagnetic material with a specific magnetisation. The tip is again attached to a cantilever arm and lowered towards the sample surface. Due to the longer range action of the magnetic interaction, MFM imaging is done at a greater distance from the sample surface than AFM processes. This stops other forces from interfering with the cantilever deflection and helps to minimise the chances of the tip or sample being damaged or having their magnetisations affected by the other. By sensing the stray field from the domain structure of the sample, an image of the magnetisation in different parts can be developed. Fig 4.3 illustrates the MFM process while Fig 4.4 shows the contrast expected when measuring a single domain using the technique.

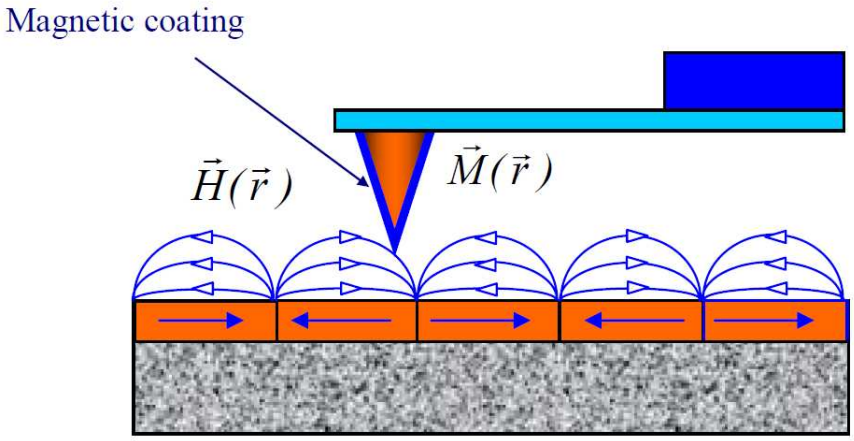

Figure 4.3: Illustration showing the source of the imaging signal in MFM imaging.

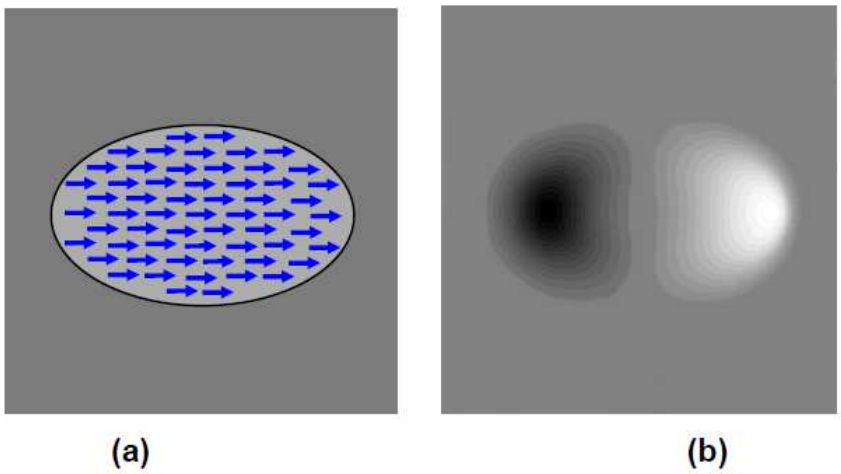

Figure 4.4: Illustration showing the MFM result expected when imaging a single magnetic domain.

Chapter 5

The Search for a Long-Range Triplet

This section details the experiments carried with the aim of measuring the long-range proximity effect within mesoscopic ferromagnets, as well as some of the peripheral work done to assist in achieving this goal. The results map how the experiments evolved as the experimental system came to be better understood, and chart the improvements in measurement techniques and fabrication techniques developed. Consideration of how the reciprocal proximity effect impacted upon the functionality of the hybrid samples led to independent experiments to probe this effect and how to suppress it. The 4 probe structure, multiple junction array and some of the 4N Ni hyquid results included in this section were completed in collaboration with Richard Marsh who was another student within the research group. This data was previously published in Richard's thesis [79]. All other experiments in this chapter and all of the experiments described in the following chapter were conducted independently.

5.1 Four Probe SFS Junction Measurements

Initial work in the project focused on the fabrication and measurement of simple devices consisting of a mescoscopic ferromagnetic disc with interfaces to two superconducting electrodes. The electrodes each then split into two separate wires to accomodate 4 probe resistance measurements of the structure. This design allowed for the most simple and direct measurement of the resistance of a mescopic ferromagnet attached to superconducting wires, and until the theoretical calculations of

Kalenkov (discussed in section 2.2.8) indicated the tiny nature of the triplet component's critical current (picoamp) there was little reason to complicate the design. This early stage of the project provided a testing ground for the 2 angle shadow evaporation fabrication processes being developed. Later in the project, alternative structures allowing different measurement methods were employed to improve the sensitivity of the experiment. These included using large arrays of junctions and incorporating the ferromagnet into an Andreev Interferometer.

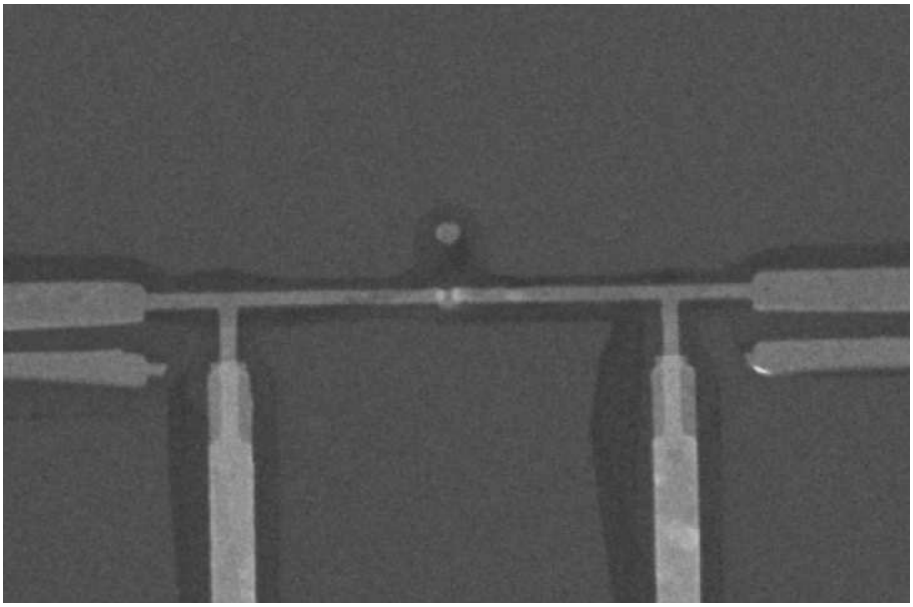

Figure 5.1: SEM image of an early sample produced using the shadow evaporation technique. It is intended for direct 4 probe measurement of a disc based SFS structure.

5.2 Multi-Junction Arrays

Large arrays of the same type of SFS junctions were designed and fabricated in an attempt to increase the signal to noise ratio at very small currents. By using a large number of junctions in series a larger voltage change would be expected as the contributions add up across the array. While some junction arrays were successfully built and measured, achieving complete strings of unbroken junctions proved extremely difficult, and successfully fabricated samples were extremely sensitive to thermal cycling during measurements. As a result new methods of probing the proximity effect within mesoscopic ferromagnets were investigated.

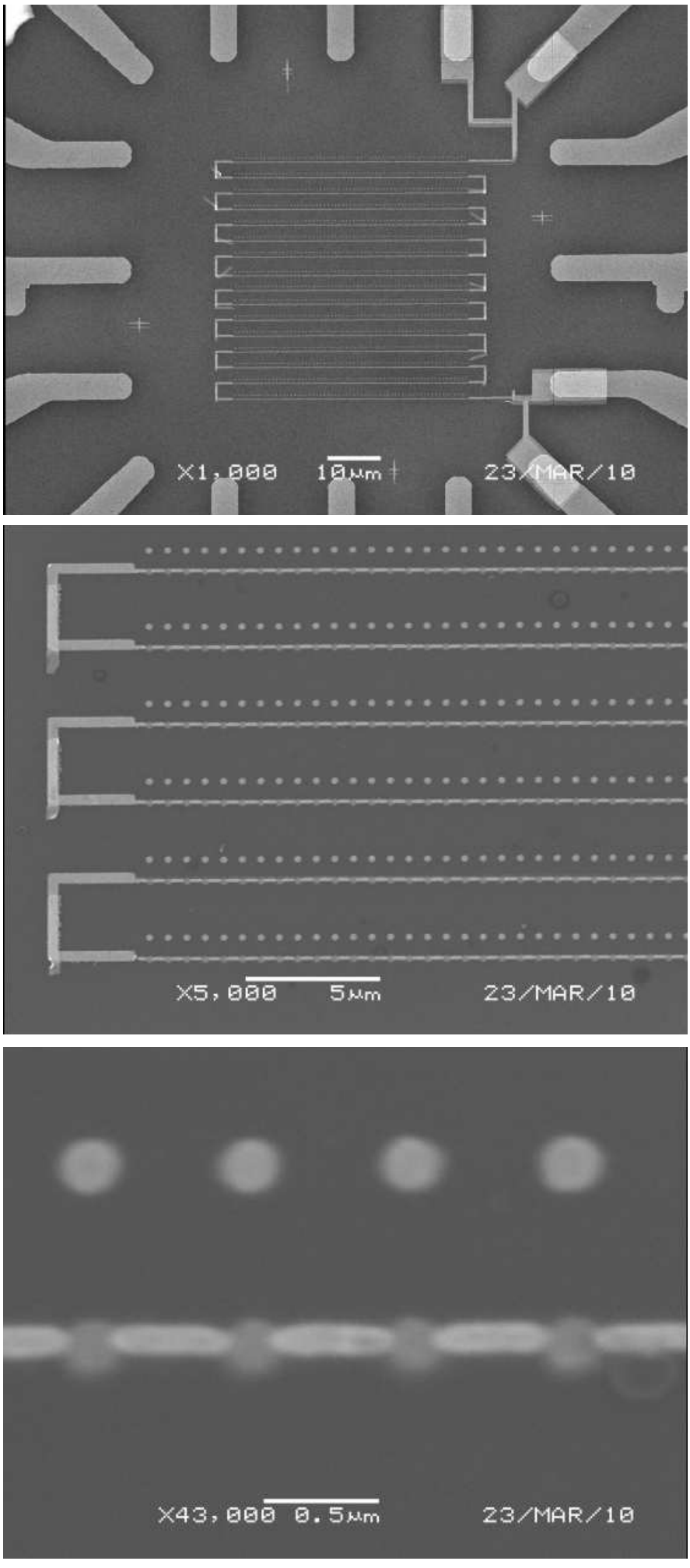

Figure 5.2: SEM images of a series array of 1064 individual junctions.

5.3 Hybrid Quantum Interference Device

Direct resistance measurements with the available measurement system were shown by Kalenkov to breach the predicted critical current of the triplet proximity effect within a circular nanomagnet contacted by superconducting wires. As a result, a new branch of sample fabrication began with the aim of incorporating the mesoscopic ferromagnet into a flux driven Andreev interferometer. The resulting device was named the Hybrid Quantum Interference Device or HyQuID. The hyquid consists again of an SFS junction incorporating an inhomogeneous nanomagnet, in this device the superconducting wires extending from interfaces on opposite sides of the ferromagenet join up to form a loop.

If a triplet component is being generated within the inhomogeneous ferromagnet, and the distance between the two superconducting electrodes is less than twice the phase breaking length within the ferromagnet, then resistance oscillations will be produced as a function of changing phase difference between the superconducting electrodes. Due to the closed loop design of the device, the phase difference between the interfaces can be varied by modulation of the circulating current. This current is controlled by varying the magnetic flux passing through the loop. By attaching further wires to the device to allow a 4 probe measurement of the device's resistance (superconductor and ferromagnet) these resistance oscillations as a result of varying magnetic field are measurable. Provided that the distance between the superconducting electrodes is greater than the singlet phase breaking length within the ferromagnet, then a functioning sample provides an indirect but uncontestable proof of superconducting phase coherent electron transport existing within the ferromagnet as a result of a long-range proximity effect. Different shapes of mesoscopic ferromagnets with their own magnetic stuctures can be substituted into the design to look for the best results.

By careful angling of the wires of the hyquid in conjunction with the exact placement of the asymmetrical undercut, it was possible to perfect a 2 angle process for hyquid fabrication which reliably produced good quality junctions while maintaining an on-chip enviroment that was free from unwanted ferromagnetic material. Further work was carried out based on the data obtained when testing the initial samples at low temperatures. By analysing each set of results it was possible for the fabrication processes to be further tailored and refined in order to gain control over various

system parameters such as the quality of the interfaces and the purity of the wires. The effect of these improvements on the fabrication processes was clearly apparent within the results obtained during measurement.

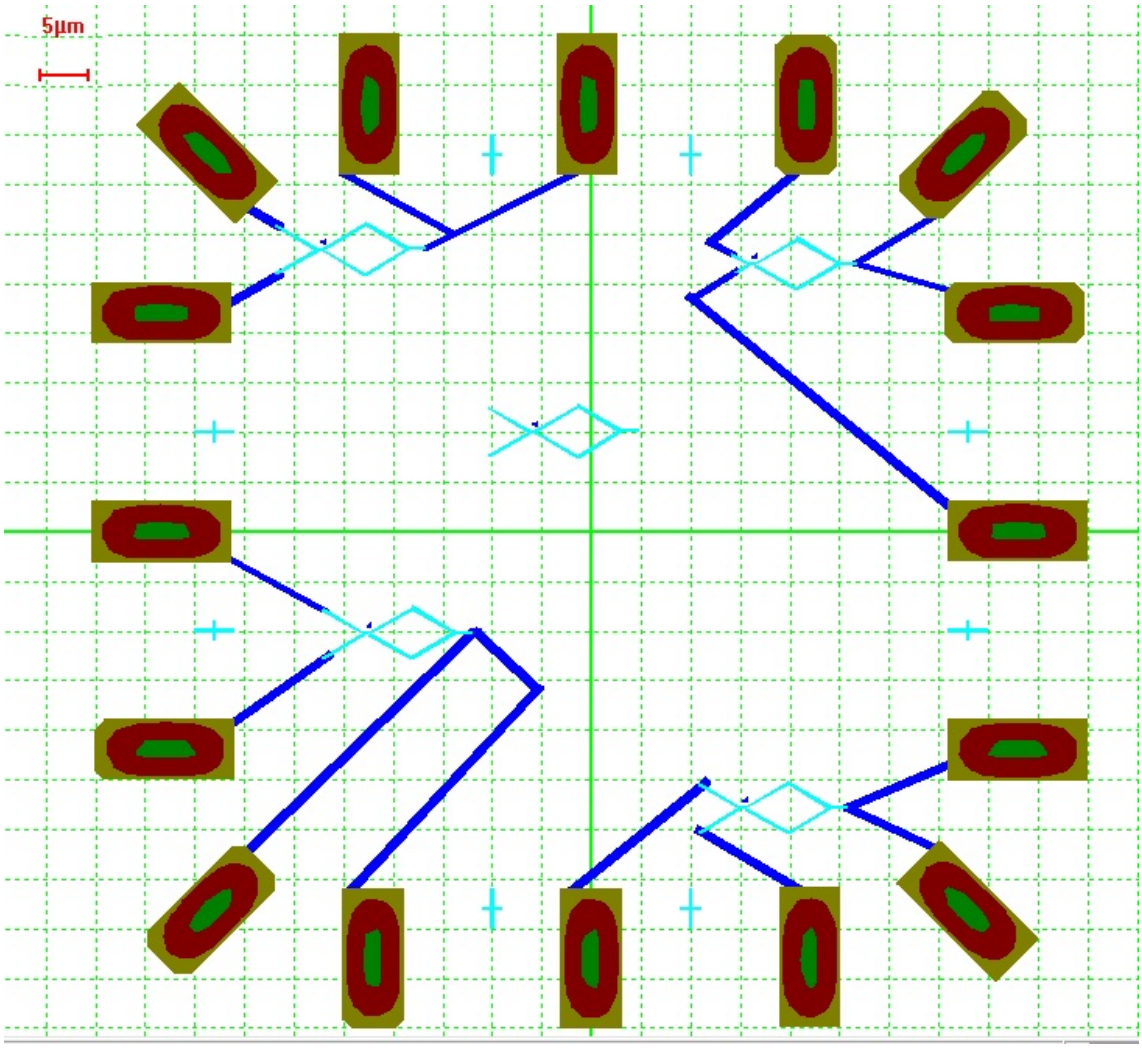

Figure 5.3: The NanoMaker design for the top layers of lithography for a hyquid based on triangular ferromagnets 450nm in size. The different colours represent different electron doses. The unconnected structure at the centre is a test piece for examining the top layer of lithography and the quality of the plasma etch on the Ge layer. The unconnected crosses are used for precisely aligning each layer of lithography with the first.

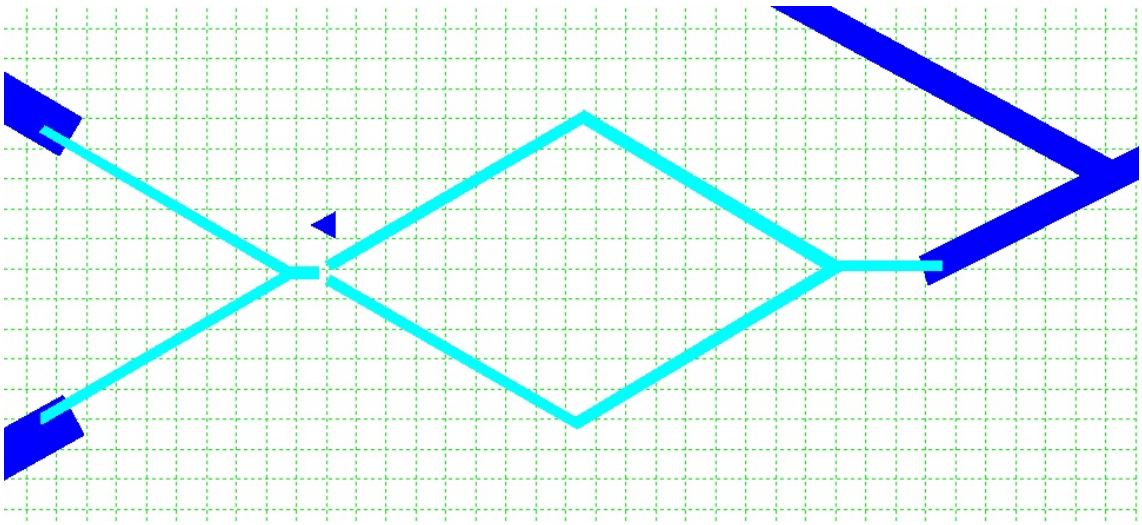

Figure 5.4: A close up of one of the structures from the design shown in Fig 5.3.

The 2 angle evaporation process for the interferometer design shown in Fig 5.4 is as follows. First the ferromagnetic material is evaporated from a steep angle resulting in the majority of the material which passes through the gaps in the germanium being caught on the resist wall but the part that passes through the triangular island landing on the substrate, this is shown in Fig 5.5. The second evaporation when done from the correct angle results in the interferometer loop and measurement connections being deposited so that the 3 tips of the electrodes are in contact with the ferromagnet as shown in Fig 5.6. The 4 point transport measurement is carried out via the labelled connections.

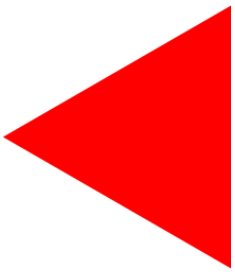

Figure 5.5: The ferromagnetic component produced on the substrate as a result of the first step of the 2 angle evaporation process .

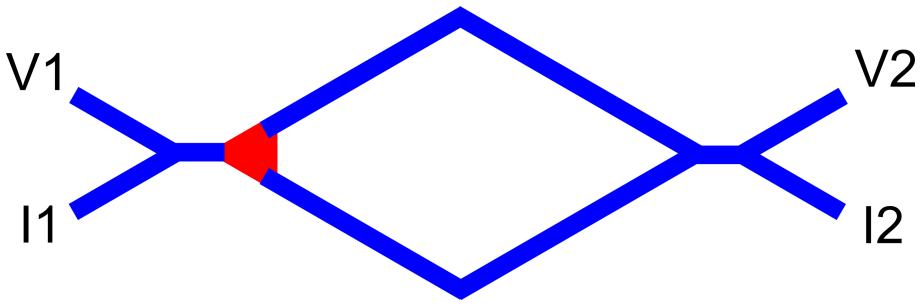

Figure 5.6: The structure resulting after the second evaporation step. If the lithography and evaporation processes are conducted correctly then the ferromagnetic component will be centrally located and in contact with all 3 electrodes. .

5.4 Superconducting Phase Coherent Effects in Silver Hyquid Reference Samples

In order to prove the validity of the interferometer design without the effect of a ferromagnetic interference medium, a set of identical interferometers were fabricated where the ferromagnetic deposition was replaced with a silver one. This resulted in structures containing comparatively short SNS junctions which would be expected to display the behaviours associated with Andreev interferometers.

5.4.1 Sample 1

Figure 5.7 shows a typical dV/dI sweep for one of these structures with a triangular Ag section taken at 240mK. At zero bias the whole structure is completely superconducting as the short length of the silver junction experiences a very strong proximity effect allowing it to carry a supercurrent with significant critical current. The completely superconducting state persists to relatively high bias currents compared with similar SFS structures, and at 61μA the complete structure experiences a mass transition from the superconducting to normal states. When the bias current is slowly reduced the normal state persists to much lower bias currents than seen when measuring the critical current. At 21μA and 11μA large transitions are observed corresponding to sections of the aluminium structure returning to the superconducting state. The peak at 9μA indicates the entrance of proximity effects within the silver component, indeed phase dependent conductance oscillations are observed at all bias currents from this peak down to the re-entrance of the fully

superconducting phase at 4.6μA.

By balancing the samples in the bias range between 4.6μA and 9μA on the retrapping curve of the dV/dI, quantum interference effects are easily observable within the silver component as shown in Figure 5.8. The period of these oscillations is 1 Gauss which exactly matches the predicted value calculated from the area of the the superconducting loop $\Delta B = \Phi_0/20\mu\text{m}^2 = 1.03\text{x}10^{-4}\text{T}$. This shows that when the interference medium is constructed of a non-magnetic normal metal, Andreev interferometers of this design produced using the modified shadow evaporation technique do indeed work as expected.

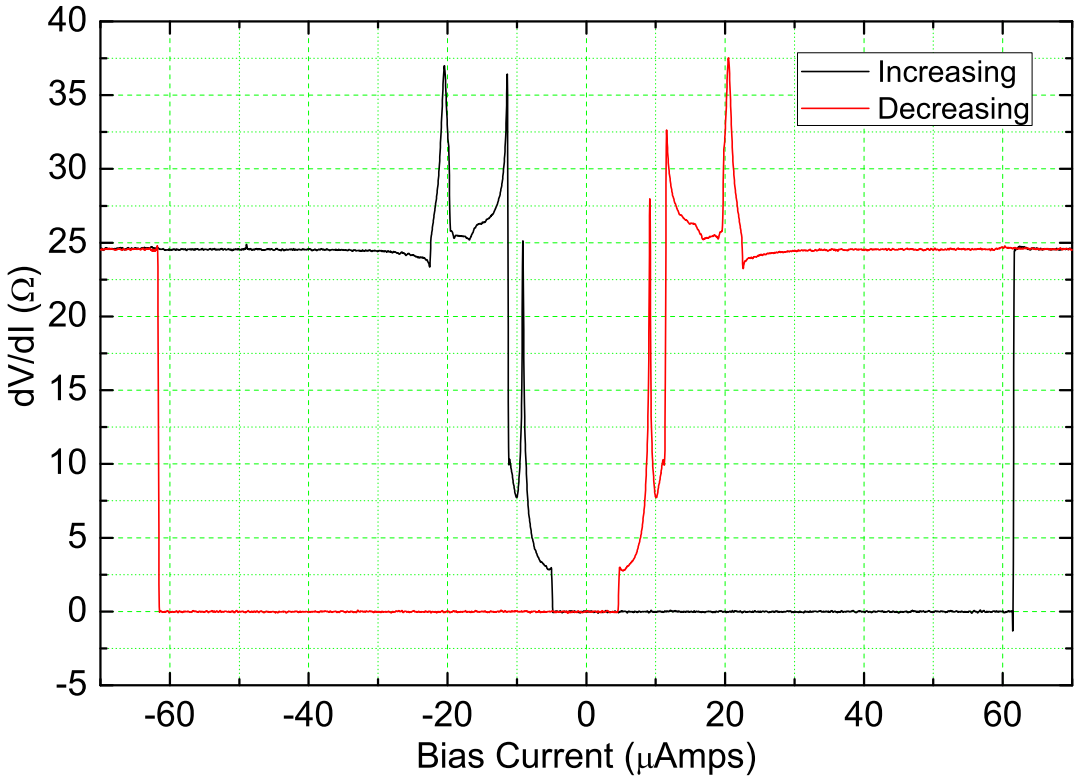

Figure 5.7: dV/dI measured at 240mK of a silver triangle hyquid interferometer.

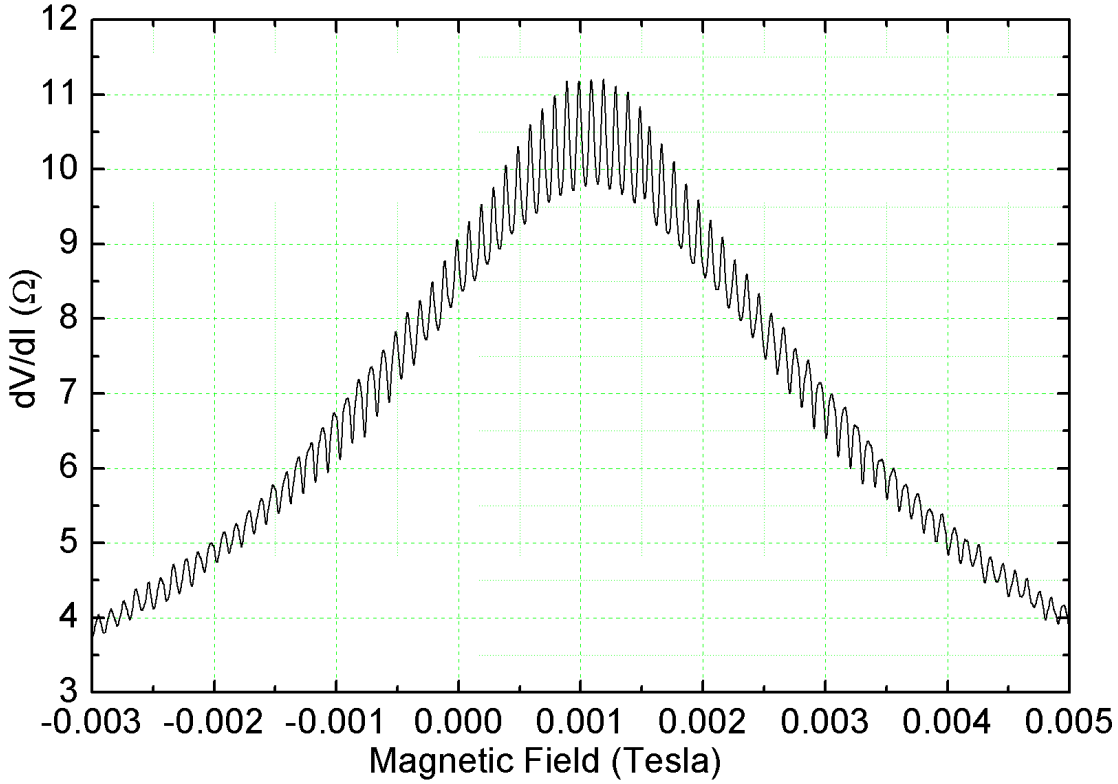

Figure 5.8: Magnetoresistance oscillations at 240mK measured at 9.06μA bias current on the retrapping curve of the silver triangle interferometer.

5.4.2 Sample 2

An interferometer was also measured in which the Ag component was disc-shaped. As the geometry of a normal metal component is not expected to affect the proximity effect we expect to see a very similar graph to that observed for the triangular sample. Figure 5.9 shows the dV/dI measured in the disc-based sample at 240mK. The critical current when driving the whole sample normal is 46.5μA. The majority of the aluminium returns to the superconducting state at a retrapping current of 12.5μA, followed by a small resistance plateau representing the existence of an SNS junction. The return from SNS to fully superconducting states occurs at 5μA. The critical current of the structure is very close to that of the triangular one, with the variation attributable to variations in the film quality between the samples. The slightly reduced retrapping current and less stable SNS state of the disc sample can be explained by the shorter junction length between the electrodes in this sample. Figure 5.10 shows some of the substructure of the dV/dI with individual steps visible within the large peak structure. Figure 5.11 shows directly measured conductance

oscillations at a set bias current of 11.5μA. Direct measurement of oscillations in this sample were difficult due to the sample's tendency to "drop" back into the superconducting state after a few seconds or minutes in the SNS state. A better picture of the oscillations is given in Figure 5.19 where a 2D image of the evolution of the dV/dI shape at varying fields is displayed. Clear oscillations are observed in both the critical and retrapping currents with an period of 1G as predicted from the area of the structure's loop.

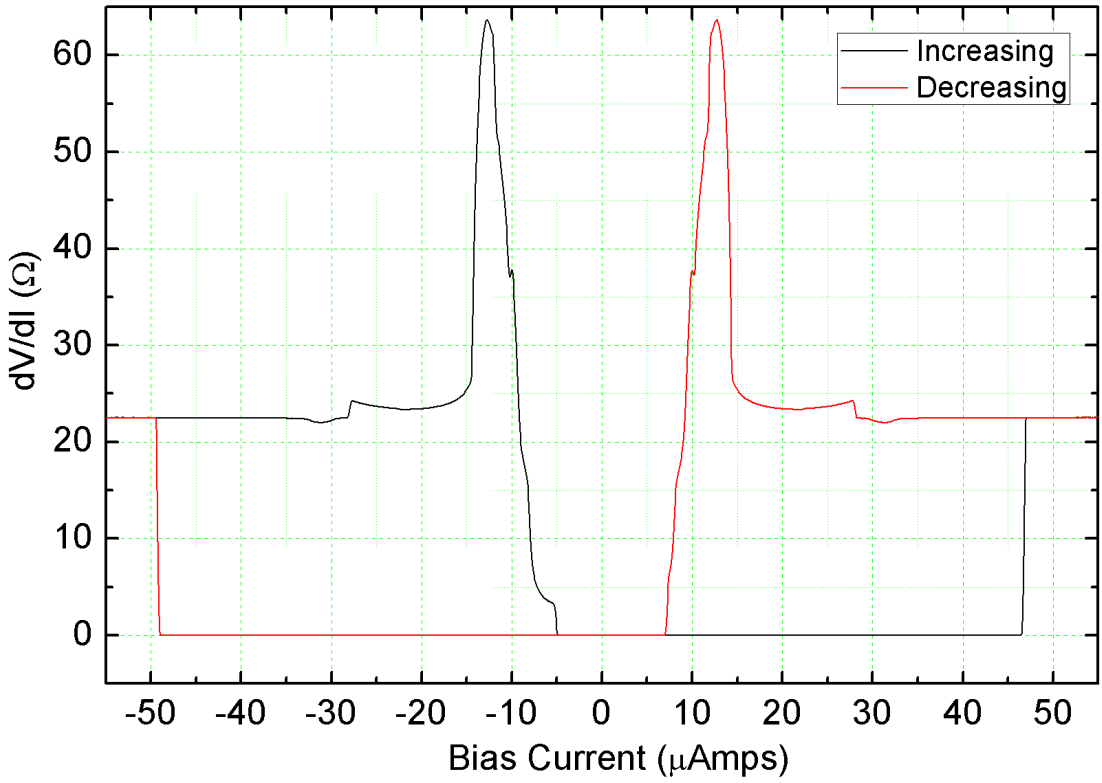

Figure 5.9: dV/dI of a silver disc interferometer. Asymmetry between the up and down sweeps at low bias currents is due to instability of normal state at these currents when reducing from a larger than critical current value. The "lip" on the up sweep of the dVdI corresponds to a small part of the system remaining normal after the main transition. By setting the bias current to a constant value in this range it becomes evident that over time the system will drop from a SNS into a fully superconducting state after a random time period. In the case of the downwards sweep, the system dropped very quickly fom the metastable normal state into the fully superconducting state. As a result there is no lip on this curve.

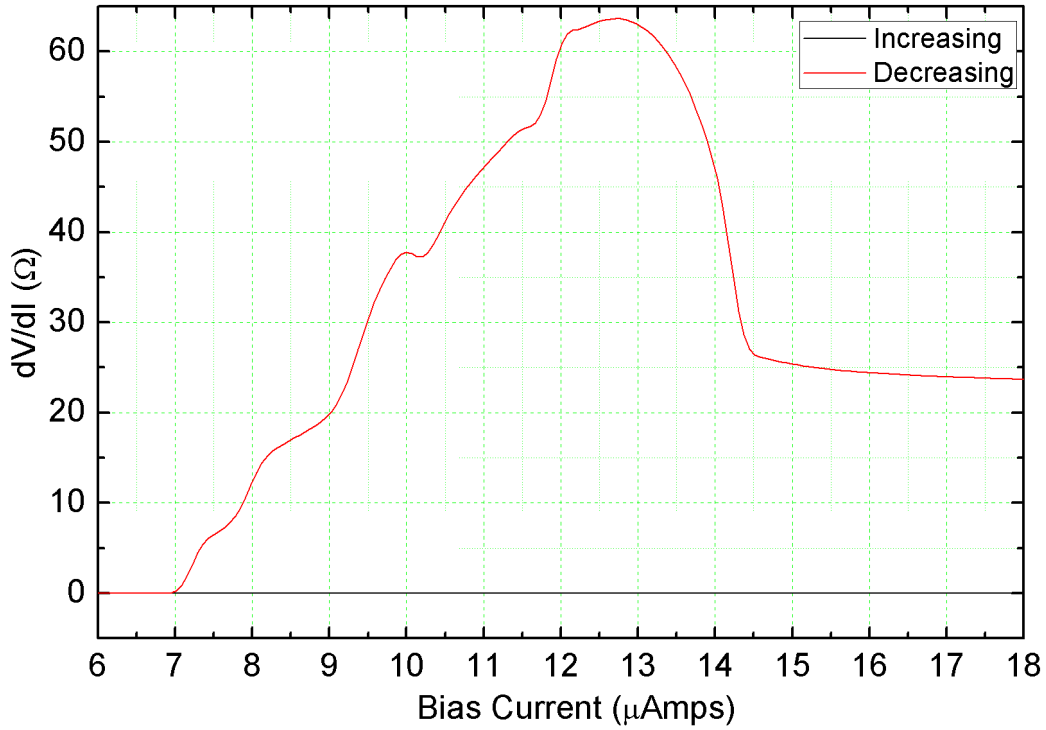

Figure 5.10: Enlarged graph of major transition in dV/dI shown in Fig 5.9. Fine structure to the peak is discernable corresponding to a number of transitions occuring at very close currents.

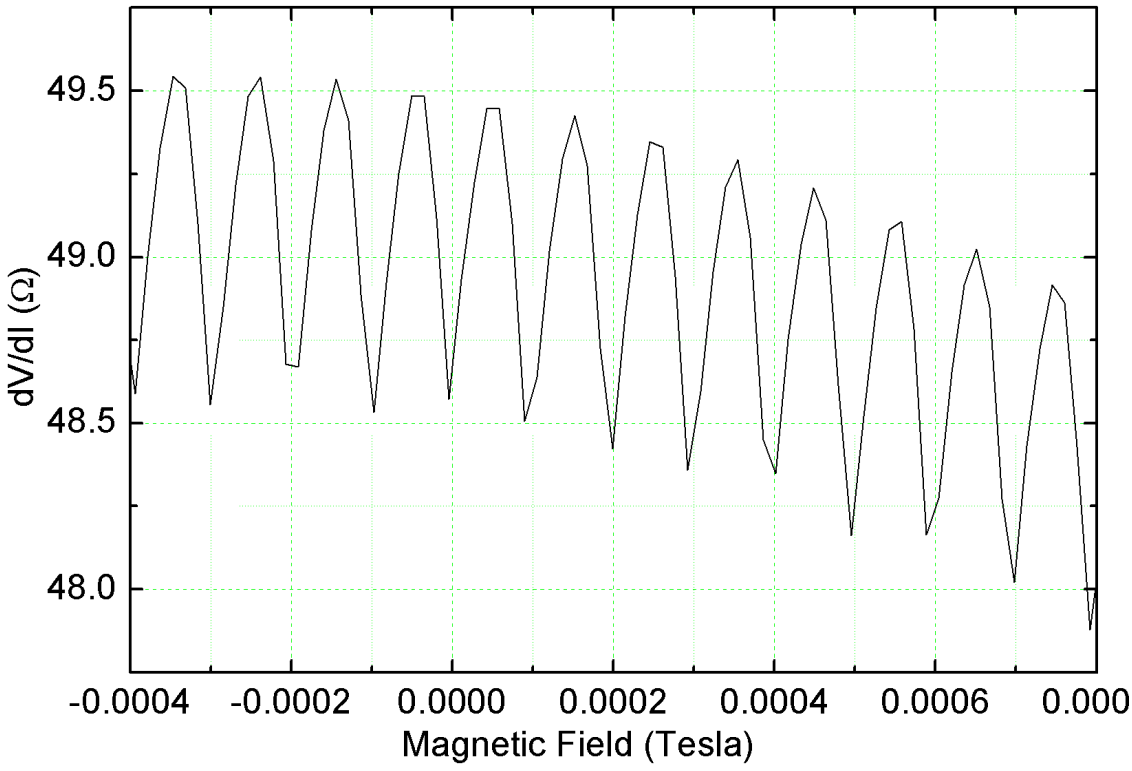

Figure 5.11: Oscillations measured in silver disc at 11.5μA bias current. .

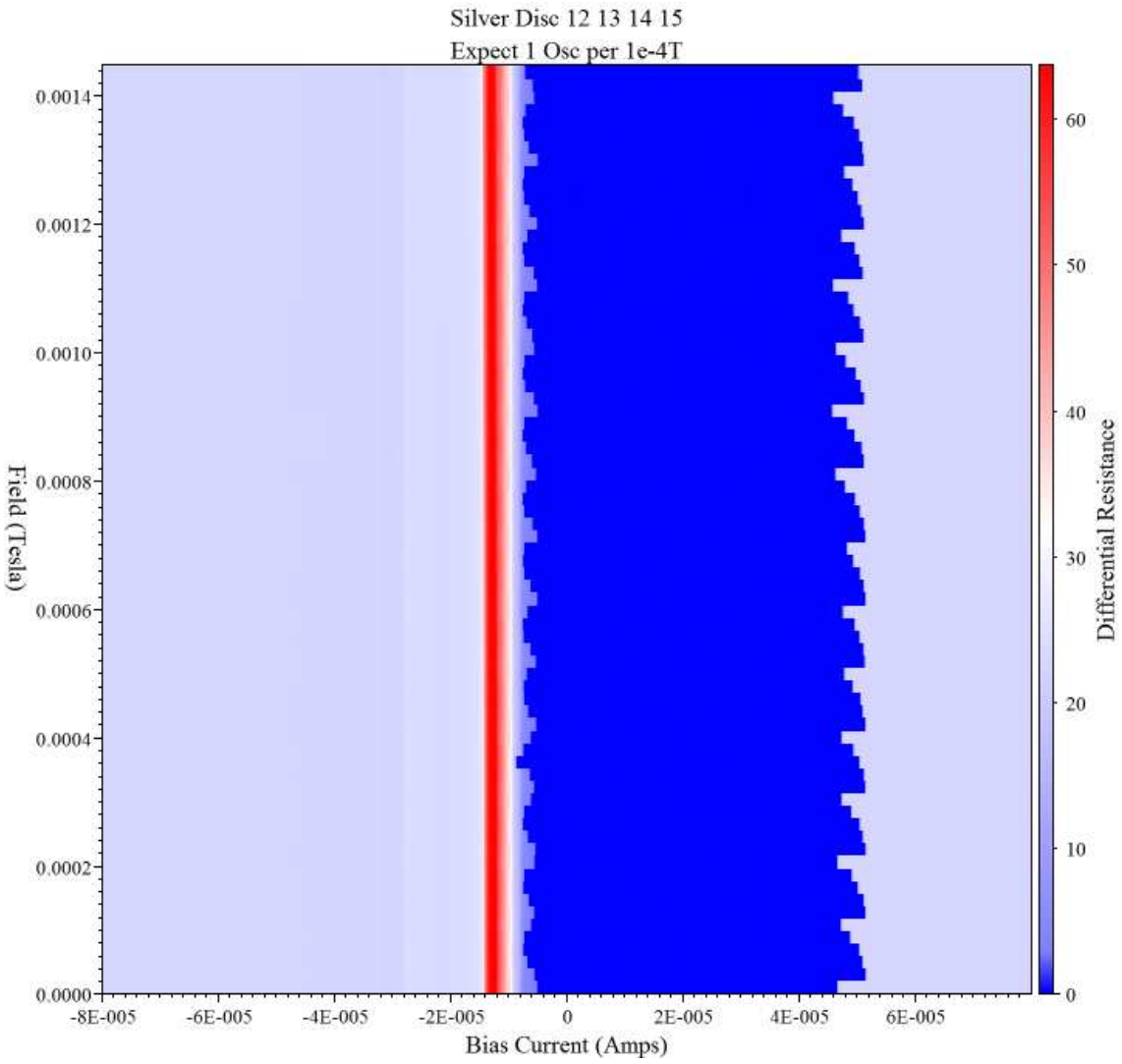

Figure 5.12: Effect of varying field upon the differential resistance curve of the Ag disc sample. Clear oscillations are observable in both the critical and retrapping currents.

As we would expect, the normal state resistances of both the disc and triangle based silver interferometers are very similar. The slight difference can be attributed to minor varations in the film or interface quality or in the separation between the aluminium electrodes on the silver. Clear interference effects were observed within the Ag section of each structure measured. This shows that without the inclusion of ferromagnetic material the geometry and fabrication processes produce highly reliable fully functioning interferometers.

5.5 Observation of Phase Coherent Effects in Hybrid Ferromagnetic-Superconducting Interferometers

Hybrid superconducting and ferromagnetic interferometers were successfully fabricated via the modified shadow evaporation technique. A small fraction of the measured samples did show the phase periodic resistance oscillations hoped for. A very wide spread of sample resistances and dV/dI shapes were observed between the samples indicating that the fabrication processes were not consistent enough to produce reliable structures. A discussion of the types of structures observed follows.

5.5.1 Micromagnetic Simulations For Mesoscopic Ferromagnetic Discs

The Object Orientated MicroMagnetic Framework was used to produce simulations of the ferromagnets used in the project. The geometrical contribution to the magnetic structure of mesoscopic ferromagnets was discussed in 2.2.3. This size range of magnets are too small to split into multiple domains and yet contain too many spins to be regarded as dipoles. As a result their geometry dictates how their spins align in an attempt to minimise the magnetostatic energy of the system. The magnetic vortex was described in section 2.2.4. Figures 5.13, 5.14, and 5.15 illustrate how the OOMMF output evolves over a period of iterations from an initial random scatter of spins to a stable magnetisation, in this case the geometry being modelled is a thin Ni disc and the final magnetisation is a vortex state.

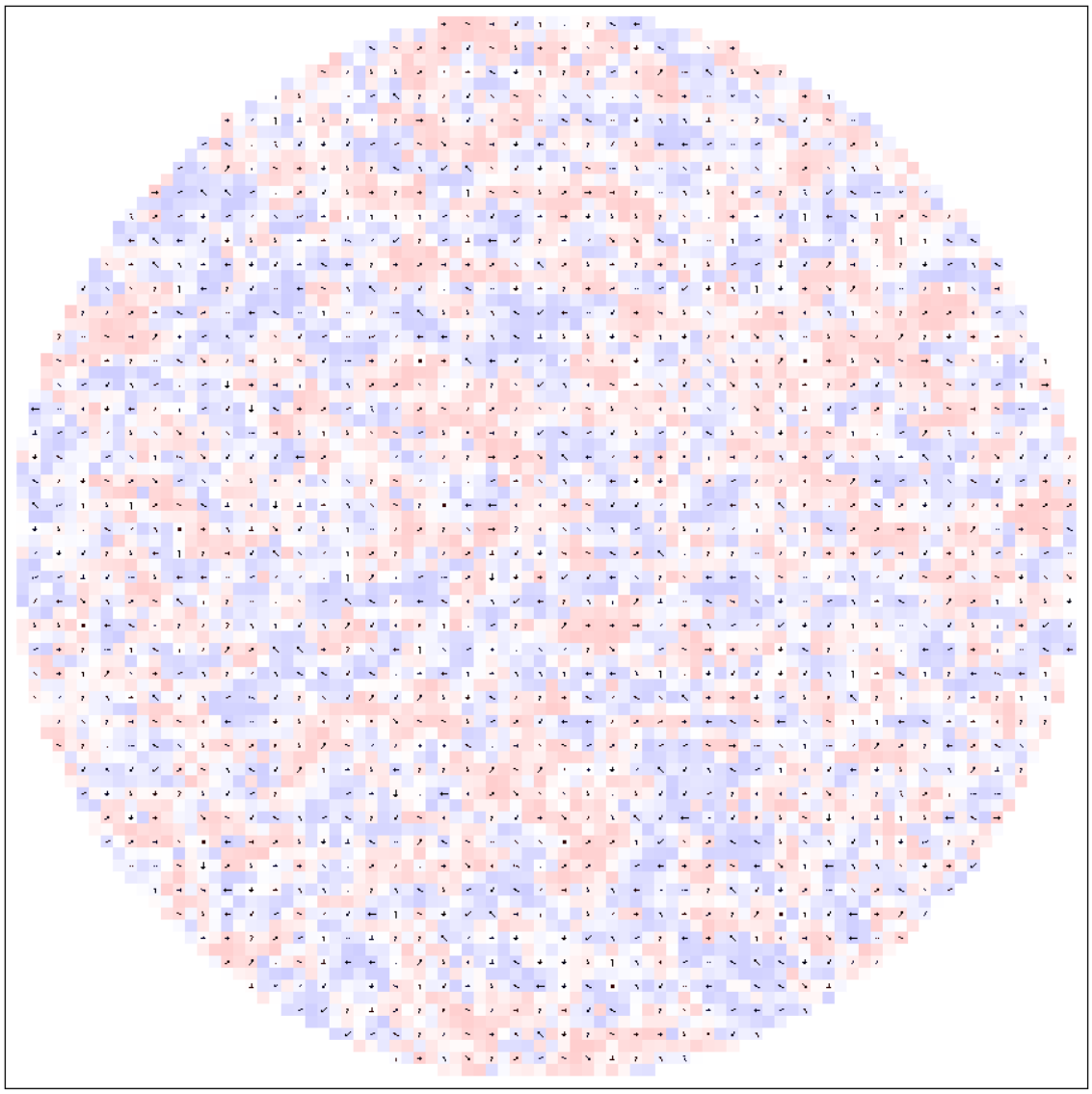

Figure 5.13: A screenshot of the random magnetisation of a 900nm Ni disc at the start of an OOMMF calculation.

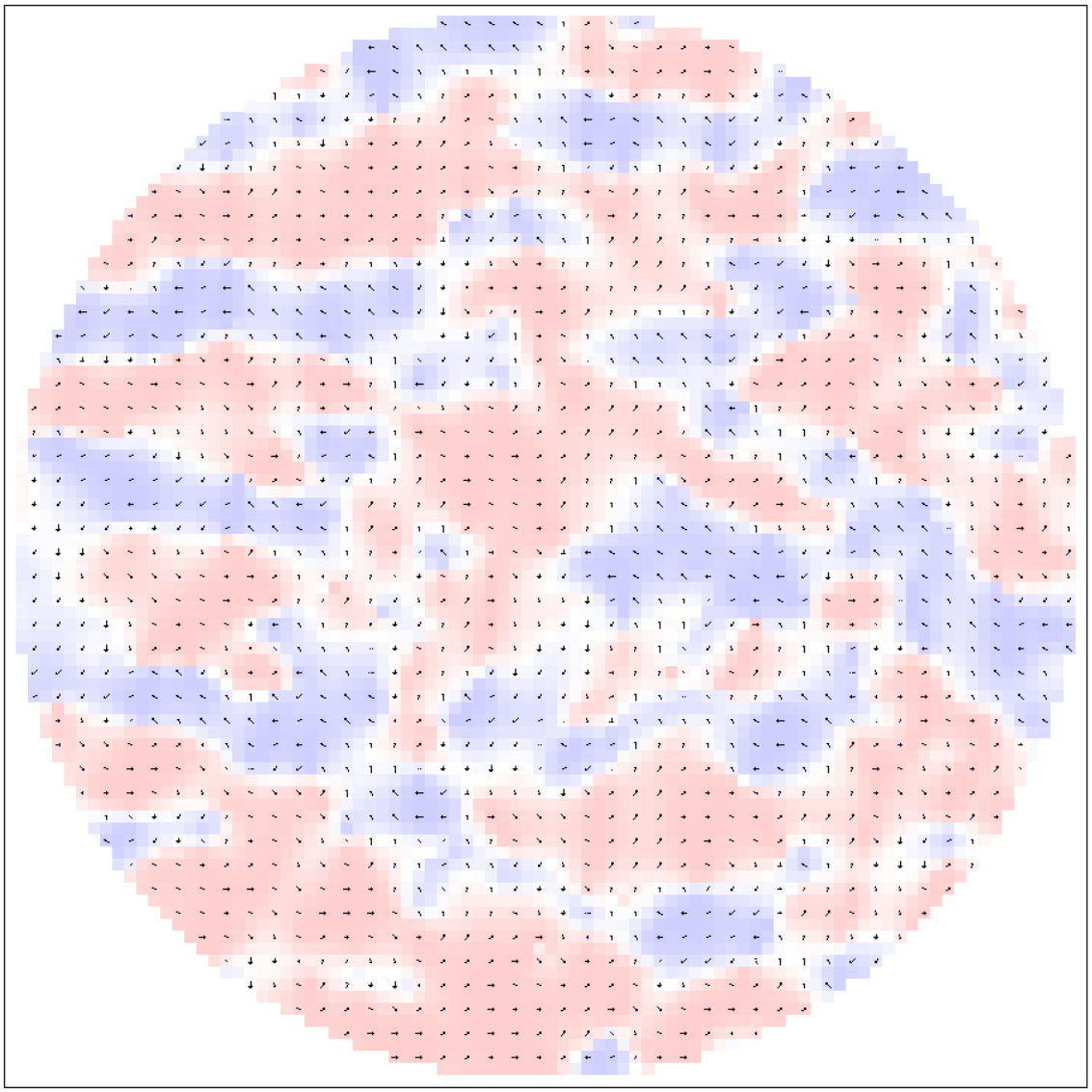

Figure 5.14: After approximately 200 iterations the random scattered spins have begun to align into ordered regions. The magnetisation will continue to evolve until a stable state is reached.

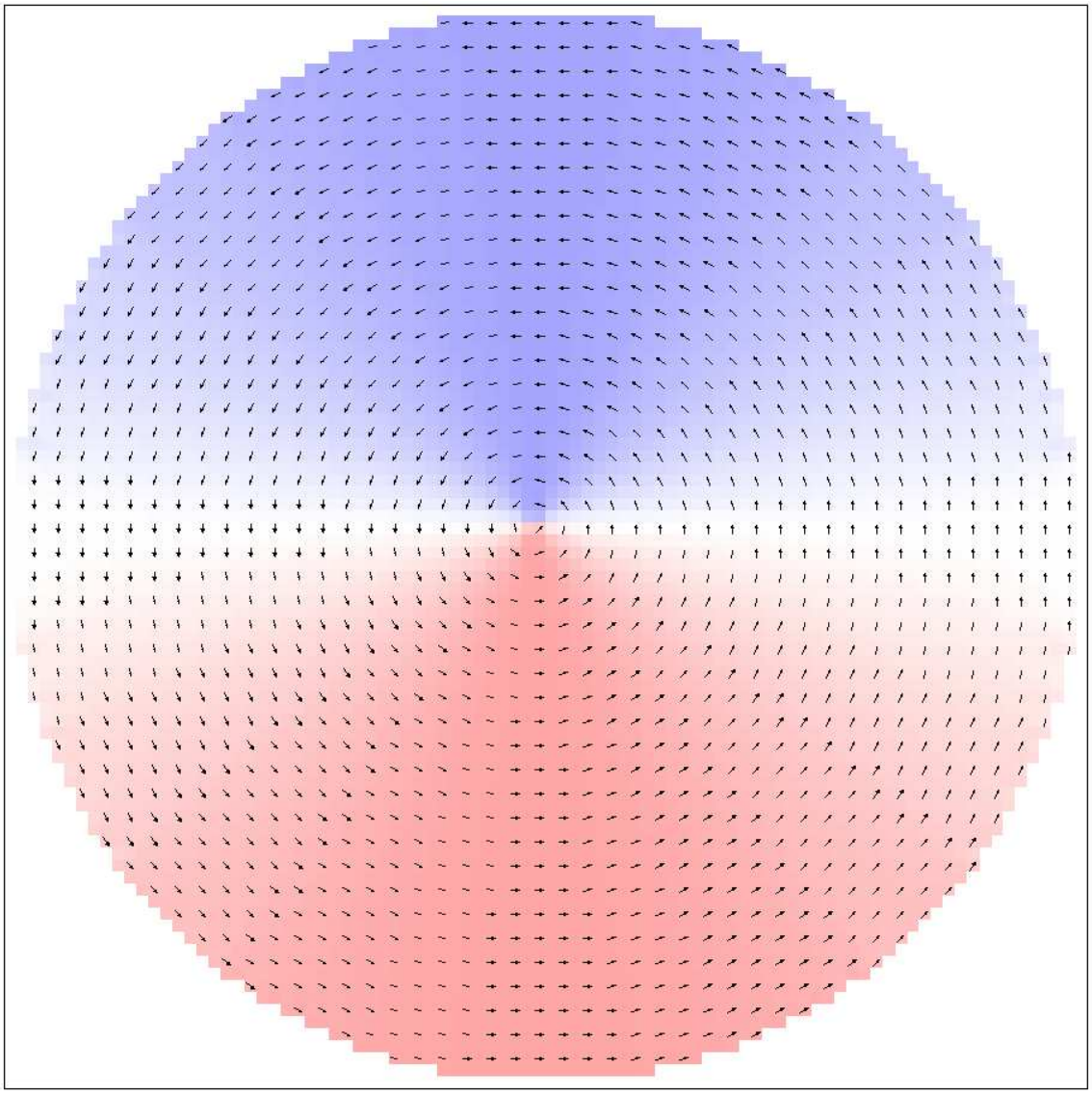

Figure 5.15: Eventually a stable energy state is reached. In this case a magnetic vortex. The number of iterations required in order to reach a stable magnetisation increases with decreasing cell size used in the calculations. Smaller cell sizes however give more accurate results. Similarly there is little correlation between the size of submicon disc and the number of iterations required, but the cell size influences the length of the calculation in all cases.

For a range of materials (Py, Co, Ni) the OOMMF results indicated that an even rotating vortex struture was by far the most likely result in the disc sizes modelled (300nm to 900nm), OOMMF results for other disc diameters and materials are shown in figures 5.16, 5.17 and 5.18. Existing experimental literature also indicated that this was the most probable outcome. Evidence of vortices in cobalt and permalloy discs in presented in [82] and [15] respectively.

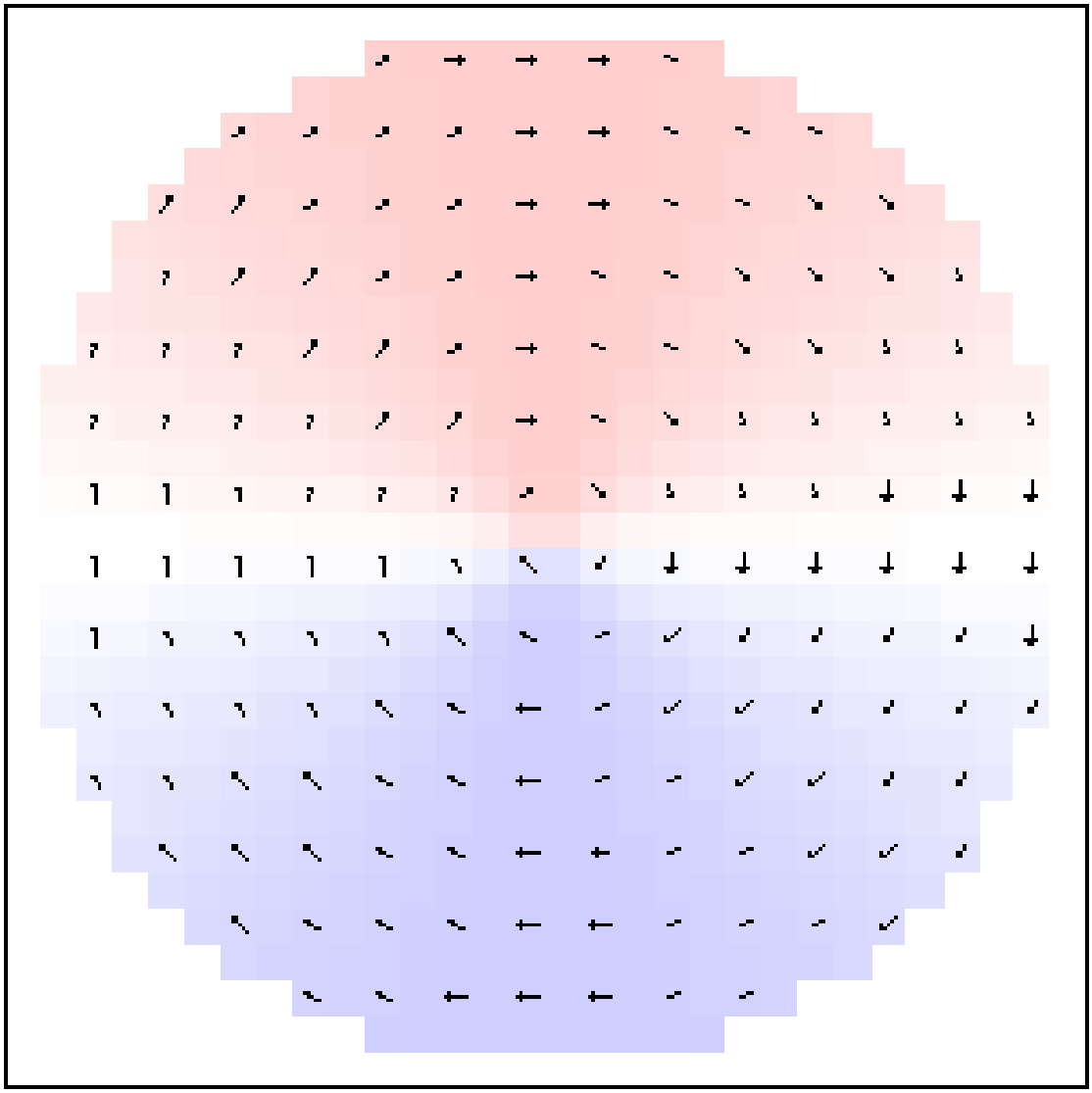

Figure 5.16: 300nm diameter Ni disc, 30nm thick which has again fallen into a vortex structure.

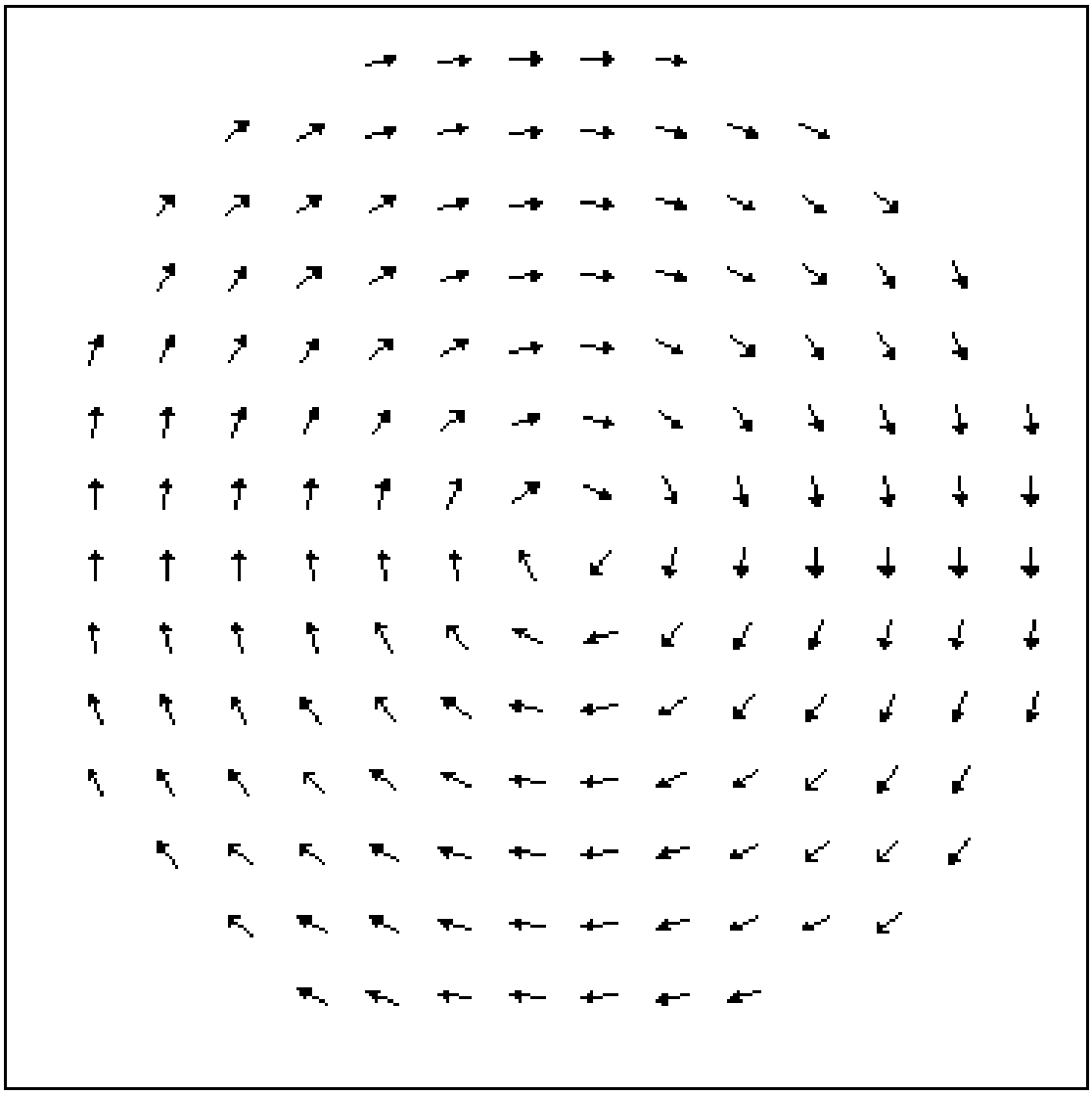

Figure 5.17: OOMMF result for a 300nm diameter permalloy disc, 30nm thick which has reached a vortex structure.

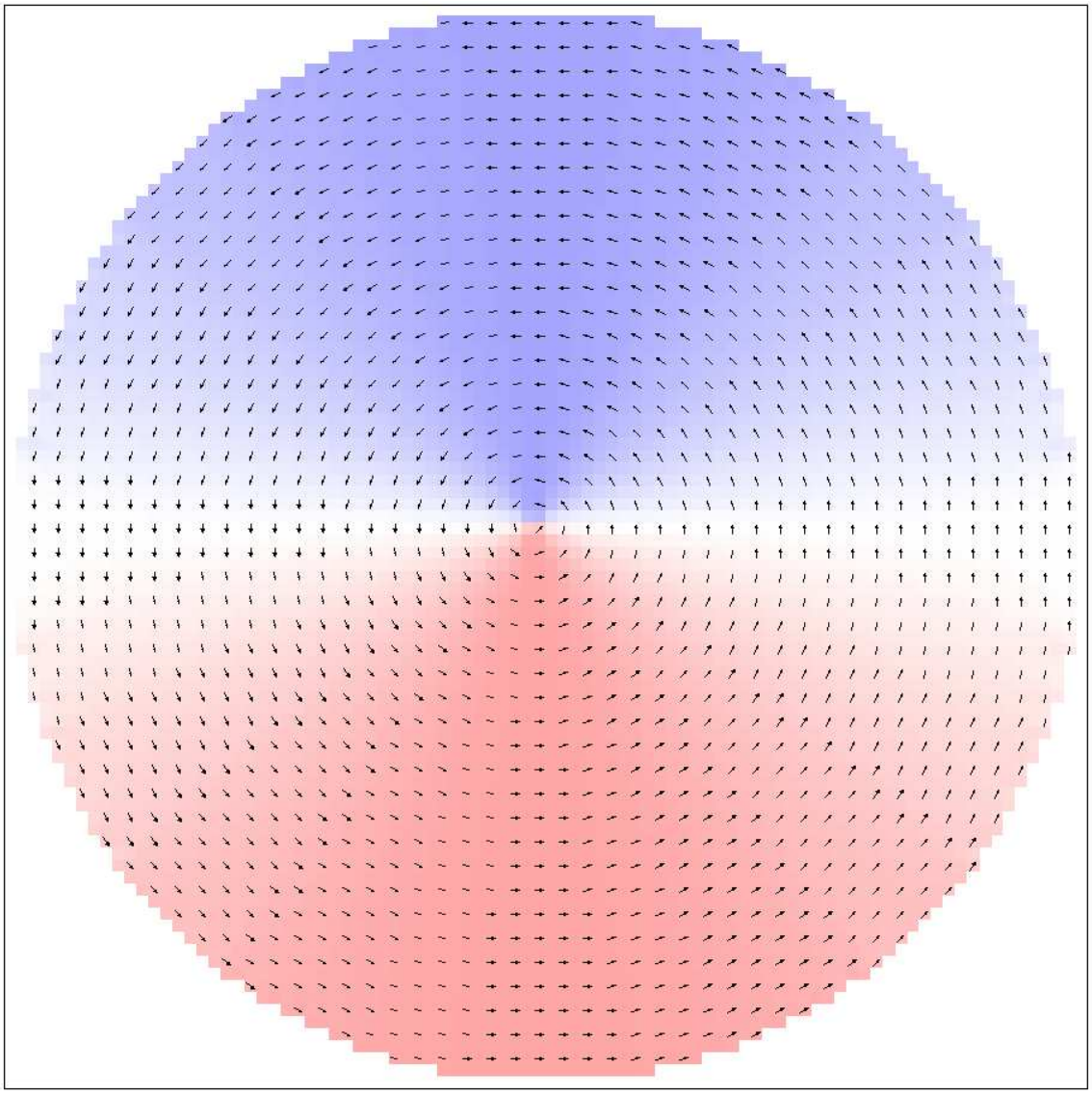

Figure 5.18: OOMMF result for a 900nm diameter Py disc, 30nm thick which has formed a vortex.

5.5.2 Measurement of Coherent Effects in Aluminium Interferometers with Nickel Discs

The nickel initially available for the project was of 99.99% (4N) purity, nickel was the preferred ferromagnet for use in the project due to its high exchange energy. A large exchange energy was shown in [69] to produce a stronger long-range component. By implementing the modified shadow evaporation technique already discussed, a number of interferometers were fabricated including 300nm discs made of this 4N nickel. The transport properties of these structures were measured at 240mK in the Heliox cryostat. Phase coherent transport was observed within a small fraction of the samples initially measured. An SEM image of one such functioning sample can

be seen in Figure 5.19. This structure consists of a slightly deformed 4N Ni disc 470nm in diameter and 21nm thick. The aluminium leads are 100nm thick and the area of the loop is $40\mu m^2$. A differential resistance measurement from -20 to 20μA revealed the lineshape shown in Fig 5.20. The critical current of the Al wires is seen at 11 μA with the normal state resistance $R_N = 72\ \Omega$. This gives $I_c R_N \approx 775\mu V$. This sample is distinctive due to the large peak observed at zero bias in its dV/dI which will be discussed in more detail later in this text. The small features observed at -4.2 and 4.2μA in the dV/dI are also of great interest. It is at these points as well as the zero bias peak that the greatest oscillations in the conductance were observed. A 2D picture of the response of the sample to changes in magnetic field was plotted by measuring dV/dIs while incrementing the field in small fractions of the flux change required for an oscillation. Direct magnetoresistance measurements were then conducted at specific bias currents where oscillatory behaviour was evident. Direct measurement of oscillations in the conductance as a function of varying field was achieved at zero bias as well as $\pm 4.2\mu$A. Clear sinusoidal oscillations were observed at each point of interest with a period of 50μT. This matches the period predicted from the loop area and the relationship $\delta B = \Phi_0/\text{Area}$. The observed oscillations are clear evidence of superconducting phase coherent electron transport through the nickel disc over uncharacteristically long distances. The oscillations are induced by the overlap of penetrating condensate wavefunctions from each of the superconducting electrodes over a distance more than two orders of magnitude greater than the singlet ferromagnetic coherence length ξ_F.

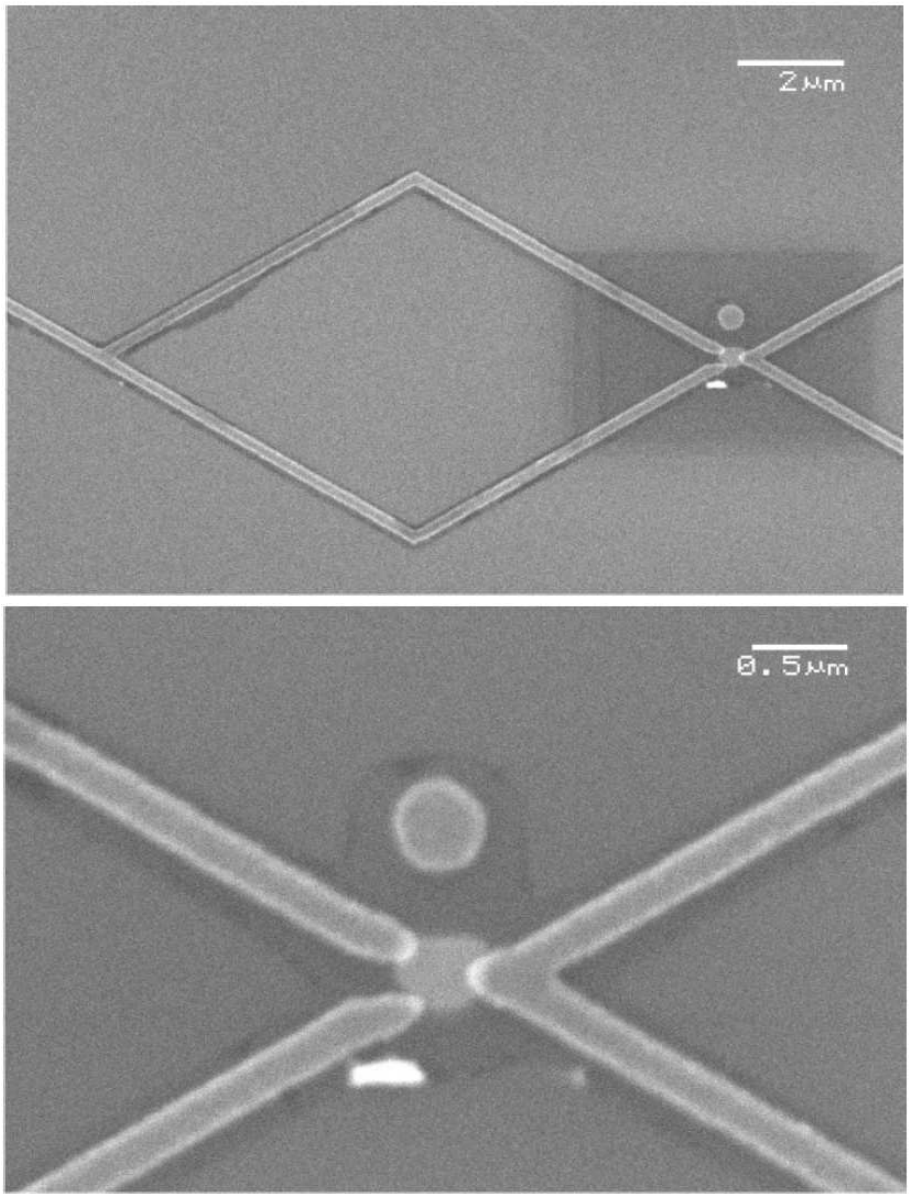

Figure 5.19: SEM images of the 4N Ni disc sample which gave the best evidence of long-range coherence.

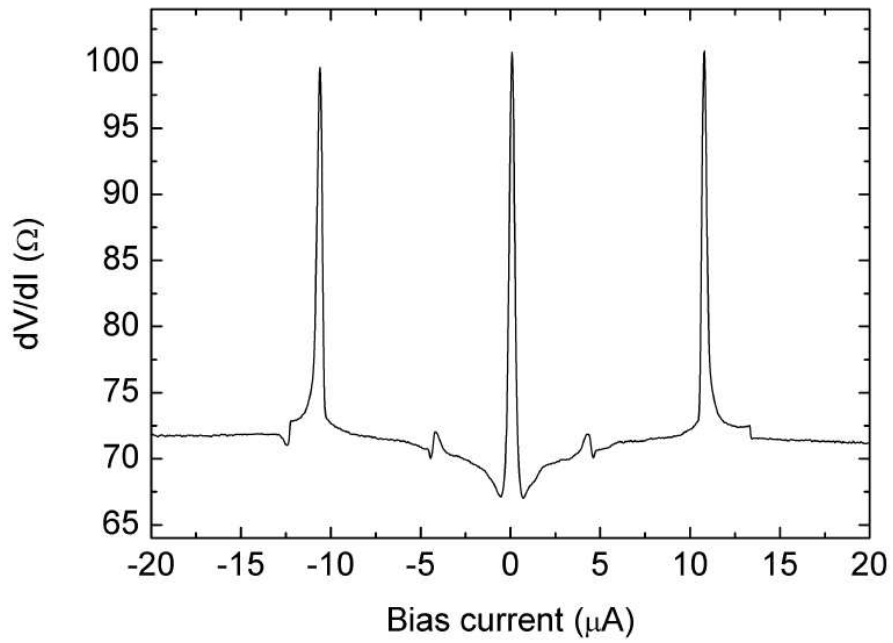

Figure 5.20: dV/dI at 240mK of the sample shown in 5.19

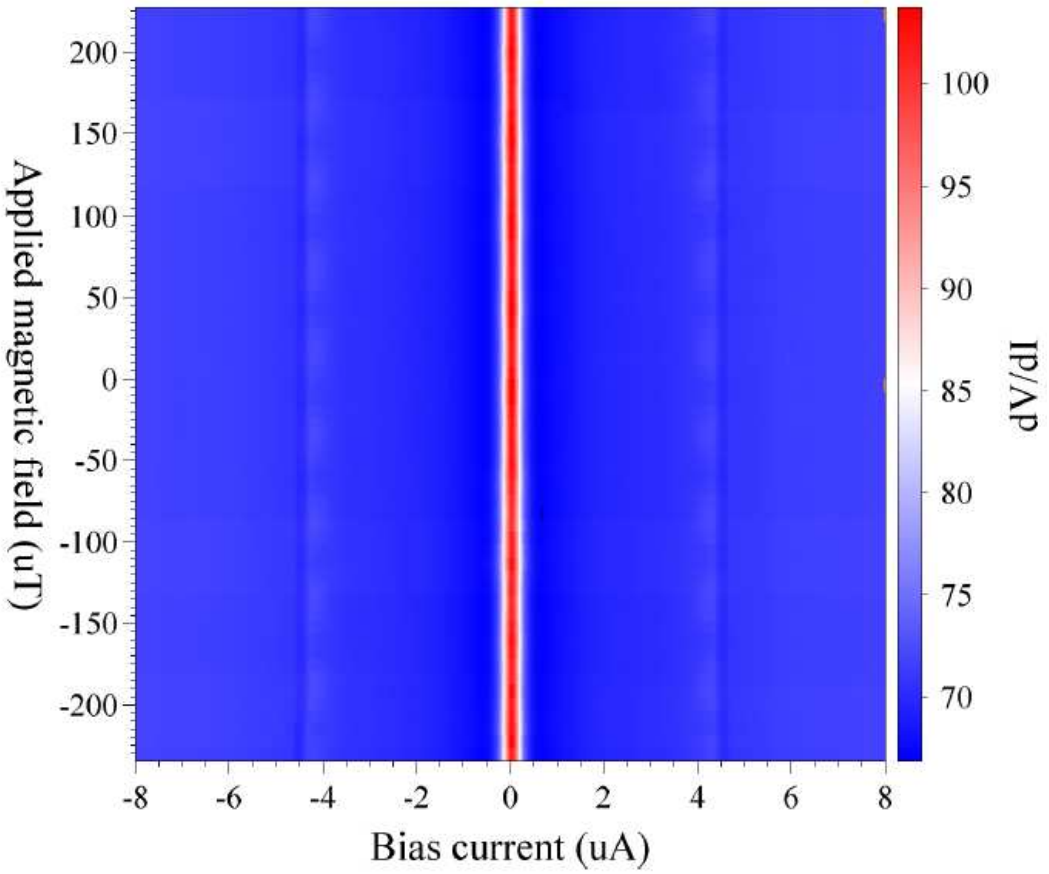

Figure 5.21: Effect of varying field upon the dV/dI shape. Some faint periodic oscillatory behaviour is visible in this contrast.

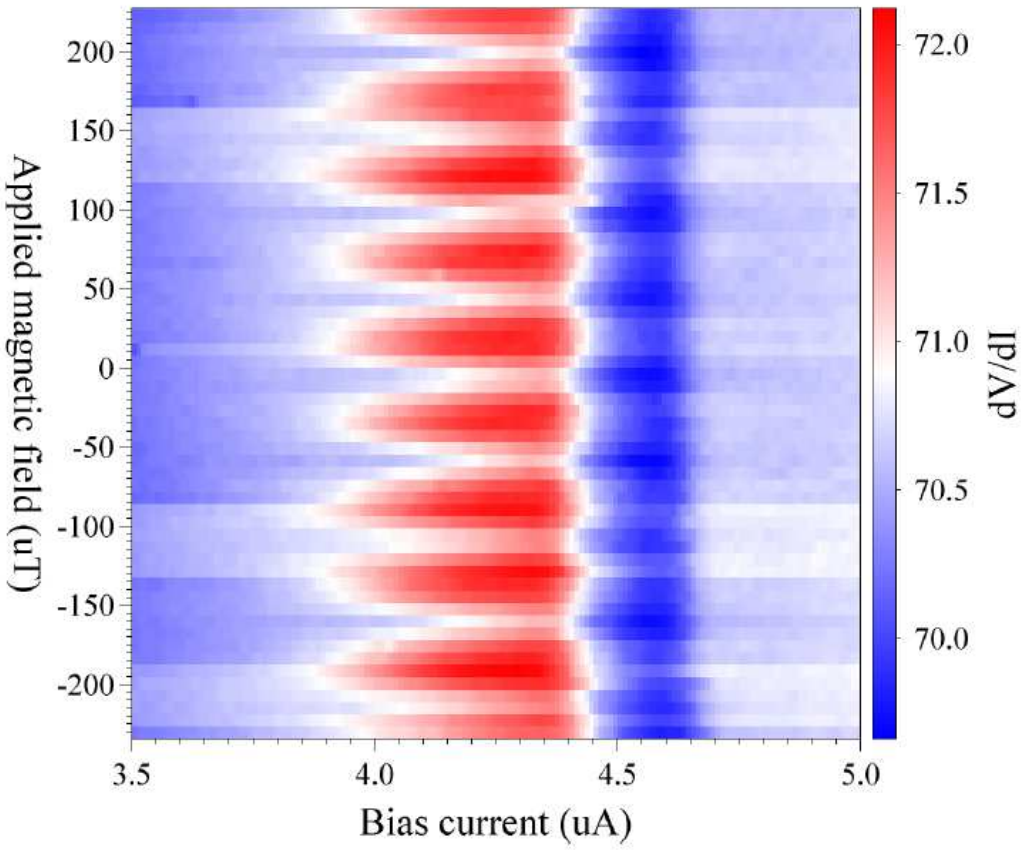

Figure 5.22: An enlarged image of the relevant oscillating feature in Fig 5.21. Here the oscillations are much more clearly defined.

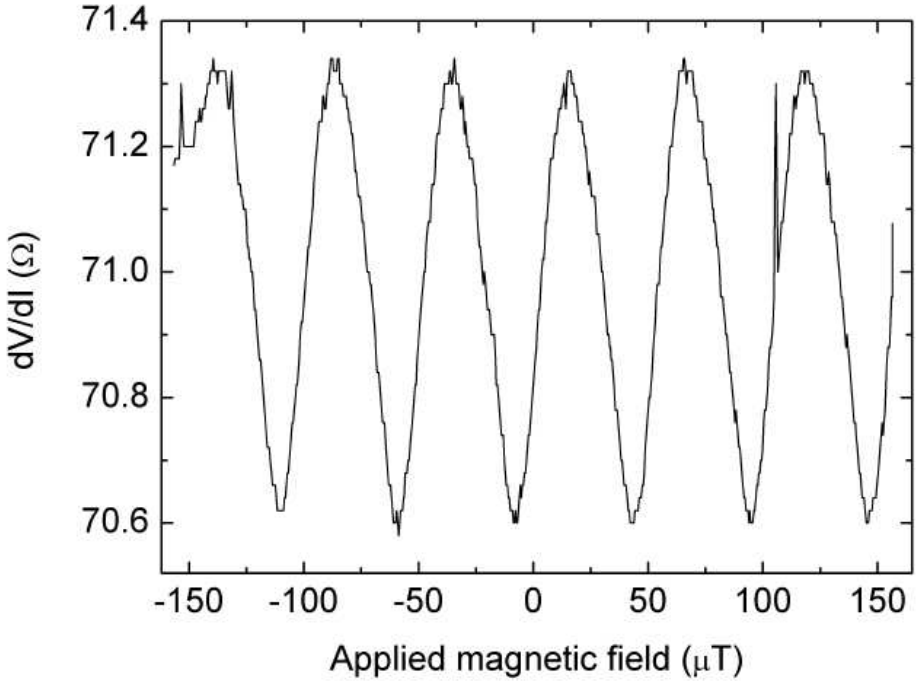

Figure 5.23: Magnetoresistance oscillations measured in the same 4N Ni sample at 4.2μA bias.

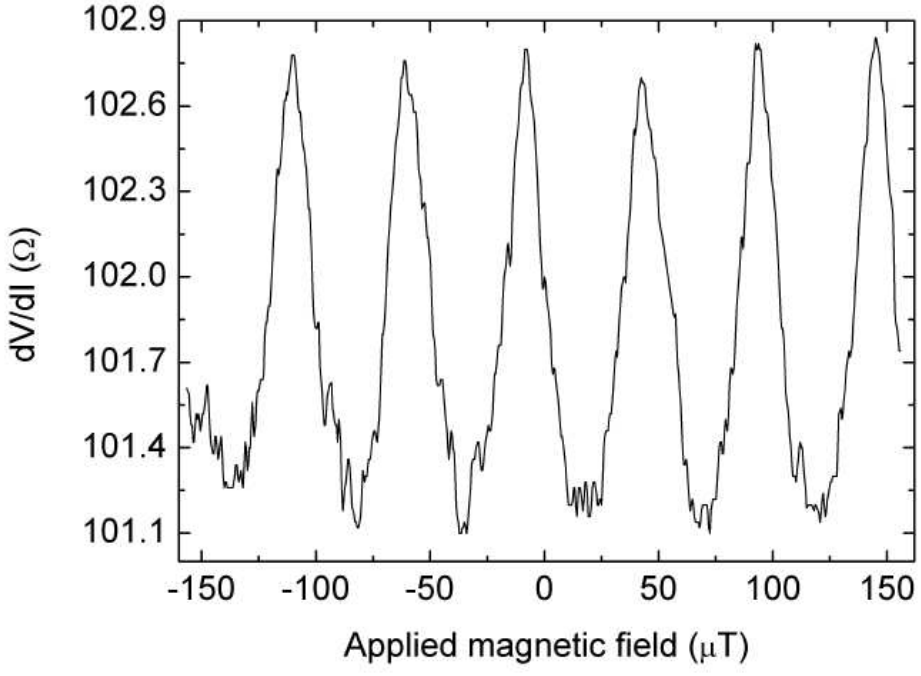

Figure 5.24: Magnetoresistance oscillations measured in the same sample at zero bias.

5.5.3 Incoherent Hybrid Aluminium-Nickel Disc Interferometers

The majority of the interferometers incorporating 4N Ni discs did not show evidence of a long-range proximity effect penetrating the ferromagnet. Figure 5.25 gives examples of the dV/dI shapes and sample resistances measured at 240mK from other 4N Ni 300nm disc interferometers which did not display oscillations. A wide range of variation was observed in the resistances of the samples in both their superconducting and normal states as well as their critical currents and overall lineshape of their differential resistance curves. These variations are indicative of fluctuations in properties of the system either through design faults or erratic fabrication procedures. The normal state resistance of the structures varies greatly between 300 and 600 ohms, and there is some significant variation in the critical current of the structures. In some cases the entire structure is seen to transition from the superconducting to normal state in one large peak while in other cases the transition is staggered over several smaller transitions at differing currents.

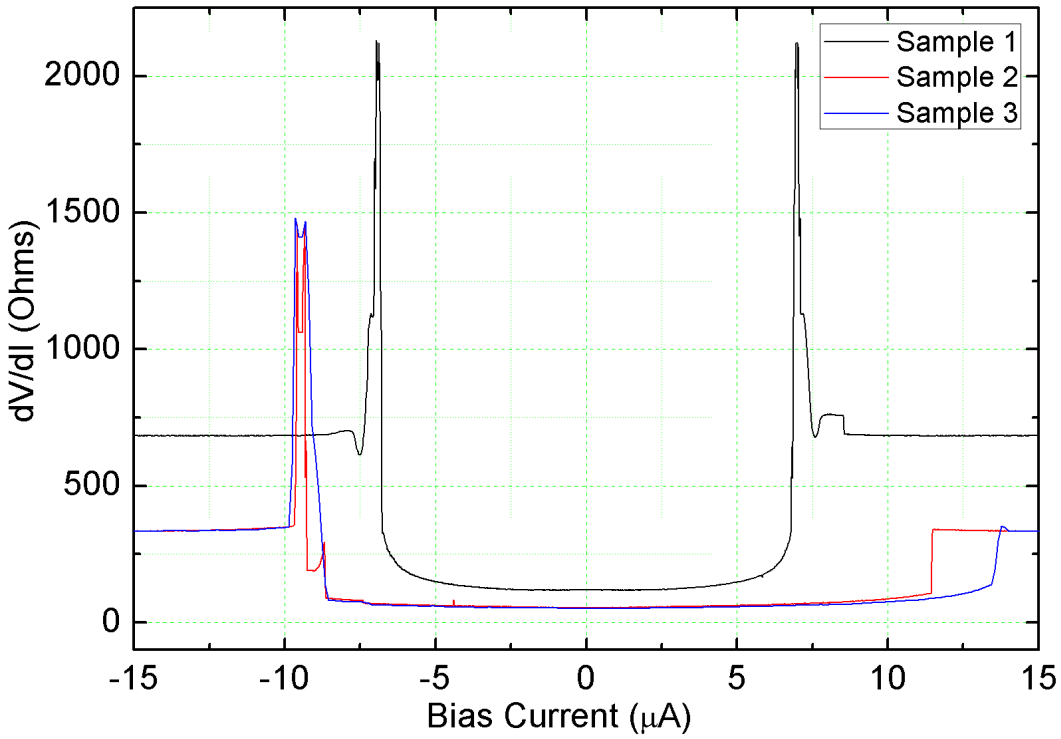

Figure 5.25: dV/dIs of measured interferometers incorporating 4N Ni discs which did not display long-range phase coherence.

5.5.4 Analysis of Variation Between Samples

To investigate the variation in transport properties between different interferometers of the same design, a number of possible causes were considered. This section constitutes a summary of the possible issues impacting upon how samples behaved. The rest of the chapter details studies carried out to investigate these variables.

The first possibility was that the magnetic structure of the discs being measured was not in fact the vortex state intended. If the disc did not incorporate the constantly rotating magnetisation of the vortex then inhomogeneities would be randomly located throughout the disc if it were in a multi domain state, or non-existent if it were in a singe domain state. In either case the lack of a reliable inhomogeneity in extremely close proximity $d < \xi_F < 5nm$ of the superconducting electrodes would prevent the generation of a long-range triplet component within the ferromagnet.

The second possibility was that a spin triplet proximity effect had in fact been generated in a greater number of the samples than had been observed. If the distance between the superconducting electrodes was larger than the phase breaking length in the system however, then no interference effects would have been observed. The average distance L_N in samples was $\approx$ 100nm and reliable fabrication of smaller electrode separations using the equipment available and the modified shadow evaporation technique was problematic. To improve the yield of samples in which a long-range proximity effect was potentially observable, it was necessary to increase the coherence length within the ferromagnet by means of lowering the temperature of the system and reducing the number of impurities within the ferromagnet. By doing so, a long-range proximity effect which was previously unmeasurable may be extended far enough to be detected.

The third contributary factor to be considered was the large peak at zero bias in the dV/dI of two of the functioning samples. While this feature was initially an unintended and uncontrolled addition to these samples, it was necessary to investigate the possibility that the feature was in fact a necessary aspect of the sample's functioning.

5.6 Experimental Study of the Influence of Geometry and Material on Magnetic Structure

Time was secured to use the MFM equipment at the National Physics Laboratory through contact with Olga Kazakova, and a set of 4N Ni discs of varying diameters fabricated for imaging. The initial samples imaged revealed the complexity and variation of the magnetic structures of these types of nanomagnets and disproved the existence of the ideal vortex state in the majority of this type of disc. As a result other geometries of mesoscopic ferromagnet were modelled using the OOMMF script and the most promising of these fabricated and imaged.

5.6.1 Magnetic Stucture of Nickel Nanodiscs

The initial MFM images obtained at NPL revealed that the magnetisation of the 4N Ni discs was more complicated than had first been hoped. Rather than the regular vortex structures predicted by the OOMMF scripts and literature, a wide range of different structures were observed even within discs fabricated on the same chip using the same processes.

In spite of the great variation apparent within the structures observed, some general trends and patterns were easily discernable within the data. All of the discs imaged displayed a multi domain structure rather than a perfect vortex, however in many samples, especially those of smaller diameters (300-600nm), the domain walls tended to form in a radial pattern reaching from the disc's centre to its edges. Furthermore the domains formed between these radial domains could be seen to be orientated in such a way that each "chased the tail" of its neighbour in order to produce a closed loop of domain magnetisation and minimise stray field. This type of fractured vortex structure was sometimes observed to include a small intense out of plane magnetisation at its centre like the vortex core, this adds further evidence to the idea that the domains are trying to form a closed domain system. The out of plane magnetisation at the cente of the discs originates from adjacent antiparallel spins from the opposite domains in the same manner as that observed in a true vortex.

Larger discs (600-900nm) were seen to display yet more complicated structures. The extra space within them allowed further disorder to develop. This commonly

manifested itself as an uneven and seemingly random jumble of domains in the centre of the disc, surrounded by a ring of more ordered domains around the outside. This outer ring of domains again attemped to form a closed domain by chasing their neighbours tails. Stray field was minimised by the even broken curl of the magnetisation around the perimeter of the disc, although the poweful magnetisation observed at the centre of the smaller discs was rarely seen due to the disordered arrangement of the domains at the disc's centre.

It should be noted that the field ranges used during searches for quantum interference oscillations were small, generally approximately $\pm 6G$. The field required to distort or adjust the structure of magnetic vortices is measured in hundreds of Gauss. As a result we expect no changes to the magnetic structure of the discs from the fields used to probe the devices for conductance oscillations.

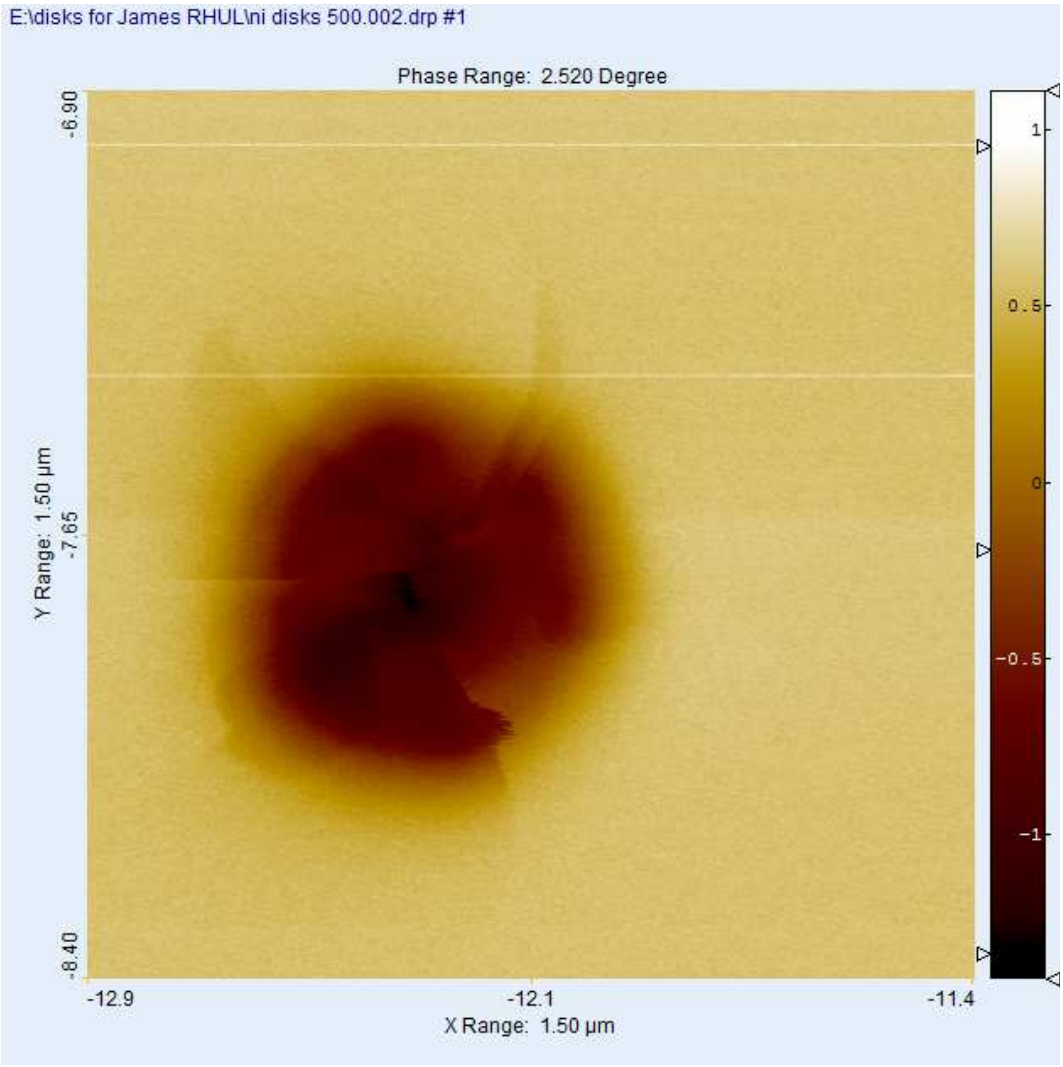

Figure 5.26: MFM image of 500nm disc fabricated from 4N Ni. The disc is 30nm thick. It has formed a multi domain state consisting of radial domain walls extending from its centre and at its centre there is a powerful out of plane magnetisation akin to a vortex core.

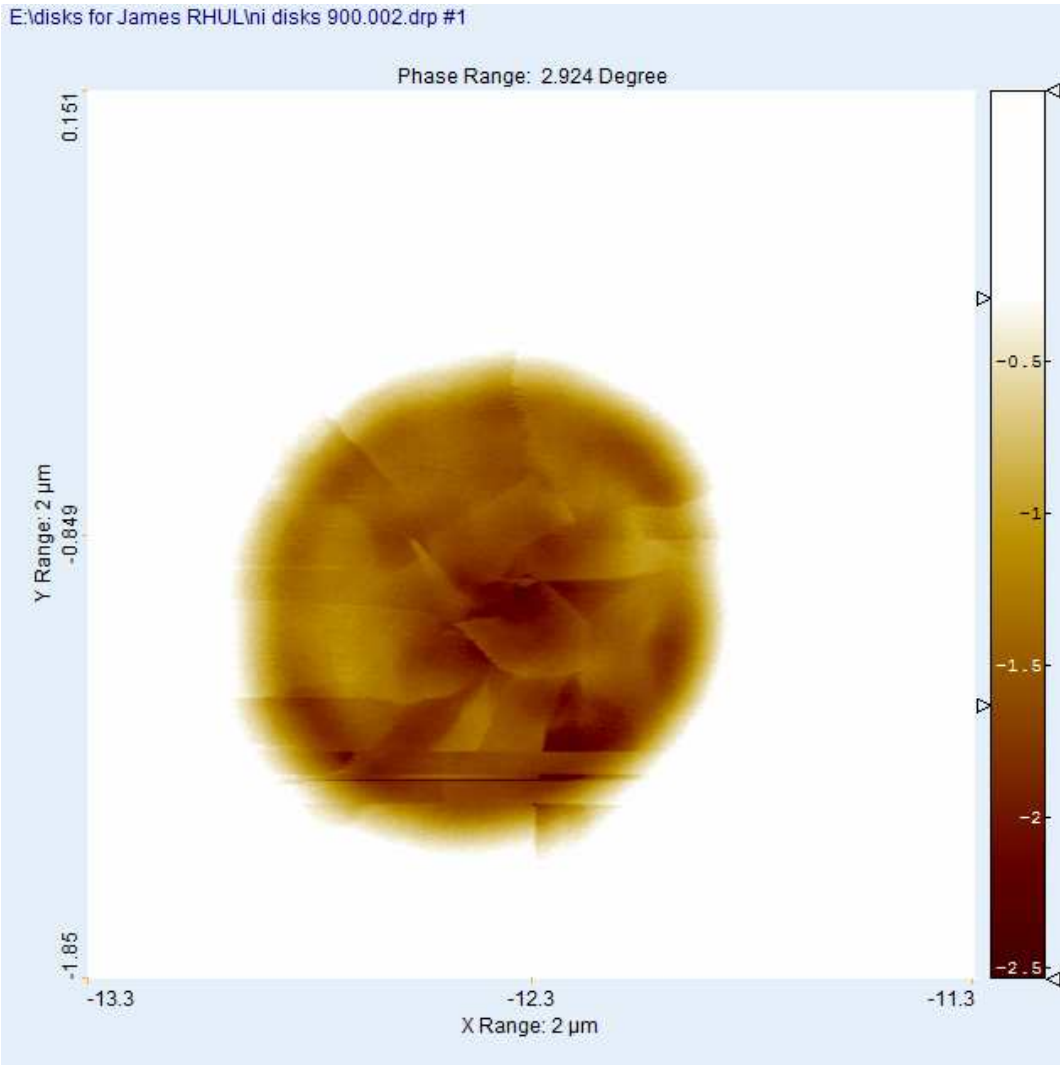

Figure 5.27: MFM image of 900nm disc fabricated from 4N Ni. The disc is again 30nm thick. The larger diameter of this disc has allowed the formation of a more complex domain structure. At its centre there is a less organised domain orientation while the outer domains again tend to chase the tail of each other in an attempt to form a closed domain and minimise stray field.

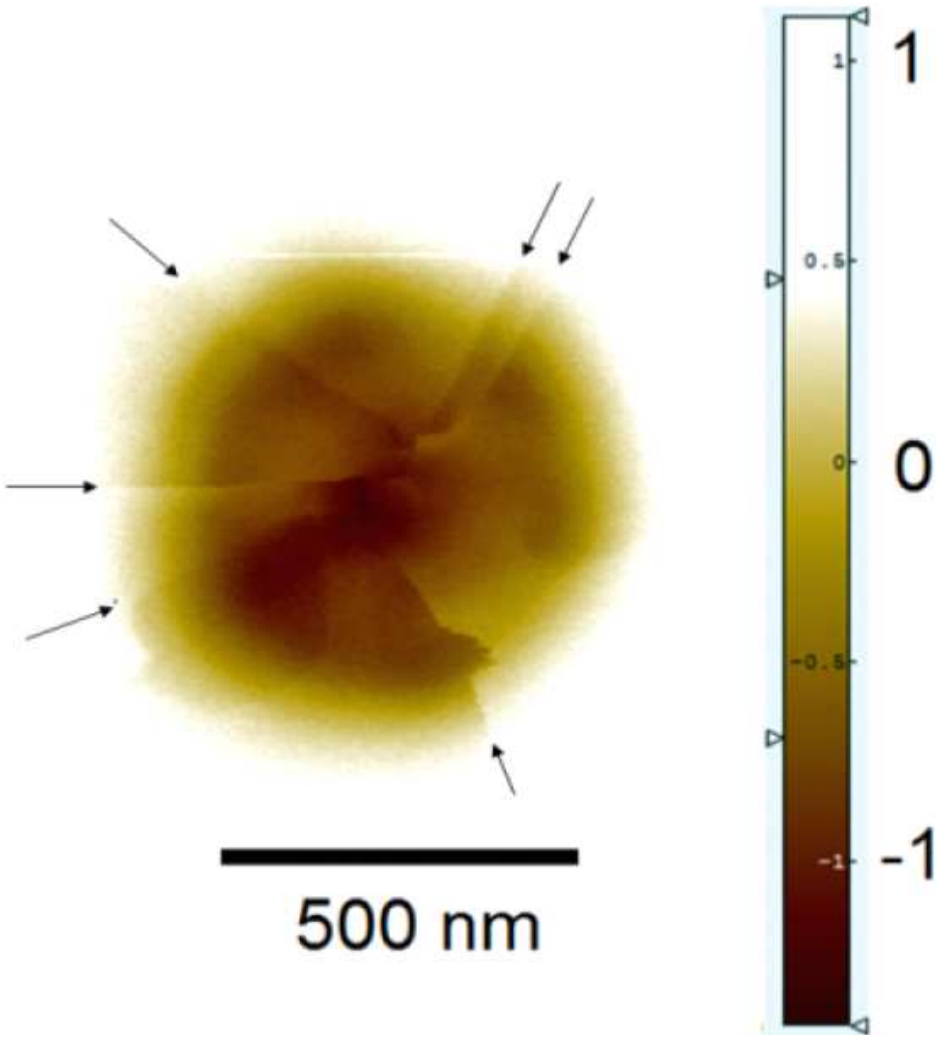

Figure 5.28: MFM of a fractured vortex magnetisation within a 4N Ni disc. The arrows indicate the positions of the radial domain walls.

There were several possible reasons for the formation of the domain walls within the discs, these included imperfections in the shape of the disc due either to problems in the lithography or lift-off processes, impurities trapped within the ferromagnet and the polycrystalline nature of the evaporated thin films. Up to this point the nickel used within the project had been of 99.99% purity (4N). To try and minimise the level of impurities in the film, a higher purity 99.999% (5N) nickel was sourced and was used in all following Ni fabrications. While the higher purity material was hoped to improve the magnetic structure, it was also known to improve the coherence length within the ferromagnet. No discernable difference was noted between the 5N discs imaged using MFM and the 4N. The same radial domain walls forming a fractured vortex state were noted in the majority of the discs fabricated from both purities of Ni. Efforts were made to further improve the quality of the

fabrication process by increasing the vacuum and chamber bake before evaporation, and maximising the efficiency of the boat source as well as the purity of the source. Despite the limited evidence of improvement in the magnetic structure between the 4N and 5N Nickels, all Ni structures fabricated after the 5N material was obtained were constructed from this because the reduced inelastic scattering within the purer material results in longer coherence and phase breaking lengths.

The discovery that the magnetisation of the discs was not an even or reliable vortex structure had major implications for the wider project. While it is possible that a long-range triplet component could be generated if a superconducting interface was placed close enough to the rotating magnetisation of a domain wall, the random positions these domain walls in any given disc made it almost impossible to know where to place superconducting electrodes for triplet studies. As a result of this, efforts were made to investigate other forms of magnetic inhomogeneity which could be engineered and precisely placed for use in experiments.

New ferromagnetic materials were also investigated in the hope of improving the magnetic structures. To this point nickel had been the chosen material for the project as its high exchange energy made it a good candidate for generating a strong triplet component [69], and it was suited to use in the 2 angle thermal evaporations possible in the clean room at Royal Holloway. In an attempt to improve the quality of the magnetic structures, high purity Ni80Fe20 permalloy was obtained and used in some studies as its low coercivity makes it an ideal candidate for studies of mesoscopic ferromagnets. While the quality of magnetic structure obtained for all geometries was better when using permalloy, the mean free path within such a material is short due to its disordered state. As a consequence, alloys such as this will be badly suited to triplet studies as their coherence length will be inhibited in the same manner as if the material were extremely impure. A small number of Py discs were fabricated and found not to show good vortex structures. Figure 5.29 is an example of such a sample. The idea of using a disc was quickly dismissed due to their unpredictable stuctures. Other mesoscopic ferromagnets incorporating specific inhomogeneities were investigated as potential substitutes.

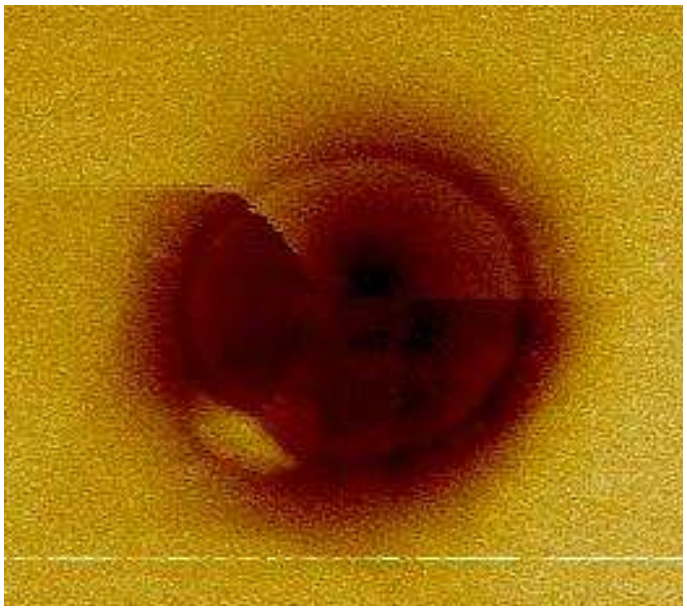

Figure 5.29: A 900nm diameter Py disc 30nm thick. A vortex has not formed.

5.6.2 Square Shaped Nanomagnets

Attention turned to the possibility of pinning domain walls at specific positions within the ferromagnet and using the local inhomogeneity of the domain wall as the necessary environment to produce the long-range triplet poximity effect. If the domain walls could be reliably pinned in the same place, then the aluminium electrodes could be placed on top. Such precise alignment of the 2 angle fabrication process using the available equipment is still very challenging.

Micromagnetic Simulation

Attempts were made to model and fabricate a variety of ferromagnetic shapes in an attempt to trap domain walls at specific points within the structure. The geometry of any potential magnet was again limited by the need for it to be possible to incorporated in the 2 angle fabrication process and accomodate aluminium electrodes at a later point. Two of the most simple designs proved to be the most effective, square and triangular shaped magnets were investigated in the hope of inducing domain walls to form between the tip of each of their points and their centre. Similar arrangements had been observed in [83] and [50]. The result would be a 4 or 3 domain closed domain structure with geometrically induced domain walls. OOMMF results for square nanomagnets follow.

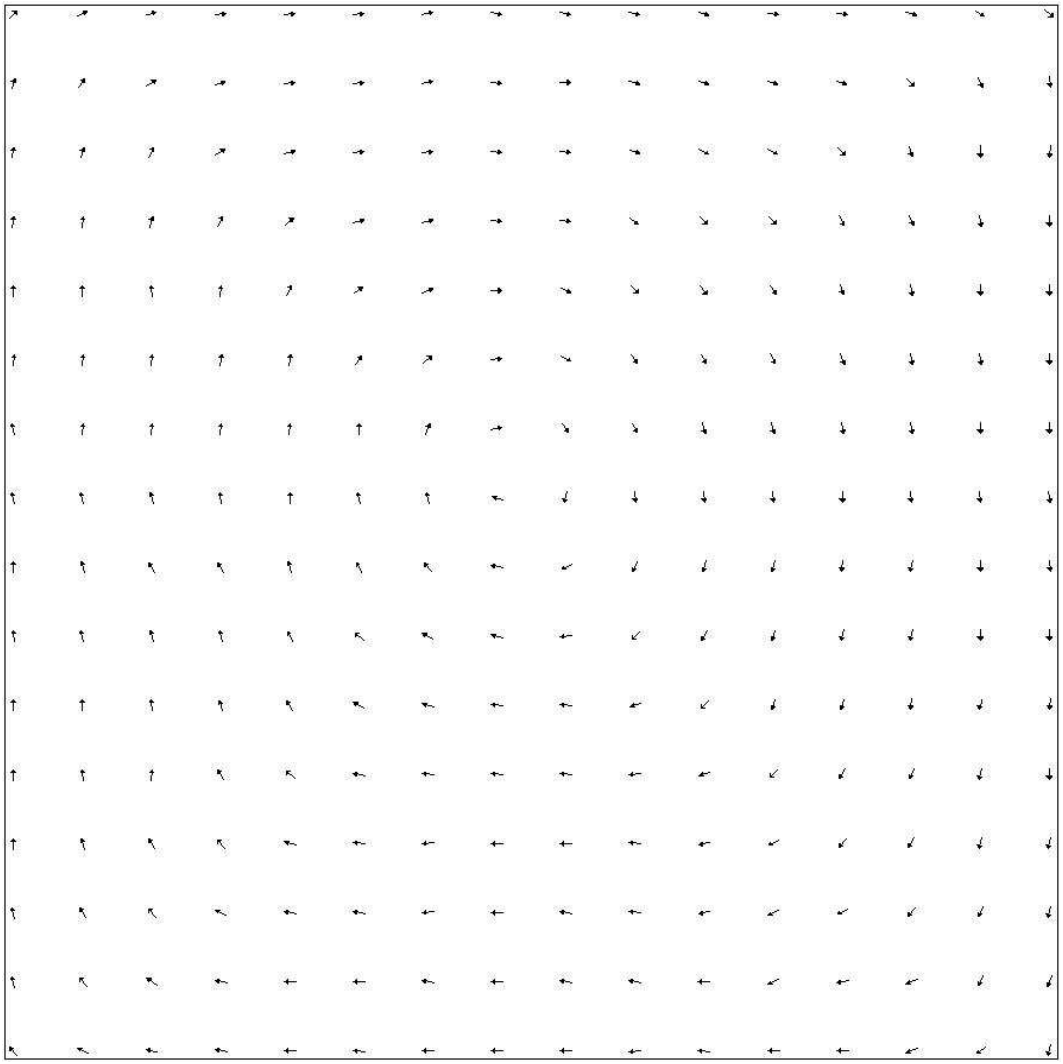

Figure 5.30: OOMMF result for a 305nm Co square of 30nm thickness. A vortex type closed domain structure is apparent. The arrows are small due to the small cell size chosen for the simulation to improve its accuracy.

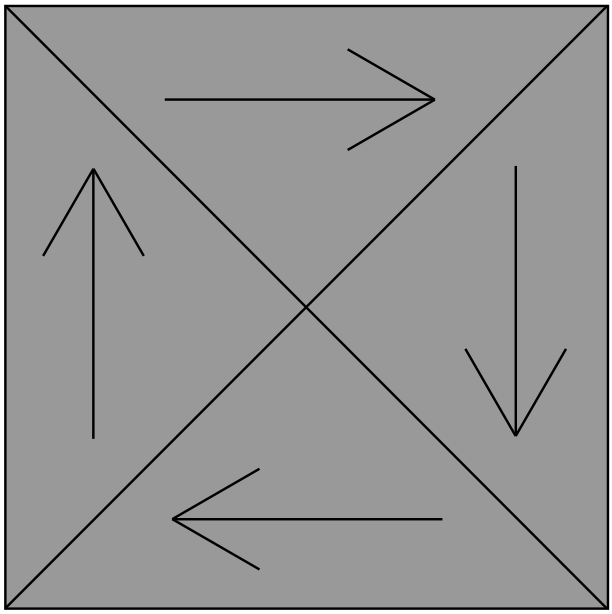

Figure 5.31: Illustration of the domain structure expected from the OOMMF result shown in 5.30.

MFM and AFM Imaging

A range of different sizes of square and triangular nanomagnets were fabricated and again imaged using the equipment at NPL. As shown in figure 5.32 the 4 domain structure occurs commonly in this geometry. A number of imaged structures, especially those of large sizes, did show more complex structures. An example of this is shown in figure 5.33.

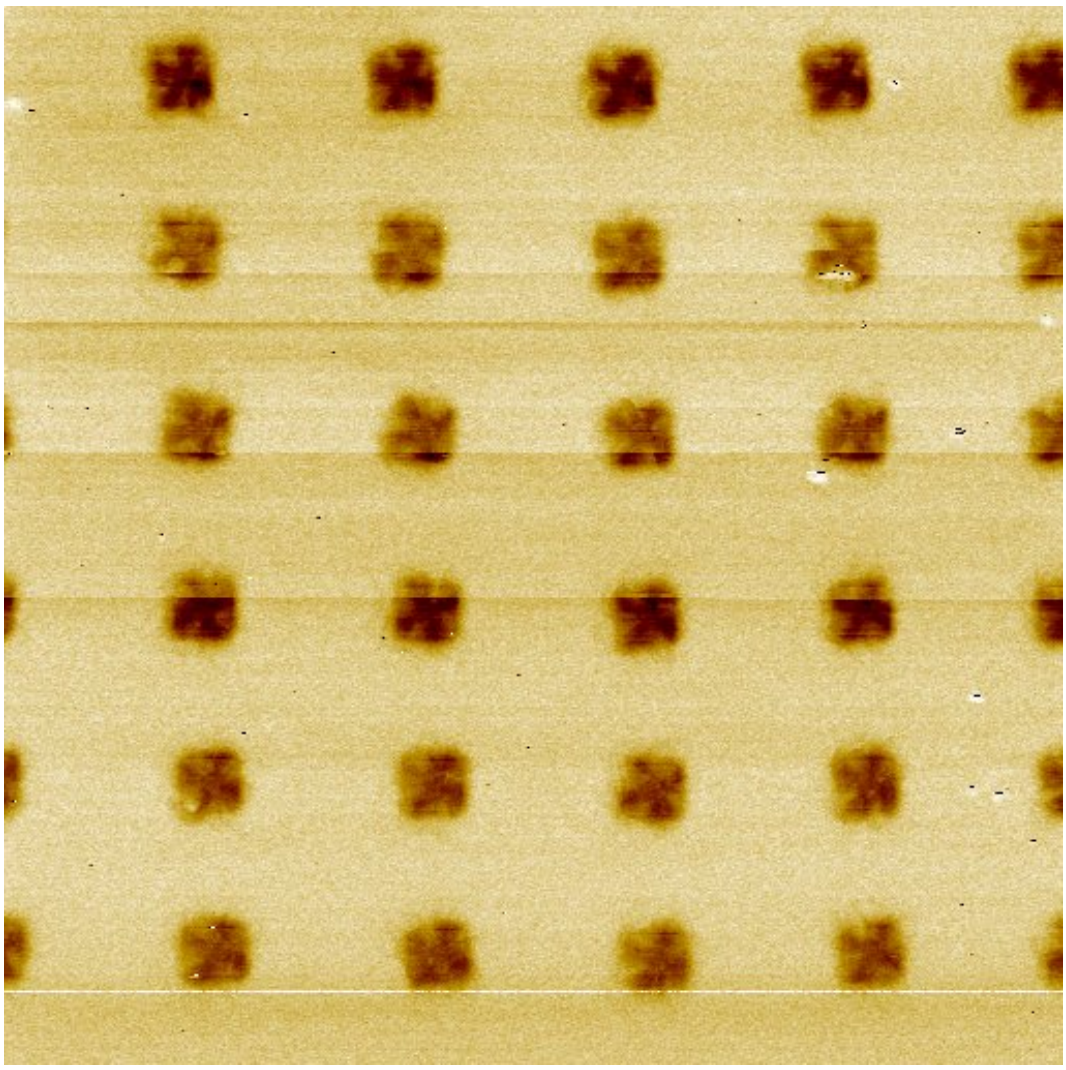

Figure 5.32: Permalloy 300nm square array showing 4 domain closed structure in the majority.

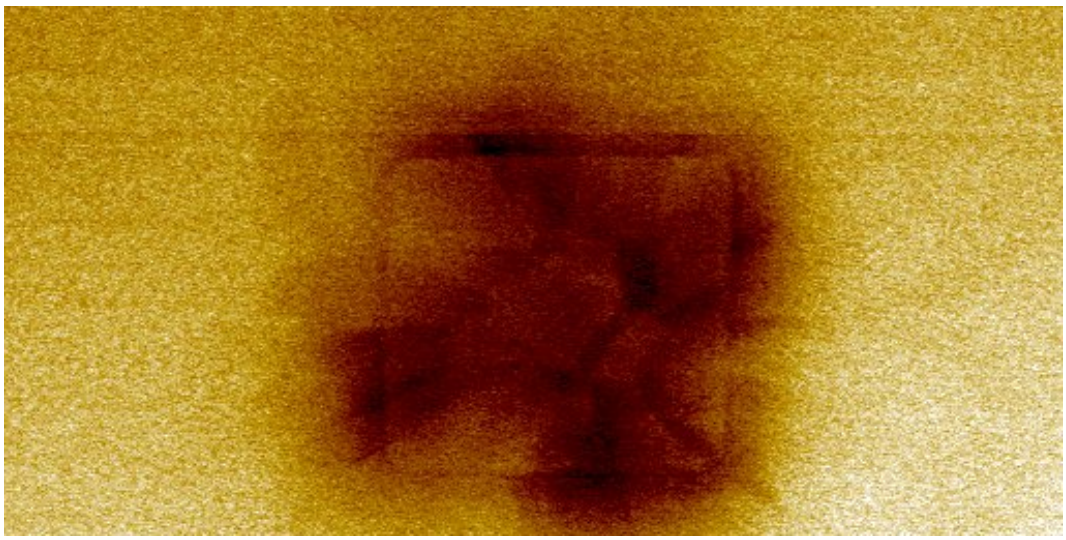

Figure 5.33: High resolution close up of a part of the square array showing the domain structure in greater detail. A fifth domain is visible at the centre of the square surrounded by the normal layout of circulating domains.

5.6.3 Triangular Nanomagnets

While the results obtained for the square shaped nanomagnets were significantly more reliable than those for the discs, a number of the square shapes did still exhibit unwanted complexities in their domain structures. As a result, further work was carried out to investigate the domain structure of triangular nanomagnets.

Micromagnetic Simulation

OOMMF results for thin equilateral triangles with side lengths ranging between 300 and 600nm were consistent in producing 3 domain, closure type magnetisations.

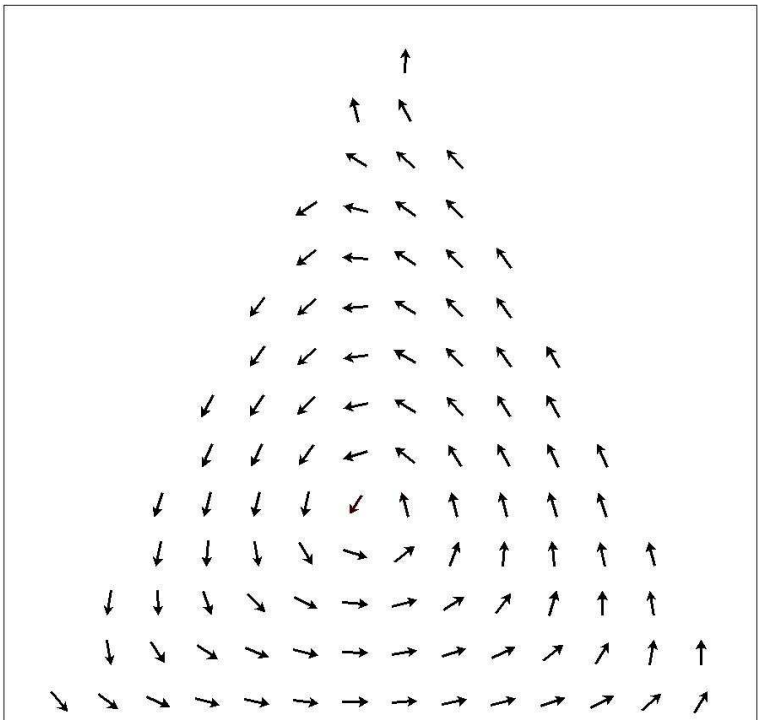

Figure 5.34: OOMMF result for a 305nm Py equilateral triangle of 30nm thickness. A vortex type closed domain structure is apparent.

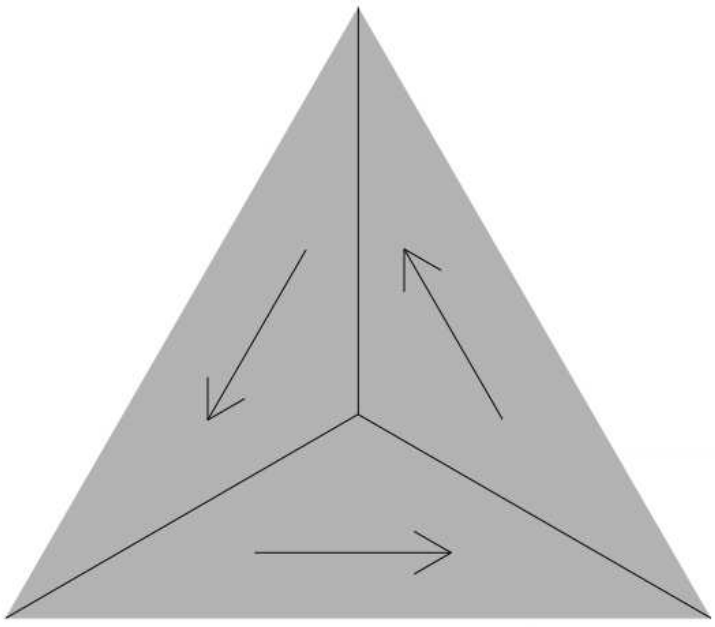

Figure 5.35: An illustration of the type of 3 domain structure indicated by the above OOMMF result.

MFM and AFM Results

A range of sizes of triangular nanomagnets were fabricated and again imaged using the MFM at NPL. The three domain structure predicted by the OOMMF results was observed in a large arrays of these magnets, and was seen to be resilient to imperfections in the geometry where structures became damaged or were not fabricated properly. In some triangular magnets a central feature was observed which was analagous to the vortex core seen in circular vortices.

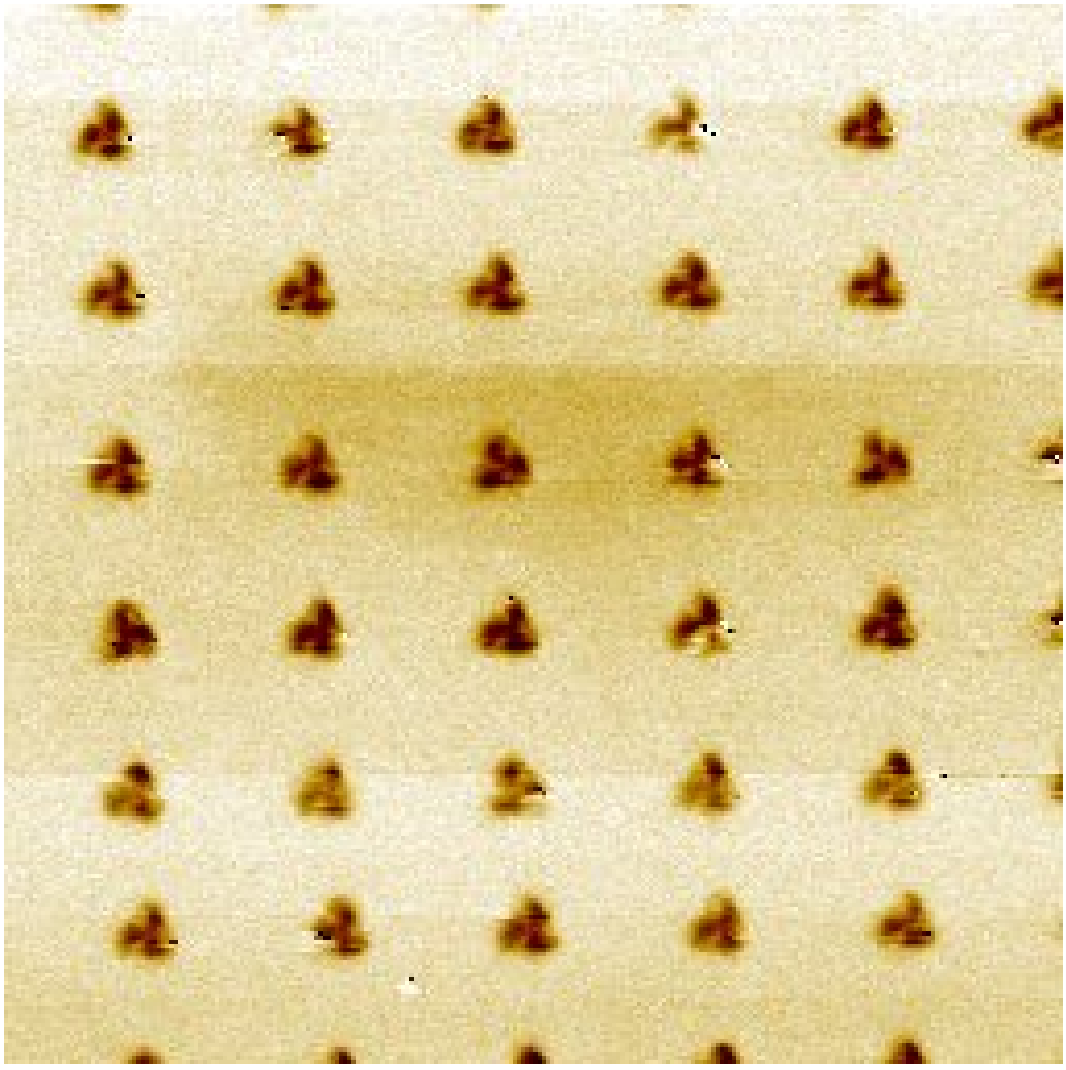

Figure 5.36: MFM image of an array of permalloy triangles showing the 3 domain structure predicted.

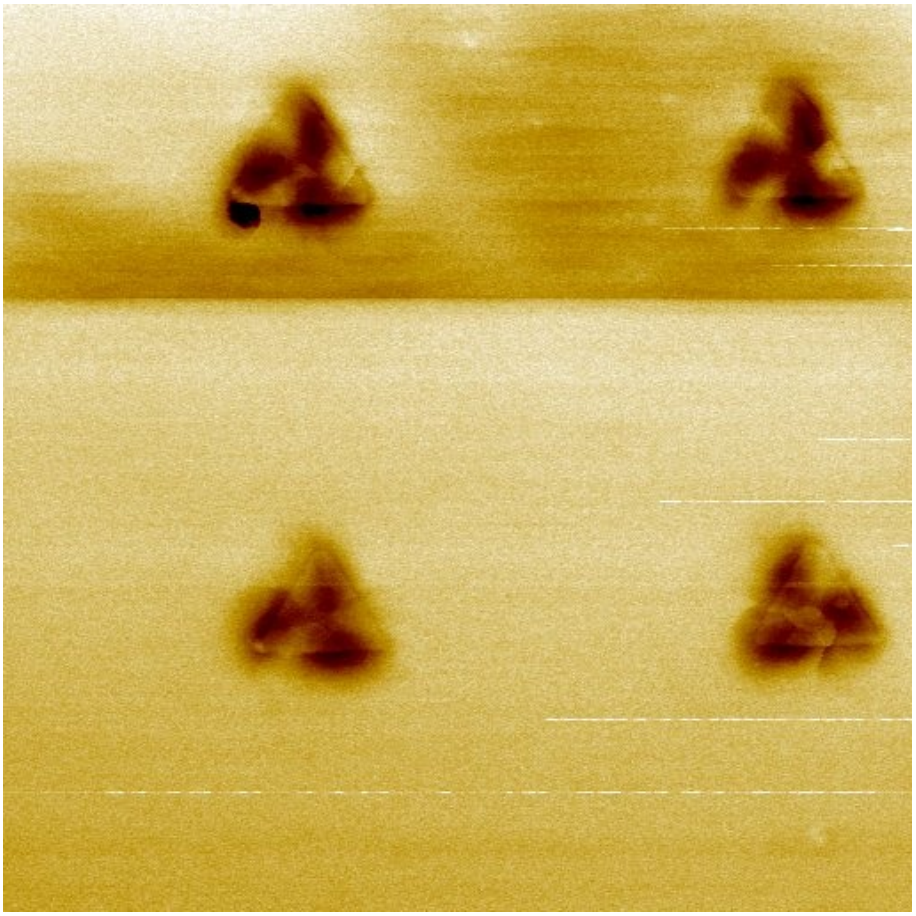

Figure 5.37: A higher resolution image of 450nm Py triangles exhibiting the 3 domain structure.

As predicted by the literature and OOMMF simulations, well-organised repeatable 4 and 3 domain structures were observed within the squares and triangles respectively. The triangular shaped magnets were found to have the most reproducible structure and as a consequence were chosen over the squares for further use in the project. The remagnetisation curves of the mesoscopic ferromagnets used in this project have not been measured. Further work could be done using MOKE to chart this behaviour.

The cause of this greater stability within the triangular structures is likely to be that fewer domain walls need to form to produce closure domain within the triangle as compared with the square, while both results have very low magnetostatic energy. The added energy cost of forming the extra domain walls in the square-shape nanostructures makes this geometry slightly less stable than the triangular one.

5.7 Low Temperature Electron Transport Measurements of Variant Hybrid Superconducting-Ferromagnetic Interferometers

This section presents the results obtained when permalloy triangles and 5N Ni triangles were substituted for the 4N Ni discs used in the previous interferometer transport measurements.

5.7.1 Aluminium-Permalloy Hybrid Interferometer Measurements

The most clearly defined and reproducible magnetic structures achieved in the magnetism study described previously were fabricated from high purity permalloy. The coherence length within such an alloy is expected to be short compared with a pure element, as the 20% of iron would behave like an impurity within the cobalt lattice greatly increasing the probability of inelastic scattering. In spite of this, a set of interferometers were fabricated around an SFS junction where the ferromagnet was a mesoscopic Py shape to investigate whether the greater contol over the magnetic structure rendered more long-range coherent samples. Data obtained from permalloy samples is displayed in Figs 5.38 to 5.44.

Several distinct types of lineshape where observed in the Py samples, and some intriguing subgap structure was observed which occurred in more than half of the measured samples. This subgap structure was not observed within the triangular Ni samples later measured and is attributed to effects caused by the improved magnetic structure of the Py. None of these interferometers displayed the phase periodic conductance oscillations hoped for. In general, normal state resistances were found to be approximately 60Ω while the zero bias resistance was approximately 50Ω. There were, however, several exceptions to this.

Changes made to the dV/dI lineshape after high current measurements or the application of external fields are interpreted as evidence of magnetic structure based effects being destroyed when the the ferromagnet's structure is changed either through spin transfer torque resulting from current flow, or changes in the external magnetic field.

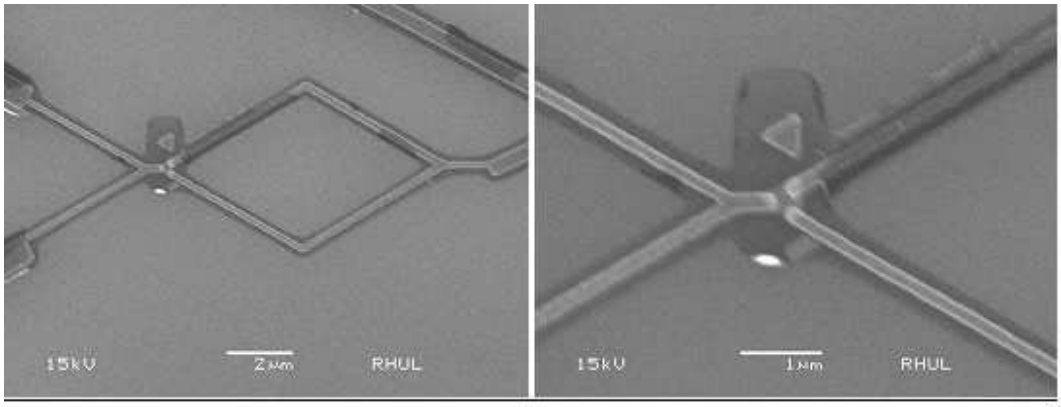

Figure 5.38: SEM images of an interferometer incorporating a Py triangle whose sides measure 600nm each. This is the size which produced the best MFM images of the triangular vortex shape.

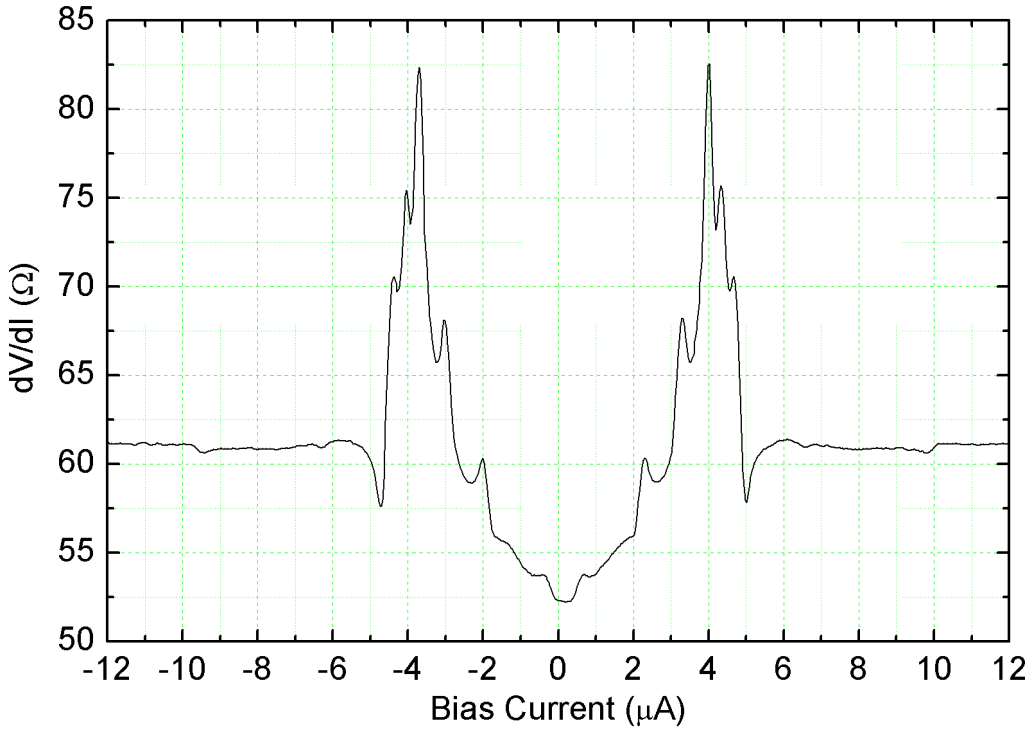

Figure 5.39: dV/dI of the sample imaged in Fig 5.38 measured at 240mK. The graph contains a larger number of features than have commonly been observed, including some intriguing subgap structure. When the dV/dI was remeasured after low field magnetoresistance measurements, it was found that the lineshape had changed and much of the detail including the subgap structure had disappeared. Modifications to the magnetic structure of the Py as a result of the current or field may explain the change in the graph.

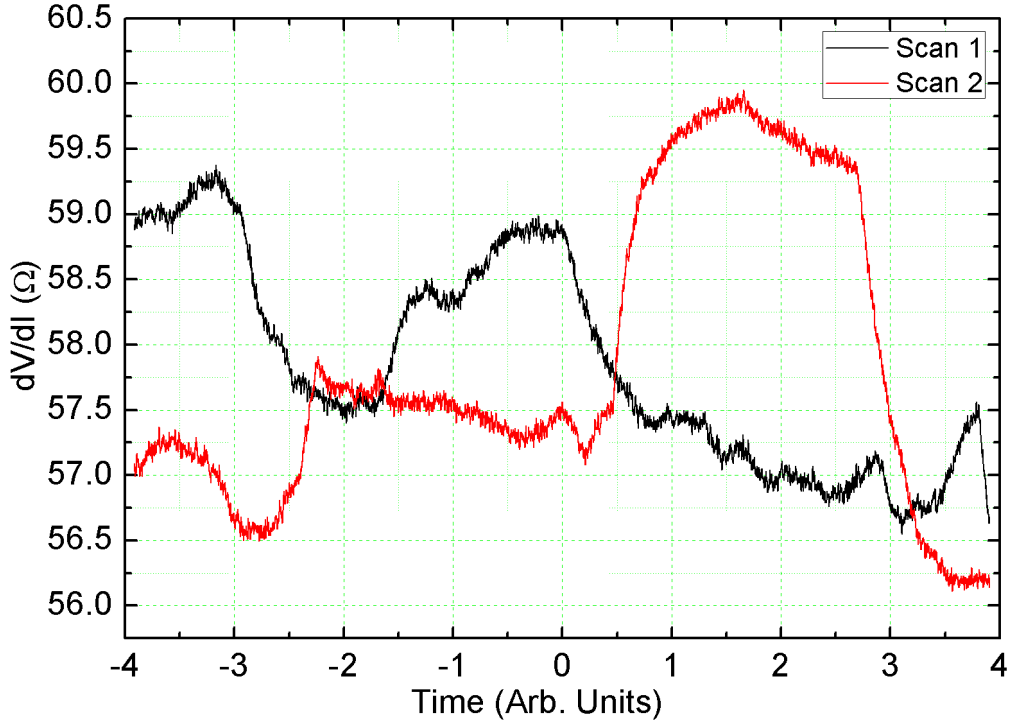

Figure 5.40: By setting the bias current in the Py sample in Fig 5.39 to sit on the first plateau of the subgap structure, and measuring magnetoresistance over small fields, random fluctuations in the conductance were measured. These were found to be time dependent rather than field dependent and have not yet been explained. The two curves represent measurements taken while ramping the field up and down. The fluctuations in the dV/dI are occuring independently of the field over a period of approximately 3 minutes for each scan.

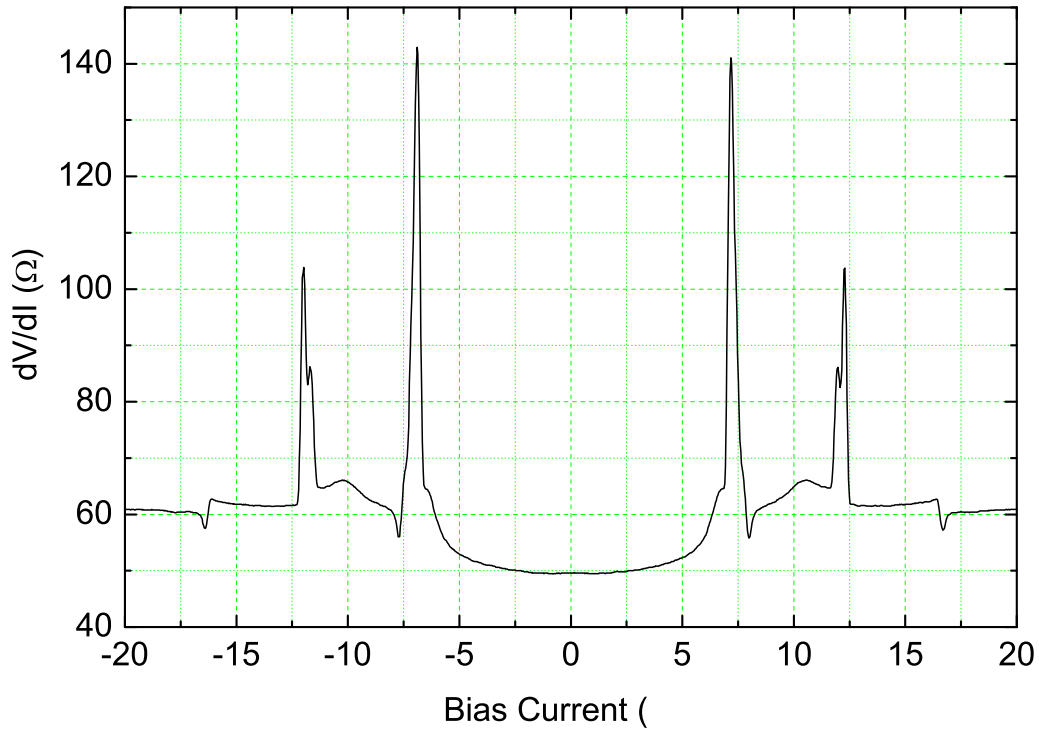

Figure 5.41: dV/dI shape measured from the same sample as shown in Fig 5.39 after being exposed to a field of 10G. The changes to the lineshape are dramatic. Similar profound changes induced by negligible field changes were observed in a later sample shown in Fig 5.57.

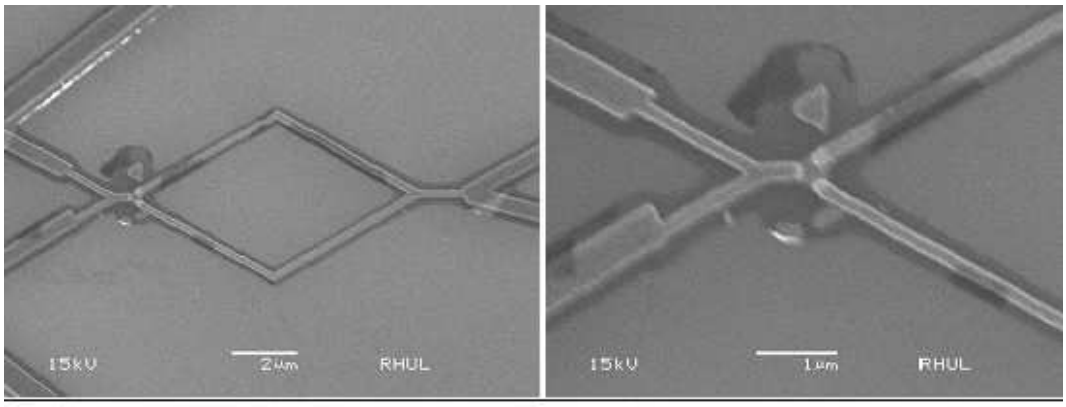

Figure 5.42: SEM of another Py sample from the same chip and thus subject to the same fabrication processes as that shown in Fig 5.38.

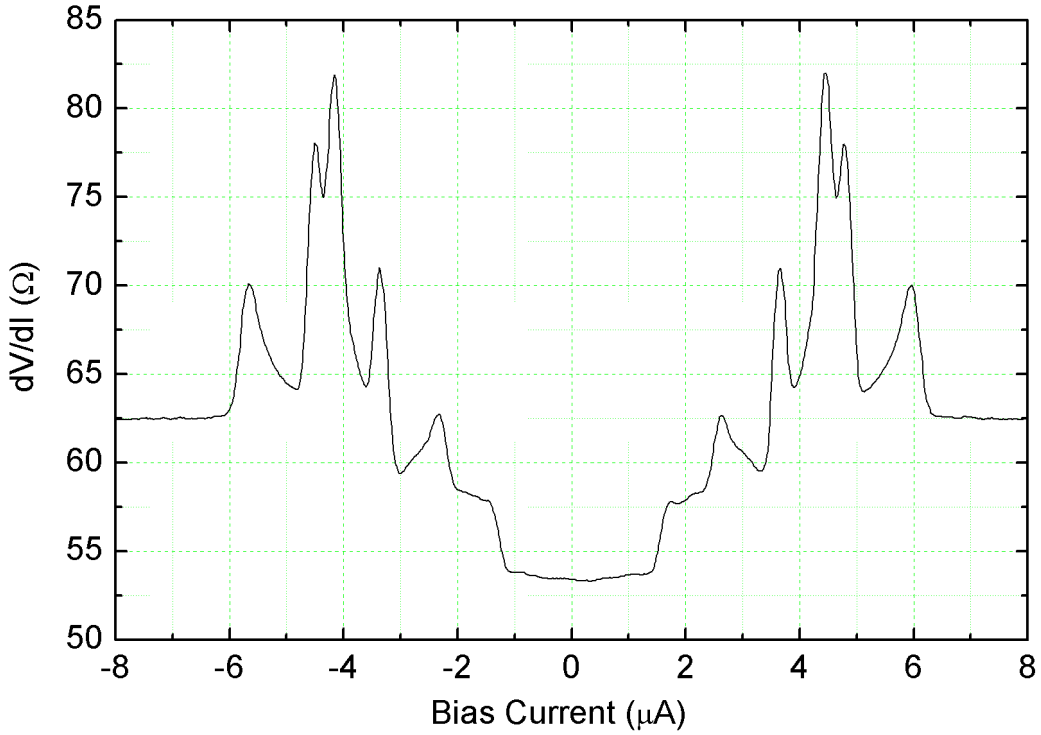

Figure 5.43: dV/dI shape during initial measurement of the sample shown in Fig 5.42.

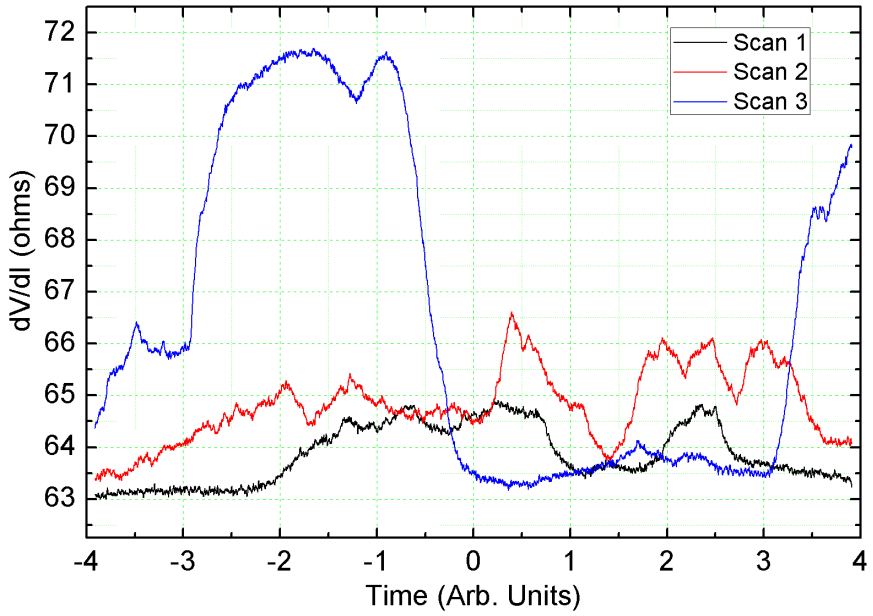

Figure 5.44: Random fluctuations were again observed at specific bias currents. This measurement was carried out at 3.467μA bias current over a period of approimately 3 and a half minutes. The observed changes were again found to be time rather than field dependent and have not yet been explained. This behaviour is very similar to that observed in Fig 5.40.

Table 5.1: Permalloy Triangle Interferometer Values

Sample	Normal State Resistance (Ω)	Zero Bias Resistance (Ω)	First Critical Current (μA)	Fine Structure?
a	60.9	49.5	6.9	No
b	62.1	53.0	3.3	Yes
c	59.1	50.2	3.3	Yes
d	71.8	63.4	3.4	Yes
e	56.1	53.7	4.71	Yes
f	96	84	4.9	No
g	116	103.2	4.1	No

5.7.2 Aluminium-Nickel(High Purity) Hybrid Interferometer Measurements

This section contains the data obtained at 240mK from those SFS structures constructed using 5N nickel. Due to the greater success observed using triangular nanomagnets during the MFM studies, this shape was used primarily within this phase of the project. A smaller number of disc-shaped samples made from this new material were also measured. While the high purity nickel had not exhibited as much reproducibility as the Py samples in the MFM studies, none of the measured Py interferometers had displayed long-range coherent transport. The longer coherence length in a pure material such as Ni was hoped to increase the probability of being able to observe any long-range phenomenon.

Significant advances were made in the reproducibility of the samples during this period. A much higher proportion of fabrications resulted in the correct geometry and via closer regulation of the vacuum environment, materials and boats used, the resistances and critical currents of these samples became more controlled. The dV/dI lineshape for both the triangular and disc samples showed significant variation in both the number and positioning of features.

Triangular Samples

In general the dV/dI of these samples showed no zero bias peak, a lack of any features below the critical current of the aluminium and a set of large peaks in close succession as the superconducting regions transition into the normal state. None of the triangular 5N Ni samples measured displayed oscillations, meaning that this material did not offer further evidence of a long-range superconducting proximity

effect.

Upon examination of the data obtained from the 5N Ni samples it was apparent that there were 2 distinct sample types. One set displayed a normal state resistance of around 20Ω and a zero bias resistance of approximately 13Ω with initial Al critical currents of approximately 12μA. The second sample type displayed normal state resistances of the order of 57Ω, zero bias resistances of the order of 30Ω and critical currents of approximately 7μA. The higher resistance samples had values almost double that of the lower resistance ones, with a critical current half that of their lower resistance versions. As each fabricated chip displayed entirely high or low resistance samples, and there was no discernable effect upon the lineshape of the dV/dIs nor sample behaviour, this variation was taken to be indicative of varying film thickness and quality between chips. A film with more impurities in it will display a higher resistance and consequently a lower critical current is observed.

Figure 5.45 shows example SEM images of a 5N Ni triangle interferometer. Figure 5.46 shows some of the lineshapes observed during differential resistance measurements of the samples. While there is some signifiant variation in the number of peaks visible during the Al transtion, the overall lineshape was very similar for all of these samples. The table shows the normal state and zero bias resistances of all of the samples, as well as the current at which the initial Al transition occurs. The values are consistent indicating improvement in the fabrication techniques since the 4N Ni samples.

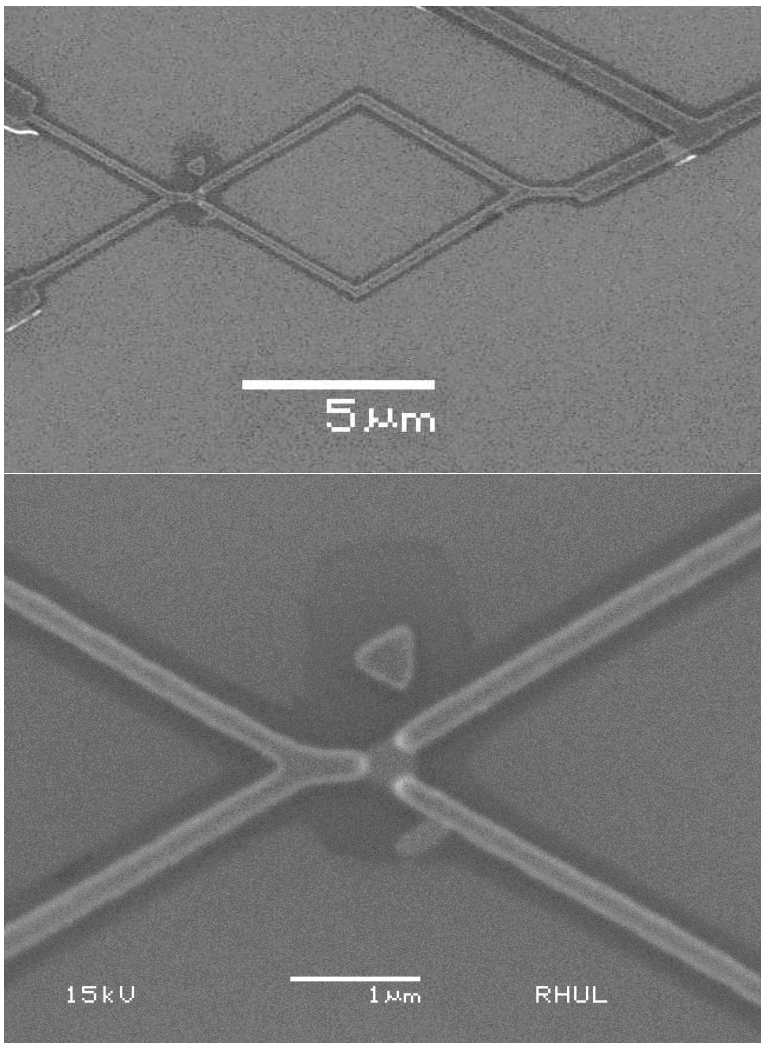

Figure 5.45: SEM images of a typical 5N Ni interferometer structure.

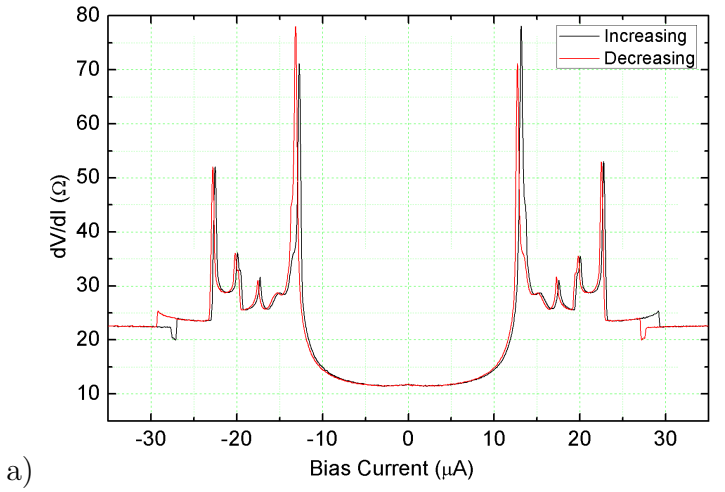

a)

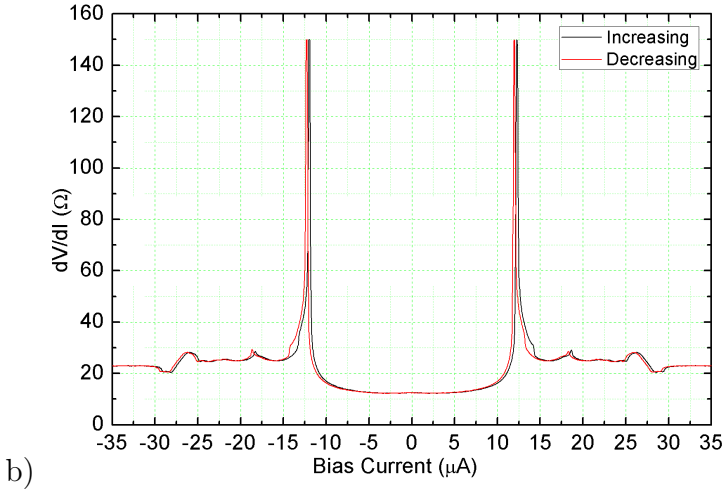

b)

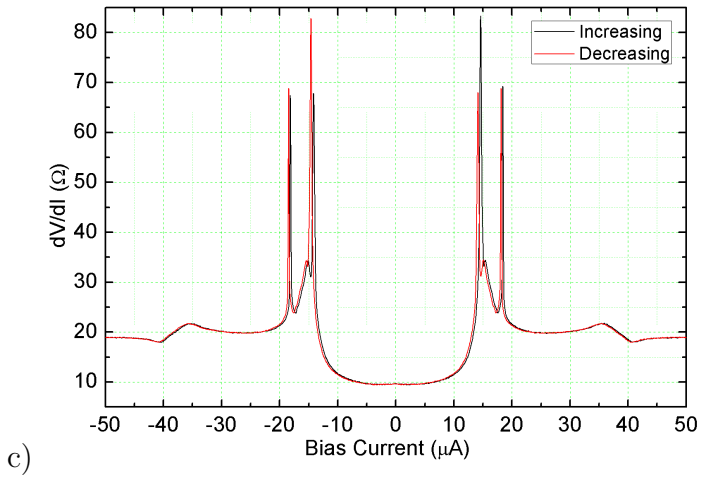

c)

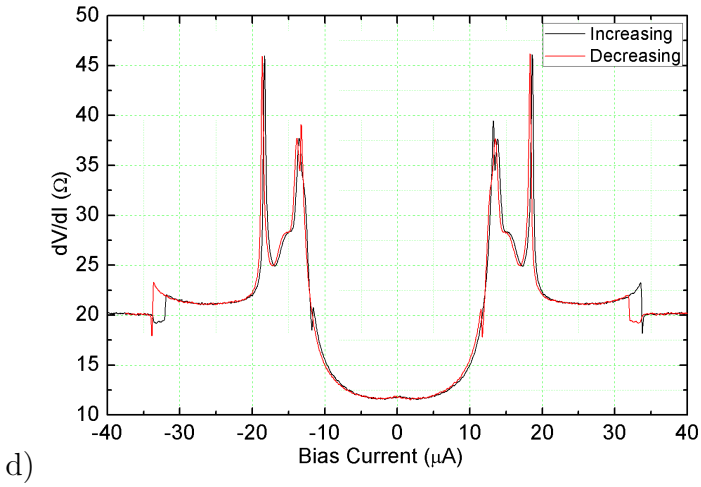

d)

Figure 5.46: Sample dV/dI graphs from 5N Ni triangle structures taken at 240mK.

Table 5.2: 5N Triangle Values

Sample	Normal State Resistance (Ω)	Zero Bias Resistance (Ω)	First Critical Current (μA)
a	23.0	11.9	12.8
b	23.0	12.67	11.9
c	19	9.6	14.1
d	20.2	11.9	12.9
e	22.7	13.1	12.5
f	22.8	12.9	12.5
g	54.0	29.4	6.9
h	63.0	33.7	5.4
i	57.6	29.7	6.6
j	46.7	35.1	6.5

Disc Samples

A small number of 5N Ni 300nm disc-shaped samples were also measured. These samples gave less reproducible results with a greater scatter in resistances and line shapes. None of the samples displayed phase periodic resistance oscillations, this can be attributed to the uncertainty in the magnetic structure already discussed in section 5.6.1.

Some of the features in the dV/dIs of both the triangular and disc samples were observed to display pronounced hysteresis. Examples of this can be seen in graphs a) and d) in Fig 5.46 as well as in Fig 5.47.

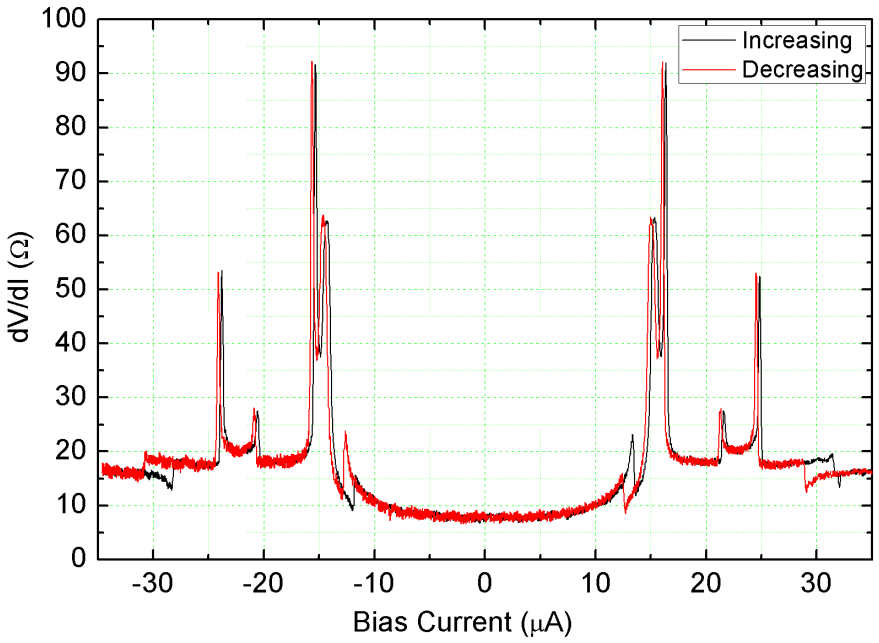

Figure 5.47: dV/dI of 300nm disc sample with hysteretic features. These may be the result of magnetic switching within the ferromagnet as a result of the spin torque exerted by the current flowing through it. The field was constant duing these measurements meaning that any changes to the magnetisation must be current driven.

5.8 Ultra Low Temperature Measurements with Increased Coherence Length

The next possible method to improve the yield of samples exhibiting the triplet proximity effect was to increase the ferromagnetic coherence length in the samples during measurement. As already suggested, it was possible that a weak triplet may in fact have been induced in some of the previously measured samples. Due to disorder within the film, reciprocal proximity effect or too high a temperature, it may not have been able to penetrate over the distances originally anticipated. While the improvements in the material purity detailed in section 5.6 will have increased ξ_F, time was secured upon a dilution refrigerator with base temperature T<50mK to conduct further measurements. By reducing the temperature of the system to approximately one fifth of that at which the earlier measurements were conducted, the coherence length of any triplet proximity effect induced would be increased giving a better chance of it being detected. The penetration depth of the singlet and opposite spin triplet states will remain negligible as they are inhibited

by the exchange field of the ferromagnet rather than inelastic scattering events. Due to the small number of connections for measurements and the limited time window available, only one cool down was possible during which two structures were loaded. To give the maximum probability of obtaining good results, both of the structures loaded were high quality interferometers incorporating SFS junctions where the ferromagnet was a 5N Ni equilateral triangle with sides of 600nm and thickness 30nm.

5.8.1 High Purity Ni Triangle Interferometer Measured in He3-He4 Dilution Fridge

Figure 5.48 contains SEM images of one of the finished samples before loading into the dilution refrigerator. Figure 5.49 is a dV/dI of the same sample measured at <50mK. There is a lack of subgap structure, which may be due to a poor magnetic structure in the nickel triangle, but a clearly defined set of transitions corresponding to the different parts of the Al structure going normal. The currents at which these features are found are 17.2μA, 18.2μA, 20.0μA and 22.0μA. These values are higher than the averages of those previously measured, which can be explained by the lower experimental temperature allowing the aluminium deeper into the superconducting state. The peak observed at 20.0μA is of special interest as when magnetic field measurements were conducted, it was found to be extremely susceptible. While no measurable change was recorded in any of the other dV/dI features over the low field range, this feature showed a continuous pronounced dependence upon field changes of a few Gauss. This behaviour is not indicative of conductance oscillations of the type sought by the experiment as the predicted period of 1 oscillation is 1 Gauss. Figures 5.50 and 5.50 illustrate the field and temperature dependence of the dV/dI peak at 20μA. From Fig 5.50 it is evident that this phenomena only manifests at temperatures below 100mK, and as such it is evidence of some coherent effect occuring within the structure which at present cannot be explained.

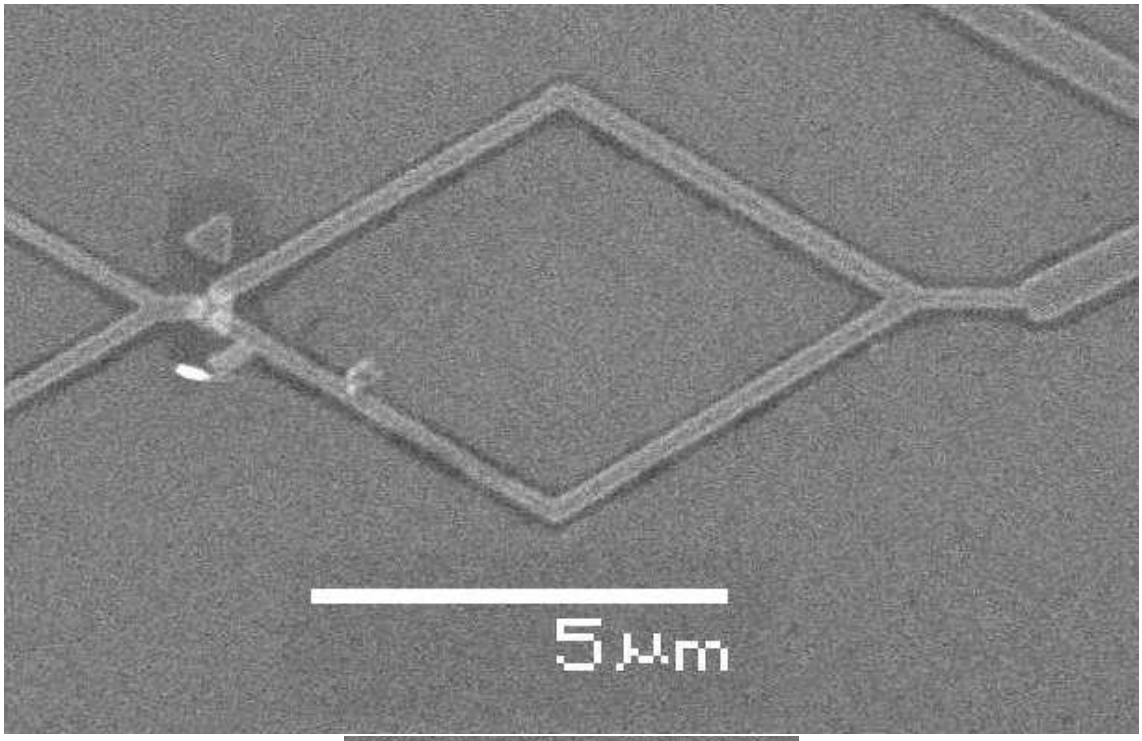

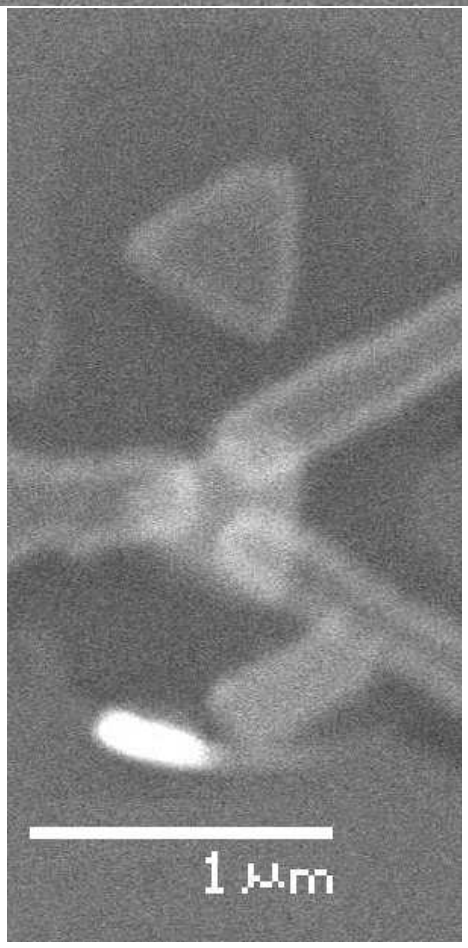

Figure 5.48: The top figure is an SEM image of the completed structure before being loaded into the dilution fridge. A close up of the SFS junction of the structure is shown below, in which the 3 Al contacts upon the Ni triangle are clearly visible.

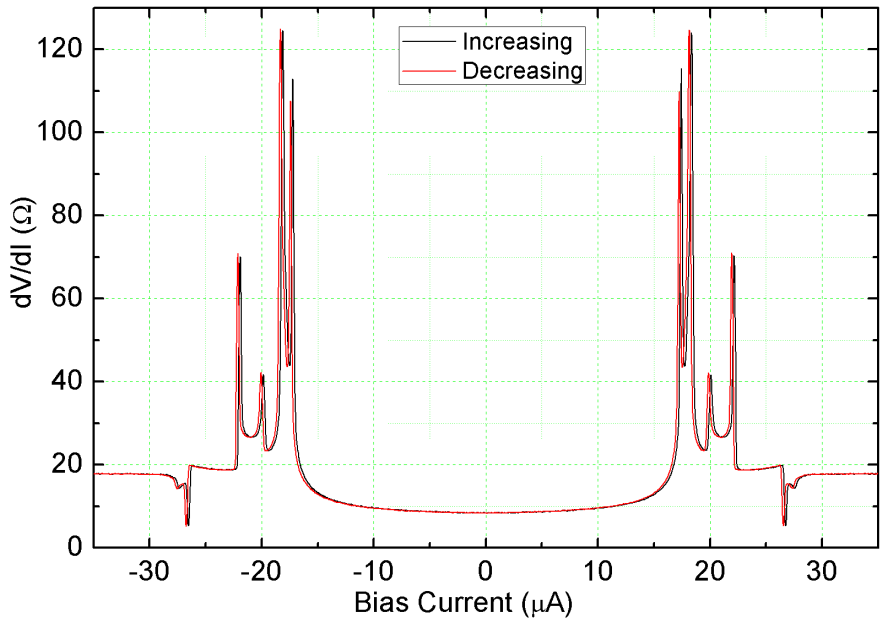

Figure 5.49: dV/dI of triangular 5N Ni sample in dilution fridge at base temperature (T<50mK).

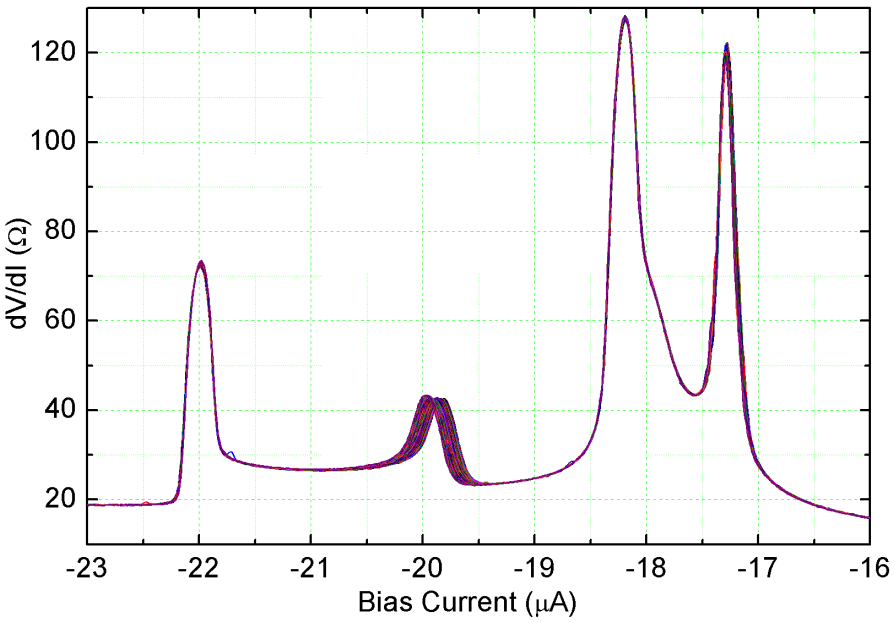

Figure 5.50: Superposition of dV/dI lines taken while incrementing the field over a range of 12G. The majority of the line sees no change while the central peak is smeared as it moves consistently with the slight change in field.

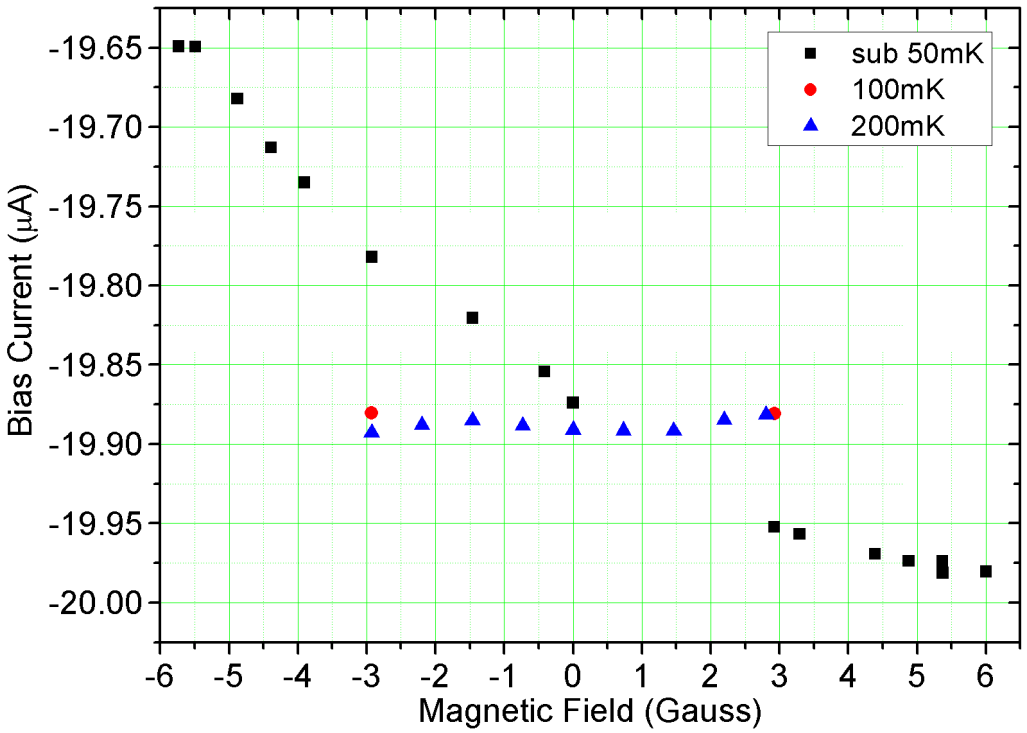

Figure 5.51: Graph showing the dependence of the small peak movement upon the temperature of the sample. The phenomenon only appears below 100mK, although it is not an oscillation of the interferometer as the period of such an oscillation would be 1 Gauss.

5.9 Control of Superconductor-Ferromagnet Coupling Using an Oxide Layer

The third possibility to investigate in attempting to secure a reliable long-range proximity effect was the interface quality between the Ni and Al. The best functioning samples so far measured had been notable for the large peak at zero bias in their dV/dI. By ascertaining the cause of this peak, then reliably reproducing it, the long-range proximity effect might be achieved. The peak of the feature at zero bias corresponded to a resistance of 70Ω. This kind of behaviour is consistent with a small tunnelling barrier existing in the junction, such as a thin layer of oxide or other contaminant building up between the deposition of the Ni and Al layers. While fabrication efforts up to this point had centred on maximisation of cleanliness and purity at all stages in the production process, it was possible that this accidental tunnelling barrier was a necessary component for the correct functioning of the sample. Nickel oxide is well known to be antiferromagnetic and the effect

of a thin layer of this material within the junction had not been considered. One possibility within the system was that the efforts to maximise the transparency of the S/F interface had been counterproductive. Such an interface would allow the ferromagnet to heavily influence the superconductor close to the interface, potentially suppressing the Cooper pair density within this region almost to zero. If this was the case then any long-range proximity effect within the ferromagnet would be dramatically reduced. With no singlet supercurrent carriers close to the interface there would be little injection into the F region and no opportunity for spin mixing processes or the development of a long-range triplet component. An investigation was mounted first to attempt to gain accurate control over the interface quality in the structures through a controlled oxidation process, and second to discover what effects, if any, such an oxide layer had upon the proximity effects within the system. The key results of this process are displayed in the following sections.

5.9.1 Interferometers with High F/S Barrier Resistance

Initial attempts to oxidise the Ni surface before the Al deposition used relatively high concentrations of O_2 for long periods (10mins) to test the general principle. This process produced promising data, although with huge resistances which far outstripped the low barriers aimed for. The zero bias peak was found to be present in all heavily oxidised samples, although they were all over oxidised with resistances of the order of several thousand ohms. Some unusual behaviour was noted in the magnetoresistance of these structures, however it was unrelated to the search for the long-range proximity effect. Theoretical work on this type of system is required to explain the behaviour observed.

Merservey and Tedrow published a number of experiments on spin polarised tunnelling between ferromagnets and superconductors in the early 1970s [84, 85]. Working with S/F junctions separated by a thin tunnelling barrier of Al_2O_3 they demonstrated directional hysteresis in the conductance arising from the spin polarisation of the Ni current carriers. Further analysis is required to compare the asymmetry observed in the dV/dIs measured from these highly oxidised samples to the existing literature on spin polarised tunnelling..

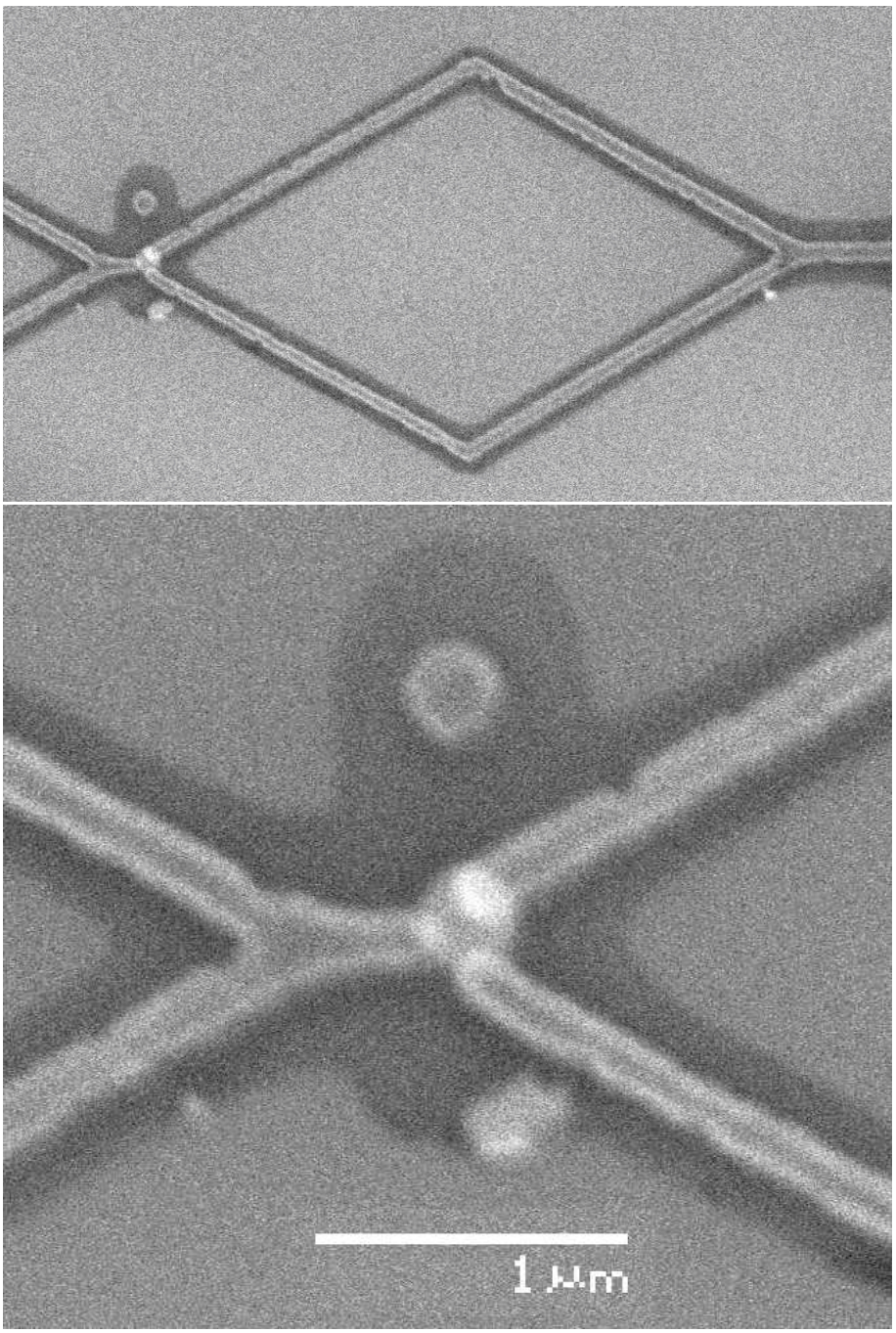

Figure 5.52: SEM images of a highly oxidised 5N Ni 300nm disc sample.

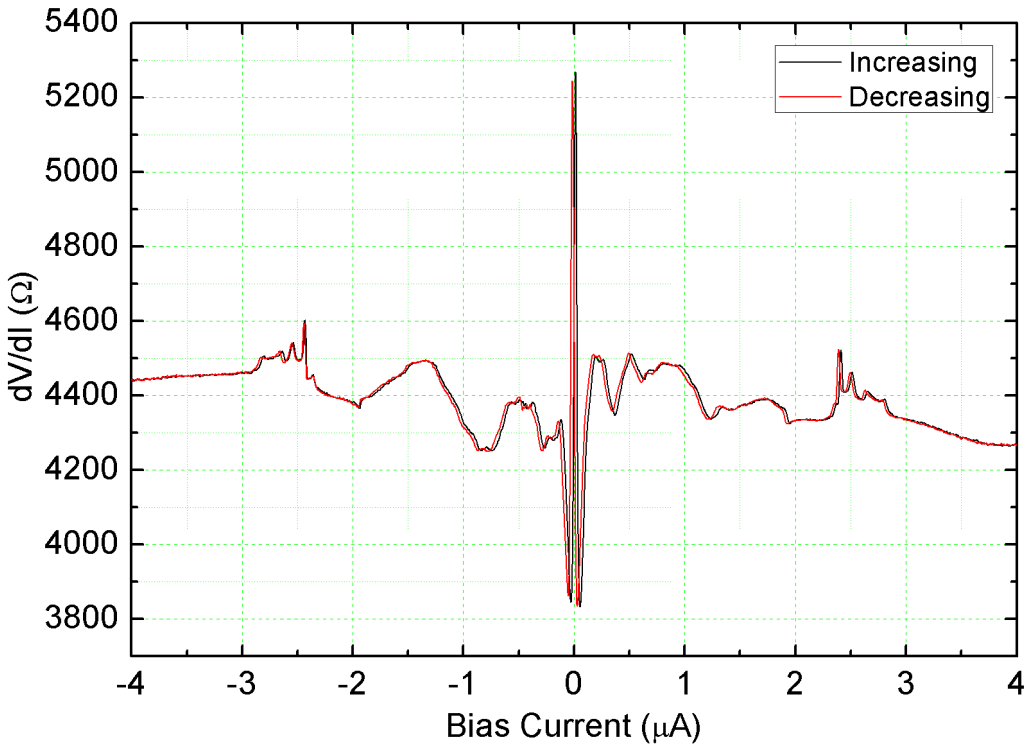

Figure 5.53: dV/dI of a highly oxidised 5N Ni disc sample with zero bias resistance $\approx 5300\Omega$. Note the huge zero bias peak and asymmetry of the graph features.

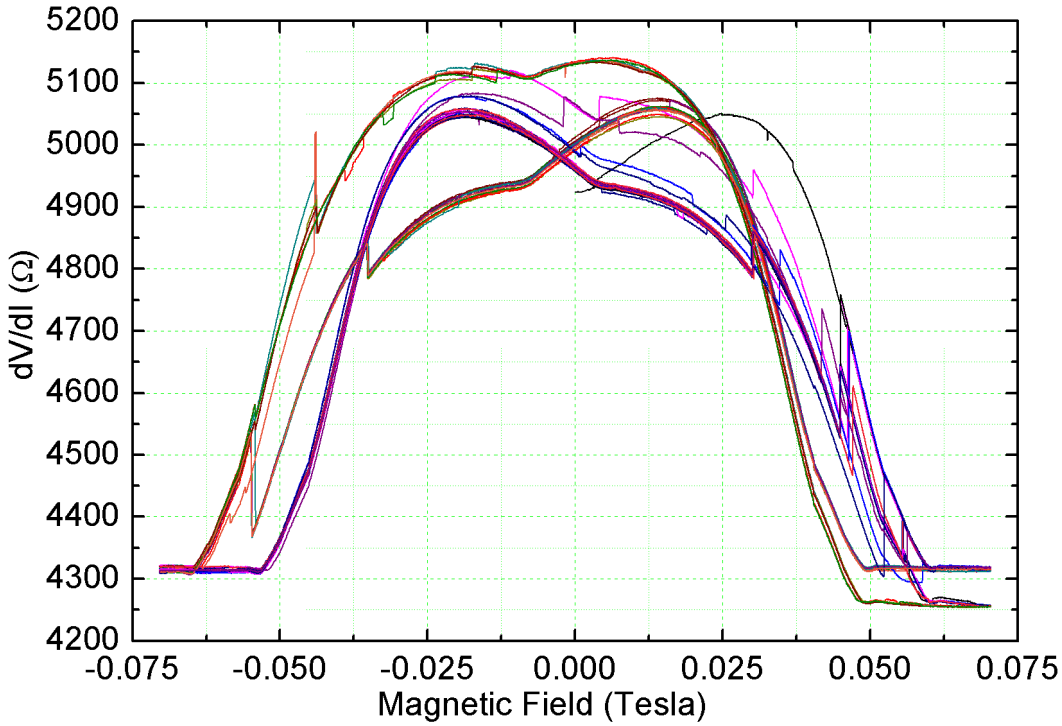

Figure 5.54: Repeated magnetoresistance sweeps at zero bias reveal the large jumps observed within these heavily oxidised samples. By repeating the measurements, patterns in where the jumps occur begin to appear.

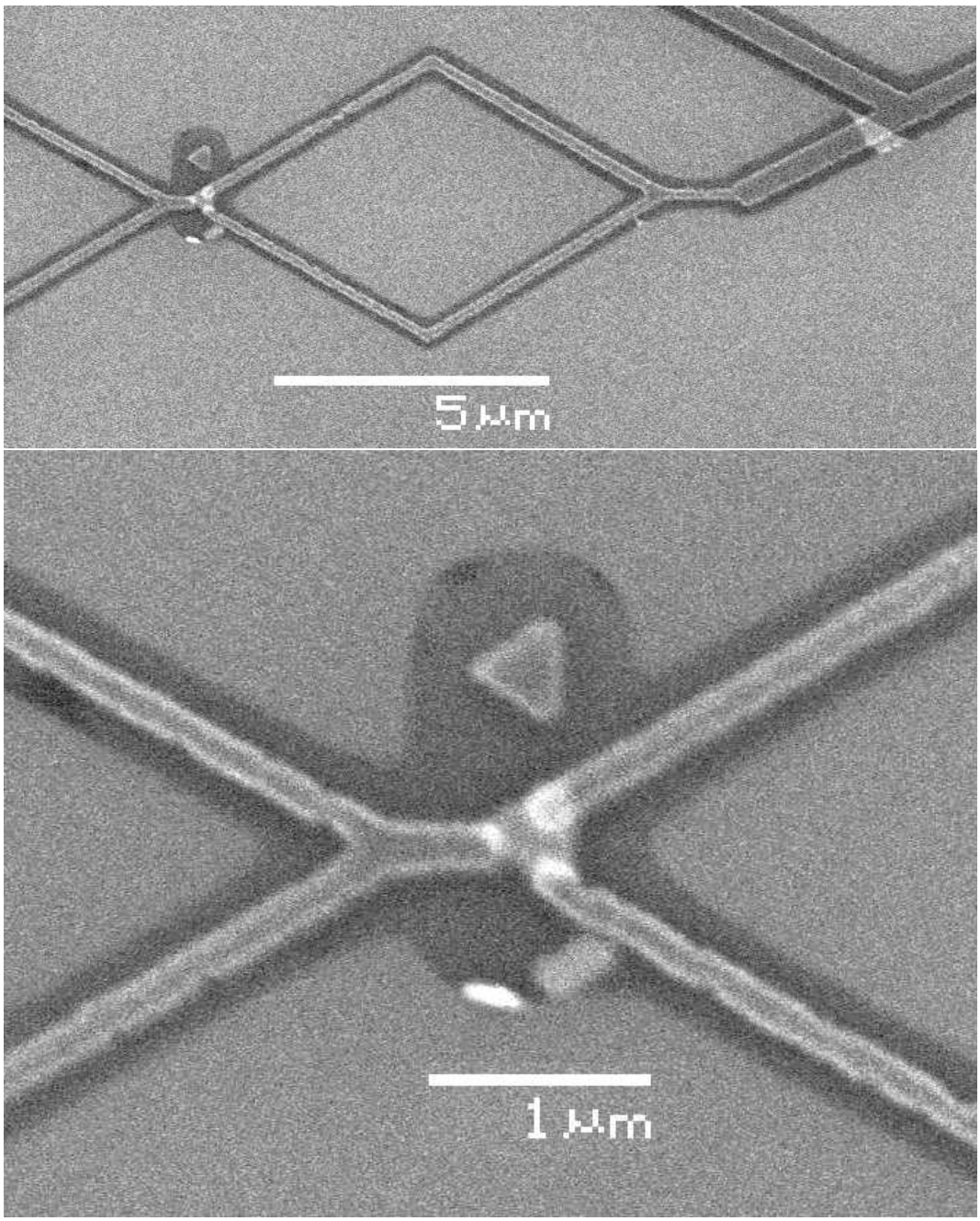

Figure 5.55: SEM images of one of the highly oxidised hyquids incorporating a 5N Ni triangle.

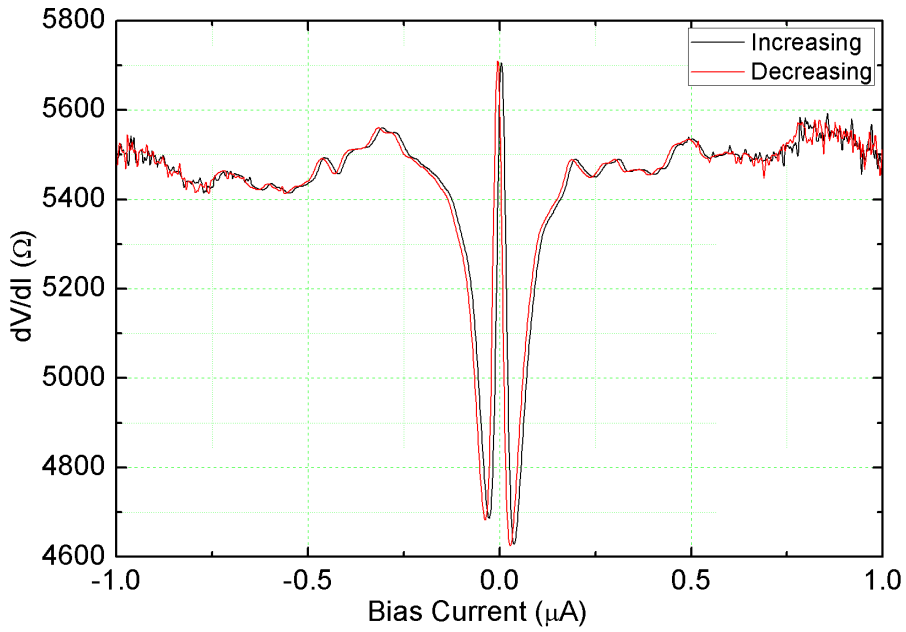

Figure 5.56: dV/dI of the highly oxidised triangular 5N Ni sample shown in figure 5.55. It has developed a thick tunnelling barrier of ≈ 5700Ω.

5.9.2 SFS Interferometers with Controlled Partial Oxidation

By repeated iterations of fabrication while varying the concentration of oxygen allowed into the vacuum chamber and the length of oxidation time, a process was achieved where small tunnelling barriers could be introduced at the SF interfaces. The barrier resistance in these samples was of the same order of magnitude as the samples which displayed the long-range proximity effect (70-100Ω). As the resistance of a structure with transparent interfaces was generally found to be of the order of 35Ω, and the oxide layer has the capacity to produce resistances of several thousand ohms, we can see that these structures contain a very thin coating of nickel oxide at the interface. This process is referred to as the partial oxidation technique.

A small number of samples made using the partial oxidation technique were measured at 240mK before time ran out for the project. While the ideal conditions for the measurements would have been at lower temperatures in the dilution refrigerator, it was impossible to secure further time on the apparatus to do this.

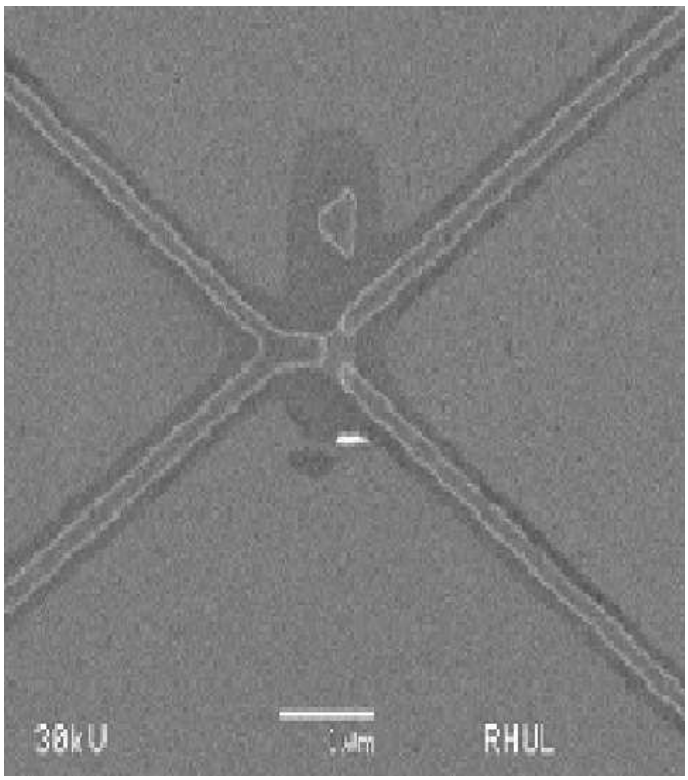

Figure 5.57: SEM of triangular shaped SFS interferometer with a low tunnelling barrier created using the partial oxidation process.

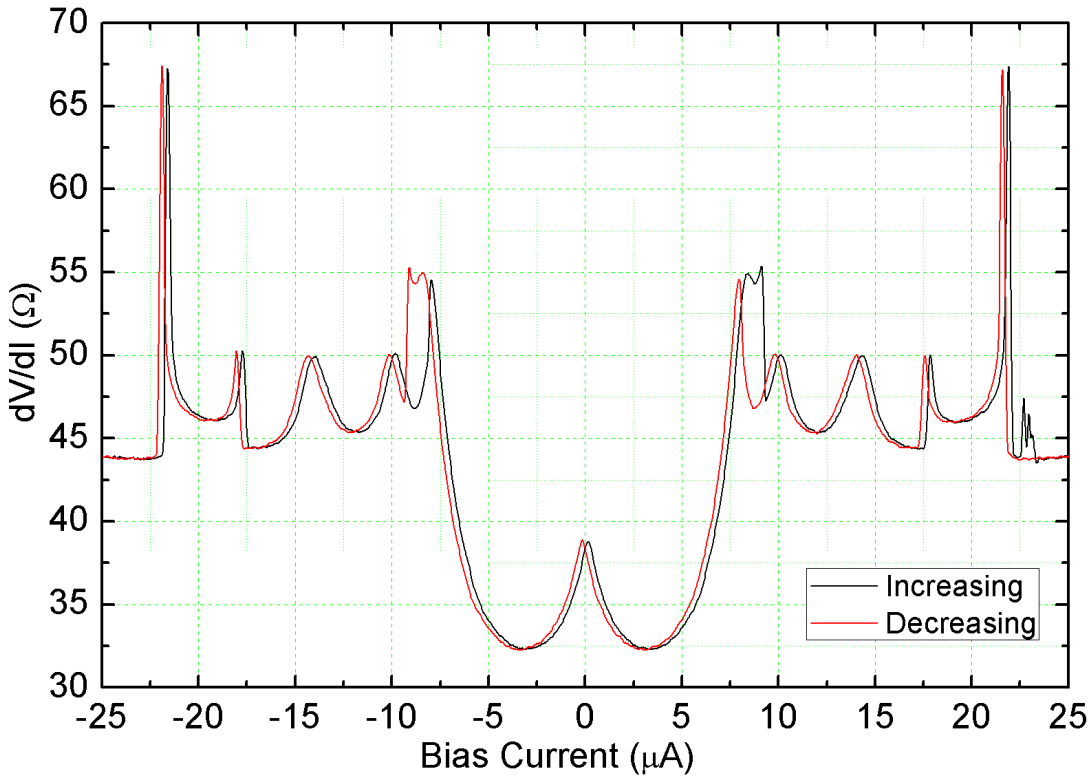

Figure 5.58: dV/dI of the sample imaged in 5.57 when measured at 240mK. The zero bias peak is apparent. There is an unusually rich set of peaks.

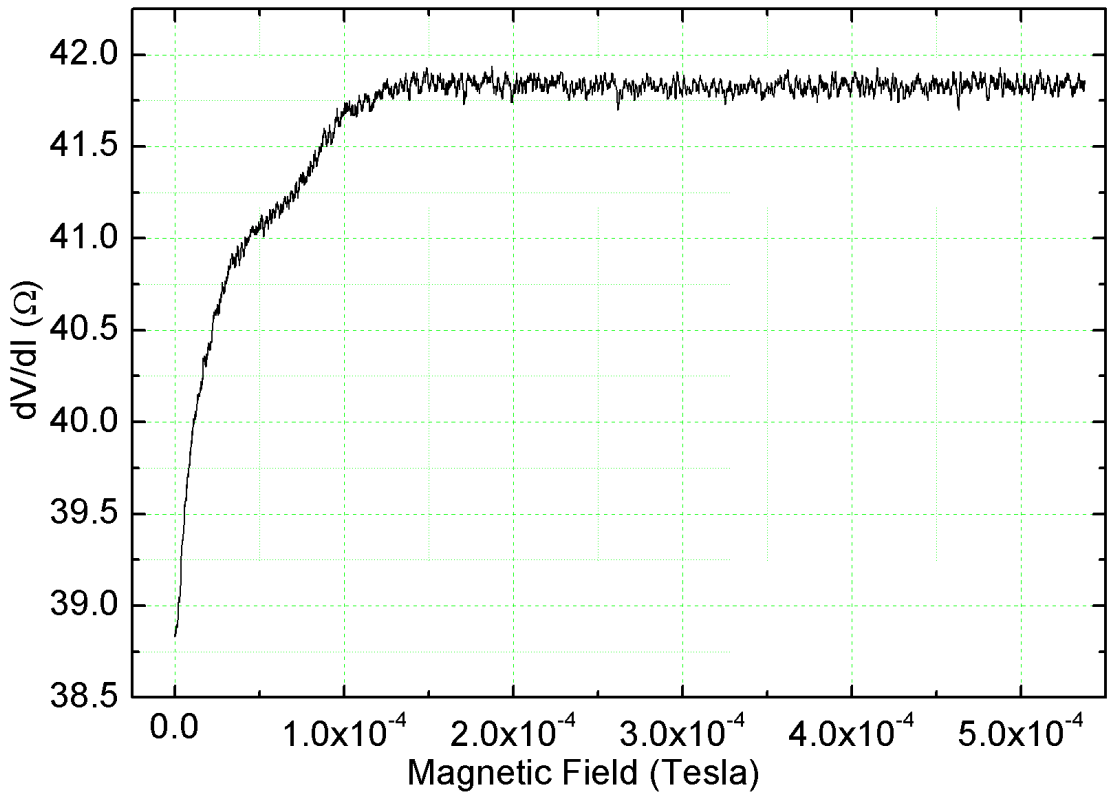

Figure 5.59: Unusual to this sample was an irreversible change in the sample's zero bias resistance when the magnetic field was first varied. The change amounted to an increase of nearly 3 ohms in the sample's zero bias resistance and was induced by a field change of approximately 1 Gauss. Such a small field change would be unlikely to affect the magnetic structure of the disc. Subsequent MFM studies conducted in applied fields by the author since this project was completed have shown no evident deformation of the magnetic stucture of Ni discs at fields less than 50G. Apart from this irreversible change, no flux induced variations in the conductance were observed in this sample at low fields.

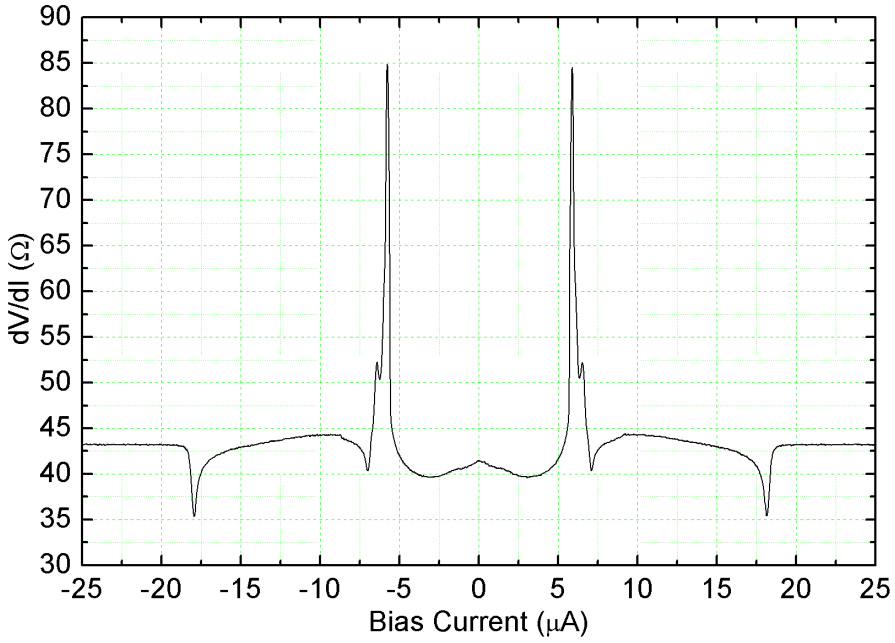

Figure 5.60: The dV/dI shape measured for the same sample after the changes induced by the small range magnetoresistance measurement. This behaviour is very similar to that seen in the permalloy sample detailed in 5.41. The changes were permanent.

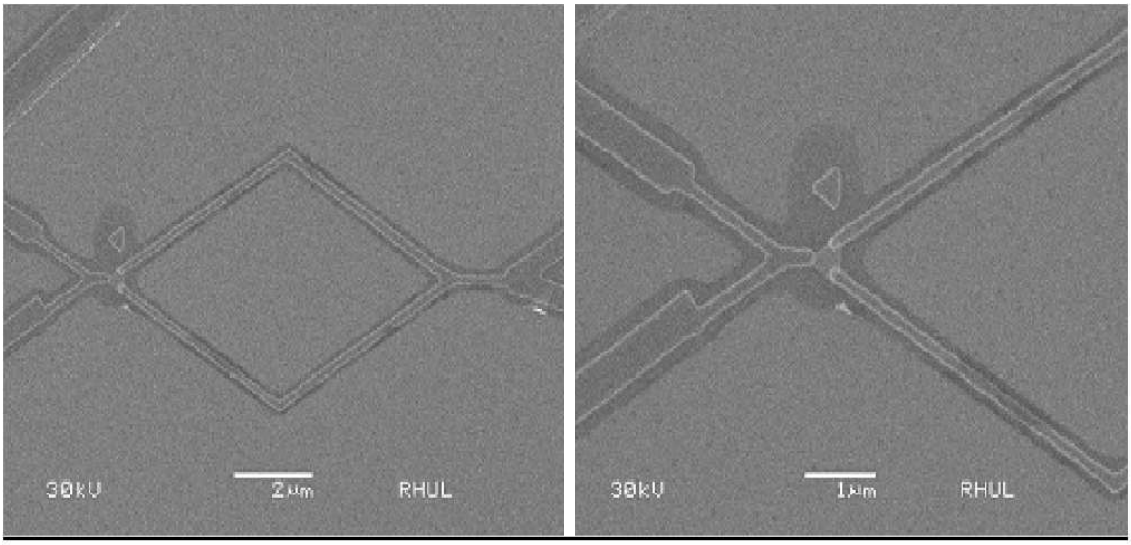

Figure 5.61: SEM image of a second high quality SFS triangle sample oxidised using the partial oxidation process.

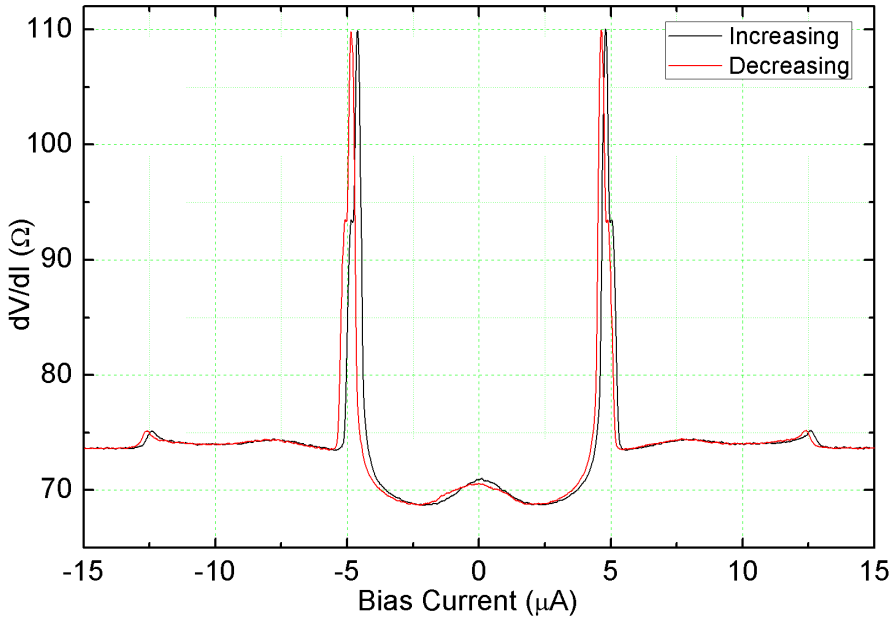

Figure 5.62: The dV/dI measured from the second partially oxidised sample at 240mK. Note that the zero bias resistance is almost exactly 70Ω. No measurable effects were induced by small field changes for this sample.

These partially oxidised 5N Ni interferometers are the most recent samples measured in the search for a long-range proximity effect within ferromagnets. A great amount of knowledge has been accumulated about how the systems work and great contol achieved over the fabrication processes and interface quality. With more time available for the project, a greater number of partially oxidised 5N Ni samples would be measured, preferably at ultra low temperatures.

Chapter 6

Quantum Interference and Phase Transitions in Mesoscopic Superconductors under Ferromagnetic Proximity Effect

6.1 The Influence of a Controlled Oxide Barrier on The Ferromagnetic Proximity Effect

As detailed in the previous chapter, the quality of the F/S interface was investigated as a possible contributor to the necessary conditions for the observation of the long-range proximity effect. Once mastered, the partial oxidation technique gave a high level of control over the size of the oxide barrier, allowing emulation of the best functioning SFS interferometers measured. The first half of this chapter details efforts to attain experimental evidence to quantify the effect of the oxide layer upon the coupling of adjacent S and F regions. As part of this investigation, a novel type of Andreev interferometer based on the ferromagnetic proximity effect was designed and implemented. Phase diagrams of the dependence of the interference medium in these devices upon temperature and junction length are presented.

6.2 Hybrid Interferometer Based Upon the Ferromagnetic Proximity Effect

In order to investigate the scientific basis for the introduction of an oxide layer, a set of modified hyquids was designed to investigate how the oxide barrier might affect the ferromagnetic proximity effect. If the layer of Ni oxide was found to shield the superconductor from the suppressing effects of the ferromagnet, then a greater density of Cooper pairs might be able to exist within the S region bordering the interface of SFS junctions. This would allow for a stonger triplet component to be generated within the F region.

To test this idea the following "Y shape" design was implemented. The design was essentially the same as that of the SNS/SFS hyquids, and was produced via the same modified shadow evaporation technique. In the case of the "Y shape" design however, the junction was formed of unbroken Al wires overlying the ferromagnetic material. Rather than measuring the penetration of a proximity effect into the ferromagnet, the aim was to drive normal a small region of the superconductor which overlayed the F region, via the penetration of the exchange field into the superconductor, and use this induced normal section as the interference medium of the device. The behaviour of the interferometer, and measurement of interference effects within the normal section of the aluminium, should then give some insight into the effect of the ferromagnet on the superconductor.

Techniques could then be tested to reduce the suppression of superconductivity within the ferromagnet. When the interface between the superconductor and ferromagnet was clean, as is expected for the unoxidised 2 angle fabrication process, an SNS junction should be induced within the Al overlying the Ni. This is due to the proximity ferromagnet driving a section of Al normal. By comparing the behaviour of a sample with an extremely clean interface with that of one which has undergone the partial oxidation process, it would be possible to see whether a thin layer of nickel oxide inhibited the reciprocal proximity effect in such samples. Evidence of this would be of the aluminium overlying the Ni having been driven normal at higher temperatures or currents in the oxidised sample, as the superconductor is not already weakened by the effect of the ferromagnet. In the most extreme case, the SNS regime would never be observed in oxidised samples as the ferromagnetic proximity effect would be too weak to affect the superconductor. The device would

function as one unbroken superconducting wire.

Each Y shape sample was always fabricated with a corresponding SFS type structure of the same geometry on the chip. Differential resistance measurements of the accompanying SFS structure allowed the properties of the interface to be measured, as well as providing a possible structure for the observation of a long-range proximity effect.

Aside from their use in examining the ferromagnetic proximity effect, these Y shape samples represent a unique system worthy of investigation for its own merit. In all other Andreev Interferometers to date, the SNS junction has been formed from a separate non-superconducting material, with two or more superconducting contacts as appropriate. In this type of system there was a mismatch between the Fermi surfaces of the two materials at the S/N interface. This would result in a proportion of the electrons incident upon the interface failing to undergo Andreev reflection, but rather being scattered back into the normal metal via a non-Andreev process. In the case of the Y Shape interferometer there is no mismatch of Fermi surfaces at the S/N boundary as the superconducting and normal regions are both made from the same aluminium. This means that all of the electrons incident on the S/N interface will undergo Andreev reflection, and thus be able to contribute to coherent effects within the device. The interferometer based upon the ferromagnetic proximity effect therefore has the potential to produce stronger measuring signals than previous devices, due to the greater efficiency of Andreev scattering at the interface.

Figure 6.1 shows an SEM image of a completed Y shape sample with a clean interface between the nickel and aluminium layers. Fig 6.2 shows the dV/dI measured from this sample at 240mK. At the lowest biases the whole sample is superconducting as the proximity effect from the ferromagnet is insufficient to kill superconductivity in the Al above it. At 9.1μA a transition occurs where the region of Al overlying the Ni goes normal. The resistance of this section is 1.02Ω. This stable resistance state persists until the much larger transitions at 27μA, which correspond to the rest of the Al wires going normal. The resistance of the whole structure is 12.6Ω.

In Fig 6.4 interference effects are measured at 240mK within the normal part of the aluminium overlying the nickel. This is done by plotting dV/dIs measured at small field increments and observing the fluctuations in the critical current of the onset of the SNS regime. While some bias current is required to achieve the SNS

junction, the oscillations are strong and clearly detectable even at the fridge's base temperature. This indicates that the reciprocal proximity effect from the ferromagnet must be powerful, as superconductivity in the adjacent region of the aluminium is strongly suppressed. The period of the oscillations is ≈ 1 Gauss, which matches that predicted from the loop size of the design ($20\text{x}10^{12}\text{m}^2$). The temperature dependence of the amplitude of the oscillations within the critical current is shown in Fig 6.6. Fig 6.7 shows the temperature dependence of the transitions between the sample's fully superconducting state and the SNS and from the SNS to the fully normal state, The SNS regime is strongly evident even at the base temperature of the fridge, with the aluminium deep within the superconducting state.

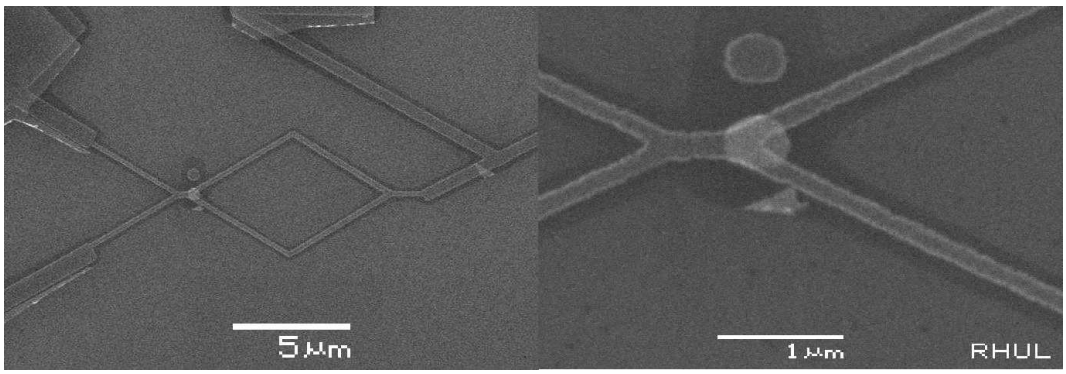

Figure 6.1: SEM image of a clean interface Y shape sample consisting of a 400nm 5N Ni disc and Al wires.

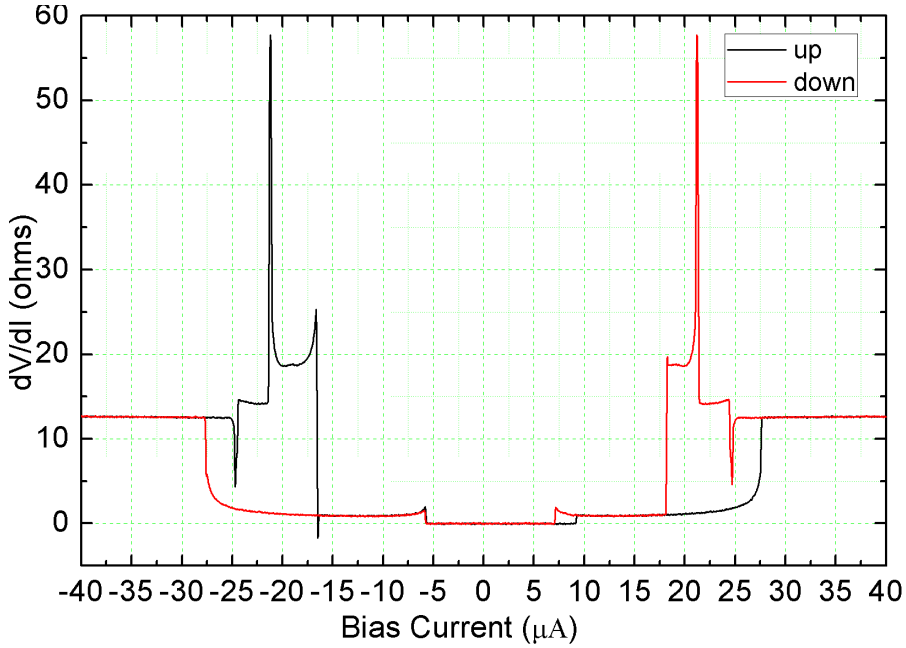

Figure 6.2: dV/dI taken at 240mK of 400nm disc clean interface Y shape sample.

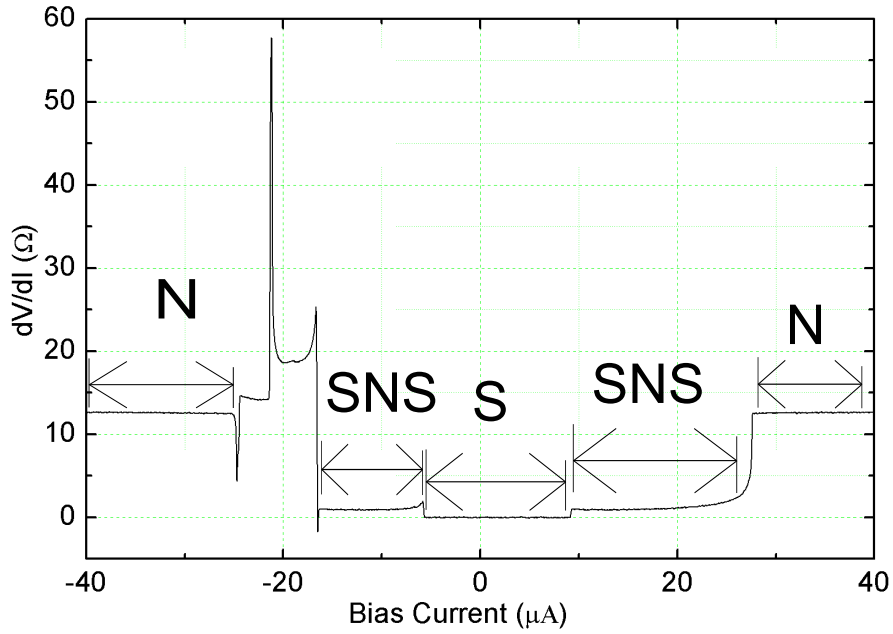

Figure 6.3: The same dV/dI as shown in Fig 6.2, with the fully superconducting (S), SNS junction (SNS) and fully normal states (N) labelled.

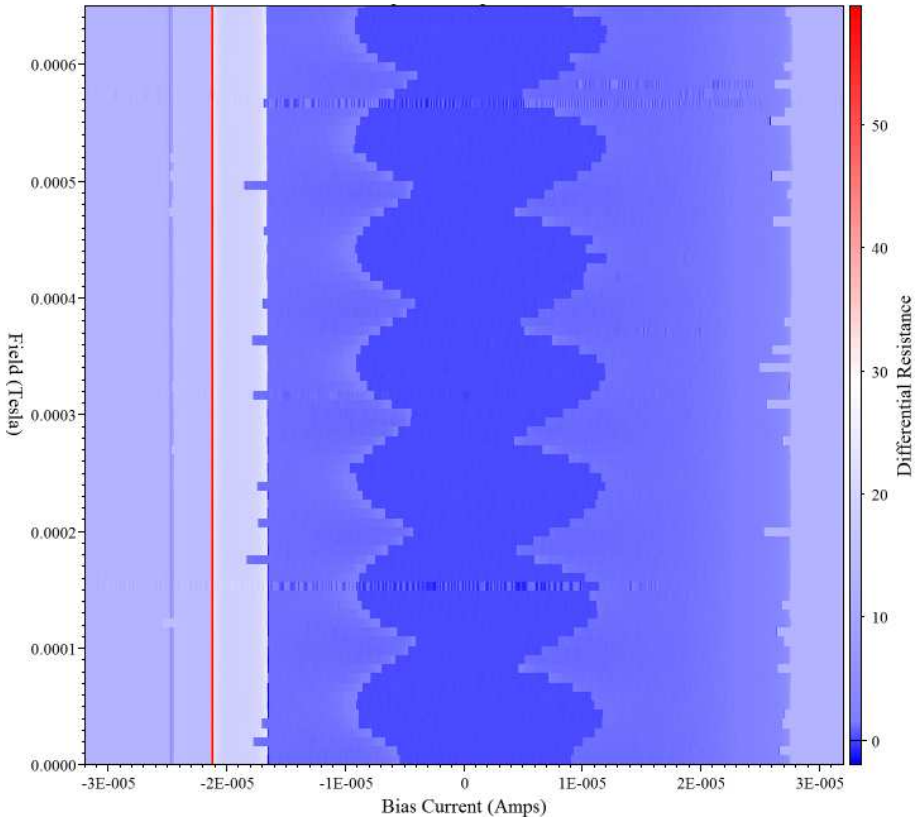

Figure 6.4: Quantum interference oscillations in the position of the transition between the fully superconducting and SNS regimes as a function of the applied field.

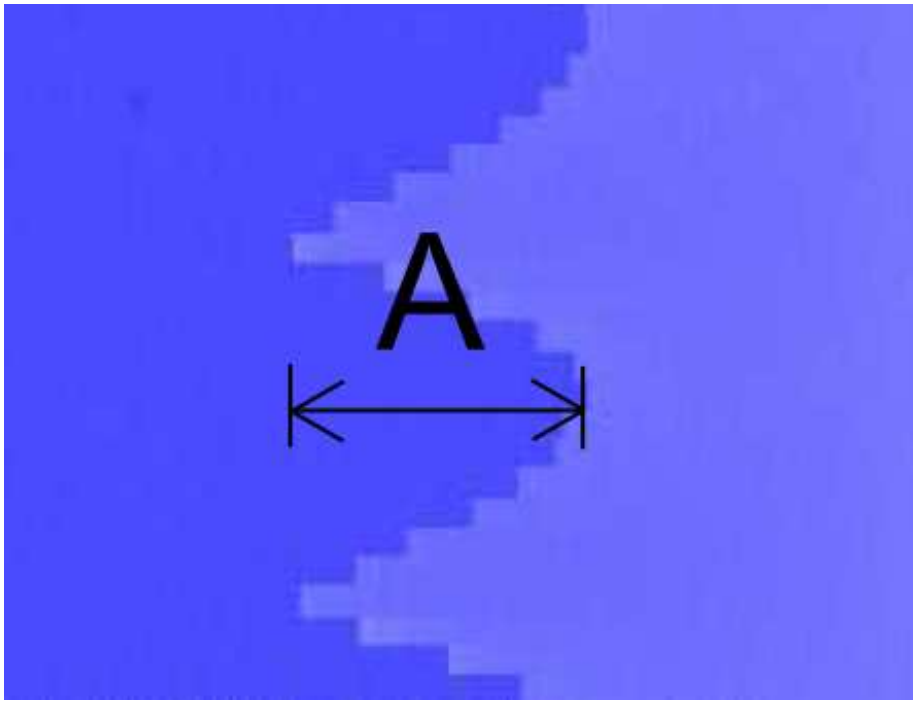

Figure 6.5: Section taken from 6.4 with the oscillation amplitude labelled.

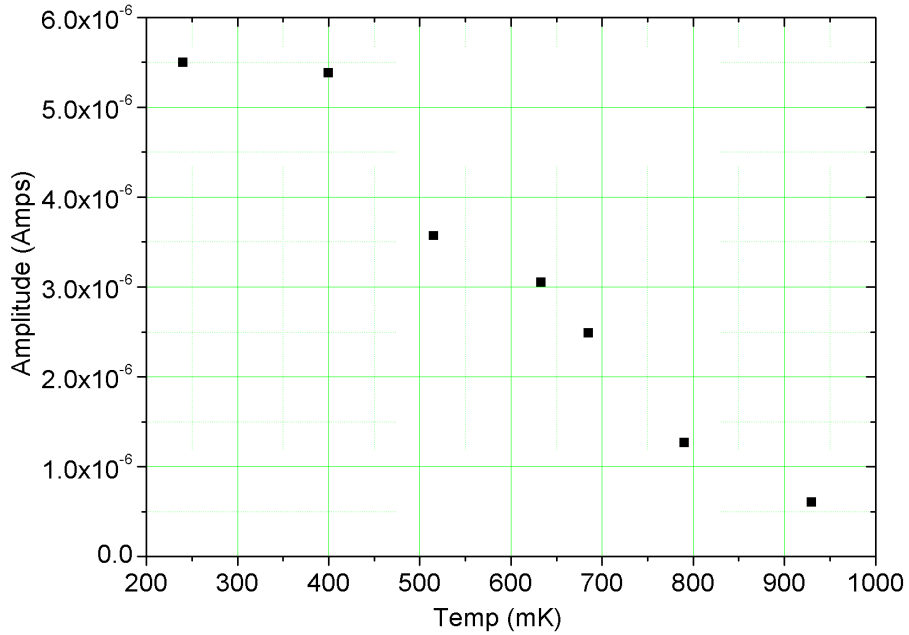

Figure 6.6: Dependence of I_c oscillation amplitude on temperature. Clear oscillations are seen from T_c down to the base temperature of the fridge.

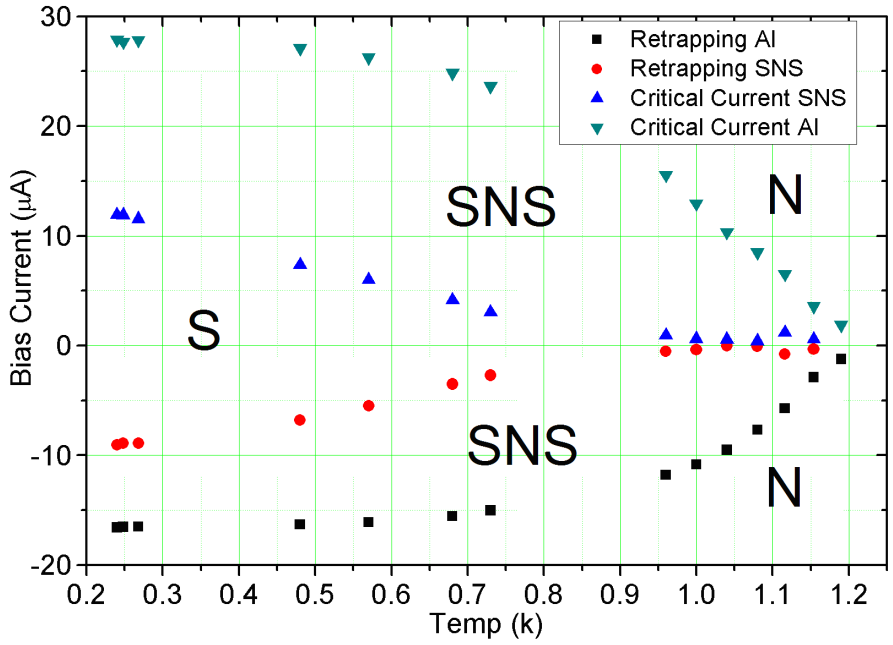

Figure 6.7: Temperature dependence of the major transitions in the dV/dI of the 400nm clean interface sample. The normal (N), SNS junction (SNS) and fully superconducting (S) phases are labelled. This plot shows the weakening of the superconducting components at temperatures close to T_c of the aluminium.

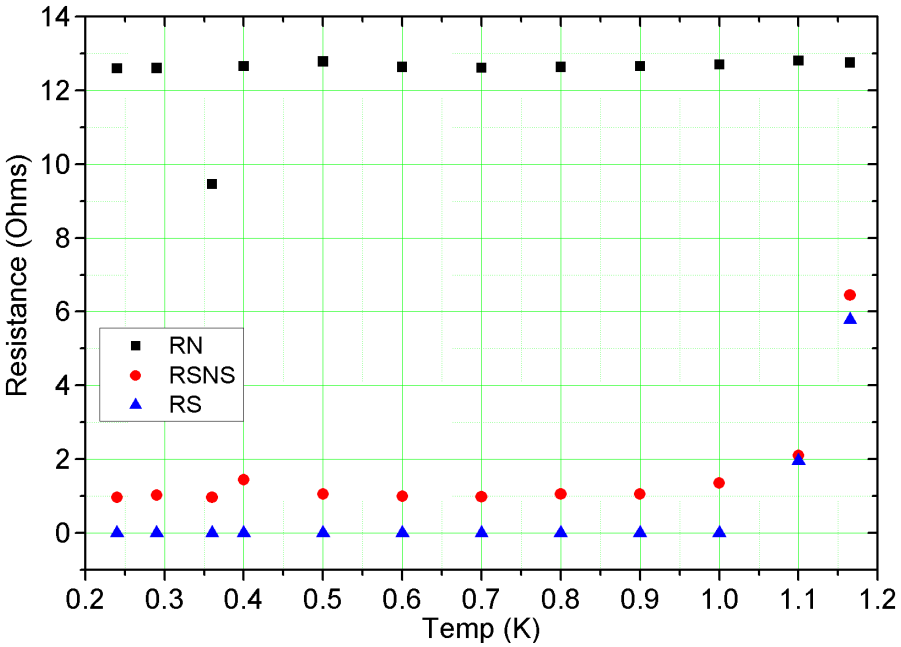

Figure 6.8: Temperature dependence of the different resistance phases of the structure. RN is the resistance when the whole structure has been driven completely normal by an applied bias current. RSNS is the resistance of the structure when the current bias is balanced to drive the weakened Al region above the Ni normal but the bulk of the Al wires are superconducting. RS is the resistance of the whole structure with zero applied bias current.

To check that the fabrication process used to produce the clean Y shape sample

was of the quality intended, measurements were carried out on its SFS analogue from the same chip. This structure was identical apart from the use of an SFS junction rather than the Y shape component. Fig 6.9 shows an SEM image of the geometry of the sample, while Fig 6.10 shows the dV/dI of this sample. The absence of a zero bias peak indicated that the fabrication has been successful in producing a transparent interface sample, with no oxide barrier between the aluminium and the nickel. Attempts to measure interference effects within this SFS structure were unsuccessful, indicating the absence of a long-range superconducting proximity effect penetrating the ferromagnet. The sample did not exhibit the hysteresis observed within its Y shape counterpart and the primary features of the dV/dI are a set of transitions beginning at 16.2μA as the different Al sections are forced into the normal state. The resistance of the structure at zero bias is 5.74Ω and in its normal state the measured resistance is 15.9Ω. The reduced critical current within the SFS type structure as compared with the Y shape is related to the weak link in the structure. Injection of spin polarised current from the ferromagnet into the superconductor may weaken it and quicken its return to the normal state.

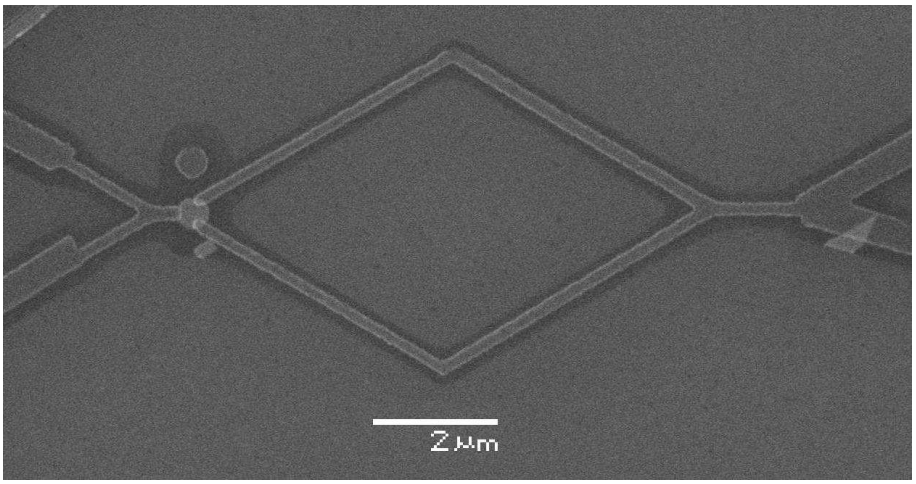

Figure 6.9: SEM image of the clean interface 400nm SFS device produced on the same chip as using the same processes as the 400nm Y shape in Fig 6.1.

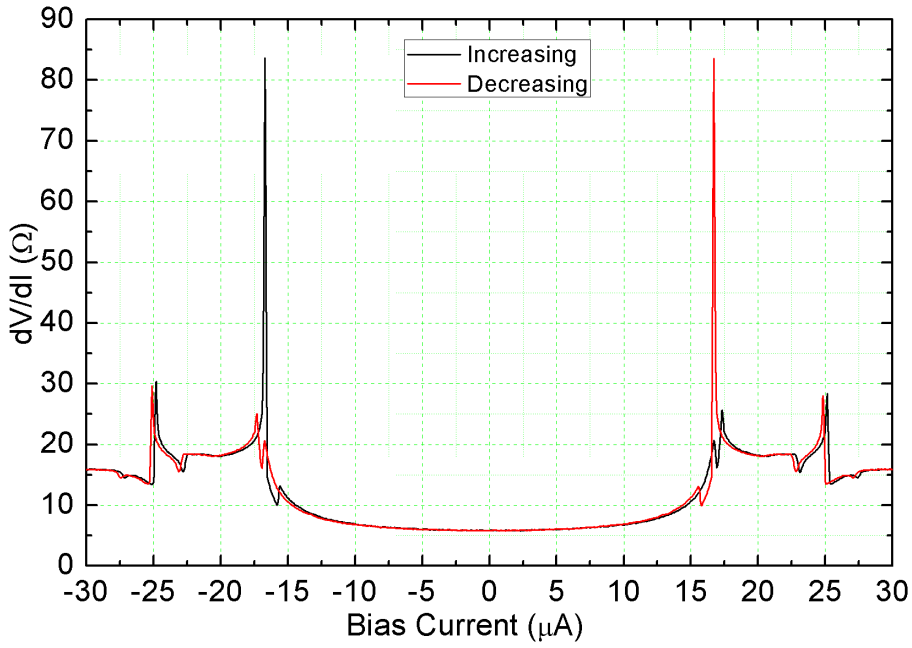

Figure 6.10: dV/dI of SFS version of clean interface 400nm 5N Ni disc Y shape. The zero bias peak is non-existent, indicating that the interface has no tunnelling barrier. The sub Al gap features are also non-existent, which further suggests a lack of proximity effects within the ferromagnet. No oscillatory behaviour was observed when the field was varied.

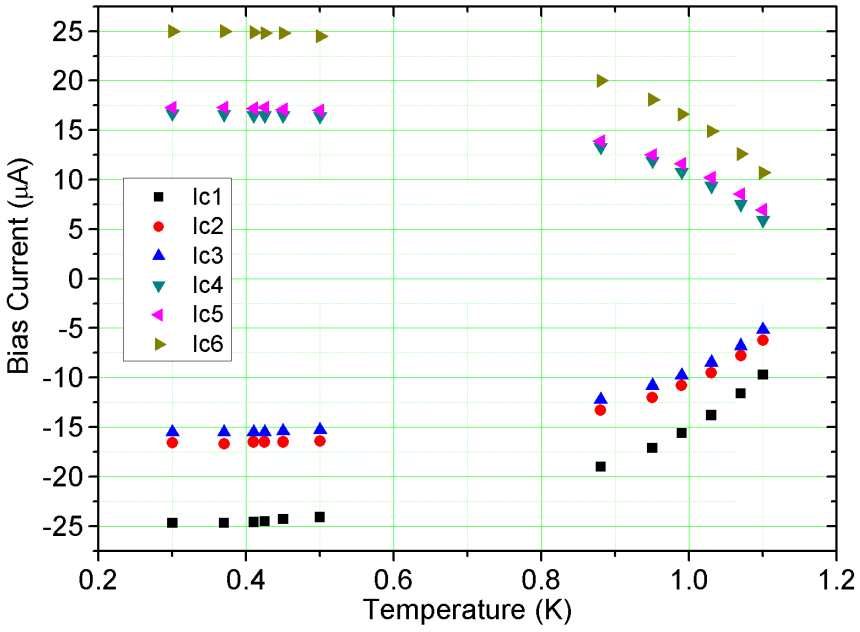

Figure 6.11: Temperature dependence of the major transitions in the dV/dI of the clean interface SFS structure incorporating a 400nm disc. The plot is far more simple than that measured from the equivalent Y shape sample. At temperatures close to 1.2K (Al T_c) the superconductor is weakened and the transitions occur at reduced currents. The primary interest in this structure was the shape of the dV/dI at zero bias at 240mK in order to monitor the interface quality of the fabrication.

The data so far described in this section was obtained for a clean interface Y shape sample, for comparison an identical set of structures was fabricated where the Ni surface was oxidised using the partial oxidation process before deposition of the Al. The effects of this oxide layer on the measurements are detailed below. The thin oxide layer in the junction makes a profound difference to the proximity effect of ferromagnet on the superconductor. An SEM image of the measured Y shape sample is included in Fig 6.12 and a dV/dI measured at 240mK is shown in Fig 6.13. This graph differs greatly from that observed for the clean interface sample. The SNS junction phase is not observed at this temperature as the sample switches immediately from the superconducting to normal states. Due to the reduced coupling with the ferromagnet, the Al sections behave as if they are one unbroken wire and as a consequence the critical current of the transition is significantly higher than that seen in the clean interface Y shape sample. The critical current in the oxidised sample is 117μA and the retrapping current 17.5μA. The critical current in the oxidised sample is $\approx$5$\times$ that of the clean interface sample. Fig 6.14 shows the dV/dI of the associated SFS sample from the same oxidised chip. A slight peak is visible at zero bias which indicates the presence of a small tunnelling barrier. The size of the peak is relatively small compared with the 70Ω one observed in the interferometer which showed conductance oscillations. The resistance peak in the sample equates to a barrier resistance of around 3Ω, despite its small size the barrier has provided a high level of shielding.

The temperature dependence of the Y shape sample was also measured. The immediate transition from fully superconducting to normal states and absence of SNS phase was found to extend almost up to the critical temperature of the aluminium (T_c=1.2K). The highest temperature dV/dI measured at 1030mK did show the entrance of the SNS junction between 8.89μA and 11.7μA when increasing the bias current and between 9.72μA and 8.89μA when decreasing the current bias, this is shown in Fig 6.16. By setting the fridge temperature and bias current to this range (1105mK) it was possible to measure flux driven conductance oscillations in the induced SNS junction, this is shown in Fig 6.17. The huge difference in temperature ranges for the observation of this phenomenon between the clean interface ond oxidised samples shows how strongly the ferromagnetic proximity effect has been hindered by the thin oxide layer.

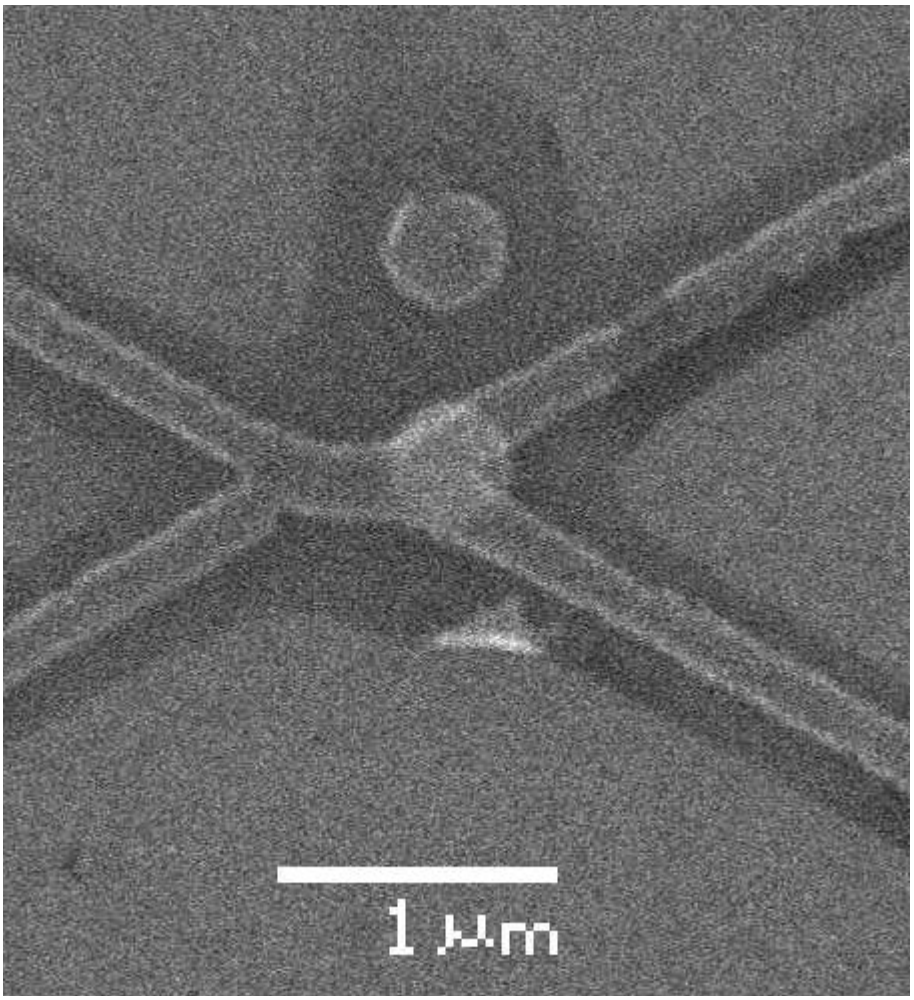

Figure 6.12: SEM of the Y shape sample where the Ni surface underwent the partial oxidation technique before the deposition of the aluminium.

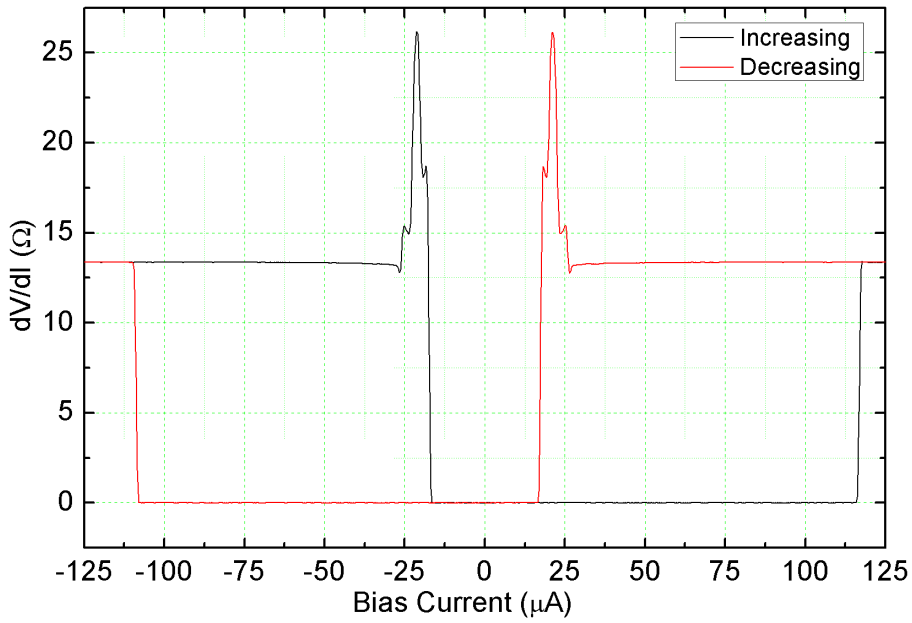

Figure 6.13: dV/dI of slightly oxidised Y shape sample at 240mK. The SNS phase seen in the clean interface sample at certain biases is not seen here as the oxide barrier has inhibited the reciprocal proximity effect of the Ni on the Al.

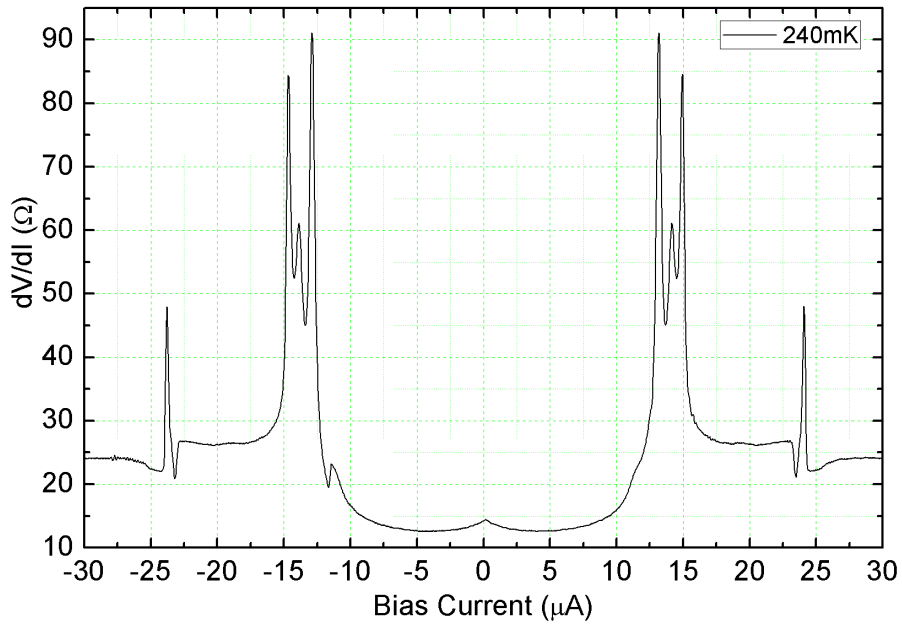

Figure 6.14: dV/dI of the SFS analogue of the slightly oxidised Y shape interferometer. The measurement was made at 240mK. The small zero bias peak corresponding to a small oxide barrier is clearly visible.

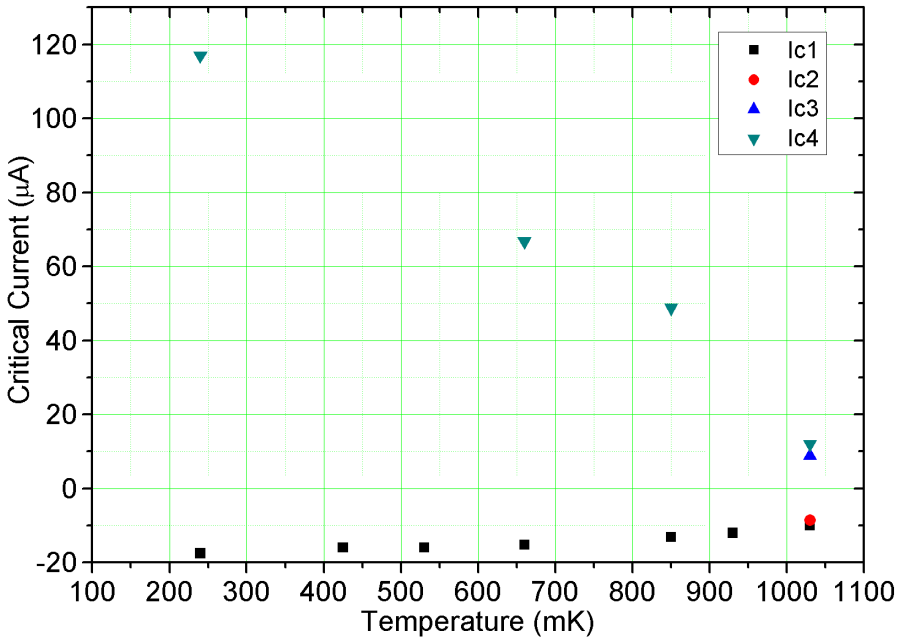

Figure 6.15: Temperature dependence of oxidised Y shape sample. The oxidised SNS regime only appears at the highest temperature measured 1030mK. In the clean interface sample the SNS region existed at the base temperature (240mK) upwards.

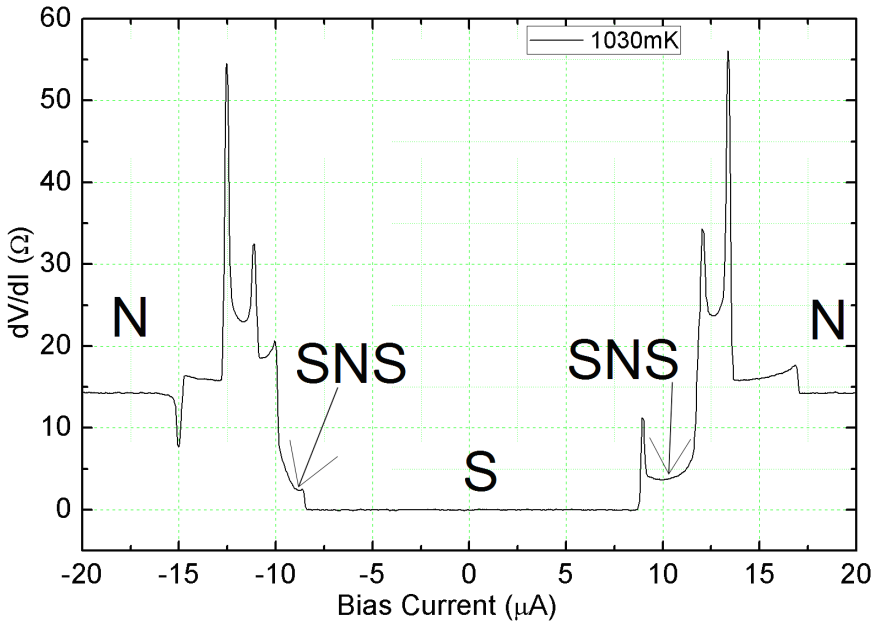

Figure 6.16: The dV/dI measured from the partially oxidised Y shape sample at 1030mK. The fully superconducting, SNS junction, and completely normal states are labelled.

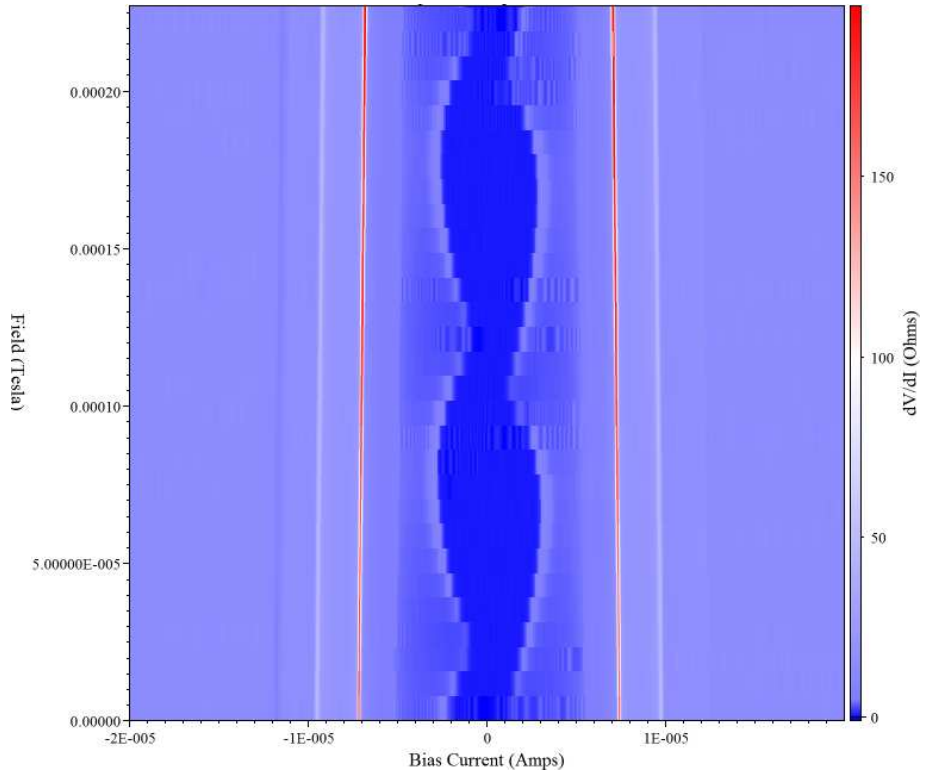

Figure 6.17: I_c oscillations measured at 1105mK. At such high temperatures the superconductor is sufficiently fragile for the weak influence of the Ni through the tunnelling barrier to produce an SNS junction within the overlying Al. At lower temperatures the oscillation is not seen as the weak proximity effect from the Ni is insufficient to induce the normal section of Al.

The cause of the suppression of the superconductor in these devices deserves some discussion. The stray magnetic field of the ferromagnet is unlikely to be the cause of the observed effect for several reasons. Almost all of the discs imaged in the project using MFM displayed some form of multi domain, fractured vortex state. While rarely displaying perfect vortex states these radial domain systems still formed closed domain systems in the plane of the disc, dramatically reducing the stray magnetic field. In many cases an out of plane feature analagous to the core in a true vortex was observed. Assuming the core in the fractured vortex state has similar properties to that in a conventional vortex it is possible to estimate the flux produced by this feature.

Given the diameter of the vortex core is approximately 15nm [86] the area of the vortex core will be approximately $1.8 \times 10^{-16}\text{m}^2$. Given a core field strength of 0.1T, the total out of plane flux produced by this feature will be 1.8×10^{-17} Wb, which is significantly smaller than the magnetic flux quantum (2×10^{-15}Wb) meaning that the contribution to the aluminium's suppression will be negligible.

The observation that a thin oxide layer at the S/F interface dramatically reduces the suppression of the superconductor is further evidence that this effect is not caused by the stray magnetic field of the nanomagnet. The magnetic field's influence would not be significantly changed by such a thin layer of contamination. The interaction of the Cooper pairs and quasiparticles within the superconductor with the exchange field of the ferromagnet will however be influenced by the introduction of the thin oxide barrier as it will prevent them from penetrating into the ferromagnet. The conclusion from this evidence is that the long range suppression of the superconductor by the adjacent ferromagnet in these experiments is caused by an exchange based ferromagnetic proximity effect as discussed in the background section 2.2.9 rather than by the penetration of stray magnetic field into the superconductor.

This evidence for the suppression of the ferromagnetic proximity effect by such a thin oxide layer also helps to explain the previous observation of a long-range proximity effect in an interferometer with a similar barrier. By suppressing the ferromagnetic proximity effect, a geater number of Cooper pairs are able to inhabit the region close to the S/F interface allowing for a greater injection into the ferromagnet. The small set of SFS samples which were created via the partial oxidation process with tunnelling barriers of this order of magnitude did not yet display a long-range proximity effect. This indicates that other variables such as the magnetic structure were not optimised in these samples. By testing a larger set of samples with this size of tunnelling barrier, we would expect to see some functioning samples in those cases where the magnetic inhomogeneity is correctly placed.

6.3 Superconducting Phase Diagrams of Interferometers with Varying Junction Lengths

Further examples of the Y shape interferometer type were fabricated, with varying diameters of the underlying Ni disc. By varying the disc size, the length of the SNS junction induced within the Al wire could be controlled. Under the correct conditions quantum interference effects were observed within the normal sections of aluminium in each sample, and phase diagrams of the state of the Ni/Al junction made.

For ease of production these samples were not produced using the modified shadow evaporation technique. A bilayer of resist was first deposited before an e-beam exposure of just the Ni disc was carried out. This was developed and a thin film of 5N Ni deposited. The sample was then removed from the vacuum chamber and the lift-off process carried out. Next a new bilayer of resist was deposited, and after careful alignment in the SEM the Al components were exposed directly on top of the Ni disc. The sample was developed and loaded into the vacuum chamber of the evaporator. Once at vacuum, the surface of the Ni was cleaned of the majority of its oxide build up via exposure to an argon plasma. The deposition of the Al thin film could then occur. While this method produced comparatively clean S/F interfaces, the results were not as transparent as those achieved using the modified shadow evaporation technique. As a result the data in the following sections is not comparable with that presented in the first section of this chapter.

The data presented in the following sections for 1 micron, 800nm 600nm and 400nm disc structures was all obtained from structures fabricated on the same chip using the same process. As a result the interface quality between the samples should be uniform, allowing comparison of the variation with junction length.

6.3.1 1 Micron Disc

Fig 6.19 shows an SEM image of a Y shape sample incorporating a 1000nm disc of 5N Ni, a closeup of the Ni region is shown in Fig 6.20. The dV/dI measured from the sample at 240mK is shown in Fig 6.21. At zero bias current, the sample is fully superconducting as at this temperature the suppression of the overlying aluminium by the nickel is insufficient to drive a section normal. This means the device is a single unbroken superconducting Al wire. At a bias current of 6.67μA a transition occurs corresponding to the weakened area of superconductor overlying the ferromagnet being driven normal. Oscillations in the position of this transition as a function of magnetic field, as well as directly measured magnetoresistance oscillations in the bias current region between this transition and the next, give further evidence that the resistance plateau between the transitions at 6.67μA and 12.8μA represents a stable SNS state in the sample. At 12.8μA bias current another set of much larger transitions occurs, these correspond to the other aluminium components in the structure being driven into a normal state. Hysteresis is again seen in the retrapping

current, with the majority of the Al components returning to the superconducting phase at 5.55μA. This leaves the SNS junction remaining above the Ni until the bias is reduced to 2.63μA, at which point the Al becomes fully superconducting once again. The resistance of the structure in the SNS state is 3.6Ω and when all parts of the structure have been driven normal it is 47.6Ω. By setting the bias current to sit within the SNS junction phase at 3.6μA, and ramping the field over a few Gauss, resistance oscillations were measured as shown in Fig 6.23. The period of these oscillations is one Gauss which matches the loop area of the sample 20x10^{-12}m^2. The amplitude of the measured oscillations is 1.3Ω. A broader picture of the oscillatory behaviour can be observed in the sample by repeating dV/dI measurements at field increments and plotting the data as shown in Fig 6.23.

The temperature dependence of the major transitions of the dV/dI curves is shown in Fig 6.24. At temperatures above 800mK the superconductor is sufficiently weak that the ferromagnetic proximity effect is sufficient to induce the SNS junction in the sample with no applied bias current.

In Fig 6.25 the variation in the dV/dI shape over a field range of 7G is shown. Clear oscillations are seen in the critical current of the fully superconducting to SFS transitions. The temperature dependence of the amplitude of these oscillations is plotted in Fig 6.26. The temperature dependence of the dV/dI transitions in a second measured 1 micron Y shape sample are shown in Fig 6.27. The behaviour is very similar to that observed in the first micron sample, indicating that these structures and their behaviour are repeatable.

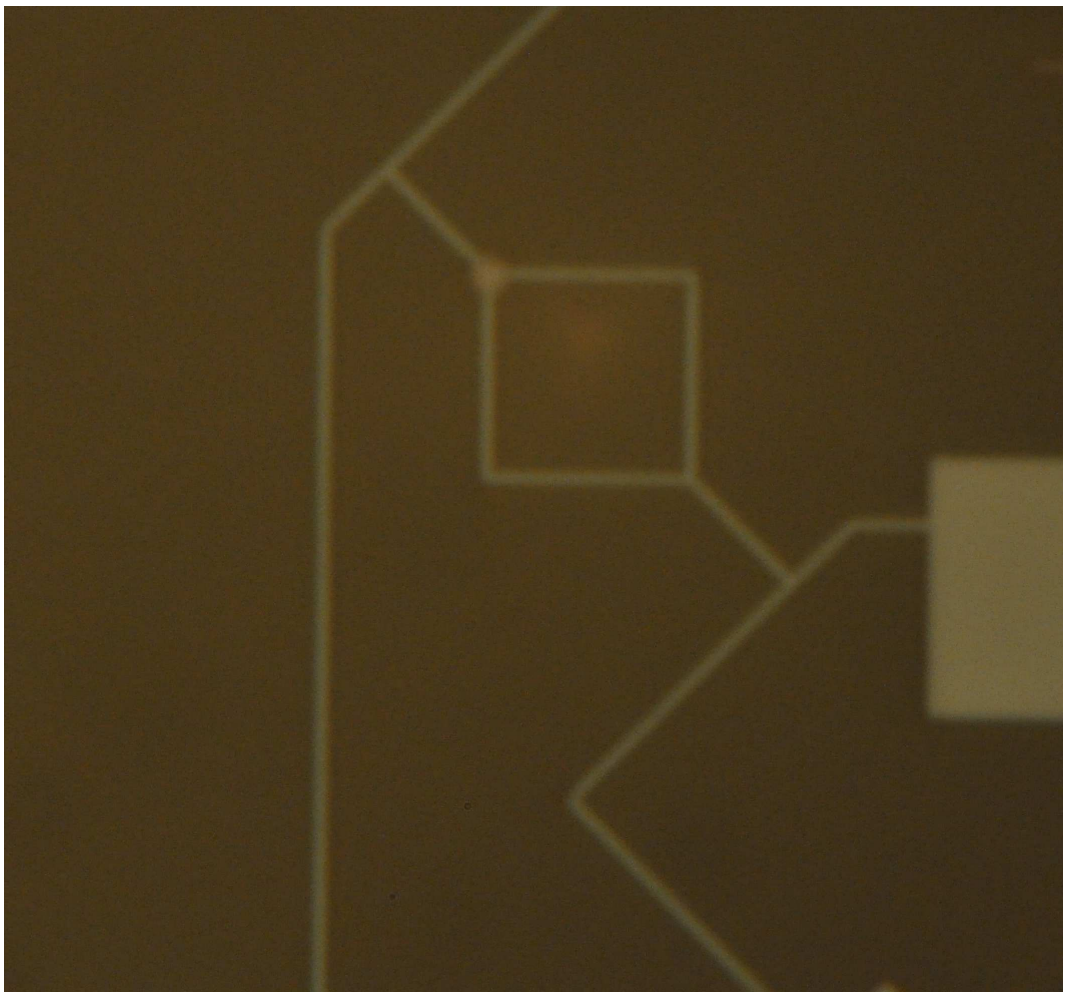

Figure 6.18: Optical microscope image of a complete Y shape structure incorporating 1μm disc.

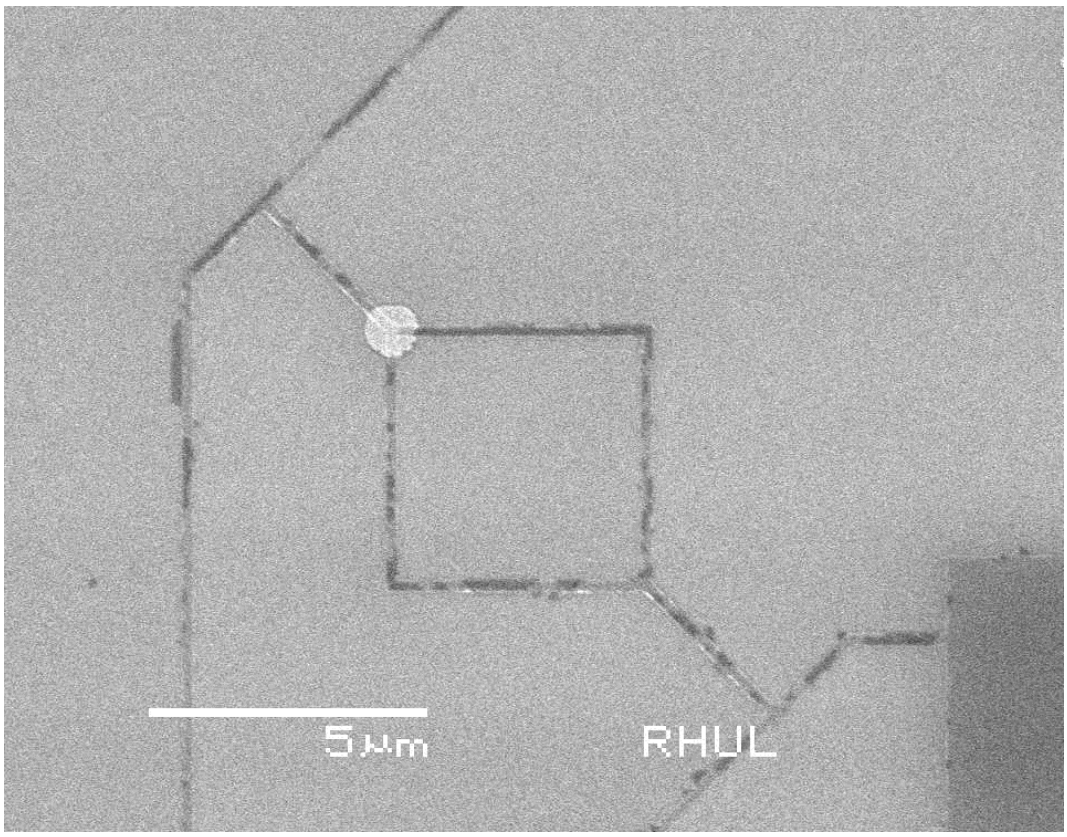

Figure 6.19: SEM of the Y shape structure shown in 6.18. The dark marks on the Al wires are residual resist from the lift-off process adhering to the surface. This does not effect the functionality of the device.

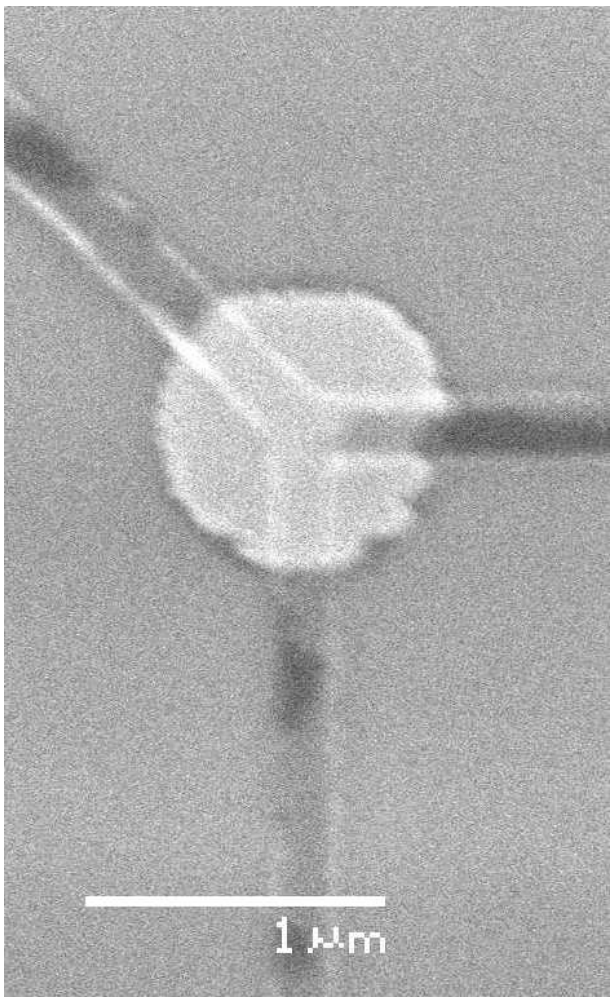

Figure 6.20: A close up SEM image of the junction of the same Y shape sample incorporating a 1μm disc.

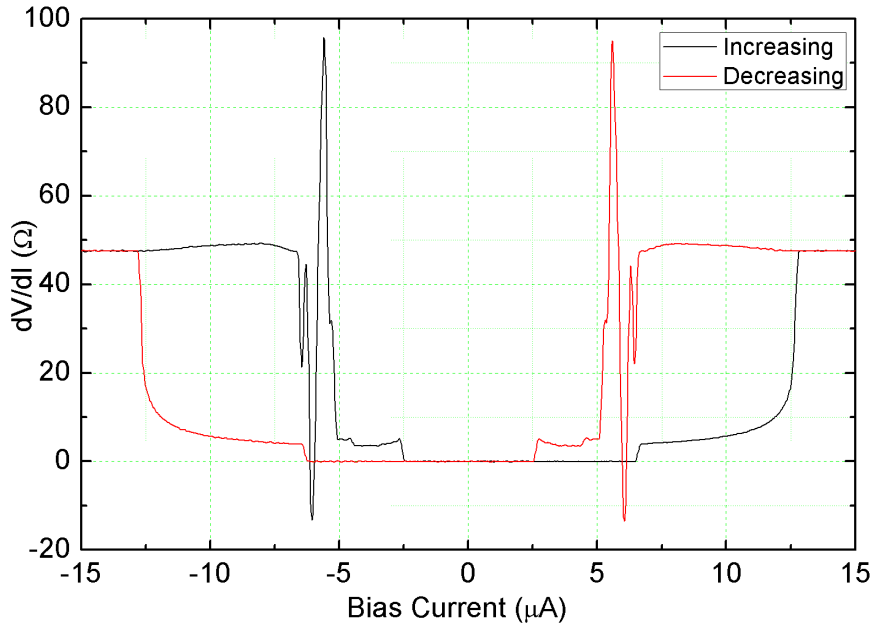

Figure 6.21: dV/dI of 1μm sample at 240mK and zero applied field. At zero and the lowest biases the resistance equals zero as the sample is in a fully superconducting state. At slightly higher biases, another plateau of stable resistance appears which corresponds to the area of aluminium directly above the nickel going normal due to already being weakened by the stray field from the magnet. At yet higher currents, a much larger transition occurs which corresponds to the other Al components of the structure being driven normal. Once the whole structure is normal the resistance remains stable.

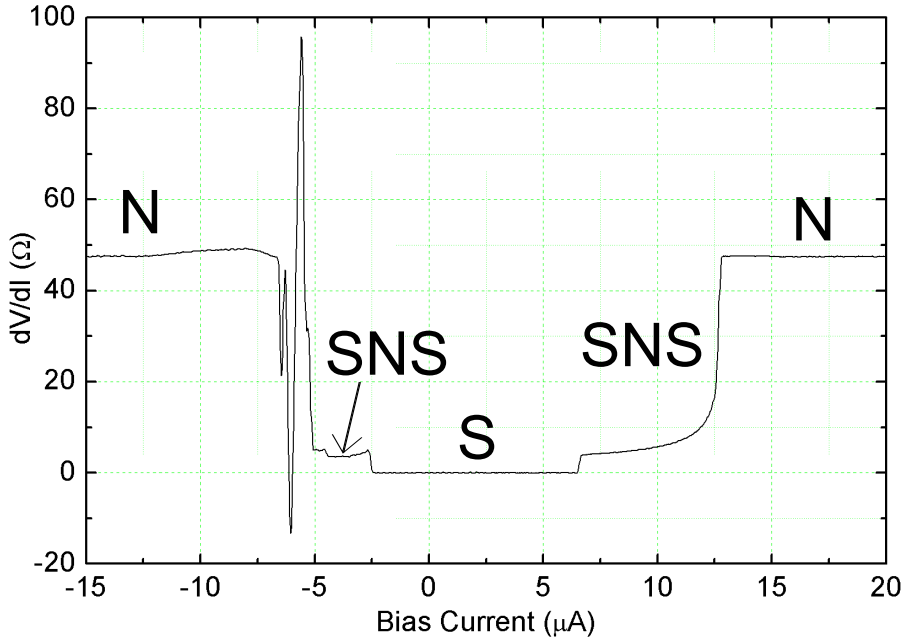

Figure 6.22: Upward sweep from 6.21 with the fully superconducting (S), ferromagetically suppressed region (SNS) and completely normal (N) states labelled.

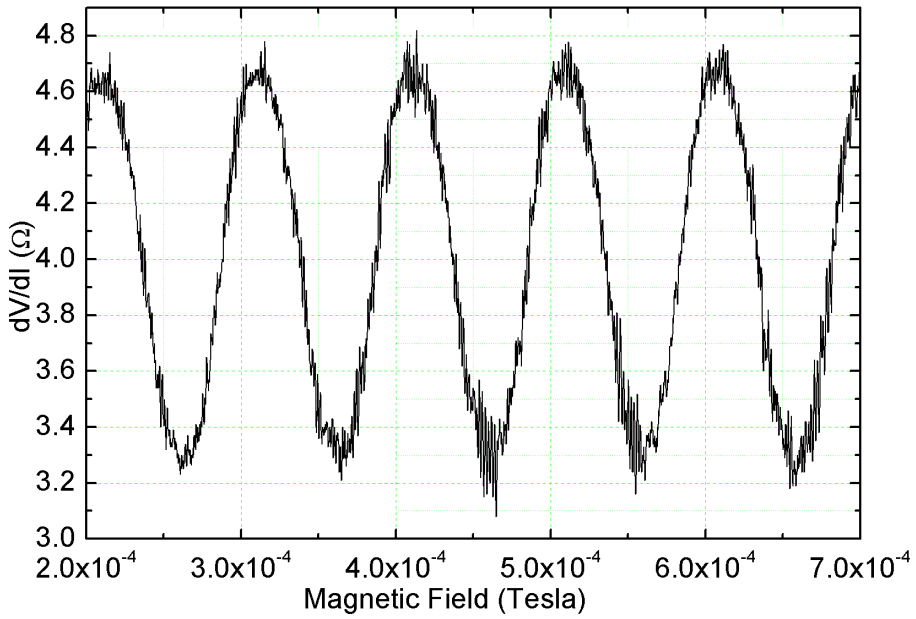

Figure 6.23: Phase periodic oscillations measured across the structure when the Al above the ferromagnet has been driven normal. The structure was first driven completely normal via the application of a large bias current, then the current gradually reduced to 3.6μA which corresponds to middle of the induced SNS junction region on the retrapping curve of the dV/dI. The observation of resistance oscillations as a function of flux at this bias indicates that this section of the graph does indeed represent a phase where the Al section above the Ni has been driven normal so that interference effects can be observed within. The period of the oscillations matches that predicted from the loop size of the design.

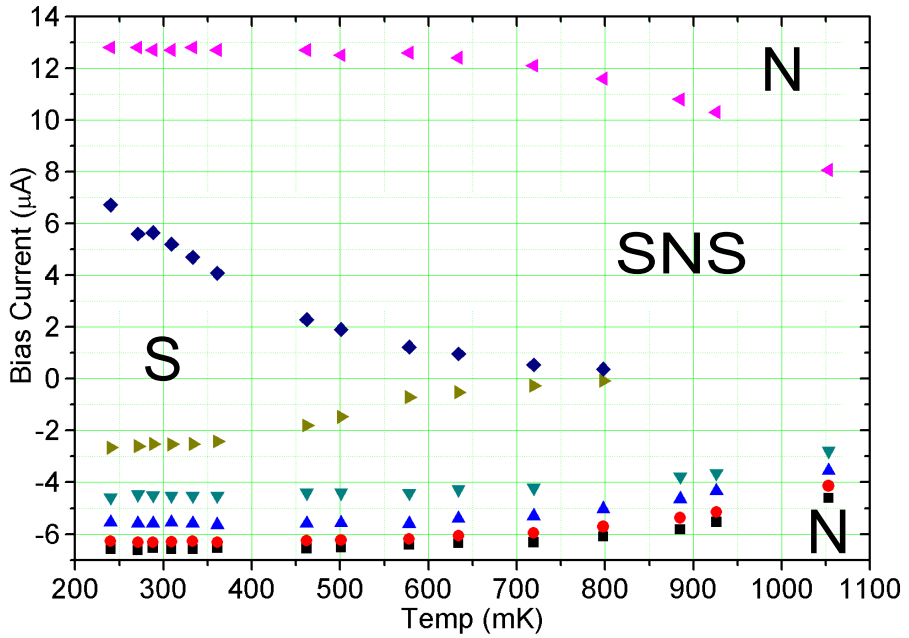

Figure 6.24: Temperature dependence of the various transitions visible in the dV/dI of the 1μm sample. The critical temperature of the aluminium is 1.2K.

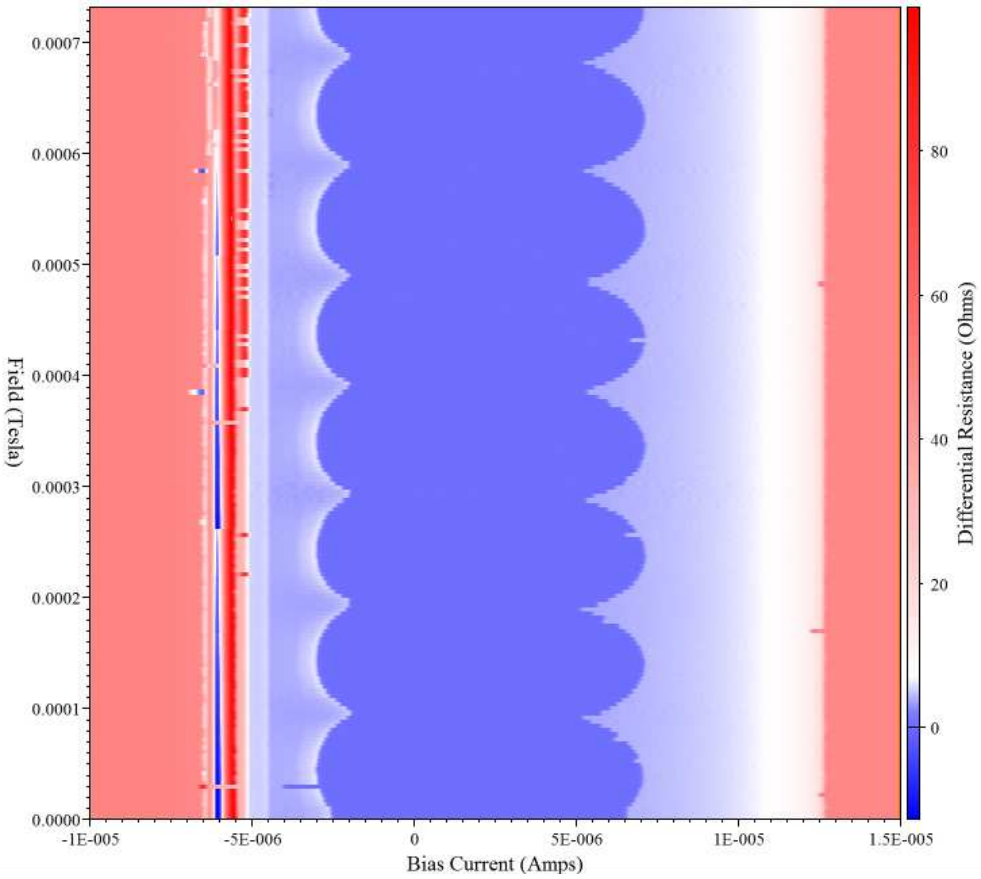

Figure 6.25: Fluctuations in dV/dI shape as a function of field. Clear oscillations are seen in the critical current of the SNS junction transition.

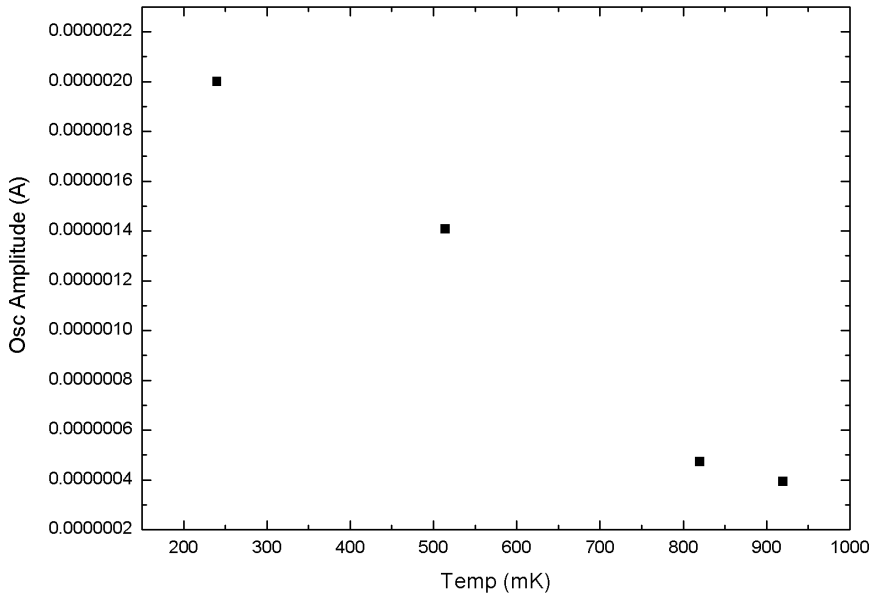

Figure 6.26: Dependence of oscillation amplitude upon temperature for the fluctuations of the first critical current.

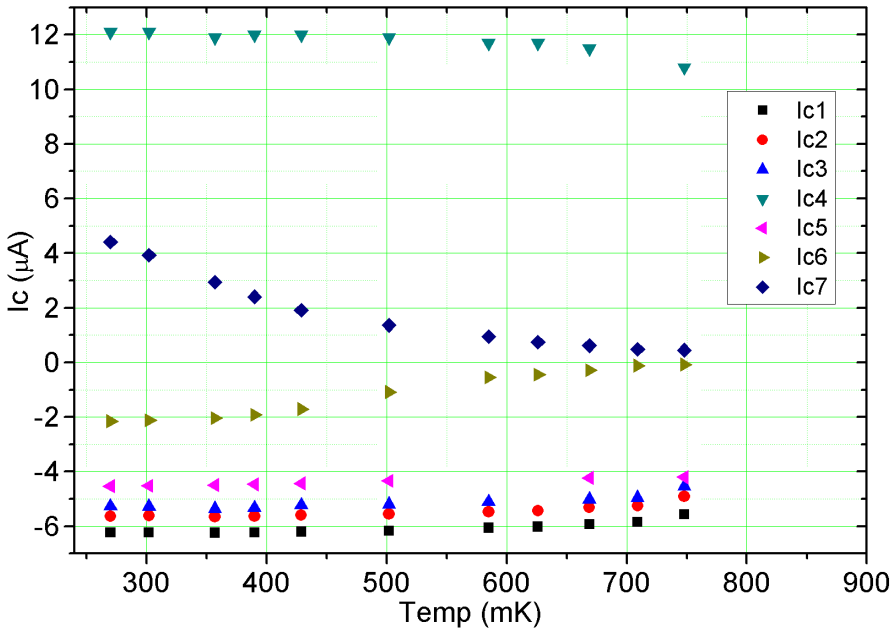

Figure 6.27: Second 1 micron sample of identical design. The dependence of the various critical currents on temperature is very similar to the first. The fully superconducting regime at zero bias again survives to around 800mK.

6.3.2 800nm Disc

The SEM image of the disc junction of the 800nm sample is shown in Fig 6.28 and the dV/dI measured at 240mK in Fig 6.29. At zero bias the entire Al wire is again fully superconducting. Driving the sample normal from its superconducting state, the entire aluminium wire is seen to go normal in one fast transition at 13.5μA bias. When the whole structure is normal its resistance is 48.1Ω. When the current is reduced a large transition at 5.80μA indicates the majority of the Al returning to the superconducting state. In a small current range beneath this a small stable resistance is seen which represents a stable SNS junction induced within the overlying Al. When in the SNS regime on the retrapping curve, the resistance of the structure is 4.5Ω. At a bias current of 4.43μA the SNS junction disappears as the Al returns to its fully superconducting state. By balancing the sample in the SNS regime, magnetoresistance oscillations can be measured as shown in Fig 6.30 where oscillations with the predicted period of 1G are measured at a bias current of 4.66μA. The amplitude of these oscillations is 1.5Ω.

The temperature dependence of the major transitions in the dV/dI of the 800nm sample is shown in Fig 6.31. Using this smaller disc a clearer image of the behaviour of the samples is seen within the temperature range available for the experiment.

The effect of varying field over 7G upon the dV/dI shape is shown in Fig 6.30. Clear oscillatory behaviour is seen in both the critical and retrapping currents with the expected period of 1G.

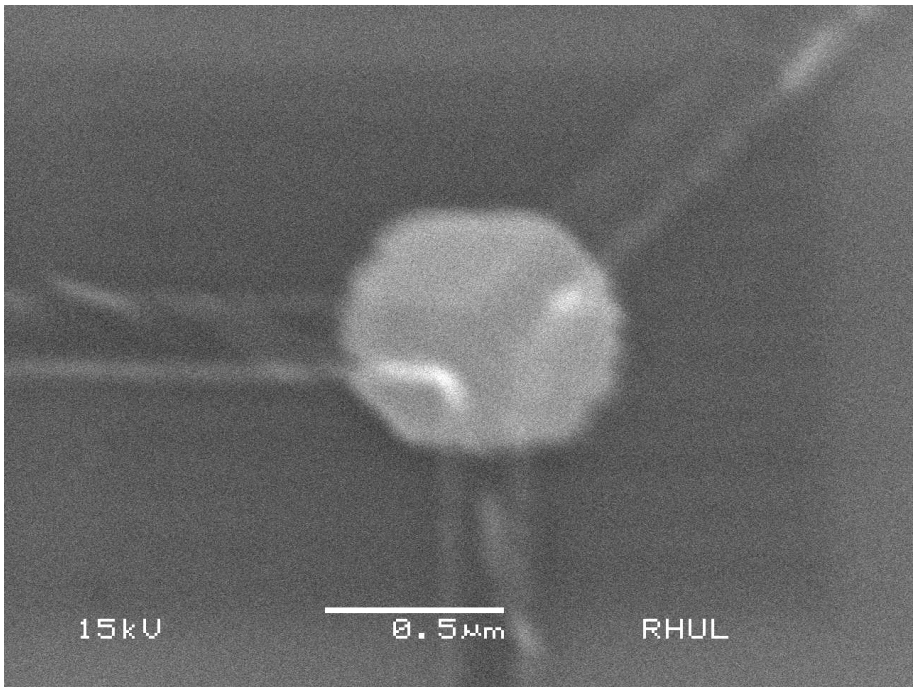

Figure 6.28: SEM of the junction in the 800nm disc structure.

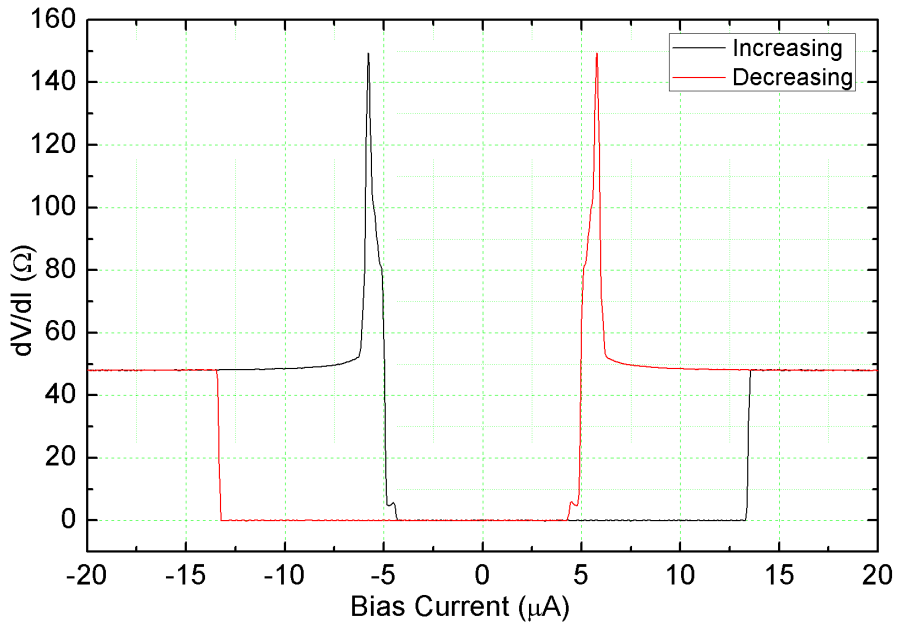

Figure 6.29: dV/dI of 800nm sample at 240mK. The resistance plateau corresponding to the SNS junction regime in the Al is smaller but still present.

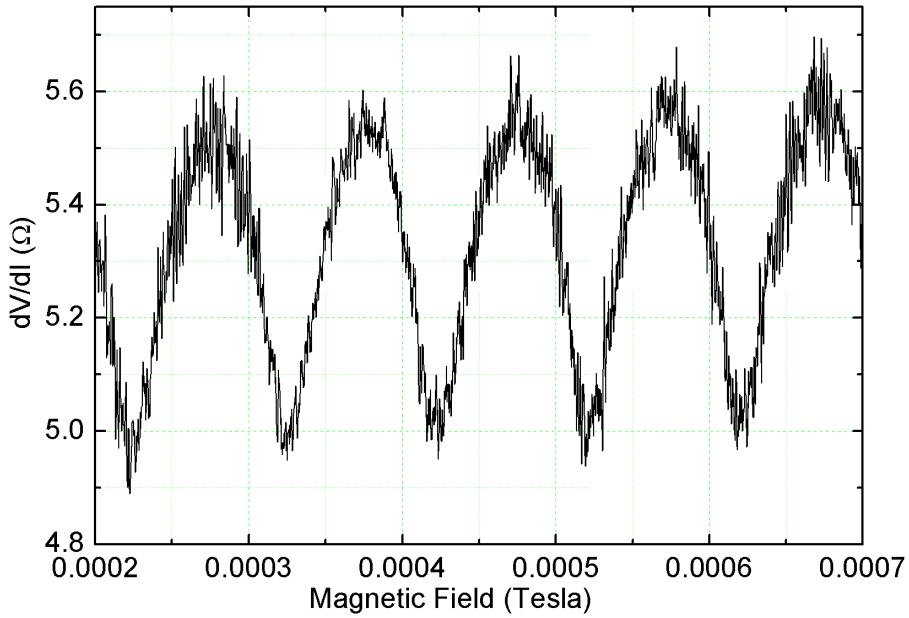

Figure 6.30: Magnetoresistance oscillations measured after first driving the structure into the normal state with a high current, then setting the bias to 4.66μA, so that the structure is balanced in the SNS state.

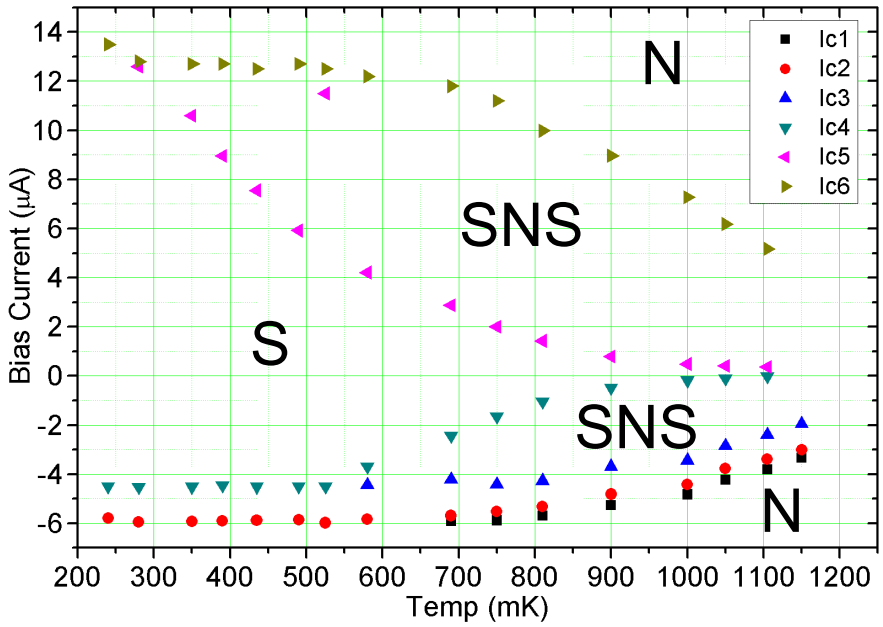

Figure 6.31: Temperature dependence of transitions in the dV/dI of the 800nm sample. A clear SNS phase where oscillations can be observed is emerging.

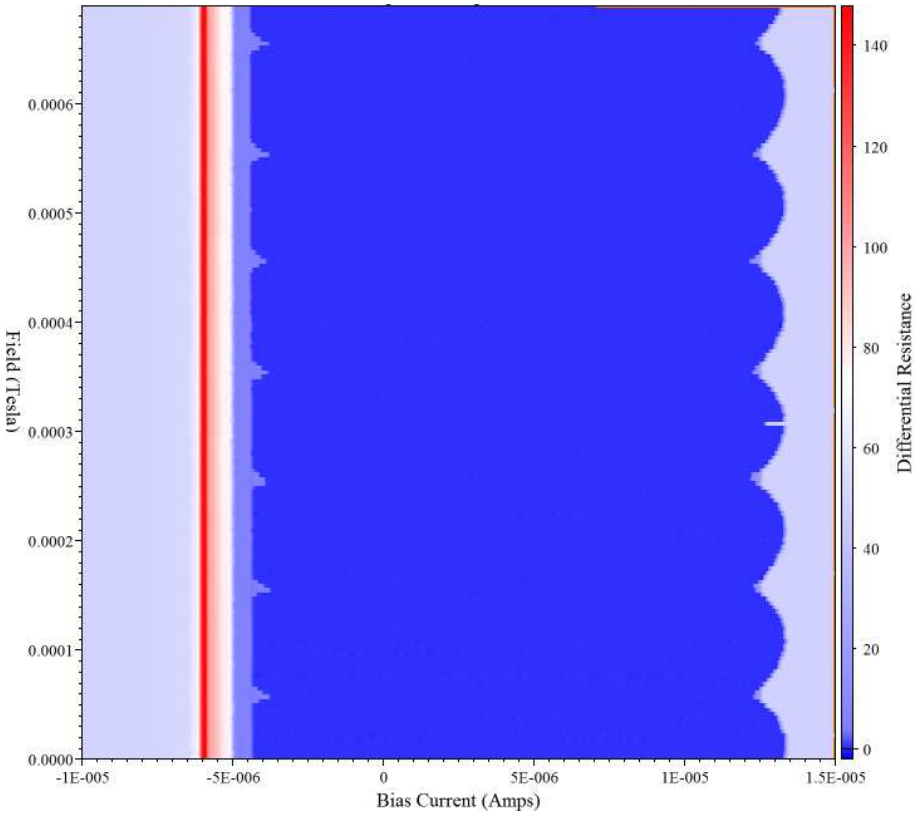

Figure 6.32: Oscillations as a function of field in the critical and retrapping currents of the 800nm sample as measured at 240mK.

6.3.3 600nm Disc

The differential resistance curve measured from the 600nm Y shape sample at 240mK is shown in Fig 6.33. The sample is fully superconducting at zero bias current and is driven completely normal in one brief transition at 23.9μA as the current is increased from zero. When reducing the current fom -15μA the bulk of the Al returns to its superconducting state at 5.29μA. A thin region still exits where an SNS junction is stable at this temperature. This SNS junction disappears as the Al becomes fully superconducting at 4.59μA. Proof of the induced SNS junction in the retrapping curve between 5.29μA and 4.59μA can be seen in Fig 6.34 where oscillations are measured as a function of magnetic field, at a bias current of 4.85μA. The period of these oscillations is again 1G as predicted. Similar oscillatory behaviour with the same period is shown in the transition between the fully superconducting and SNS states with varying field is shown in Fig 6.35.

The temperature dependence of the major transitions in the dV/dI is shown in Fig 6.36. Again the smaller disc size allows a better picture of the phase diagram to

be observed. A clearly defined temperature and bias current range in which the SNS junction exists is evident. Outside of this temperature range the critical current of the sample moves between the S and N states without establishing an SNS state, the SNS regime in the retrapping regime persists weakly to lower temperatures.

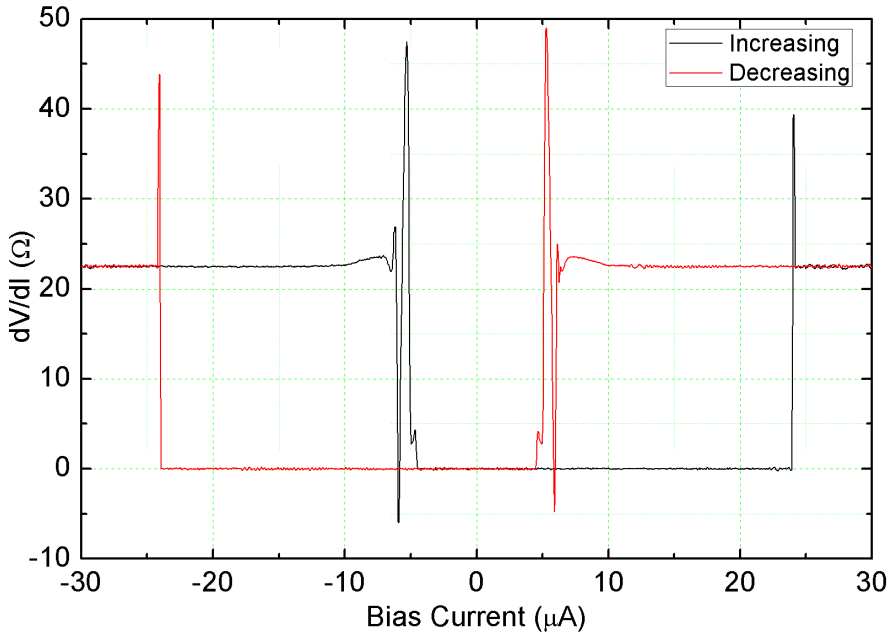

Figure 6.33: dV/dI of 600nm disc sample at 240mK. The stable SNS state is again smaller although still visible in the retrapping section of the curve.

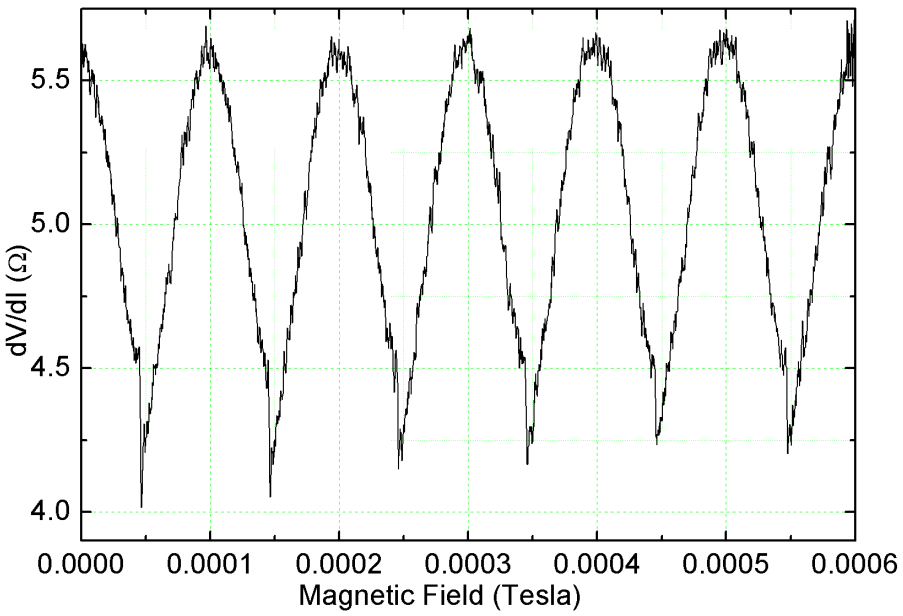

Figure 6.34: Conductance oscillations measured as a function of flux through the interferometer loop. Again the structure was driven normal by the application of a high bias, which was then reduced to 4.85μm to rest within the SNS regime.

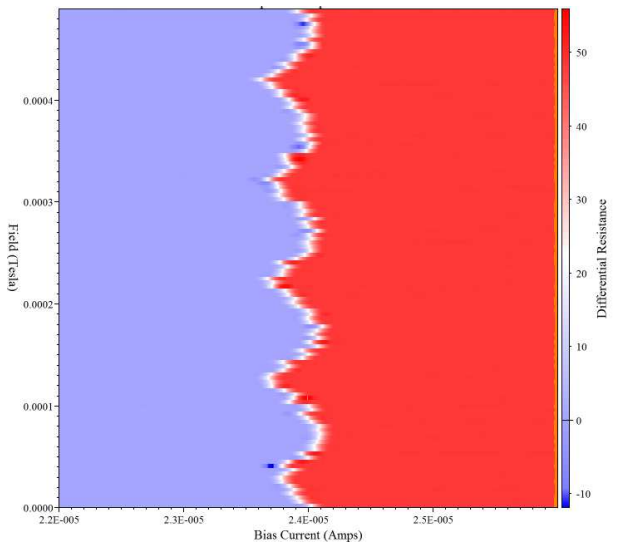

Figure 6.35: 2D plot showing oscillations in the transition from fully superconducting to SNS phases as a function of the applied field.

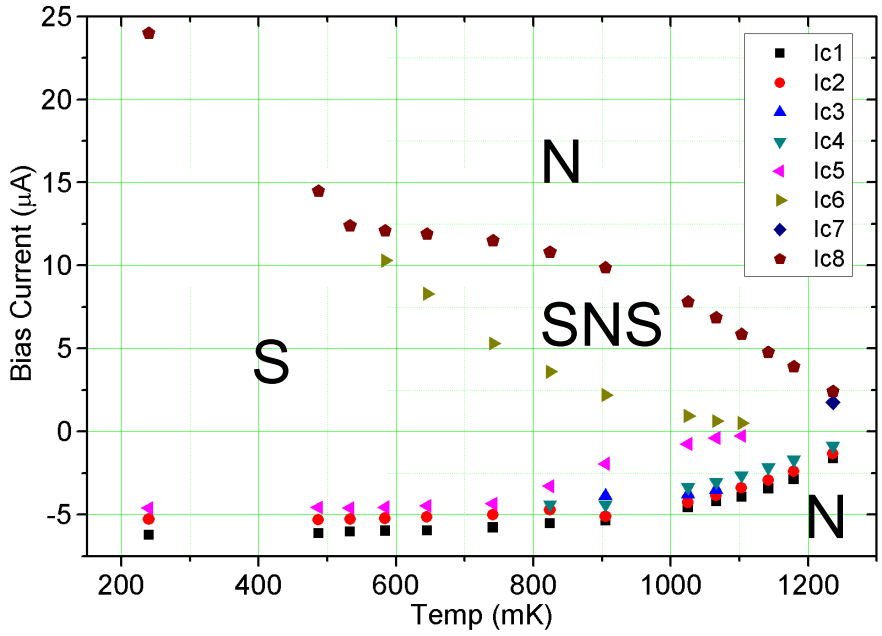

Figure 6.36: Temperature dependence of transitions in the dV/dI of the 600nm disc sample.

6.3.4 400nm Disc

The dV/dI of the 400nm Y shape sample measured at 240mK is shown in Fig 6.37. To drive the sample from its fully superconducting into its completely normal state a bias current of 67μA is required, at which point the whole Al wire changes at once. Similarly when the current is reduced, a single large peak at 5.8μA signifies the

return of the whole Al component to the fully superconducting state. No resistance plateau is seen below this retrapping current indicating that no SNS regime is stable at this temperature. This agrees with the data collected from the other disc radii which indicate that the smaller the disc size, and therefore the less powerful the ferromagnetic proximity effect, the higher the temperature required for the SNS junction to form. Further evidence for this can be seen in Fig 6.38, which shows the temperature dependence of the major transitions in this sample. The SNS junction is only seen to appear at temperatures of 1K or higher, and is only stable within a very small range of bias currents.

In spite of the lack of a stable SNS regime, direct measurement of conductance oscillations as a function of magnetic field was still possible. By setting the bias current to sit at the peak of the retrapping transition at 5.8μA, the messy oscillations shown in Fig 6.39 were measured at 240mK.

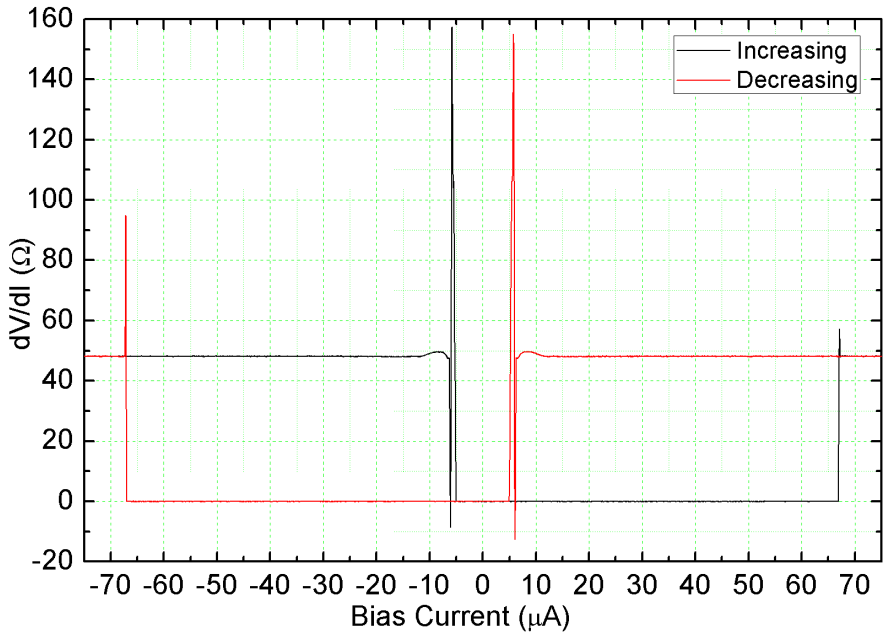

Figure 6.37: dV/dI of 400nm disc structure at 240mK. The SNS phase is again reduced.

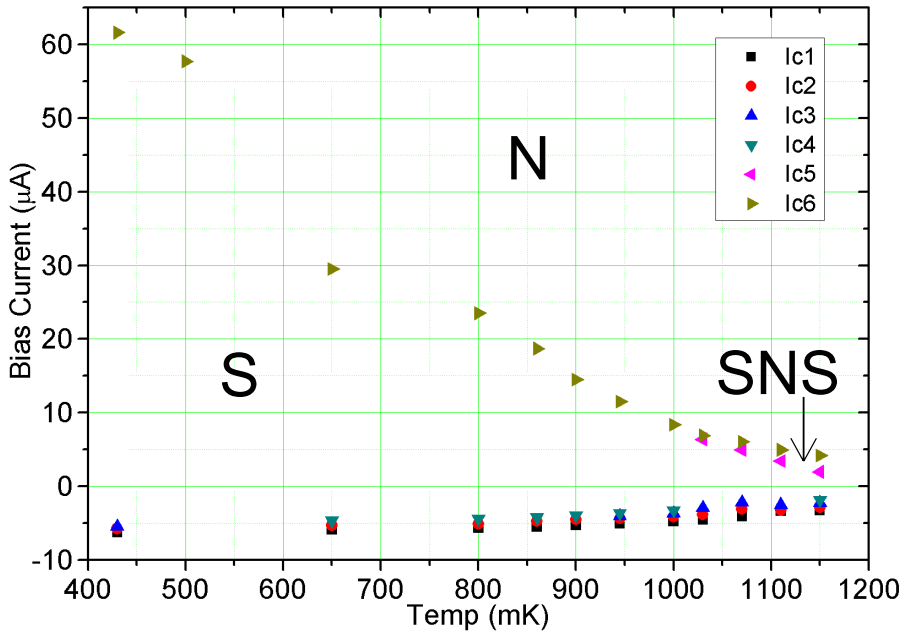

Figure 6.38: Temperature dependence of the transitions in the dV/dI of the 400nm disc structure.

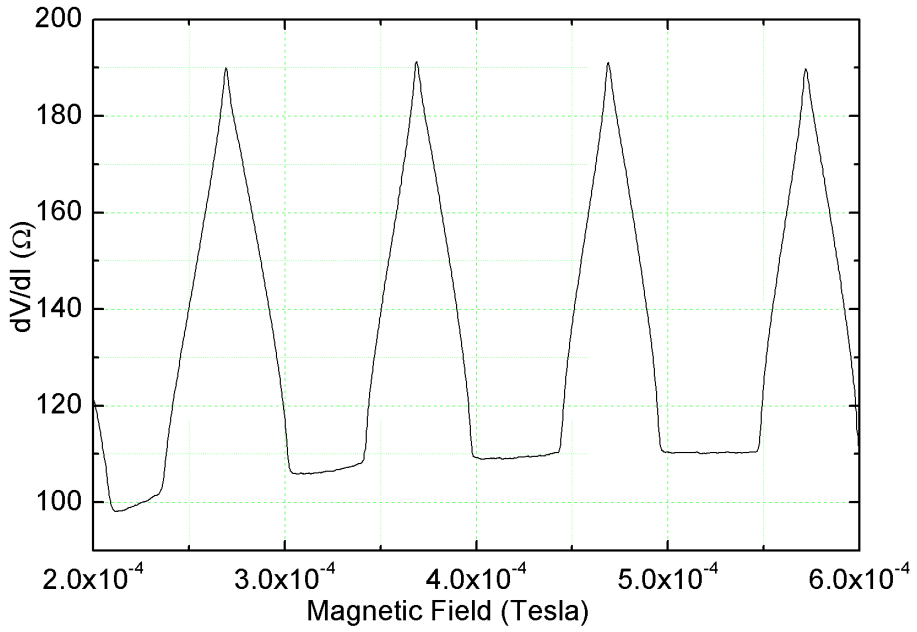

Figure 6.39: Phase periodic oscillations in the resistance of the 400nm sample. Measurement carried out at 5.8μA bias after first driving the sample normal with a high current. The unusual shape of the oscillations can be attributed to resting at a bias current slightly too low for complete sinusoidal oscillations to manifest. Due to the small range of bias currents in which stable oscillations were observable in this sample, this was the best example of oscillatory behaviour obtainable.

The steep dependence of the critical current values at 240mK on the diameter of the Ni disc is shown in Fig 6.40. The smaller discs exhibit much higher critical

and retrapping currents, as the superconductor is less inhibited by the ferromagnetic proximity effect or spin polarised current injection. Superconductivity within the entire device is significantly weakened at larger disc diameters.

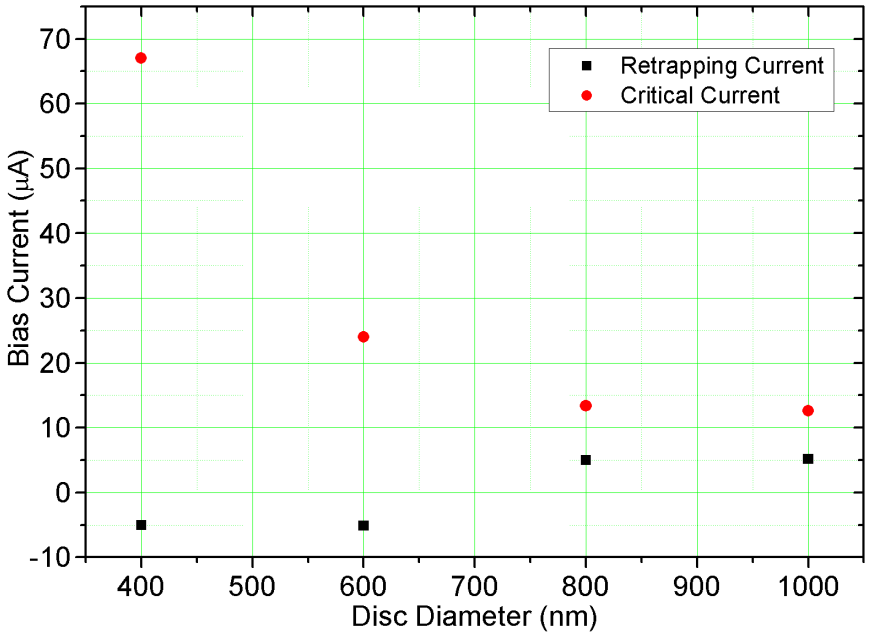

Figure 6.40: Dependence of major transitions upon diameter of the Ni disc.

6.4 Discussion of the Results

Dubos and collaborators published theoretical work on the Josephson critical current in long mesoscopic SNS junctions [29]. While some additional factors will be introduced via the ferromagnetic component of the Y shape structures, there is likely to be great similarities between their behaviour and the results obtained by Dubos et al.

In their paper they derive an expression to approximate the critical current in a diffusive junction at higher temperatures close to T_c where $K_BT >> E_{Th}$.

$$eR_NI_c = 64\pi K_BT\sum_{n=0}^{\infty}\frac{L\Delta^2 exp(-L/L_{\omega_n})}{L_{\omega_n}[\omega_n+\Omega_n+\sqrt{2(\Omega^2+\omega_n\Omega_n]})} \tag{6.1}$$

where L is the junction length, R_N is the resistance of the normal metal, $\omega_n = (2n+1)\pi K_BT$ is the Matsubara frequency, $\Omega_n = \sqrt{\Delta^2+\omega_n^2}$ and $L_{\omega_n} = \sqrt{\hbar D/2\omega_n}$

By taking only the first term (n=0) of the summation where

$\omega_n = \pi K_BT$, thus $L_{\omega_n} = \sqrt{\hbar D/2\pi K_BT}$ which is the coherence length (L_c) and for high temperatures near T_c where the energy gap is much smaller than the thermal

energy ($\Delta \ll K_B T$), $\Omega_n = \omega_n = \pi K_B T$

a simplified approximation can be made. Assuming a structure with a set junction length, it is possible to amalgamate the constants to simplify the equation. This can be reduced to

$$I_c \propto T^2 \frac{L}{L_c} e^{-L/L_c} \tag{6.2}$$

as the coherence length is given by

$$L_c = \sqrt{\frac{\hbar D}{2\pi K_B T}} \tag{6.3}$$

this can be further simplified to

$$I_c \propto T^2 \frac{1}{\sqrt{T}} e^{-R\sqrt{T}} \tag{6.4}$$

We can therefore say that

$$I_c = A T^{3/2} e^{(-R\sqrt{T})} \tag{6.5}$$

where A and R are two unknown variables. Using this simplified model, Mathematica was used to provide best fits to the data obtained for the gapless samples in the previous section. The results for the 1micron, 800nm, 600nm and 400nm discs are shown in Figs 6.41, 6.42, 6.43 and 6.44. The values of A and R for each fit are included in the figure captions.

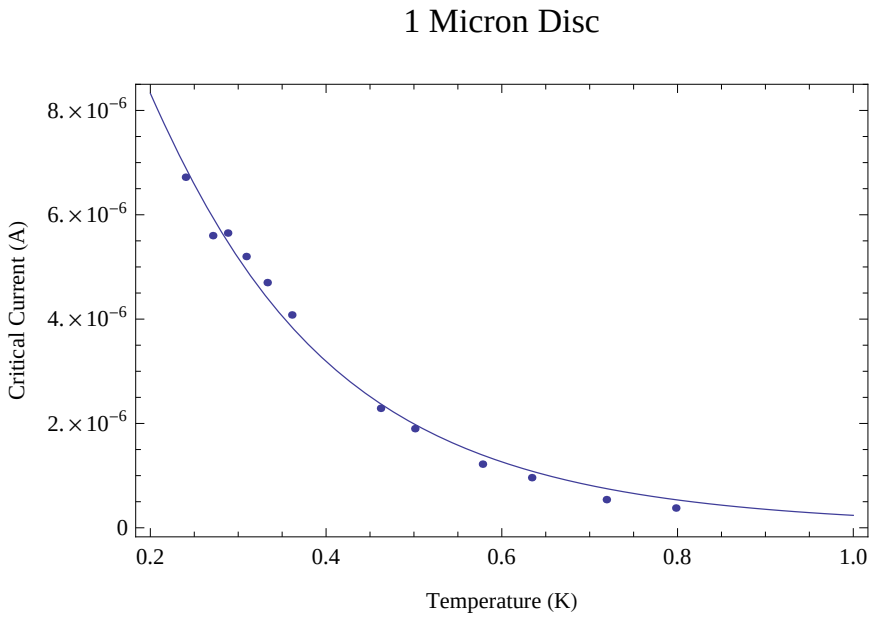

Figure 6.41: Mathematica fit for the critical current data obtained for the 1 micron sample. A = 0.0116241 R=-10.7936

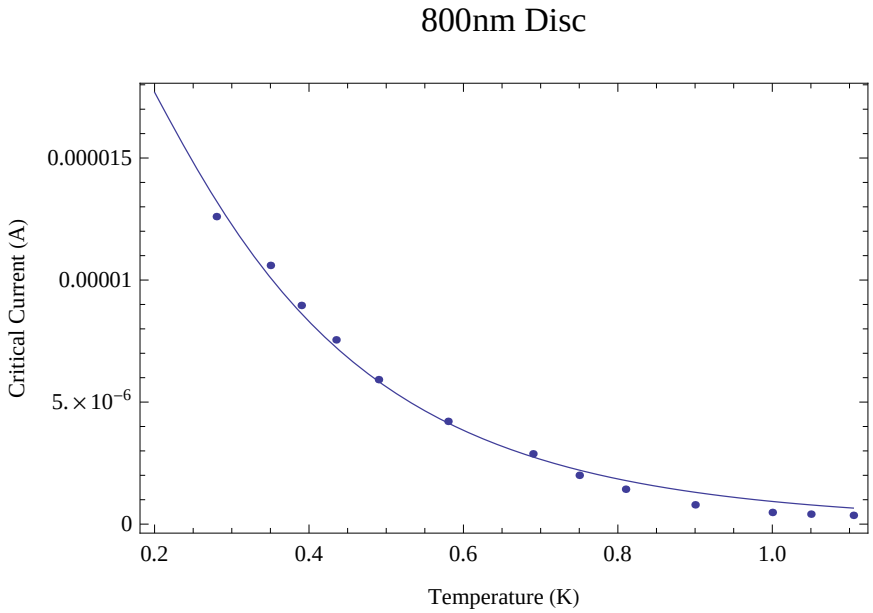

Figure 6.42: Mathematica fit for the critical current values obtained for the 800nm sample. A = 0.0953424 R = -9.16407

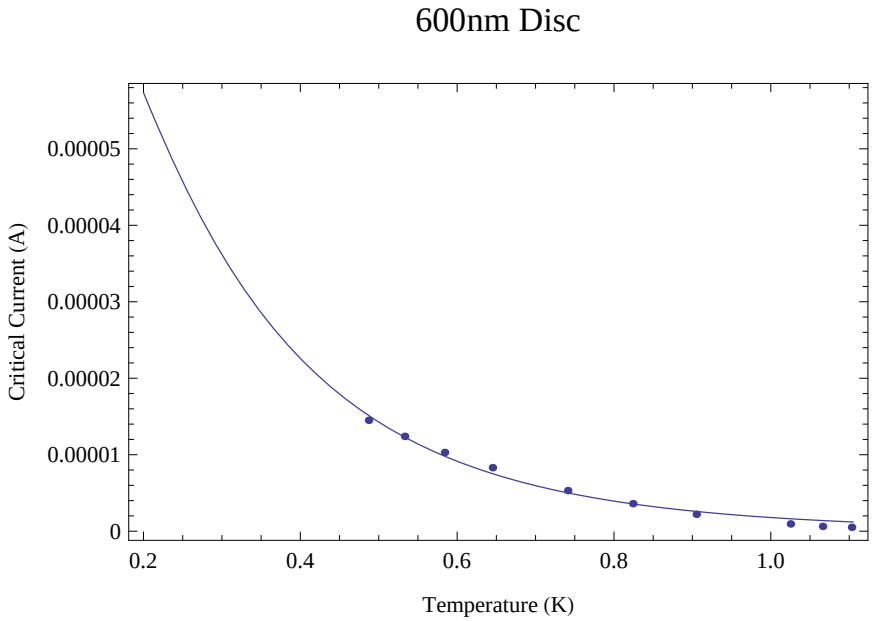

Figure 6.43: Mathematica fit for the critical current values obtained for the 600nm sample. A=0.0747858 R=-10.6416

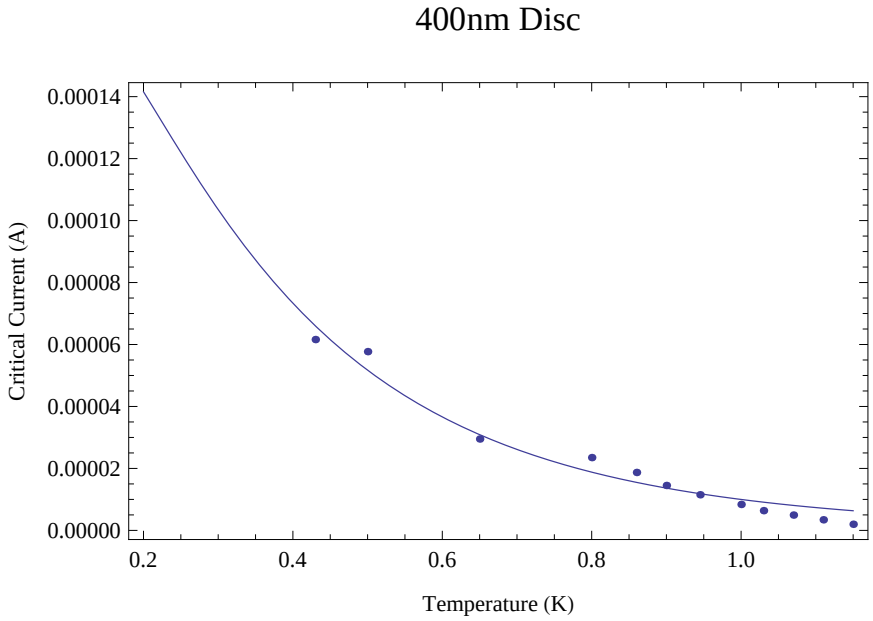

Figure 6.44: Mathematica fit for the critical current values obtained for the 400nm sample. A = 0.0953424 R= -9.16407

In the limit of very long junctions, equation 6.1 simplifies to

$$eR_N I_c = \frac{32}{3+2\sqrt{2}} E_{Th} \left[\frac{L}{L_T}\right]^3 e^{-L/L_T} \tag{6.6}$$

using this equation it is possible to calculate values for A and R in this limit, the closest experiment to these conditions is that incorporating a 1μm disc.

$$D = \frac{\nu_F l}{3} \approx 0.01 \tag{6.7}$$

where $\nu_F \approx 10^6 m/s$ and $l \approx 30 \times 10^{-9}$m

$$E_{Th} = \frac{\hbar D}{L^2} = 1.05 \times 10^{-24} \tag{6.8}$$

$$Ł_T = \sqrt{\frac{\hbar D}{2\pi K_B T}} = 1.1 \times 10^{-7} \frac{1}{\sqrt{T}} \tag{6.9}$$

$$eR_N I_c = 4.32 \times 10^{-21} T^{3/2} e^{-9.09\sqrt{T}} \tag{6.10}$$

where $e = 1.6 \times 10^{-}19$ Coulombs and $R_N = 3.47\Omega$, the normal section resistance of the 1μm Y shape sample in the SNS state. We get

$$I_c = 0.0076 T^{3/2} e^{-9.09\sqrt{T}} \tag{6.11}$$

The table 6.1 below shows the values obtained for the variables A and R via both Mathematica fitting to the data for the 1μm sample and the calculation in equation 6.11. For this longest junction the values fitted to the data are in reasonable agreement with the SNS theory.

Table 6.1: Calculated and Mathematica fit values for 1 micron Y shape

Source	A	R
Fit	0.0116241	-10.7936
Calculated	0.0076	-9.09

In table 6.2 the Mathematica fit values for all disc diameters are shown. The variables fluctuate randomly, with no evident dependence on the junction length. In conventional SNS junctions the length of the normal section is dictated by the length of the component made of that material. When the junction is induced by ferromagnetic proximity effect, its length is not given just by the diameter of the disc. The ferromagnet's range of influence may extend further than the region of superconductor overlying it. The strong impact of the interface quality on F/S coupling, and the variations in magnetic structures between the samples, will both impact on the penetration of the ferromagnetic proximity effect into the aluminium

independent of the disc size.

Table 6.2: Mathematica fit values for all disc diameters

Diameter	A	R
1000nm	0.0116241	-10.7936
800nm	0.0953424	-9.16407
600nm	0.0747858	-10.6416
400nm	0.0953424	-9.16407

Further evidence for the dramatic effect of minor changes in interface transparency can be seen by comparing the data acquired from the clean interface Y shape sample made using the modified shadow evaporation technique shown in Figs 6.1 - 6.8 with that obtained from the 400nm sample produced using the 2 stage fabrication shown in Figs 6.37 to 6.40. The maximum possible interface transparency is produced via the modified shadow evaporation technique. The 2 stage fabrication employs an Ar plasma etch to remove the majority of the accumulated nickel oxide before deposition of the Al layer. While the Ar etch is effective, some traces of contaminants still remain. These oxide remnants are seen to have a massive effect upon the F/S coupling as can be seen from the Al critical currents. The disparity is most pronounced at the fridge's base temperature where the critical currrent of the shadow evaporation fabricated sample is 27.7μA, yet the critical current of the Al in the 2 stage fabricated sample at the same temperature is 66.9μA. The sample produced using the modified shadow evaporation technique has a much lower critical current due to the increased ferromagnetic proximity effect penetrating the superconductor. This suppression of the superconductor is dramatically reduced in the 2 step fabricated sample, this results in a critical current more than twice that observed in the shadow evaporation fabricated sample. The capacity for variations in the oxidation to affect the device's functioning is a likely explanation for the random fluctuations in A and R observed in table 6.2. Differences in the magnetic structure of the discs may also result in variations in the suppression of the Al.

In this project the ferromagnetic proximity effect in mesoscopic systems is investigated in more detail than has been done previously. New theoretical work will be required to explain the results obtained.

Chapter 7

Conclusion

The primary goal of the project was to measure an unusually long-range proximity effect penetrating an inhomogeneous ferromagnet from a superconductor via generation of spin triplet correlations. The experiment was designed with careful consideration of previous experiments conducted within the field and existing theoretical models.

Hybrid Andreev interferometers comprising superconducting and inhomogeneous ferromagnetic parts were designed and fabricated in the clean room at Royal Holloway. Nanofabrication techniques were developed to allow the deposition of multiple materials without the need to break vacuum. To do this the shadow evaporation technique was tailored to suit the experimental requirements, resulting in a new, unique fabrication process. An asymmetric undercut and precise placement of the wires allowed all the extraneous ferromagnetic material to be caught on the resist wall during evaporation, and removed during the lift-off process. This resulted in a magnetically clean on-chip environment.

When measured at 240mK, superconducting phase coherent transport was observed in Al interferometers incorporating 4N Ni discs 300nm in diameter. This effect was seen to penetrate the ferromagnetic material two orders of magnitude further than predicted for singlet superconductivity. Analysis of the differences between the data from the 400nm 4N Ni disc interferometers provided several system variables which might facilitate or hinder the long-range proximity effect.

Based on this analysis, a range of studies were carried out to investigate how these variables affected the data. MFM imaging of the 300nm 4N Ni discs revealed their magnetic stucture to be significantly more complicated than initially hoped,

with a tendency towards a fractured vortex formed of randomly placed domains. As a consequence, further OOMMF modelling and MFM imaging of new geometries and materials was carried out in an attempt to pin stable reproducible inhomogeneities in mesoscopic ferromagnets. Triangles were found to be the best shape for such magnets, while permalloy was found to produce the clearest magnetic structures. Interferometers incorporating Py triangles were measured at 240mK. Although no long-range coherence was observed, a greater number of the permalloy samples exhibited features in their dV/dIs below the Al critical current. The use of ultra-low temperatures in further experiments would increase the probability of observing coherent transport in these samples.

In an attempt to increase the coherence length of the system some interferometers were made incorporating high purity 5N Ni triangles, these were measured both at 240mK and at <50mK. Some hints of coherent effects were observed below 100mK.

The final study carried out in the search for triplet superconductivity was an attempt to reduce the ferromagnetic proximity effect penetrating the superconducting electrodes by introducing a thin oxide layer at the S/F interface. A fabrication technique was mastered which allowed the partial oxidation of the Ni surface before the deposition of the Al layer. A small number of hybrid interferometers incorporating partially oxidised 5N Ni triangles were fabricated and measured. None of the small number measured at low temperature showed evidence of a long-range superconducting proximity effect. The incorporation of a partially oxidised interface to the samples was justified by experimental data clearly showing how such a thin barrier inhibits the ferromagnetic proximity effect within the superconductor.

The search for a long-range proximity effect within inhomogeneous ferromagnetic material produced definitive proof that such a phenomenon is possible within the types of nanostructures examined in the project. Significant advances were made in controlling the properties of the system to optimise the effect. Further work should include the measurement of a greater number of partially oxidised 5N Ni triangle hybrid interferometers to provide better statistics on their functionality. Due to the problems in pinning specific magnetisations within Ni structures, it is quite probable that in the few structures of this type so far measured there was not a suitable inhomogeneity close enough to the superconducting electrode for a long-range triplet component to be generated.

In future studies, the greatest potential for further observation of a triplet prox-

imity effect would be achieved via the use of partially oxidised permalloy triangles incorporated into hybrid aluminium (or higher T_c superconductor) interferometers. These devices should then be measured at ultra low temperatures to optimise the penetration of any proximity effects within the permalloy and mitigate the high level of disorder within the alloy.

The ferromagnetic proximity effect was also studied, with several key results. A strong dependence was found between the quality of the S/F interface and the penetration of the ferromagnetic order parameter into the superconductor. The more transparent the interface the greater the suppression of the superconductor.

A novel interferometer based upon a strong ferromagnetic proximity effect inducing a SNS junction within an overlying Al wire was developed, and quantum interference phenomena observed within such devices. As already stated in Chapter 6, this interferometer type has the potential to produce greater amplitude signals than previous designs based on multi material SNS junctions. This is due to elimination of non-Andreev scattering at the S/N interface. The possibility of 100% signal modulation in correctly biased devices also makes them an attractive prospect. Further work should include the measurement of the noise properties of these devices. The properties of short SNS junctions induced via the ferromagnetic proximity effect were also measured, and clear phase diagrams showing their behaviour were obtained.

A number of the results obtained in this project have no explanation in existing theories, and should serve as a basis for the development of new theoretical work.

Bibliography

[1] R. Holm and W. Meissner. *Z.Physik.*, 74:715, 1932.

[2] M. Eschrig. Spin-Polarized supercurrents for spintronics. *Physics Today*, 64:1:43, 2011.

[3] Victor M. Edelstein. Triplet superconductivity and magnetoelectric effect near the s -wave-superconductor˘ normal-metal interface caused by local breaking of mirror symmetry. *Phys. Rev. B*, 67:020505, Jan 2003.

[4] V. Petrashov, V. Antonov, S. Maksimov, and R. S. Shaikhaidarov. Conductivity of mesoscopic sstructure with ferromagnetic and superconducting regions. *JETP Letters*, 59:8:551–555, 1994.

[5] M. Giroud, H. Courtois, K. Hasselbach, D. Mailly, and B. Pannetier. Superconducting proximity effect in a mesoscopic ferromagnetic wire. *Phys. Rev. B*, 58:R11872–R11875, Nov 1998.

[6] V. T. Petrashov, I. A. Sosnin, I. Cox, A. Parsons, and C. Troadec. Giant mutual proximity effects in ferromagnetic/superconducting nanostructures. *Phys. Rev. Lett.*, 83:3281–3284, Oct 1999.

[7] V. Chandrasekhar J. Aumentado. Mesoscopic ferromagnet/superconductor junctions and the proximity effect. *Phys. Rev. B*, 2001.

[8] F. S. Bergeret, A. F. Volkov, and K. B. Efetov. Long-range proximity effects in superconductor- ferromagnet structures. *Phys. Rev. Lett.*, 86:4096–4099, Apr 2001.

[9] I. Sosnin, H. Cho, V. T. Petrashov, and A. F. Volkov. Superconducting phase coherent electron transport in proximity conical ferromagnets. *Phys. Rev. Lett.*, 96:157002, Apr 2006.

[10] I. T. M. Usman, K. A. Yates, J. D. Moore, K. Morrison, V. K. Pecharsky, K. A. Gschneidner, T. Verhagen, J. Aarts, V. I. Zverev, J. W. A. Robinson, J. D. S. Witt, M. G. Blamire, and L. F. Cohen. Evidence for spin mixing in holmium thin film and crystal samples. *Phys. Rev. B*, 83:144518, Apr 2011.

[11] T. S. Khaire, M. A. Khasawneh, W. P. Pratt, and N. O. Birge. Observation of spin-triplet superconductivity in co-based Josephson junctions. *Phys. Rev. Lett.*, 104:137002, Mar 2010.

[12] S. D. Bader. Opportunities in nanomagnetism. *Rev. Mod. Phys.*, 78:1–15, Jan 2006.

[13] R. P. Cowburn, D. K. Koltsov, A. O. Adeyeye, M. E. Welland, and D. M. Tricker. Single-domain circular nanomagnets. *Phys. Rev. Lett.*, 83:1042–1045, Aug 1999.

[14] D. H. Kim, E. A. Rozhkova, I. V. Ulasov, S. D. Bader, T. Rajh, M. S. Lesniak, and V Novosad. Biofunctionalized magnetic-vortex microdiscs for targeted cancer-cell destruction. *Nature Materials*, 9:165171, 2010.

[15] T. Shinjo, T. Okuno, R. Hassdorf, K. Shigeto, and T. Ono. Magnetic vortex core observation in circular dots of permalloy. *10.1126/science.289.5481.930*, 2000.

[16] J. Bardeen, L. N. Cooper, and J. R. Schrieffer. Theory of superconductivity. *Physical Review*, vol. 108, Issue 5:1175–1204, 1957.

[17] E. Fermi. *Rendiconti Lincci*, 145-9, 1926.

[18] P. A. M. Dirac. *Proceedings of the Royal Society*, Series A 112 (762) 661-77, 1926.

[19] A. Rose-Innes. *Introduction to superconductivity*. Oxford, New York, Pergamon Press, 1977.

[20] K. K. Likharev. *Dynamics of Josephson Junctions and Circuits*. CRC Press, 1986.

[21] W.S. Corak, B.B. Goodman, and C.B. Satterthwaite. *Phys. Rev.*, 96:225, 1946.

[22] Andrei Mourachkine. *Room-temperature Superconductivity*. Cambridge Int Science Publishing, 2004.

[23] B. D. Josephson. Possible new effects in superconductive tunnelling. *Physics Letters*, 1:251, 1962.

[24] P. W. Anderson and J. M. Rowell. Probable observation of the Josephson superconducting tunneling effect. *Phys. Rev. Lett.*, 10:230–232, Mar 1963.

[25] D. A. Cardwell and D. S. Ginley. *Handbook of superconducting materials, Volume 1*. IOP, 2003.

[26] J. F. Annett. *Superconductivity, Superfluids, Condensates*. Oxford University Press, 2004.

[27] De Gennes. *Rev. Mod. Phys*, 36(1):225–237, 1964.

[28] C. Checkley. *Andreev Interferometry of Flux Qubits Driven By Radio Frequency Field*. PhD thesis, Royal Holloway, University of London, 2009.

[29] P. Dubos, H. Courtois, B. Pannetier, F. K. Wilhelm, A. D. Zaikin, and G. Schön. Josephson critical current in a long mesoscopic S-N-S junction. *Phys. Rev. B*, 63:064502, Jan 2001.

[30] K. K. Likharev. *Sov. Tech. Phys. Lett.*, 2, 12, 1976.

[31] A. F. Andreev. Thermal conductivity of the intermediate state of superconductors. *Sov. Phys. JETP*, 19:1228, 1964.

[32] P. M. Ostrovsky, M. A. Skvortsov, and M. V. Feigelman. Density of states in a mesoscopic SNS junction. *Journal of Experimental and Theoretical Physics Letters*, Volume 75, Issue 7,:pp 336–341, April 2002,.

[33] V. T. Petrashov, V. N. Antonov, P. Delsing, and R. Claeson. Phase memory effects in mesoscopic rings with superconducting “mirrors”. *Phys. Rev. Lett.*, 70:347–350, Jan 1993.

[34] V. T. Petrashov, V. N. Antonov, P. Delsing, and R. Claeson. Phase controlled mescopic ring interferometer. *JETP Letters*, 60(8):606–611, 1994.

[35] V. T. Petrashov, V. N. Antonov, P. Delsing, and R. Claeson. Phase controlled conductance of mesoscopics structures with superconducting mirrors. *Physical Review Letters,*, Vol. 74, No. 26:p. 5268–5271., 1995.

[36] I. D. Landau and E. M. Lifschitz. *Physik Z. Sowjetunion*, 8. 153, 1935.

[37] David Jiles. *Introduction to Magnetism and Magnetic Materials*. Chapman and Hall, 1991.

[38] P. A. Tipler and R. Llewellyn. *Modern Physics*. Worth Publishers, Incorporated, 1999.

[39] V. L. Mironov, O. L. Ermolaeva, S. A. Gusev, A. Yu. Klimov, V. V. Rogov, B. A. Gribkov, O. G. Udalov, A. A. Fraerman, R. Marsh, C. Checkley, R. Shaikhaidarov, and V. T. Petrashov. Antivortex state in crosslike nanomagnets. *Phys. Rev. B*, 81:094436, Mar 2010.

[40] T Fischbacher, M. Franchin, G. Bordignon, and H. Fangohr. A systematic approach to multiphysics extensions of finite-element-based micromagnetic simulations: Nmag. *IEEE Transactions on Magnetics*, 43:2896–2898, 2007.

[41] T. Schrefl D. Suess R. Dittrich H. Forster V. Tsiantos W. Scholz, J. Fidler. "scalable parallel micromagnetic solvers for magnetic nanostructures",. *Comp. Mat. Sci.*, 28:366–383, 2003.

[42] ITL/NIST. *OOMMF User's Guide*, 2004.

[43] D. G. Porter and M. J. Donahue. Precession axis modification to a semi-analytical Landau-Lifshitz solution technique. *Journal of Applied Physics*, Volume:103 , Issue: 7:07D920 – 07D920–3, 2008.

[44] X. Feng and P. B. Visscher. Coarse-graining Landau-Lifshitz damping. *Journal of Applied Physics*, 89:11, 2001.

[45] D Tanabe, K andChiba, J. Ohe, S. Kasai, H. Kohno, S. E. Barnes, S. Maekawa, K. Kobayashi, and T. Ono. Spin-motive force due to a gyrating magnetic vortex. *Nature Communications*, Vol. 3 Article number: 845, 2012.

[46] A. Wachowiak, J. Wiebe, M. Bode, M. Morgenstern, and R. Wiesendanger. Direct observation of internal spin structure of magnetic vortex cores. *Science*, 18:577–580, 2002.

[47] V Novosad, K. Yu. Guslienko, H. Shima, Y. Otani, K. Fukamichi, N. Kikuchi, O. Kitakami, and Y. Shimada. Nucleation and annihilation of magnetic vortices in sub-micron permalloy dots. *IEEE Transactions on Magnetic*, Vol 37 No 4, 2001.

[48] K. S. Buchanan, A. Hoffmann, V. Novosad, and S. D. Bader. Translational-mode dynamics of exchange-biased vortices. *Journal of Applied Physics*, 103, 07B102, 2008.

[49] K. L. Metlov and K. Y. Guslienko. Stability of magnetic vortex in soft magnetic nano-sized circular cylinder. *arXiv:cond-mat/0110037v11*, Oct 2001.

[50] M. Jaafar, R. Yanes, D. Perez de Lara, O. Chubykalo-Fesenko, A. Asenjo, E. M. Gonzalez, J. V. Anguita, M. Vazquez, and J. L. Vicent. Control of the chirality and polarity of magnetic vortices in triangular nanodots. *Phys. Rev. B*, 81:054439, Feb 2010.

[51] S. Yakata, M. Miyata, S. Honda, H. Itoh, H. Wada, and T. Kimura. Chirality control of magnetic vortex in a square py dot using current-induced oersted field. *Appl. Phys. Lett.*, 99,:242507, 2011.

[52] A. I. Buzdin. Proximity effects in superconductor-ferromagnet heterostructures. *Rev. Mod. Phys.*, 77:935–976, Sep 2005.

[53] E. A. Demler, G. B. Arnold, and M. R. Beasley. Superconducting proximity effects in magnetic metals. *Phys. Rev. B*, 55:15174–15182, Jun 1997.

[54] A. Buzdin et al. *JETP Lett*, 53:321, 1991.

[55] T. Kontos, M. Aprili, J. Lesueur, and X. Grison. Inhomogeneous superconductivity induced in a ferromagnet by proximity effect. *Phys. Rev. Lett.*, 86:304–307, Jan 2001.

[56] V. V. Ryazanov, V. A. Oboznov, A. Yu. Rusanov, A. V. Veretennikov, A. A. Golubov, and J. Aarts. Coupling of two superconductors through a ferromagnet: Evidence for a pi junction. *Phys. Rev. Lett.*, 86:2427–2430, Mar 2001.

[57] M. Eschrig and T. Lffwander. Triplet supercurrents in clean and disordered half-metallic ferromagnets. *Nature Physics*, 4:138 – 143, 2008.

[58] P. Fulde and R. A. Ferrell. Superconductivity in a strong spin-exchange field. *Phys. Rev.*, 135:A550, 1964.

[59] A. I. Larkin and Yu. N. Ovchinnikov. *Zh. Eksp. Teor. Fiz.*, 47:1136, 1964.

[60] F. S. Bergeret, A. F. Volkov, and K. B. Efetov. Josephson current in superconductor-ferromagnet structures with a nonhomogeneous magnetization. *Phys. Rev. B*, 64:134506, Sep 2001.

[61] F.S. Bergeret, A.F. Volkov, and K.B. Efetov. Nonhomogeneous magnetization and superconductivity in superconductor/ferromagnet structures. *Physica C: Superconductivity*, 367(14):107 – 116, 2002.

[62] F. S. Bergeret, V. V. Pavlovski, A. F. Volkov, A., and K. B. Efetov. Transport and triplet superconducting condensate in mesoscopic ferromagnet-superconductor stuctures. *International Journal of Modern Physics B*, 16(10):1459–1478, 2002.

[63] A. F. Volkov, A. Anishchanka, and K. B. Efetov. Odd triplet superconductivity in a superconductor/ferromagnet system with a spiral magnetic structure. *Phys. Rev. B*, 73:104412, Mar 2006.

[64] J. Linder, Y. Takehito, and S. Asle. Identifying the odd-frequency superconducting state by a field-induced Josephson effect. *arXiv:0712.0134*, 2008.

[65] Audrey Cottet. Inducing odd-frequency triplet superconducting correlations in a normal metal. *Phys. Rev. Lett.*, 107:177001, Oct 2011.

[66] J. W. A. Robinson, J. D. S. Witt, and M. G. Blamire. Controlled injection of spin-triplet supercurrents into a strong ferromagnet. *Science*, 329(5987):59–61, 2010.

[67] R. S. Keizer, S. T. B. Goennenwein, T. M. Klapwijk, G. Miao, G. Xiao, and A. Gupta. A spin triplet supercurrent through the half-metallic ferromagnet CrO2. *Nature*, 439,:825–827, 2006.

[68] M. Houzet and A. I. Buzdin. Long range triplet Josephson effect through a ferromagnetic trilayer. *Phys. Rev. B*, 76:060504, Aug 2007.

[69] Mikhail S. Kalenkov, Andrei D. Zaikin, and Victor T. Petrashov. Triplet superconductivity in a ferromagnetic vortex. *Phys. Rev. Lett.*, 107:087003, Aug 2011.

[70] T. Tokuyasu, J. A. Sauls, and D. Rainer. Proximity effect of a ferromagnetic insulator in contact with a superconductor. *Phys. Rev. B*, 38:8823–8833, Nov 1988.

[71] F. S. Bergeret, A. Levy Yeyati, and A. Martin-Rodero. Inverse proximity effect in superconductor-ferromagnet structures: From the ballistic to the diffusive limit. *Phys. Rev. B*, 72:064524, Aug 2005.

[72] F. S. Bergeret, A. F. Volkov, and K. B. Efetov. Induced ferromagnetism due to superconductivity in superconductor-ferromagnet structures. *Phys. Rev. B*, 69:174504, May 2004.

[73] M. A. Sillanp, T. T. Heikkil, Lindell R. K., and Hakone P. J. Inverse proximity effect in superconductors near ferromagnetic material. *Europhys. Lett.*,, 56 (4):pp. 590–595, 2001.

[74] Jing Xia, V. Shelukhin, M. Karpovski, A. Kapitulnik, and A. Palevski. Inverse proximity effect in superconductor-ferromagnet bilayer structures. *Phys. Rev. Lett.*, 102:087004, Feb 2009.

[75] D. F. Kyser and N. S. Viswanathan. *J. Vac. Sci. Technol.*, 12:1305–1308, 1975.

[76] Stock image available in clean room at Royal Holloway. Author unknown.

[77] T. A. Fulton and G. J. Dolan. Observation of single-electron charging effects in small tunnel junctions. *Physical Review Letters*, 59:109–112, 1987.

[78] C. Wasshuber. http://www.iue.tuwien.ac.at/phd/wasshuber/node51.html.

[79] Richard Marsh. *Superconducting Phase Coherent Transpot in Nano-Engineered Ferromagnetic Vortices.* PhD thesis, Royal Holloway, University of London, 2012.

[80] P. Das, R. de Bruyn Ouboter, and K.W. Taconis. A realization of a London-Clarke-Mendoza type refrigerator. *Plenum Press, New York, 1965*, 1964.

[81] V. L. Mirinov. *Fundamentals of Scanning Probe Microscopy*. Russian Academy of Sciences, 2004.

[82] M. Natali, I. L. Prejbeanu, A. Lebib, L. D. Buda, K. Ounadjela, and Y. Chen. Correlated magnetic vortex chains in mesoscopic cobalt dot arrays. *Phys. Rev. Lett.*, Volume 88, Number 15, 2002.

[83] S. Yakata, M. Miyata, S. Honda, H. Itoh, H. Wada, and T. Kimura. Chirality control of magnetic vortex in a square py dot using current-induced oersted field. *Applied Physics Letters*, Volume 99 , Issue 24, 2011.

[84] P.M. Tedrow and R. Meservey. Spin-dependent tunneling into ferromagnetic nickel. *Phys. Rev. Lett.*, 26:4:192–195, 1971.

[85] P. M. Tedrow and R. Meservey. Spin polarization of electrons tunneling from films of Fe, Co, Ni, and Gd. *Phys. Rev. B*, 7:318–326, Jan 1973.

[86] J. E. Villegas and I. K. Schuller. Controllable manipulation of superconductivity using magnetic vortices. *Superconductor Science and Technology*, 24, 2011.